THE EFFECT OF SPINNING CONDITIONS ON THE GAS PERMEATION PERFORMANCE OF HOLLOW FIBRE MEMBRANES

by

SIMON J. SHILTON BSc (Hons)

A thesis submitted for the degree of

Doctor of Philosophy

at the University of Strathclyde

Department of Chemical and Process Engineering

University of Strathclyde

Glasgow

1992

CONTAINS

DISKETTE

TO ALLISON

ACKNOWLEDGEMENTS

I would like to thank:

Dr G. Bell, BSc, PhD, CEng, MIChemE and **Professor J. Ferguson**, BSc, ARCST, PhD, DSc, CChem, FRSC for the opportunity they provided and for their steady supervision.

The Science and Engineering Research Council for funding.

Mr K. M. Campbell, Mr W. Barr, Mr J. Clark and their **technical staff** for workshop assistance.

Dr A. M. Vaidya, BEng, PhD and **Dr N. E. Hudson**, TD, BSc, PhD for helpful discussion.

Mr J. Morrow and **Mrs V. A. Dunn** for laboratory assistance.

Professor C. D. Grant, BSc, PhD, CEng, FIChemE and **Professor M. L. Hitchman**, BSc, DPhil, CChem, FRSC for allowing use of departmental facilities.

ABSTRACT

An investigation of the effect of spinning conditions on the gas transmission properties of hollow fibre membranes has been carried out.

A hollow fibre spinning rig was designed and fabricated. This included the construction of a novel tube-in-orifice type spinneret. Gas permeation apparatus was also designed and assembled allowing membrane modules to be tested at pressures of up to 100 bar.

Polysulphone and polyacrylonitrile membranes were spun from solutions in dimethylformamide using a dry jet wet spinning technique. Membranes were produced under various spinning conditions and then characterised with respect to physical properties, morphology, gas permeability and selectivity. Carbon dioxide, methane, oxygen and nitrogen were used as test gases. The effect of coating the membranes with silicone was also examined. The work focused on rheological influences during spinning and thus the spinning dopes were rheologically characterised under shear and elongation.

A computer program was written to solve the problem of flow of a power law fluid through a concentric annulus. This enabled the conditions of shear in the spinneret to be determined. Gas transfer through asymmetric membranes was modelled allowing fine details of fibre structure to be deduced from gas permeation characteristics. The structural information was used to interpret the relationship between spinning conditions and fibre properties.

Spinning dopes were found to be thinning in shear and extension and exhibited signs of viscoelasticity especially by virtue of Trouton ratios.

All uncoated membranes displayed gas transmission properties symptomatic of pore flow. Once coated, the polysulphone fibres exhibited separation qualities characteristic of solution diffusion. Polyacrylonitrile membrane selectivities were unimproved on coating due to the very low intrinsic permeability of the polymer. As a consequence, observations were centred on polysulphone fibres.

Membrane surface porosity, active layer thickness and effectiveness of coating determine the degree to which the intrinsic separation potential of a polymer is realised. Polymer intrinsic selectivity was found to increase with dope extrusion rate. The elevated levels of shear in the spinneret may enhance the orientation of polymer molecules. Increasing the jet stretch ratio during spinning had a detrimental effect on polymer intrinsic selectivity. Increased elongation possibly results in an unfavourable polymer structure.

Actual membrane selectivities were disappointing. It is likely that a modest improvement in coating would significantly boost separation performance.

The suggested effects of dope extrusion rate and jet stretch ratio should be confirmed in the future by direct measurement of polymer orientation.

CONTENTS

Enclosure: 3 ½ " Floppy Disk - Flow Model Software

Located in Back Cover Recess

LIST OF FIGURES

LIST OF TABLES

[a] Coating Solution - 3% w/w Silicone in Hexane

[a] Coating Solution - 3% w/w Silicone in Hexane

[b] Coating Solution - 15% w/w Silicone in Hexane

LIST OF GRAPHS

LIST OF SYMBOLS

A	Membrane Surface Area
A_f	Cross Sectional Area of Fibre
A_p	Fraction of Membrane Surface Area that is Pores (Surface Porosity)
A_{SP}	Dope Extrusion Area of Spinneret
α_j^i	Separation Factor
α	Constant
C	Concentration
C_D	Spinning Dope Concentration
d_O	Fibre Outer Diameter
d_L	Fibre Lumen Diameter
D	Diffusion Coefficient (Diffusivity)
d_f	Solid Fibre Diameter
d_{SP}	Plain Orifice Spinneret Diameter
d_m	Molecular Diameter
DER	Dope Extrusion Rate
$\dot{\epsilon}$	Strain Rate
ϵ	Strain
ξ	Normalised Radius of Spinneret
F	Force
g	Acceleration due to Gravity
$\dot{\gamma}$	Shear Rate
h_{gap}	Height of Dry Jet Gap
J	Flux
JS	Jet Stretch Ratio
K	Constant

L	Length or Thickness
L_O	Thickness of Active Layer of Membrane
L_S	Thickness of Silicone Coating Layer
L_P	Depth to which Silicone Penetrates Pores
LER	Linear Extrusion Rate (Extrusion Speed)
$\overline{M}_W$	Weight Average Molecular Weight of Polymer
M	Molecular Weight
M_1	First Tensile Modulus
M_2	Second Tensile Modulus
$\dot{M}$	Mass Flowrate of Polymer
N_1	Normal Stress
N	Avogadro's Number
N_P	Number of Pores per unit Membrane Surface Area
η	Shear Viscosity
η_E	Elongational Viscosity
$[\eta]$	Intrinsic Viscosity
η_O	Zero Shear Rate Viscosity
η_R	Relative Viscosity
η_{Red}	Reduced Viscosity
η_{SP}	Specific Viscosity
n	Constant
θ	Wetting Angle
ρ	Density
ρ_D	Dope Density
ρ_B	Bulk Density
ρ_L	Linear Density

ρ_P	Polymer Density
ρ_S	Solvent Density
P	Pressure
ΔP	Pressure Difference
PP	Partial Pressure
P_o	Atmospheric Pressure
$\acute{P}$	Permeability Coefficient
P	Permeability
Q q	Flowrate
r	Radius of pore
r	Radius
r_0	Radius at which Shear Stress is Equal to Zero
R_1	Inner Radius of Spinneret
R_2	Outer Radius of Spinneret
RH	Relative Humidity
S	Solubility Coefficient
σ_I	Interfacial Surface Tension
σ	Tensile Stress
$\sigma = R_1/R_2$	Spinneret Aspect Ratio
τ	Shear Stress
t	Time
T_R	Trouton Ratio
T	Temperature
$\acute{U}$	Fibre Contraction Factor
U	Velocity
V_f	Fibre Velocity (Wind-up Speed)
v	Fibre Porosity (Void Volume Fraction)
V	Velocity

WIR	Water Injection Rate
WUS	Wind-up Speed
x	Distance
y	Mole Fraction
Ω	Selectivity
λ	Mean Free Path
λ	Normalised Radius at which Shear Stress is Equal to Zero

Subscripts:

E	Elongation
i, j	Component Gases
f, p	Feed, Permeate

Chapter 1 Introduction

1.1 Historical Overview

The first recorded experiments using gas separation membranes were carried out by Mitchell [1] in 1831. Mitchell observed the rates of escape of ten gases from india rubber balloons under identical conditions. He demonstrated that CO_2 passed through the rubber substantially faster than H_2 and discovered a hundred fold difference between the speed of permeation of CO and NH_3. Mitchell also noticed that the rapidly permeating gases were absorbed by the rubber to a significant degree.

It was with the first synthetic membranes that Fick [2] in 1855 performed his classical studies, 'Uber Diffusion'. He prepared the membranes from collodion (nitrocellulose) only ten years after Schoenbein's [3] accidental synthesis of the material in 1845. Fick stated that diffusive flux within a medium is proportional to the concentration gradient of the diffusing species in the direction of interest. The constant of proportionality is defined as the diffusion coefficient or the diffusivity.

In 1866 Graham [4] demonstrated that when air permeated natural rubber the permeate was sufficiently enriched in oxygen to relight a glowing splint. As a result of his measurements of gas transfer through natural rubber, Graham proposed the 'Solution Diffusion' mechanism of transport. Graham's postulation still forms the basis of

current understanding regarding the penetration of gases through non-porous membranes. When a gas at one face of a membrane is at a greater pressure than at the other it dissolves to a higher equilibrium concentration in that face of the membrane. The gas then diffuses through the membrane down the concentration gradient to the low pressure face where it evaporates maintaining the correct equilibrium concentration at the low pressure side.

The solution diffusion model was first quantified by von Wroblewski[5] in 1879. He demonstrated that a gas dissolves into a polymer to a concentration that is directly proportional to the pressure above the membrane (i.e. Henry's Law is obeyed). Combining this with Fick's law, von Wroblewski was first to define the 'Permeability Coefficient'. He showed that in general gas flux was directly proportional to the pressure difference across the membrane and inversely proportional to membrane thickness. He defined the constant of proportionality as the permeability coefficient and showed that this corresponded to the product of diffusivity and solubility. Gases separate through membranes because their permeabilities differ. The selectivity of a membrane to any two gases is simply the ratio of permeability coefficients.

Despite early knowledge, it has only been in the last twenty years that the potential for separating gases by membranes has begun to be realised. Early work was mainly limited to research purposes because membranes capable of separating gases could only be produced by techniques that resulted in very low permeabilities. The practical feasibility for industrial scale gas separations came about quite suddenly through the developments in membrane production for the liquid phase separation process of reverse osmosis. In 1962 Loeb and Sourirajan[6] produced asymmetric cellulose acetate membranes by a phase inversion technique. These membranes comprised a thin essentially non-porous skin layer, typically 0.1 to 1.0 micron in thickness, supported on a highly porous readily permeable substructure which was about 1000 times thicker than the active layer. Conventional membranes of the time were commonly 100-200 microns in thickness. The effective thickness of the revolutionary asymmetric membrane was in the order of 1000 times less, resulting in much higher fluxes. The way was open for rapid advancement in the membrane gas separation field.

However, the basic requirements of gas separation membranes, namely high permeability and high selectivity, remain in conflict. This problem is alleviated considerably by the use of hollow fibre membranes. The development of this membrane geometry began in the mid 1960's for use in both reverse osmosis[7] and gas

separation applications. In 1967, Dupont[8] produced a gas permeator based on hollow fibres. The launching of their 'Permasep' gas permeator followed in the early 1970's. Hollow fibres give an extremely large surface area per volume of membrane module. High fluxes can therefore be achieved whilst maintaining adequate membrane selectivity.

Although the development of asymmetric hollow fibre membranes has gone a long way to producing successful gas separations, the quest for improved selectivities goes on. Even if the skin region of a gas separation membrane possesses but a few pores or imperfections then the membrane is rendered useless because of the resultant drastic reduction in selectivity. Monsanto[9] have pioneered coating techniques that tackle this problem. A thin layer of silicone, a highly permeable elastomeric polymer, is applied to the membrane surface which plugs any pores or 'pinholes'. The coating material does not carry out the separation but simply allows the membrane to exhibit a selectivity closer to its intrinsic capabilities with no additionally imposed decrease in permeability. The Monsanto 'Prism Separator' launched in 1979, the first real commercial success in membrane gas separation, is based on silicone coated polysulphone hollow fibre membranes[10].

Polymers and membrane manufacturing techniques that will give improved gas selectivities and permeabilities are being vigorously pursued, especially in the USA and Japan. Composite membranes and surface treatments such as plasma polymerisation are being researched as well as effort being made to tailor make polymers on a molecular level to facilitate desired separations. Much of this current work, however, especially that involving hollow fibre technology, is subject to commercial confidentiality and features only sporadically in the patent literature.

1.2 Membrane Technology Survey and Project Outline

The purpose of this project was to investigate the factors important in determining the performance of gas separation hollow fibre membranes. The fibres were fabricated by means of a dry jet wet spinning process, commonly used for the production of asymmetric hollow fibre membranes[11]-[14]. The research mainly focused on the rheological aspects of fibre spinning. The conditions of shear in the spinneret during extrusion of the spinning dope were analysed and related to fibre performance. The effect of jet stretch (flow under elongation) during the spinning process was also investigated.

Gas transfer through asymmetric membranes was modelled allowing fine details of fibre structure and morphology to be deduced from gas permeation characteristics. This structural information was used to interpret the effect of spinning conditions on the gas separation performance of the hollow fibre membranes produced.

Membrane separation generally is now a well established technology, particularly because of the successful processes of reverse osmosis[15], ultrafiltration[16] and dialysis. Some of these processes are on a substantial scale, such as in the desalination of brackish and sea water[17]. Membrane separations, often attractive because of the avoidance of the high energy costs associated with a

phase change, have become economically competitive because of the development of high flux asymmetric membranes and the ability to fabricate such membranes in the form of hollow fibres. In a given module volume, hollow fibres provide up to 30 times the surface area offered by spiral wound flat sheet membranes. Another advantage of hollow fibres is their self supporting nature; flat sheet membrane modules require complex supports and spacers.

In recent years, further progress in membrane science has resulted in the successful application of membrane technology to the separation of gases of industrial interest. A number of large scale membrane plants for the separation of hydrogen from various industrial gas streams[18][19] and for the recovery of carbon dioxide in enhanced oil recovery[20][21] are presently in operation. However, the number of membrane processes which are commercially viable is currently limited because of the lack of membranes with a sufficiently high selectivity and permeability toward a spectrum of different gases.

Current research into improving membrane gas separation adopts various approaches. At the applications and process development side of the technology attention is being directed at process design techniques such as the use of multi-stage membrane cascades[22][23] or continuous membrane columns [24]. This approach makes use of the membranes that are already available. The other extreme of the technology

involves polymer chemistry. Highly permeable and selective polymers are being sought for particular gas separations. Such research occurs at the molecular scale focusing on the modification of the chemical structure of the polymer[25][26].

Even if a polymer is produced with favourable intrinsic separation properties, suitable membrane fabrication techniques must be established. A research scale flat sheet must be translated into a successful industrial scale membrane process. Asymmetric hollow fibres are especially relevant to this end.

Few workers publishing in the open literature are concerned with the investigation of the fundamental scientific aspects behind spinning hollow fibre membranes for gas separation. Much of the work concerned with spinning hollow fibres, especially that appearing in the patent literature[27], is of an empirical nature and describes tried and tested 'recipes' for the production of membranes[28]-[30].

The slightest presence of surface pores or pinholes, corresponding to surface porosities > 10^{-9} [31] (fraction of surface area that is pores) ruins the gas separation potential of a membrane. As a consequence freshly spun asymmetric hollow fibres invariably have to be post treated. The technique in the most successful gas

separation membranes (Monsanto's Prism Separators[18], based on polysulphone hollow fibres) has been to block the surface pores by coating with silicone, a highly permeable but relatively unselective elastomeric polymer. Coating allows the membrane to exhibit gas separation properties approaching the intrinsic capabilities of the membrane polymer.

Other techniques to produce effective gas separation membranes involve the fabrication of composite membranes. Porous hollow fibres, akin to ultrafiltration membranes, are spun and this substructure is subsequently overlaid with a thin non-porous active layer involving a highly selective polymer. Plasma polymerisation techniques have been developed for this purpose[32][33]. Alternative methods of applying the active layer on to the porous support include immersion, spraying and interface polymerisation procedures[34][35].

The quest to improve gas separation has also involved annealing[34] as well as in situ chemical modification of the membrane surface. Polysulphone hollow fibre surface treatments have included contact with gaseous SO_3 [36] and reaction with NH_3/CH_3OH solution [37]. The production of gas separation membranes by the pyrolysis of hollow polymer fibres has also been reported[38].

In the event of silicone coating it is still the membrane polymer as spun that is responsible for gas permeation performance. Thus the optimisation of the spinning conditions remains of vital importance with respect to determining the separation potential of the hollow fibres even if the membranes do suffer from surface pores in their freshly spun form. Obviously if the phase inversion process could be developed to such a degree as to eradicate surface pores then all to the good but this is not a prerequisite for research examining the influence of spinning conditions on polymer properties and fibre morphology to be directly relevant with regard to gas separation.

Silicone as a coating material may have its limitations when polymers other than polysulphone are considered. It has been shown for instance that at surface porosities equivalent to those in successful polysulphone based membranes, silicone coating has a negligible effect on the selectivity of polyacrylonitrile hollow fibres[39]. This is due to the low intrinsic permeability of the polyacrylonitrile polymer. Thus alternatives to silicone as a coating material would have to be employed in some cases. If neither suitable coating techniques nor adequately improved phase inversion with respect to decreasing surface porosity proved possible for any polymer of interest then the production of a composite membrane would have to be addressed.

A rudimentary investigation of the spinning process must be regarded as valid. Few workers have pursued this path, probably due to the technical difficulties in producing hollow fibre membranes and the disappointment of surface pores. The limited published work that *has* been carried out with a fundamental approach to the production of gas separation hollow fibre membranes[36][40][41] has focused on aspects of the phase inversion process. Due to the complexity of the polymer precipitation process such work, although successful in improving fibre performance by virtue of altering coagulation conditions and including various additives in the spinning solution, inevitably tends to the empirical.

This project seeks to improve fundamental knowledge of gas separation hollow fibre fabrication by adopting a rheological perspective, analysing the effects of shear and elongation experienced in the spinning line. Key principles and aspects of fibre formation of general significance as well as those relating to rheological conditions are identified.

Much of the literature associated with this research program has been referred to in the main body of the thesis. It was felt that the use of 'local' literature citation and discussion was appropriate in this work because of the range of material addressed.

The remainder of this first chapter considers general topics relating to membrane separation and fibre spinning technology.

1.3 Membrane Processes

The main processes involved in membrane technology are listed in **Table 1.1.** Details of membrane structure, materials being separated and driving forces are given. In principle, material transport is always a consequence of the chemical potential gradient across the membrane [42]. The membrane processes differ in the importance of the various terms associated with chemical potential.

The ranges covered by pressure driven membrane processes within the complete particle size spectrum are shown in **Figure 1.1.** Obviously, the boundaries of each process are not as sharp as suggested. At present, the pressure differences technically applied in reverse osmosis are up to 100 bar. If the membrane retains only macromolecules or particles with an insignificant osmotic pressure, the necessary operating pressure can be much lower (2-10 bar). In this case, the process is termed ultrafiltration. Fundamentally, there is no sharp distinction between ultrafiltration and reverse osmosis; the two merge into each other like ultrafiltration and microfiltration.

Membrane Process	Membrane Type/ Pore Radius (nm)	Separation Mechanism	Driving Force	Material Retained	Material Permeating
Microfiltration	Porous 50-10,000	Sieving	Pressure < 5 bar	Suspended Matter (Silica, Bacteria etc)	Water and Dissolved Species
Ultrafiltration	Microporous 1-100	Sieving	Pressure < 10 bar	Biologicals, Colloids, Macromolecules	Water, Salts, Organics
Dialysis	Microporous/ Non-porous	Solution Diffusion/ Sieving	Concentration	Dissolved and Suspended Material (Mwt > 1,000)	Water, Salts, Low Mwt Organics
Electrodialysis	Microporous/ Non-porous	Counter-ion Transport	Electric Field	Non-ionic and Macromolecular Species	Ions
Reverse Osmosis	Microporous/ 0.2-2 Non-porous	Solution Diffusion (Preferential Sorption/ Capillary Flow)	Pressure < 100 bar	Virtually all Suspended and Dissolved Matter	Water
Pervaporation	Non-porous < 0.5	Solution Diffusion	Permeate Side: Difference between Saturation Pressure and Partial Pressure	Less Permeable Liquid	More Permeable Liquid
Gas Separation	Non-porous < 0.5	Solution Diffusion	Pressure < 80 bar	Less Permeable Gas	More Permeable Gas

Table 1.1 Membrane Processes

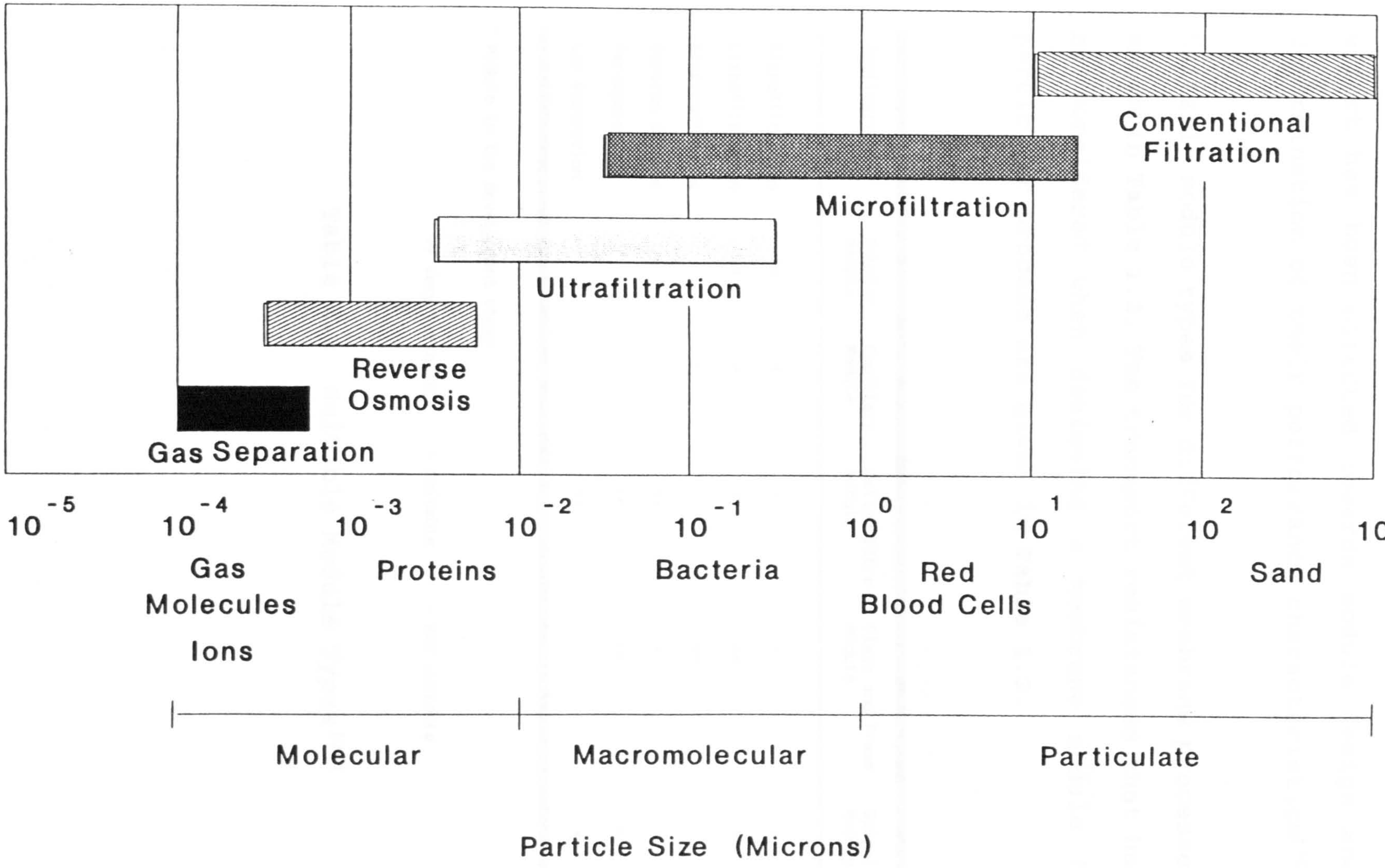

Figure 1.1 Range of Application for Pressure Based Membrane Processes

The central part of any membrane plant is the module, i.e. the technical arrangement of the membranes. Considerable effort has been directed towards module design and the determination of their performance characteristics[34].

Suitable module types for different membrane processes are shown in **Table 1.2.** The transport resistances that have to be considered when designing a membrane module for a particular process are given in **Table 1.3.**

Application	Tubular Module	Capillary Module	Hollow Fibre Module	Plate and Frame Module	Spiral Wound Module
Microfiltration	++	+	-	-	-
Ultrafiltration	++	+	-	++	+
Electrodialysis	-	-	-	++	-
Reverse Osmosis	+	-	++	+	++
Pervaporation*			++	++	++
Gas Separation	-		++	-	++

* Module in the development stage

++ Very suitable + Suitable - Not suitable

Table 1.2 Suitable Module Types[34]

Factor	Ultrafiltration and Reverse Osmosis	Pervaporation	Gas Permeation
Concentration Polarisation	✓	✓	
Friction Losses - Feed	✓		✓
Friction Losses - Permeate	✓	✓	✓
Flow Pattern		✓	✓
Heat Transfer		✓	

Table 1.3 Transport Resistances Affecting Various Membrane Processes[34]

1.4 Gas Transfer Through Membranes

The solution diffusion principle first suggested by Graham[4] in 1866 still forms the basis of current understanding regarding gas permeation through polymers. Penetrant migration within the polymer is controlled by molecular diffusion. The solution equilibrium occurring at the gas/membrane interfaces establishes the overall concentration gradient in the polymer.

Polymer chains are in a constant state of thermal agitation and penetrant molecules are involved in a sequence of activated unit diffusion steps or jumps with a directional bias determined by the concentration gradient within the polymer. The mobility of the gas molecules is far higher than that of the polymer chains and as a consequence the kinetic behaviour of the polymer chains is rate controlling. A diffusional jump can be considered to consist of the localisation of sufficient thermal energy in the polymer near the penetrant to open a momentary hole or passage of adequate size to permit the penetrant to progress to a new position in the polymeric medium[43].

The diffusion coefficient, D is a measure of the diffusive mobility of the penetrant in the polymer and is defined as the ratio of penetrant flux, J to concentration gradient, $\frac{\partial C}{\partial x}$

$$J = - D \frac{\partial C}{\partial x} \quad \text{----------} \quad 1.1$$

This equation is known as Fick's first law [2] which states that diffusive flux within a medium is proportional to the concentration gradient of the diffusing species in the direction of interest.

By elemental mass balance, the more general diffusion equation known as Fick's second law, can be derived from equation 1.1

$$\frac{\partial C}{\partial t} = \frac{\partial}{\partial x} D \left(\frac{\partial C}{\partial x}\right) \quad \text{----------} \quad 1.2$$

Where t = Time

Fick's second law can be used to solve problems of unsteady state diffusion by integration with the appropriate boundary conditions[44].

As well as the diffusion coefficient, the solubility coefficient, S is a fundamental system parameter. The diffusing species will have a particular equilibrium solubility in the polymeric membrane. The solubility coefficient, analogous to Henry's law constant, relates the pressure of the penetrant in the gas phase to the dissolved concentration in the membrane surface, thus

$$C = S\,P \qquad \text{---------- 1.3}$$

where P = Penetrant (partial) pressure in gas phase

The permeability coefficient, $\acute{P}$ is the quantity commonly used to characterise the gas permeation performance of a polymer. Referring to equation 1.1, integrating with respect to x gives

$$J = \frac{D}{L}\,(C_h - C_l) \qquad \text{---------- 1.4}$$

where Subscripts h and l refer to the high and low pressure faces of the membrane

and L = Membrane thickness

Combining equations 1.3 and 1.4 gives

$$J = \frac{D\,S}{L}\,(P_h - P_l)$$

and thus

$$Q = \frac{\acute{P}}{L}\,A\,\Delta P \qquad \text{----------} \quad 1.5$$

where Q = Gas flowrate

A = Membrane area

and Permeability coefficient, $\acute{P} = DS$

The independent measurement of D and S is frequently required in fundamental studies of diffusion. The time lag technique of Daynes[45] and Barrer[46], one example of unsteady state mass transfer, is most commonly used to carry out such measurements. Essentially, in this technique one side of a membrane is pressurised with gas and the amount of gas which permeates the membrane is measured as a function of time. The time profile of the permeating gas can be inferred from a solution of Fick's second law of diffusion[47] (equation 1.2). When steady state is finally achieved the diffusion coefficient is evaluated from the extrapolated intercept of the linear portion of the permeation profile with the time axis. The permeability coefficient is determined from the slope of

the linear portion of the profile and solubility coefficient is simply the ratio of the permeability and diffusion coefficients.

Diffusion of gases through polymers is often complicated by the dependence of the diffusion and solubility coefficients on concentration and time[48]. Such is the case, for instance, when the penetrant is highly soluble in the membrane: the polymer structure tends to become swollen or plasticized and the diffusion and solubility coefficients become functions of sorbed concentration and time. Basic permeation measurements involving such systems yield effective or mean permeability coefficients[49] which are only valid over a limited range of test conditions.

The permeation of gases through polymers is also sensitive to temperature. The temperature dependence of permeability, diffusion and solubility coefficients can be represented by Arrhenius-type equations[50].

If gas permeation is monitored over a temperature range which includes the glass transition temperature of the polymer, T_g, then two distinct modes of transport can be identified: a sharp change in slope of the Arrhenius plots (e.g. log $\dot{P}$ versus 1/T) occurs near T_g.

The perception of gas transport through rubbery polymers ($T > T_g$) is grounded in the solution diffusion model where the polymer medium behaves in a fluid-like manner. Due to the mobility of the polymer molecules, high permeabilities and low selectivities are characteristic of rubbery polymers e.g. silicones.

Permeation mechanisms in rubbers are not applicable to glassy polymers ($T < T_g$). Transport parameters, such as diffusion coefficients determined from lag time tests, appropriate in the rubbery state do not fully account for permeation through glassy polymers. Transport behaviour below T_g deviates from a purely solution diffusion based model and is explained by the dual mode sorption theory which has been developed to deal with gas permeation in glassy polymers[51]. In comparison to rubbers, glassy polymers such as polysulphone and polyacrylonitrile exhibit low permeabilities but significantly superior selectivities.

For the purposes of this work and in many situations involving practical membrane research, it is unnecessary to expound the intricacies of gas permeation which are relevant to fundamental studies of diffusion. In the literature, permeation characteristics of membrane polymers are simply quoted in terms of overall permeability, diffusion and solubility coefficients whether the polymer is in the glassy or the rubbery state.

Indeed, in the papers which address the subject of diffusion in a theoretical manner, the gas permeation properties of polymers are still given in the form of overall permeability coefficients[50][52].

The above discussion is pertinent to permeation through non-porous polymers. However, asymmetric phase inversion membranes seldom have completely non-porous active layers and thus Knudsen diffusion and viscous flow components frequently contribute to gas permeation.

Knudsen diffusion and viscous flow are fully addressed in section 5.2 where gas transfer through asymmetric membranes has been modelled. A membrane dominated by either of these two pore flow mechanisms exhibits very poor separation properties. Selectivity based on Knudsen diffusion is simply the ratio of the molecular weights of the penetrant gases. In the case of viscous flow selectivity is simply the ratio of gas viscosities.

There has been little systematic work recorded in the literature on the permeation of gas mixtures in polymers. When gas mixtures permeate polymers three types of behaviour are possible[53]. In the simplest, the flux of each component is equivalent to that of the pure gas at the same partial pressure driving force across the membrane i.e. no penetrant penetrant interaction occurs. When one or more of the gases has a plasticizing effect on

the polymer the flux of all other gases is increased. When dual mode sorption and diffusion are important, two gases compete for the adsorption sites and the more strongly adsorbed depresses the flux of the less strongly adsorbed provided the adsorbed molecules have any mobility in the polymer.

The equations used in membrane gas permeation measurements, including those relating to gas mixture tests, are given in section 3.5.1.

1.5 The Phase Inversion Process of Membrane Production

Membrane technology includes such processes as microfiltration, reverse osmosis and gas separation. The membranes used in the various separation processes differ considerably in their structure, function and in the way they are produced[54]. Fabrication techniques for the different membrane types are recorded in patents and publications but they take the form of detailed preparation recipes which are deeply rooted in empiricism. Initially, the production of microporous polyethylene tubes involving extrusion and thermogelation may appear to have little in common with the casting of skinned asymmetric flat sheets by wet coagulation. However, a fundamental approach reveals that both membranes are formed as a result of completely general laws of precipitation. The process of polymer precipitation is commonly referred to as phase inversion. In fact, most polymeric membranes no matter their structure or mass transport characteristics are fabricated by the phase inversion process.

In addition, the spinning of synthetic fibres in the textile industry and the extrusion of plastic sheets and films are frequently governed by the phase inversion process. Thus wide overlaps in technology occur between membrane science and the sheet and fibre manufacturing

industries. It should also be pointed out that overlaps occur not only by virtue of phase inversion but also in rheological aspects of fabrication.

This research project was primarily concerned with rheological influences in the preparation of gas separation hollow fibre membranes. Thus the conditions of phase inversion, such as coagulation bath temperature and composition and spinning solution components, were held constant during fibre production. Since phase inversion effects were not directly investigated, this discussion will be brief.

Strathmann[55][56] and Kesting[57][58] are the most prominent researchers in the phase inversion field and the following material is based on their work.

The phase inversion process involves the conversion of a homogeneous polymer solution of two or more components into a two phase system with a solid, polymer rich phase forming the rigid membrane structure and a liquid, polymer poor phase forming the membrane pores. Under certain conditions of temperature and composition homogeneity must therefore be thermodynamically unfavourable. The resultant miscibility gap causes the system to split into two distinct equilibrium phases. To obtain an open network morphology both phases require to be continuous. If only

the solid phase is continuous a closed cell structure is achieved and if the solid phase is discontinuous a polymer powder will be formed.

Three different techniques are used to prepare polymeric membranes by phase inversion: the thermal process, the dry process and the wet process. The latter is the most widely used and it is in fact a wet spinning technique that is employed in this work for the production of hollow fibre membranes. A short description will be given of the first two techniques but the rest of the discussion will concentrate on the phase inversion mechanisms of the wet process.

1. The Thermal Process (Thermogelation)

This process utilises a latent solvent, that is a substance which is a solvent for the polymer of interest at elevated temperatures (> 200^{o}C) and a non-solvent at lower temperatures. On cooling the polymer solution enters a miscibility gap and consequently separates into a solid polymer phase and a liquid phase.

2. The Dry Process

This method involves the evaporation of a volatile solvent from a polymer solution comprising polymer, solvent and non-solvent. This three component mixture is completely miscible over a certain composition range but on the loss of solvent enters a miscibility gap and the solid membrane structure is formed.

3. The Wet Process

This is the most common phase inversion technique and is used for the preparation of symmetric microfiltration membranes as well as for manufacturing asymmetric skin-type membranes. The process involves the addition of a non-solvent to a homogeneous polymer solution. The polymer solution or prenascent membrane may have a flat geometry as in the casting of sheet membranes or may take the form of a filament as in the spinning or extrusion of hollow fibre membranes. In either case, polymer precipitation is brought about by the addition of a non-solvent usually in the form of a coagulation bath. The precipitation process can be illustrated with the aid of a three-component phase diagram shown schematically in Figure 1.2. The diagram represents equilibrium at one particular temperature.

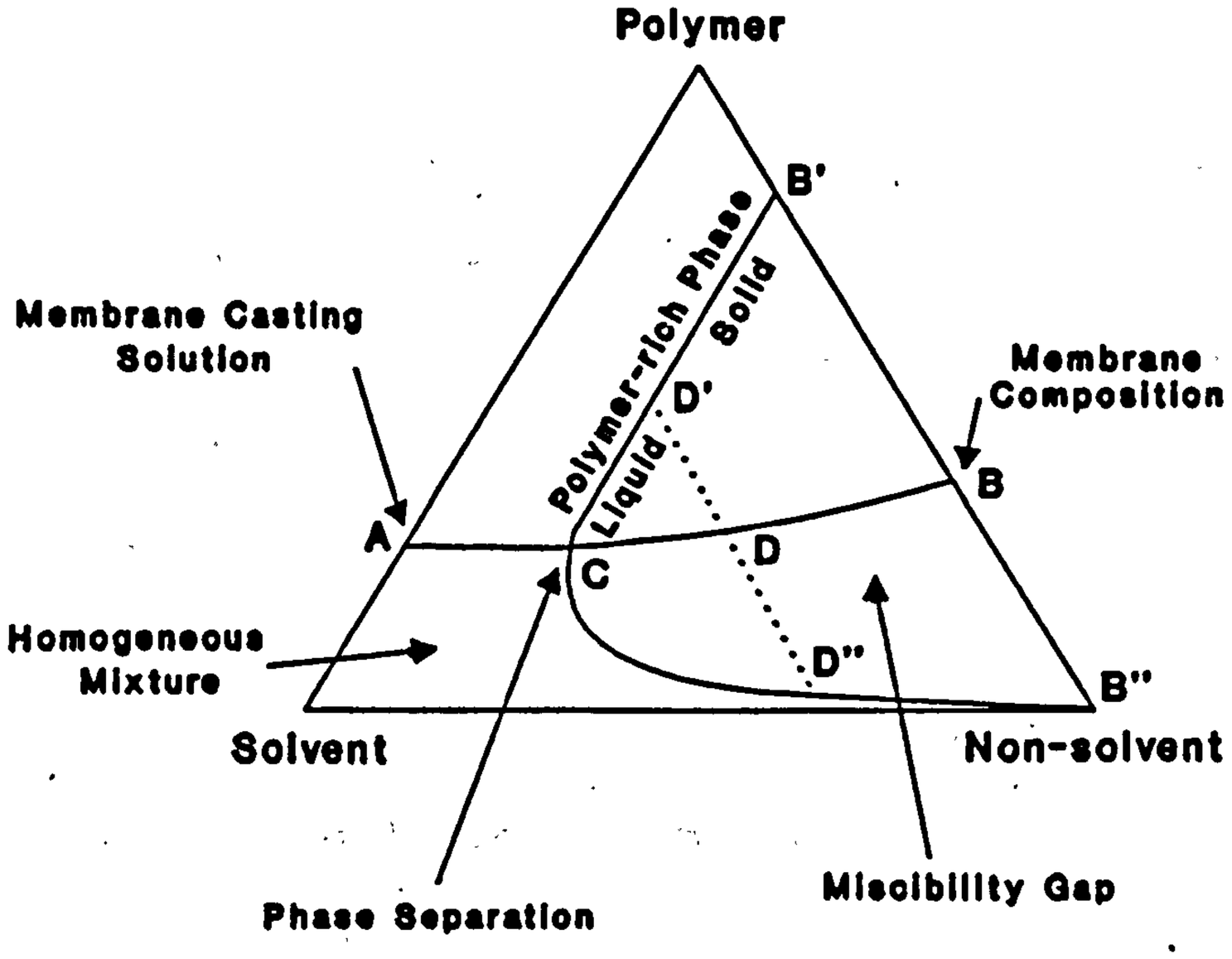

Figure 1.2 Three Component Phase Diagram (Isothermal)

The phase diagram shows a miscibility gap over a large range of compositions. If a non-solvent enters a homogeneous solution consisting of polymer and solvent, as indicated by the point A on the solvent-polymer line, and if solvent is lost from the system at roughly the same rate as non-solvent addition, the composition of the mixture will change following the line A - B. At point C, the composition of the system will reach the miscibility gap and two separate phases will begin to form: a polymer rich phase represented by the upper boundary of the miscibility gap and a polymer poor phase represented by

the lower boundary. At a certain system composition, D the concentration in the polymer-rich phase, D' will be high enough to be considered as solid. At this point the membrane structure is more or less determined. Further exchange of solvent and non-solvent will lead to the final formation of the membrane, the porosity of which is determined by point B. Point B represents the mixture of the final solid polymer network, B' and the liquid phase, B'' which is virtually free of polymer and solvent.

The precipitation pathway is illustrated in Figure 1.3 which shows a coagulation front midway through a cast film. The letters A - D refer to the critical points in the precipitation process as shown in the phase diagram.

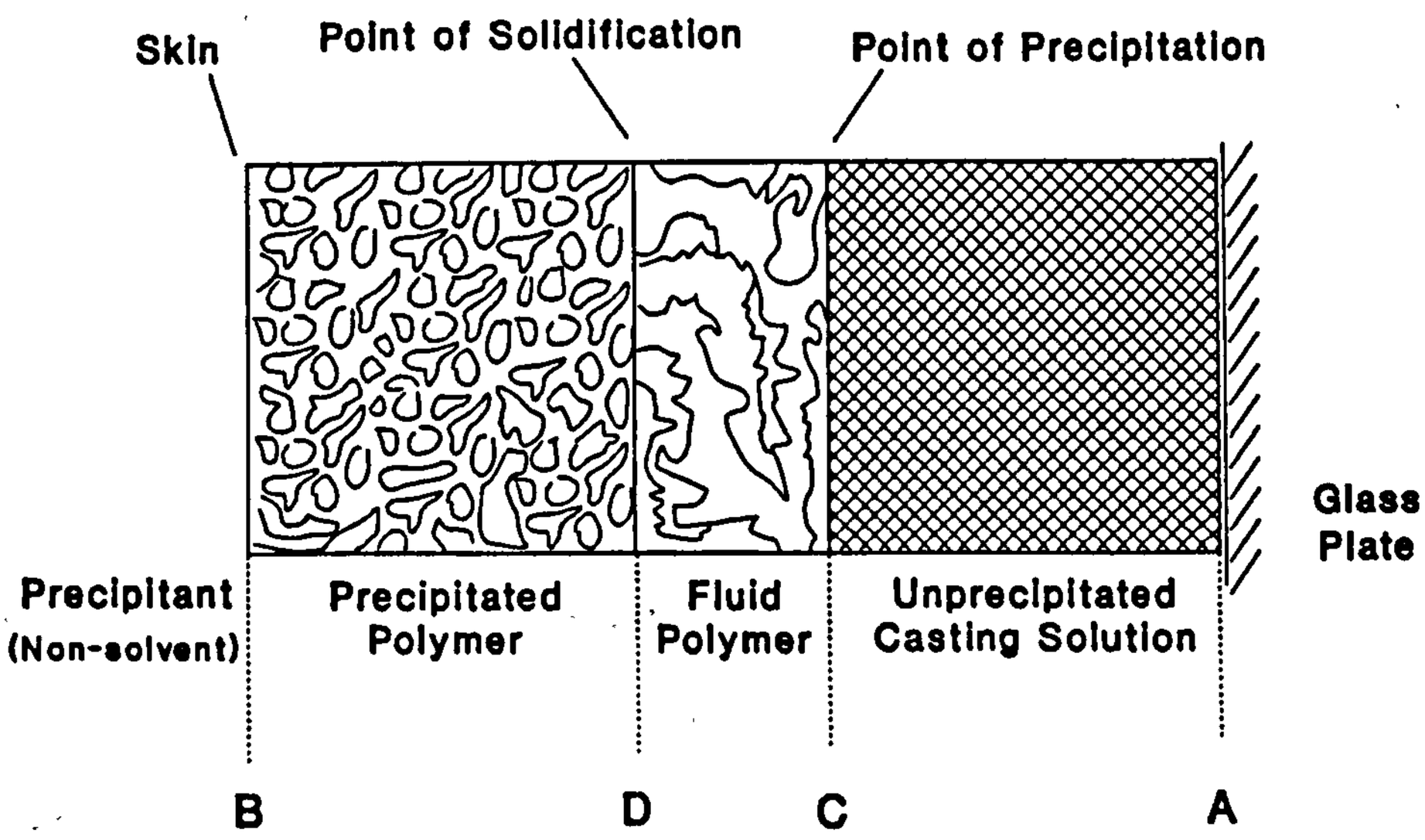

Figure 1.3 Coagulation Front in Cast Film

The description of the phase inversion process using a phase diagram is based on the assumption of thermodynamic equilibrium. The phase diagram shows the conditions under which the system is inclined to separate and the composition of the corresponding equilibrium phases. In terms of membrane structure, overall porosities can be predicted from the phase diagram but no information is provided regarding pore size or morphological variations within the membrane cross section; such as whether the membrane has a symmetric or asymmetric structure or a dense skin at the surface. These parameters are determined by kinetic effects, which depend on the local properties of the system such as component diffusion coefficients, viscosity and the chemical potential gradients which drive diffusion. These properties are continually changing and transient states of equilibrium are not achieved. Due to the complexity of the actual phase separation mechanism, studies which relate the conditions of phase inversion to membrane morphology tend to be qualitative and discussive.

Characteristic membrane structures can generally be correlated with the rate of precipitation of the polymer. A decrease in precipitation rate, such as is caused by increasing the polymer concentration in the casting solution or adding solvent to the precipitant, results in a shift from a finger-type structure to a sponge-type structure.

To explain the formation of symmetric or skinned asymmetric, finger or sponge-type membrane morphologies, the concentration profile of the non-solvent through the precipitating membrane should be considered.

If the transfer of non-solvent from the coagulation bath to the membrane interface is slow and rate limiting, as in the case of a vapour phase precipitant, then precipitation is slow and a flat concentration profile is developed in the coagulating film. On a microscopic scale, because of thermal molecular motions, there are randomly distributed areas of high polymer concentration which act as nucleation centres for polymer precipitation. With time the overall non-solvent level in the film increases and full precipitation is achieved. A homogeneous porous membrane structure is obtained without a dense skin region.

If non-solvent transfer from the coagulation bath is rapid, as in the case of a pure liquid precipitant (pure water), internal diffusion of the non-solvent within the film becomes rate limiting and a steep concentration profile is established. At the film surface the concentration of the precipitant soon reaches a value resulting in phase separation. Due to the steep gradient of polymer chemical potential, there is a net movement of polymer towards the surface which leads to the formation of the membrane skin. The skin then hinders the transfer

of precipitant into the rest of the film resulting in a flattening of the non-solvent concentration profile. A more uniform precipitation then occurs which tends to give a regular porous substructure.

The formation of fingers as opposed to the sponge-type structure described above, is more complex. Skin formation is identical in both types of structure. However, in some instances of rapid precipitation, shrinkage stresses in the polymer cause skin failure. The resultant openings in the skin allow penetration of precipitant which causes the growth of fingers. Another finger forming mechanism involves the build up of solvent vapour in substructure domains. If no precipitant intrusion has occurred the finger cavity walls have a skinless open cell structure.

A high polymer concentration in the casting solution tends to prevent both finger forming mechanisms: a stronger skin layer helps to prevent precipitant penetration and a lower level of solvent decreases the likelihood of vapour cavities.

The phase inversion mechanisms discussed above should not be confused with the production of dense non-porous polymer structures. Such entities are produced in sheet or fibre form by complete solvent evaporation from a two component polymer solution, cooling of a thermoplastic polymer melt or by cross-linked polymerisation.

1.6 Technology of Fibre Spinning

The spinning of man-made textile fibres is a well established technology which has been extensively reported. The three principal techniques employed in the manufacture of textile fibres are listed below. The first two methods tend to produce dense non-porous filaments.

1. Melt Spinning The molten polymer is extruded through a plain circular orifice spinneret into a cooling zone, most often gaseous, and solidification of the material occurs.

2. Dry Spinning The polymer is dissolved in a volatile solvent forming the spinning solution. Solidification of the filament is due to the evaporation of the solvent in a heated zone.

3. Wet Spinning Polymer solution is extruded through the spinneret into a bath where the action of a non-solvent causes filament solidification.

The wet spinning technique produces porous fibres and is exactly the wet process of phase inversion described in the previous section.

General principles of fibre production relating to the wet process can be readily applied to the spinning of hollow fibre membranes. However, an annular spinneret, with injection of internal coagulant on extrusion, is necessary in the manufacture of hollow fibres. The design of such a spinneret is considered in section 2.2.1.

The difficulties of quantitative assessment associated with membrane production are also shared by the textile industry with respect to wet spinning of fibres. Rheological effects due to shear in the spinneret and post extrusion elongation are combined with the phase inversion process to produce a particular fibre structure. The problem is summed up by Ziabicki [59], 'The effects of spinning conditions on the structure and properties of solution-spun fibres cannot yet be treated in a rational, systematic way.'

Studies relating the conditions of phase inversion to fibre morphology are similar whether carried out by fibre or membrane scientists. However, a number of observations regarding rheological influences and orientation have been carried out in textile research but such work in relation to membrane manufacture is very rare.

Paul [60] showed that the orientation of acrylic fibres was influenced by jet stretch ratio (elongation) in wet spinning. Birefringence evidence suggests that this

orientation is concentrated in the fibre skin[61]. Perepelkin and Pugatch[62] demonstrated that in the spinning of polyvinylacetate fibres, orientation was influenced by dope extrusion rate (shear rate in the spinneret) at constant jet stretch ratio.

The effect of rheological conditions during spinning on the performance of hollow fibre membranes has been considered by one group of workers[13]. The effect of shear in the spinneret was shown to influence the properties of ultrafiltration membranes. It was explained that orientation due to shear was frozen into the fibre skin resulting in surface pore elongation. This distortion of surface pores affected ultrafiltration characteristics.

No papers relating rheological influences during spinning to the performance of gas separation hollow fibre membranes were found by the author.

Chapter 2 Apparatus and Methods

2.1 Polymer Solution Preparation

All apparatus associated with this research was designed and fabricated by the author. The apparatus for polymer solution preparation is shown in **Figure 2.1.** The required

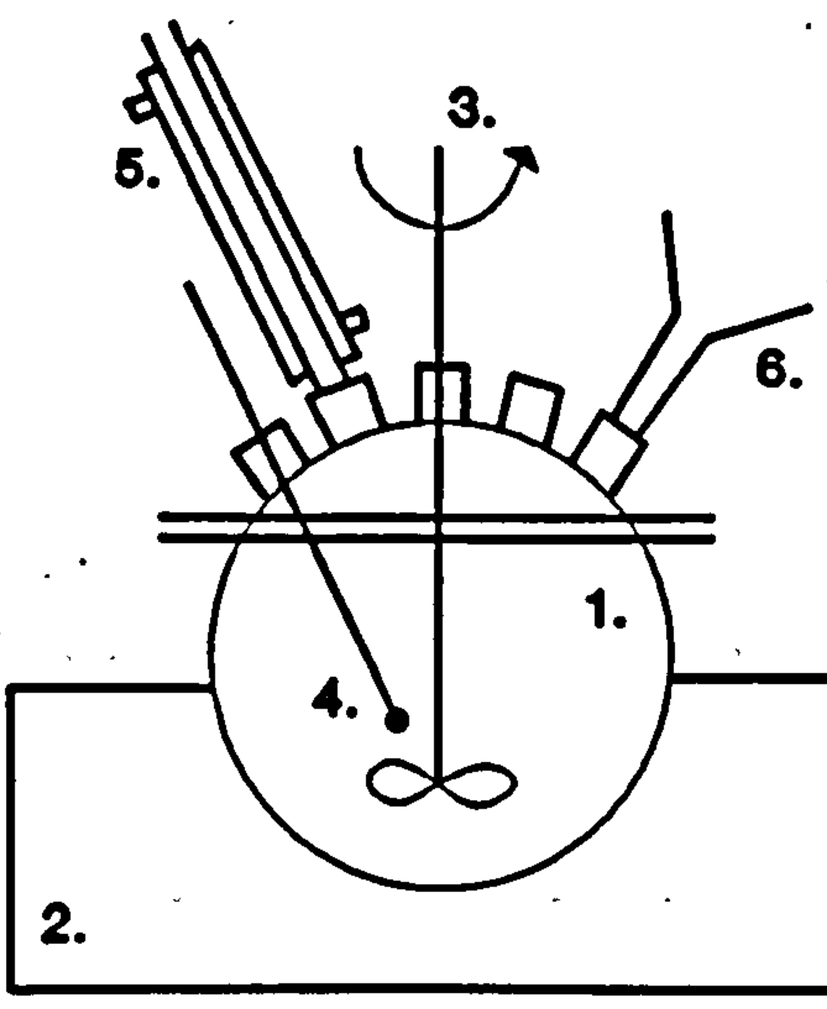

1. Flanged Spherical Glass Vessel **2. Heating Mantle** **3. Motor and Stirrer**

4. Thermometer **5. Condenser** **6. Solids Addition Shute**

Figure 2.1 Polymer Solution Preparation Apparatus

quantity of pre-dried solvent was placed inside the 1 litre vessel. The stirrer was set at medium speed and solvent maintained at ambient temperature. The required amount of polymer (solid pellets or powder) was added over a few minutes to prevent agglomeration. The temperature of the vessel contents was then raised to 80°C and the stirrer increased to maximum speed. A homogeneous polymer solution was obtained after approximately five hours depending on

the desired concentration. A powerful stirrer was required in order to maintain high speed as the viscous polymer solution was formed. The stirrer motor selected for this work was a 50W thyristor speed controlled DC shunt wound motor geared for a maximum speed of 780 rpm. The advantage of this type of motor was its ability to maintain a constant set speed as torque increased. The polymer solution (dope) was allowed to cool, degassed and transferred into storage bottles. Batches of 500-750 ml of dope were produced.

Table 2.1 gives polymer and solvent details.

Polymer	Polysulphone UDEL P-1700	Amoco Chemicals
	Polysulphone UDEL P-3500	Amoco Chemicals
	Polyacrylonitrile P82	Courtaulds
Solvent	N,N-Dimethylformamide	Aldrich Chemicals

Table 2.1 Polymer and Solvent Details

2.2 The Spinning of Hollow Fibres

2.2.1 Hollow Fibre Spinneret

The spinneret is the single most important item in successful hollow fibre production. It must be able to extrude the polymer solution in the shape of a hollow cylinder with outer diameter in the region of 0.1-1.0 mm. The main feature of the extrusion orifice is its annular shape which may be of several designs [63]. The tube or capillary in orifice spinneret is the most versatile and is the most suitable for hollow fibre membrane production. It allows control of the fibre inner diameter (hence wall thickness) by the flow of an internal injection fluid through the capillary. When water is used as the injection fluid, as was the case in this work, coagulation of the polymer solution also occurs at the point of extrusion. This gives the fibre immediate structure thus considerably improving spinnability.

It soon became apparent that no spinneret could be obtained from industry or elsewhere for use with this project. The technology behind spinneret manufacture is not willingly shared. It was therefore decided to design and fabricate a spinneret. Glass spinnerets were investigated initially but these were unsuitable. An effective stainless steel spinneret was then produced. The basic design concept was taken from a Monsanto patent [64]

and after a series of trials and modifications the successful spinneret was fabricated. **Figure 2.2** shows the final hollow fibre spinneret design.

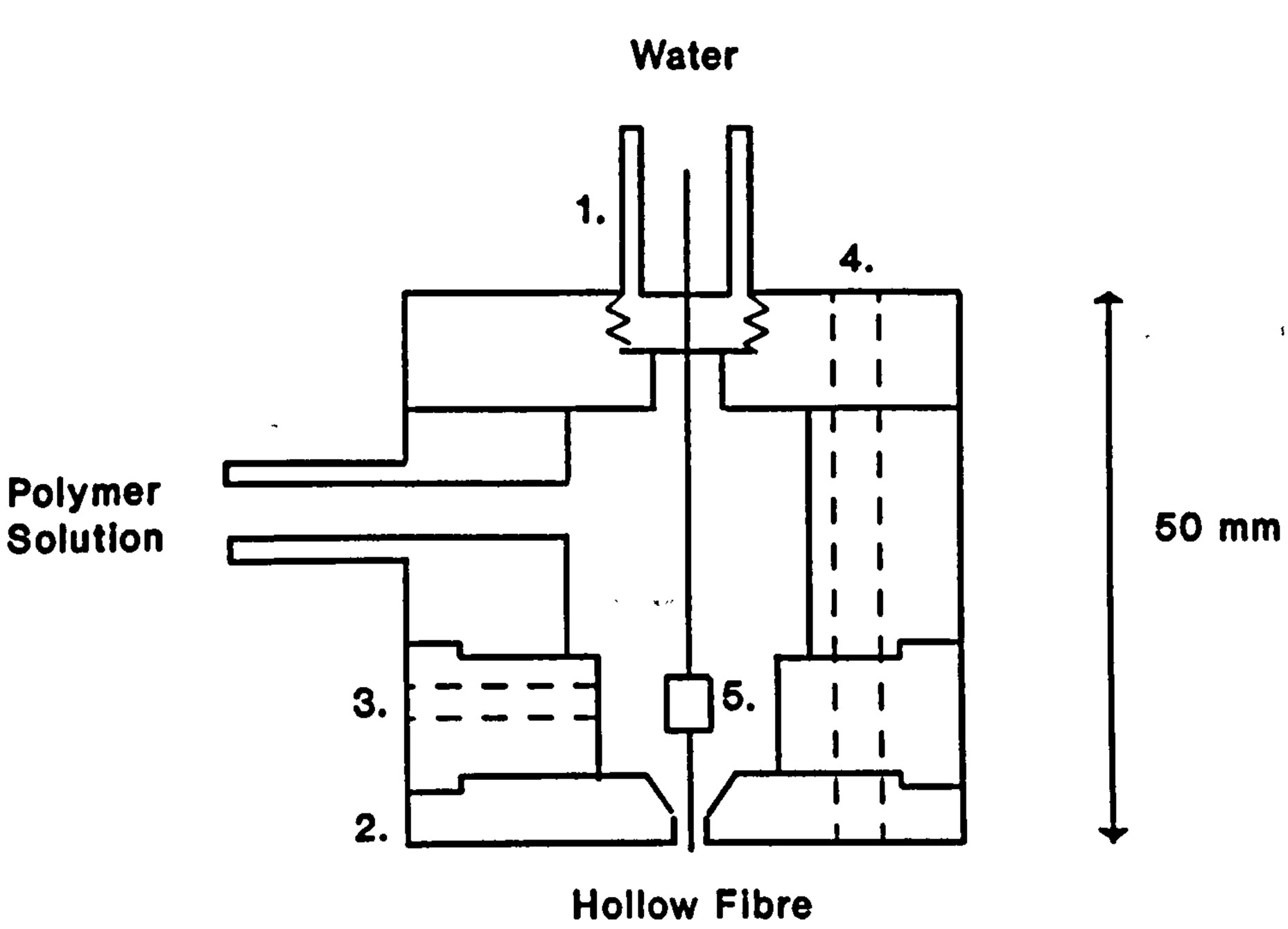

1. Capillary Unit 2. Base Plate 3. Capillary Guide Screw (3 at 120°)
4. Assembly Screw (3 at 120°) 5. Capillary Guide Button

Figure 2.2 Hollow Fibre Membrane Spinneret

The main advantages/features of this design are:

1. In-situ adjustment of capillary, axially and radially. This allows accurate alignment of capillary into the centre of the base plate orifice. This is critical in producing good fibres. It is also useful to have axial adjustment to allow the capillary tip position to be varied from flush to slightly protruding.

2. Interchangeable base plates and capillary units to allow variation of orifice dimensions:

		OD(mm)	ID(mm)		D(mm)
Spinneret 1.	Capillary Unit	0.330	0.178	Base Plate Orifice	0.600
Spinneret 2.	Capillary Unit	0.510	0.255	Base Plate Orifice	1.000

3. Multi-plate assembly can be easily dismantled to allow cleaning.

4. Profiled base plate to improve flow characteristics.

5. Withstands high working pressures.

2.2.2 Hollow Fibre Spinning Apparatus and Methods

Figure 2.3 shows the hollow fibre spinning apparatus. The stainless steel dope reservoir was filled with polymer solution and immersed in a water bath to allow the temperature of the solution to be controlled. The dope was then fed to the spinneret via a gear pump. The reservoir was kept under nitrogen pressure (20 psig) as a precaution against any bubble formation/cavitation in the line to the pump. The gear pump (Slack and Parr - SPLA 0.3 ml/rev) was driven by a 50W thyristor speed controlled DC shunt wound motor geared to a maximum speed of 40 rpm. The motor had a double gear reduction so as to give steady rotation even at the lower speeds. This dope delivery system allowed polymer solution to be accurately and smoothly delivered to the spinneret in the desired flowrate range of 0.3-10 ml/min. An in line filter prevented any extraneous material being passed to the spinneret from the gear pump. A 7 micron filter was used. The filter size was no smaller because of concern over excessive pressure drop when spinning the more viscous dopes.

The water pump must also provide an accurate and pulse free supply of water to the spinneret. The required water flowrate range was 0.1-5 ml/min. A peristaltic pump was unsuitable because of pulsing and a gear pump was unsuitable because of the low flowrate range and the fact that water is not of a sufficiently high viscosity to make

1. *Nitrogen*
2. Dope Reservoir
3. Gear Pump
4. Filter (7 Micron)
5. Spinneret
6. Water Pump
7. Hollow Fibre
8. *Motor Driven Roller D=8cm*
9. Motor Driven Wind-up Roller D=16cm
10. Heat Transfer Coil
11. Refrigeration/Heating Unit
12. Coagulation Bath Length=160cm
13. Washing/Treatment Bath Length=140cm
14. Wind-up Bath

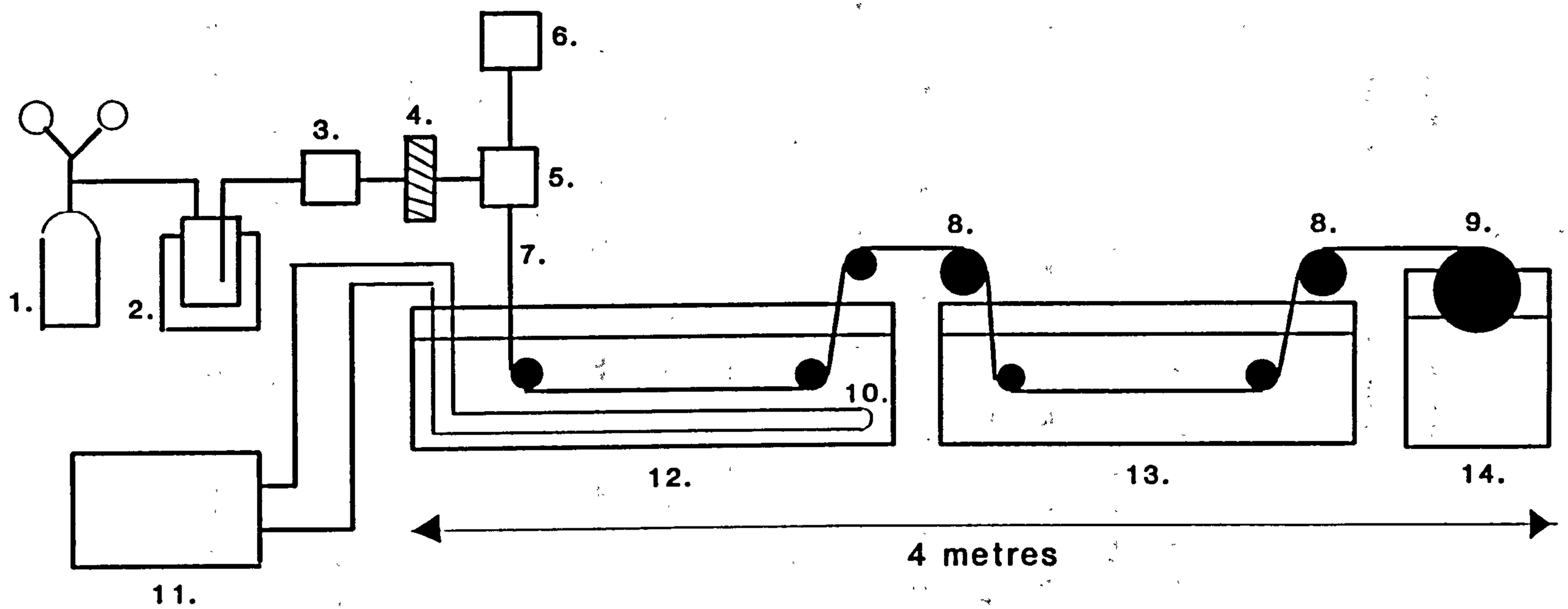

Figure 2.3 Hollow Fibre Membrane Spinning Apparatus

a gear pump attractive. A ram and syringe type infusion pump (Braun Medical - Unita S) was finally purchased and it performed the task of feeding water to the spinneret perfectly. The flowrate could be set automatically at 0.005 ml/min intervals from 0.005 ml/min to 5.000 ml/min via a digital panel on the front of the pump.

The dope was passed through the spinneret and extruded through the annular orifice. Water passed through the capillary section of the spinneret and was injected into the middle of the polymer solution as it was extruded thus forming the basis of a hollow fibre. This incipient filament travelled through an air gap before being passed via a series of rollers first through the coagulation bath and then the washing/treatment bath. Lastly the fully formed hollow fibre was wound up without overlap on the final wind-up drum. This drum had a diameter of 16cm and thus after a single traverse cut the fibres opened out to a suitable working length of 50cm. This produced manageable fixed length fibre bundles and obviated any messy wind off procedure and subsequent fibre cutting. The fibres were then steeped in water for 48hrs to remove any residual solvent. They were then hung to dry vertically for 72hrs in a controlled environment laboratory before being stored.

The speed of the fibre filament as it passed through the baths was controlled by the two 8cm Diameter motor driven rollers. The initial speed of the extruded filament through the coagulation bath was controlled by the first roller. If any secondary stretching or drawing is required this is carried out in the second bath by having a speed differential between the second roller and the first. The tip speed of the final wind-up drum was always set at that of the second 8cm Diameter roller. The three rollers were driven by 50W thyristor speed controlled DC shunt wound motors each geared to the appropriate speed range required of the roller:

Roller	Speed Range
1st (D=8cm)	3-75rpm = 1-30cm/s
2nd (D=8cm)	6.5-160rpm = 3-70cm/s
Wind-up (D=16cm)	3.5-85rpm = 3-70cm/s

The temperature of the coagulation bath was controlled to within 0.1°C (possible range -40 °C to +80°C) by a refrigeration/heating unit which circulated heat transfer fluid through the coil running along the bottom of the bath. The refrigeration/heating unit (Camlab FR/FT 800 with external circulation and temperature controller) was purchased after a fairly detailed design of the heat transfer system had been carried out.

2.3 Preparation of Hollow Fibre Modules (Potting-up)

Figure 2.4 shows the design of the hollow fibre membrane module. Each module usually comprised 10 fibres. A 3cm length of 1/4" OD stainless steel tubing was cut and two high pressure Swagelock nuts were fitted to each end. This formed the tube sheet which could be easily fitted into the high pressure

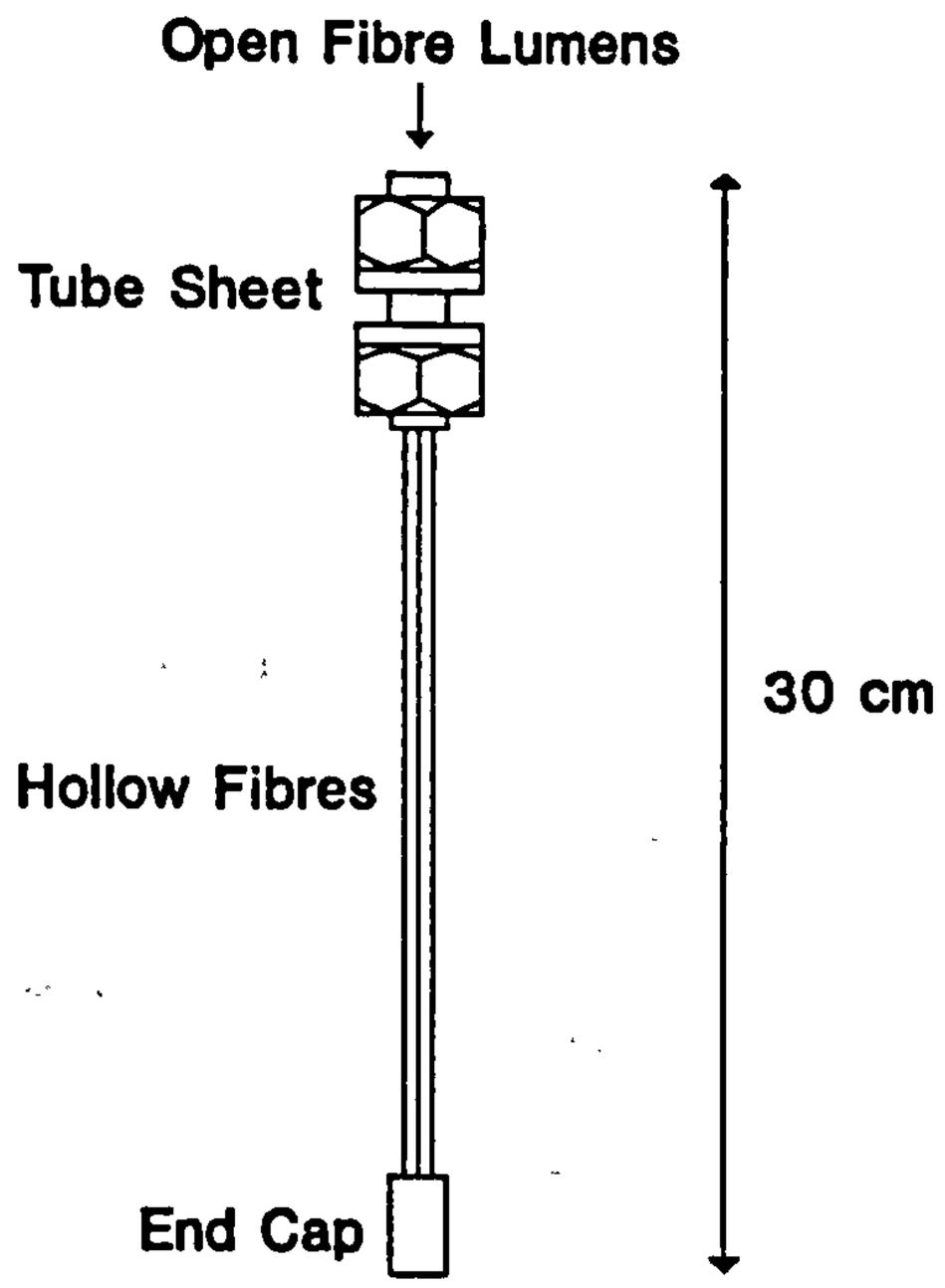

Figure 2.4 Hollow Fibre Membrane Module

chamber of the gas permeation apparatus **(Figure 2.7)**. The apparatus for sealing or potting-up the hollow fibres in the tube sheet is shown in **Figure 2.5**. Batches of about ten modules were potted-up at once in a rack. The fibres pass through the perspex guide tubes into the tube sheets and finally protrude from the end of the soft silicone tubing sections. The perspex tube made sure that the fibres were aligned properly in the tube sheet. Degassed potting-up resin was passed via a syringe up through the silicone tubing until it reached the top of the tube sheet. The syringe was then removed and the silicone tubing sealed with a metal clip to prevent resin leakage.

Care had to be taken during injection to avoid the resin coming in contact with the perspex tube since this resulted in either smearing the fibres with resin, if the problem was detected, or damaging the fibres at removal.

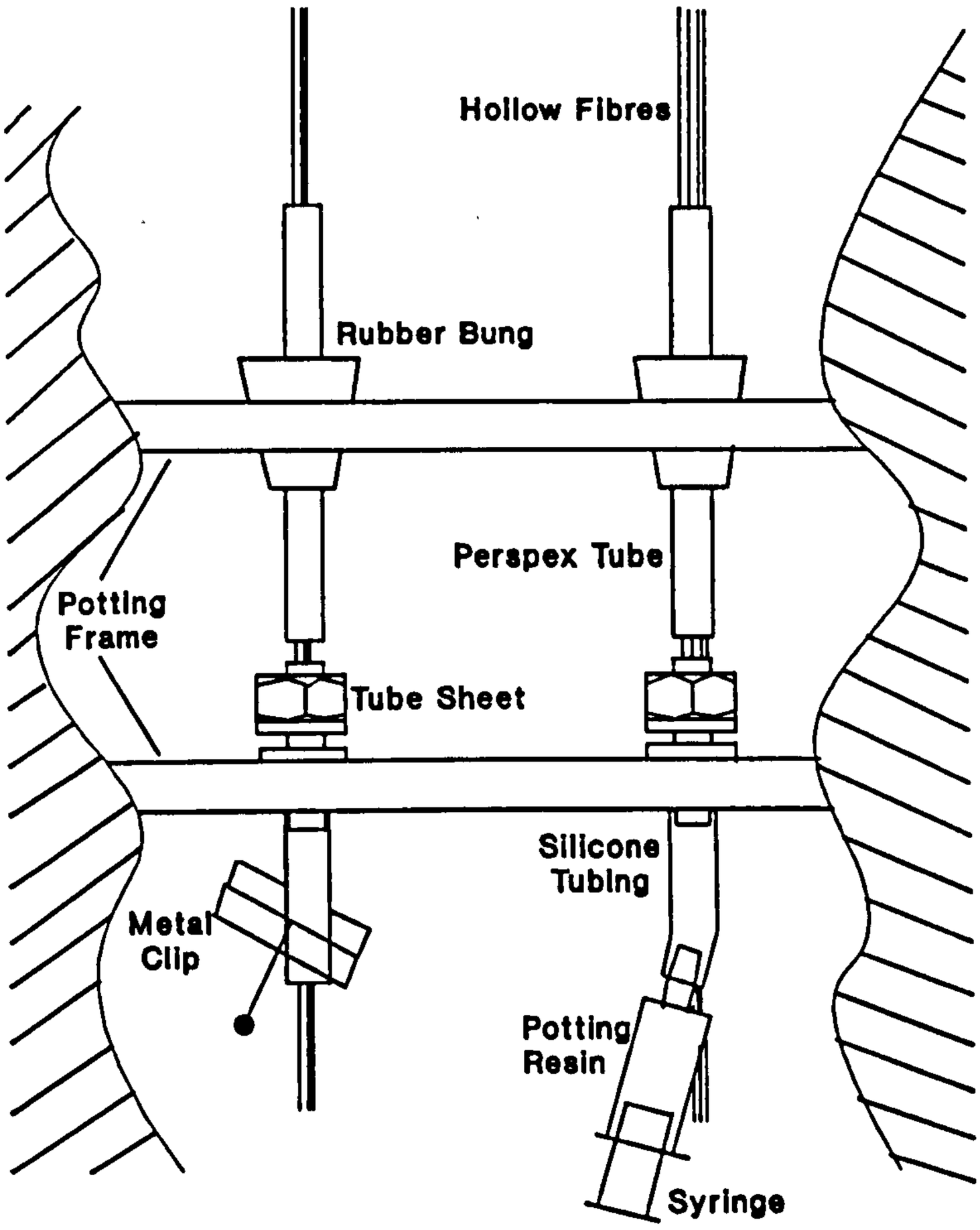

Figure 2.5 Hollow Fibre Potting-up Apparatus

The fibres were left for 1 day to allow the resin to solidify. The units were then removed and a clean cut was made with a razor blade through the silicone tubing and resin at the end of the tube sheet to reveal the fibre openings potted in the resin. The fibres were then cut to give a module length of approximately 30cm. The remaining fibre ends were sealed with resin in small aluminium end caps. This was carried out with the fibre modules simply lying horizontally on the laboratory bench. The modules were further left for 2 days to allow the resin to fully harden. They were finally placed vertically in a storage rack in a clean environment.

Various types of potting-up resins were investigated shown in **Table 2.2.**

Resin Type	Properties
RS Components Two Component Epoxy Potting Compound	Hard and brittle when set, unable to be cut. **Unsuitable**
RS Components Two Component Polyurethane Potting Compound	Too soft when set, unable to achieve clean cut revealing open fibre lumens. **Unsuitable**
CasChem Inc.(N.J.,U.S.A) Two component Polyurethane Potting Compound	Ideal hardening properties, cuts very cleanly and hardens to give a strong tube sheet. **Suitable - Type used**

Table 2.2 Investigation of Potting-up Materials

2.4 Hollow Fibre Coating Apparatus and Methods

The fibres were coated with a highly permeable elastomeric silicone polymer. The purpose of the coating was to fill any surface pinholes or imperfections which render the fibres useless for gas separation. Blocking these cavities results in a decrease in permeability but improved selectivity. Coating may be regarded as a standard procedure which allows the hollow fibre to exhibit permeation properties closer to the inherent characteristics of the membrane polymer itself.

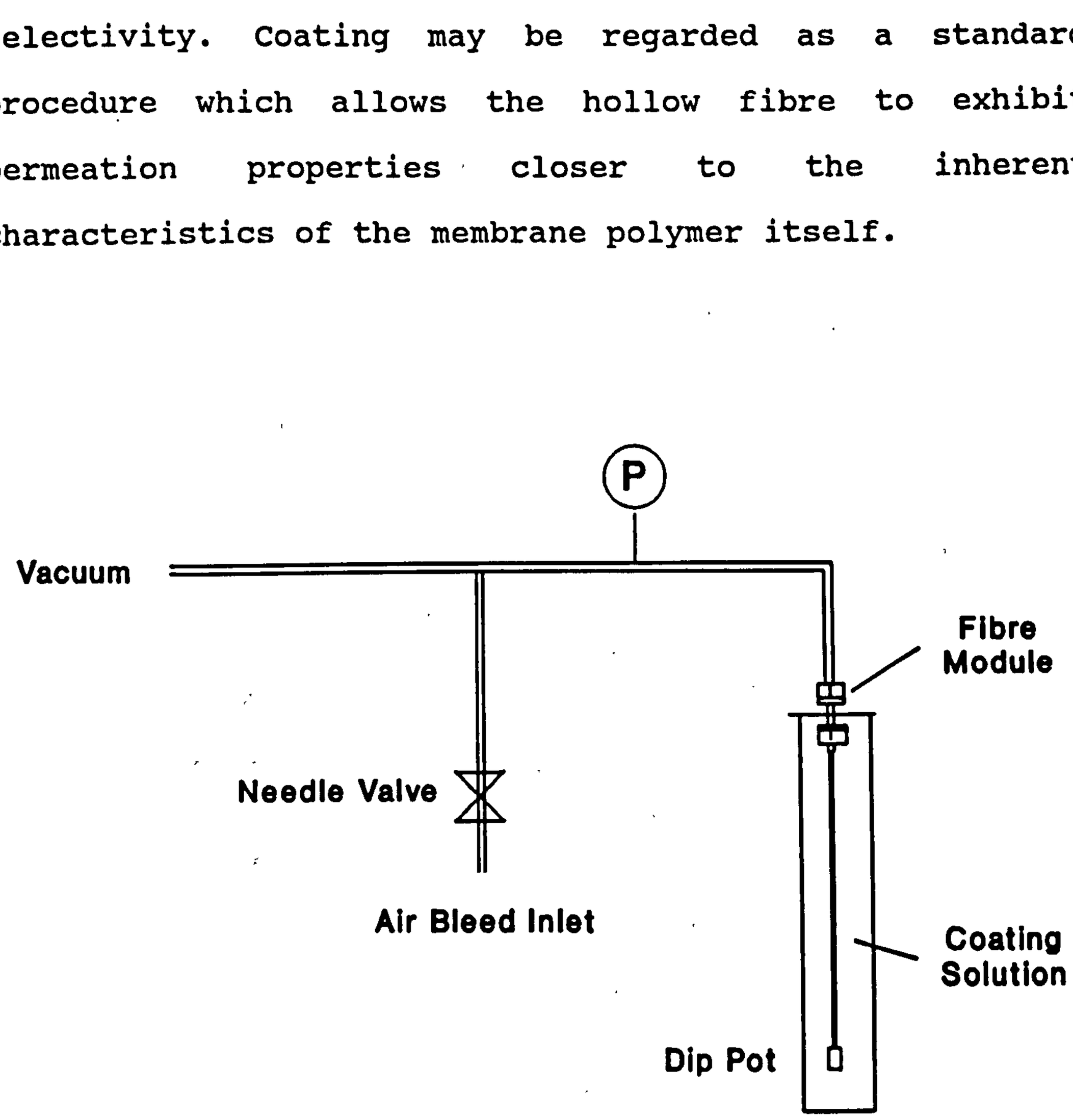

Figure 2.6 Hollow Fibre Coating Apparatus

The fibres were coated in their modular form by dipping into a dip pot full of coating solution and applying a vacuum (10"Hg) to the fibre lumens. The coating was carried out at ambient temperature. **Figure 2.6** shows the fibre coating apparatus.

The solvent used to prepare the coating solution must satisfy two criteria:

1. Readily dissolve the silicone coating polymer.
2. Must be inert with respect to the membrane polymer.

Possible coating solvents were investigated. The results are shown in **Table 2.3.**

Solvent	Suitability
Methylene Chloride	Readily dissolves silicone and membrane polymers. **Unsuitable**
Xylene	Readily dissolves silicone. Partially dissolves membrane polymers. **Unsuitable**
Hexane	Readily dissolves silicone. Completely inert towards membrane polymers. **Suitable**

Table 2.3 Investigation of Coating Solvents

Two potential silicone coating polymers were examined shown in **Table 2.4.**

Silicone	Solvent Base	Curing
Dow Corning 200/1000cs Silicone	None	Self curing at room temperature
Petrarch MB PS254 Silicone	Methylene Chloride	Self curing at room temperature

Table 2.4 Silicone Coating Polymers

Both silicones dissolved in hexane and formed coatings. However the use of the Petrarch product was rejected because of the methylene chloride present. Dow Corning silicone (200/1000cs) in hexane was therefore used as the coating medium in this work. Two different coating solution strengths were employed: 3% w/w and 15% w/w silicone in hexane.

After the coating period (15 mins) the fibres were removed from the coating solution and allowed to cure for a number of days before being tested.

2.5 Hollow Fibre Gas Permeation Apparatus and Methods

Figure 2.7 shows the gas permeation apparatus. All fittings and components were stainless steel and rated to high pressure.

The test gas cylinder was connected directly to the rig via a flexible high pressure stainless steel hose. The pressure in the permeation chamber was controlled by either of the two pressure regulators depending on the pressure range required. The pressure regulators were suitable to cater for all test gases. This system allowed the various test gases to be easily interchanged.

The cylinder pressure was indicated on the 0-350bar gauge positioned immediately after the flexible hose. The pressure in the permeation chamber was indicated on the gauge positioned between the pressure regulators and the chamber itself. A 0-40bar gauge was used for low to medium pressure tests and a 0-100bar gauge for medium to high pressure tests.

The permeation chamber consisted of a 30cm section of thick walled 1" OD stainless steel pipe sealed at both ends by stainless steel plugs welded into position. The chamber was drilled and tapped at both ends and at a height of 3cm from the top to incorporate bulkhead fittings. The test gas inlet line was fitted to the bottom

1. Flexible High Pressure Hose
2. Pressure Gauge 0-350bar
3. Pressure Gauge 0-40bar or 0-100bar
4. Pressure Gauge 0-1bar
5. High Pressure Regulator
   Delivery Pressure 35-240bar
6. Low Pressure Regulator
   Delivery Pressure 0-60bar
7. Temperature Control Water Jacket
8. Needle Valve
9. Solenoid Valve (1)
10. Solenoid Valve (2)
11. Automatic Gas Sampling Valve
12. GC/PC Interface

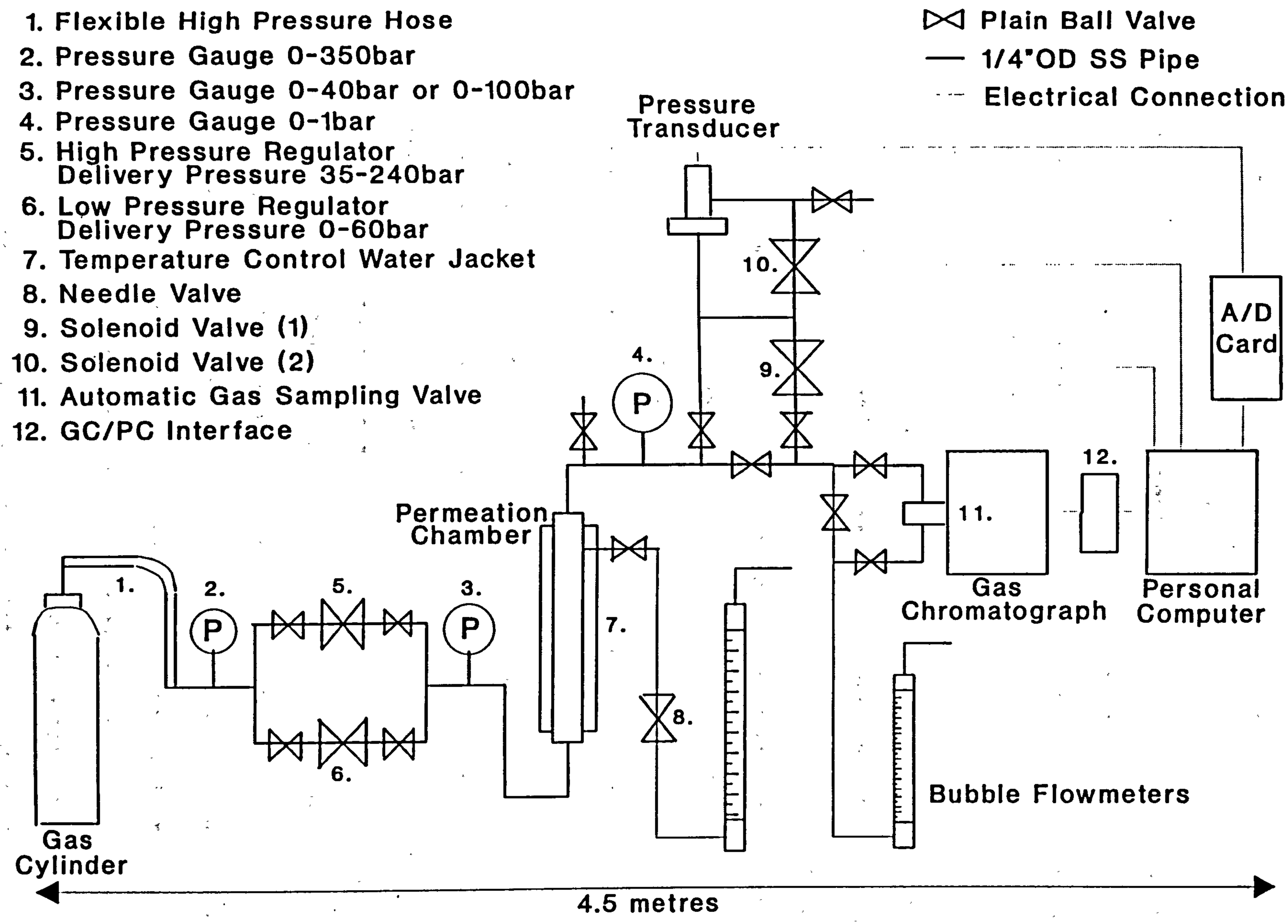

Figure 2.7 Hollow Fibre Gas Permeation Apparatus

of the chamber and the shell side gas exit line was fitted to the side. The fibre modules were placed inside the chamber and fixed into position by tightening the bottom tube sheet nut onto the top bulkhead fitting. The top tube sheet nut was then connected to the permeate line thus fully incorporating the fibre module into the rig. The permeation temperature was controlled by means of a water jacket fitted to the outside of the chamber.

When gas mixtures were tested a shell side flowrate through the permeation chamber was required to ensure a constant gas composition on the outside of the fibres. This flowrate which was usually set at ten times that of the permeate was controlled by a needle valve carefully sized for the task. The shell side gas flowrate was measured by a bubble flowmeter venting to atmosphere.

The gas passing through the hollow fibres flowed along the permeate line and vented to atmosphere either through a second bubble flowmeter or via an automatic permeation rate measurement system. This computer interfaced facility comprised solenoid valves and a differential pressure transducer. The computer determined the gas flowrate by shutting off the permeate line and then measuring the rate of pressure rise. The pressure transducer and analogue to digital converter were specified to allow a pressure rise of 0-100 mbar in the line. The solenoid valves were activated by relay switches. Interfacing software was

written to manage the apparatus which once calibrated (to establish system volume) permitted the permeate flowrate to be automatically measured and recorded at specified time intervals.

When testing gas mixtures, the permeate must also pass through the automatic gas sampling valve of the gas chromatograph. The on-line gas chromatagraph periodically sampled the permeating gas and carried out an analysis of its composition.

The pressure in the permeate line was indicated on the 0-1bar pressure gauge. This pressure was usually negligible but may be noticeable when gases pass through the automatic gas sampling valve at high flowrate.

The permeability of the hollow fibres was evaluated by measuring the gas permeation rate at particular chamber pressures. The selectivity of the membranes is merely the ratio of the permeabilities. When gas mixtures are tested the calculations are based on the partial pressures of the different permeating species.

The gas chromatograph selected for this apparatus was a Perkin-Elmer 8500 with hot wire detector. One of two different column types was used depending on the gas mixture under test: a '5Å Molecular Sieve' column was used for N_2/O_2 tests and a 'Poropack Q' column for CO_2/CH_4

tests. The data processing was carried out by the Amstrad 1640 personal computer using a Nelson Analytical integration system. Suitable methods of analysis and subsequent data handling had to be established for the different gas mixtures tested.

Before the chamber pressure was increased during tests the vent ball valve immediately downstream of the permeation chamber was opened and the first permeate line ball valve was closed. This served as a safety precaution against tube sheet or fibre failure causing a sudden pressure increase in the permeate line. This protected the low pressure gauge, the automatic permeation rate measurement equipment, the automatic gas sampling valve and the permeate bubble flowmeter. The gas chromatograph internals are never subjected to line pressure.

All pressure gauges were blow-out protected and the bubble flowmeters were positioned behind a perspex safety shield.

Table 2.5 shows the test gases used. All gases were purchased from Air Products.

Gas and Grade	Maximum Cylinder Pressure
Pure N_2 High Purity	200 bar
Pure O_2 High Purity	200 bar
Pure CO_2 High Purity	60 bar
Pure CH_4 Instrument Grade Purity	200 bar
N_2/O_2 Gas Mixture 50/50 Mole% Analysis Certificate	200 bar
CO_2/CH_4 Gas Mixture 50/50 Mole% Analysis Certificate	80 bar

Table 2.5 Details of Test Gases

Chapter 3 Experimental and Characterisation

3.1 Some Basic Principles of Spinning

3.1.1 Polymer Mass Balance Over Spinning Line

On extrusion the mass flowrate of polymer, $\dot{M}$ is given by

$$\dot{M} = DER\ \rho_D\ C_D \quad \text{----------} \quad 3.1$$

where DER = Dope extrusion rate

ρ_D = Dope density

C_D = Dope concentration

In the spinning line, $\dot{M}$ is given by

$$M = V_f\ A_f\ \rho_B \quad \text{----------} \quad 3.2$$

where V_f = Fibre velocity (wind-up speed)

A_f = Cross sectional area of fibre

ρ_B = Bulk density of fibre

The primary stretch ratio or jet stretch ratio of the fibre, JS is defined as

$$JS = \frac{V_f}{LER} = \frac{V_f}{DER/A_{SP}} \quad \text{---------- 3.3}$$

where LER = Linear extrusion rate or extrusion speed

A_{SP} = Dope extrusion area of spinneret

The mass per unit length or linear density of the fibre, ρ_L is simply

$$\rho_L = \rho_B A_f \quad \text{---------- 3.4}$$

Combining equations 3.1 to 3.4 we obtain the following simple expression which shows the relationship between spinning conditions and the linear density of the hollow fibre produced.

$$\rho_L = \frac{\rho_D C_D}{JS} A_{SP} \quad \text{---------- 3.5}$$

3.1.2 Fibre Porosity

Fibre porosity or void volume fraction, v is given by

$$v = 1 - \frac{\rho_B}{\rho_P} = 1 - \frac{\rho_L}{A_f \rho_P} \qquad \text{---------- 3.6}$$

where ρ_P = Density of polymer

Assuming no volume change on mixing, the dope density can be calculated from

$$\rho_D = \frac{\rho_P \rho_S}{\rho_S C_D + \rho_P (1 - C_D)} \qquad \text{---------- 3.7}$$

where ρ_S = Density of solvent

From equations 3.5, 3.6 and 3.7 it can be seen that

$$v = 1 - \frac{\rho_S C_D}{\rho_S C_D + \rho_P (1 - C_D)} \frac{A_{SP}}{A_f} \frac{1}{JS} \qquad \text{---------- 3.8}$$

In the ideal case the volume of the resultant hollow fibre equals that of the extruded polymer solution. Thus

$$A_{SP} = A_f \, JS \; (IDEAL) \qquad \text{----------} \quad 3.9$$

Combining equations 3.8 and 3.9 gives the expression for ideal porosity which is purely dependent on dope characteristics.

$$\nu_{Ideal} = 1 - \frac{\rho_S \, C_D}{\rho_S \, C_D + \rho_P \, (1 - C_D)} \qquad \text{----------} \quad 3.10$$

The degree of departure from the ideal porosity can be expressed by the contraction factor, υ defined as

$$\upsilon = \frac{\nu_{Ideal} - \nu}{\nu_{Ideal}} \qquad \text{----------} \quad 3.11$$

3.1.3 Fibre Dimensions

Due to the complexity of the coagulation (phase inversion) process there is no obvious way to define the exact relationship between fibre lumen diameter, d_L, fibre outer diameter, d_o and spinning conditions. However, by adopting an idealised perspective, expressions for d_L and d_o can be obtained.

From equation 3.9

$$A_f = \frac{\pi}{4} \left(d_o^2 - d_L^2 \right) = \frac{A_{SP}}{JS} \qquad \text{----------} \quad 3.12$$

Assuming no depletion of injected water volume, two extremes can be identified when considering lumen diameter.

1. The lumen diameter is fixed at point of extrusion and no slip occurs between dope and water, giving

$$\frac{\pi}{4} d_L^2 = \frac{WIR}{DER} A_{SP} \qquad \text{----------} \quad 3.13$$

where WIR = Water injection rate

2. The lumen diameter is established after jet stretch (primary stretch) and no slip occurs between dope and water at this point, thus

$$\frac{\pi}{4} d_L^2 = \frac{WIR}{DER} \frac{A_{SP}}{JS} \quad \text{---------- 3.14}$$

In Case 1. lumen diameter is independent of JS (unlikely in reality). Combining equations 3.12 and 3.13 the following expression for outer diameter is obtained.

$$\frac{\pi}{4} d_O^2 = A_{SP} \left(\frac{1}{JS} + \frac{WIR}{DER} \right) \quad \text{---------- 3.15}$$

In Case 2. lumen diameter is a function of JS and in this instance the expression for fibre outer diameter is as follows (combining equations 3.12 and 3.14).

$$\frac{\pi}{4} d_O^2 = \frac{A_{SP}}{JS} \left(1 + \frac{WIR}{DER} \right) \quad \text{---------- 3.16}$$

As will be shown later, actual fibre dimensions are represented quite effectively when these two simple models are considered together.

In the simple case of extruding a fibre through a plain circular orifice

$$d_f = \frac{d_{SP}}{\sqrt{JS}} \qquad \text{---------- } 3.17$$

where d_f = Fibre diameter

d_{SP} = Spinneret orifice diameter

3.2 Details of Spinning Campaigns

A rheological approach to the spinning of hollow fibre membranes has been taken in this work. The main spinning parameters identified for investigation were dope concentration, C_D, dope extrusion rate, DER and jet stretch ratio, JS. These key variables allow the effects of shear in the spinneret and subsequent post extrusion elongation to be studied with respect to fibre structure and gas permeation performance.

When considering the influence of one variable it is important to keep the other factors constant. The spinning campaigns shown in **Appendix A.** were designed to accommodate this. Spinneret dimensions, coagulant temperature and composition, dope temperature and height of dry jet gap were all fixed throughout. Water injection rate relative to polymer extrusion rate was also fixed (with the exception of the first spinning campaign which was essentially a practice run).

Much of the work involved spinning dopes of polysulphone (P1700) in dimethylformamide. However, a detailed study of polyacrylonitrile (P82) was also carried out as well as an additional spinning campaign involving polysulphone (P3500).

3.3 Rheological Characterisation of Spinning Dopes

3.3.1 Polymer Molecular Weight and Intrinsic Viscosity

The intrinsic viscosities of the polymers of interest were determined using a Ubbelohde capillary viscometer. Full details of the tests can be found in **Appendix C. Graph 3.1** shows reduced viscosity, η_{Red} against concentration, C for the three polymers in dimethylformamide.

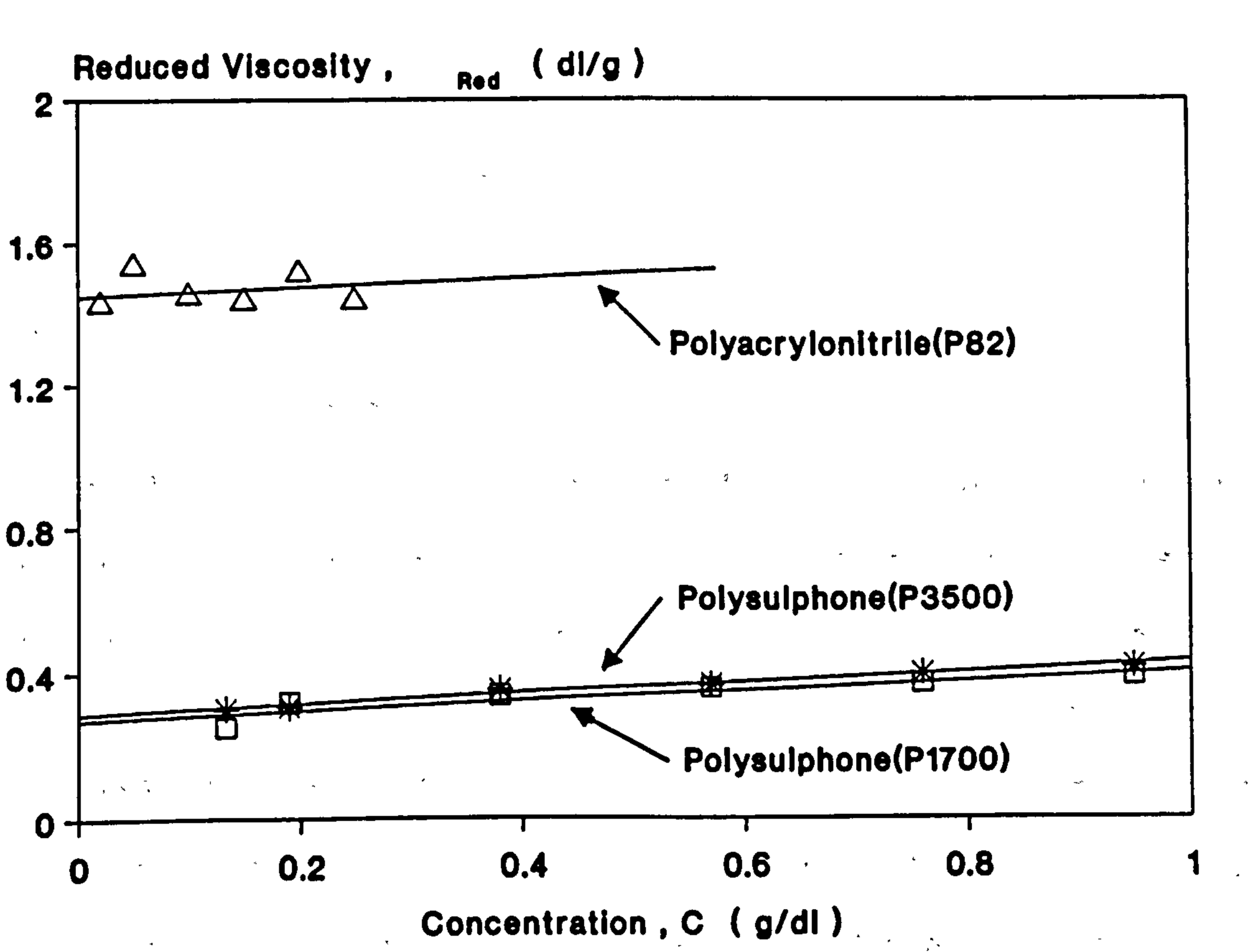

Graph 3.1 Polymer Reduced Viscosity Data

The intrinsic viscosity, [η] is simply the intercept with the vertical axis in **Graph 3.1** i.e.

$$[\eta] = (\eta_{Red})_{C=0} \quad \text{----------} \quad 3.18$$

The weight average molecular weight of the polymer, $\overline{M_w}$ can be calculated using the intrinsic viscosity from the Mark-Houwink-Sakurada[65] equation:

$$[\eta] = K\,\overline{M_w}^{\alpha} \quad \text{----------} \quad 3.19$$

where K and α are empirical constants for a particular polymer and solvent system.

The intrinsic viscosity and molecular weight details are presented in **Table 3.1.** K and α values for polysulphone in dimethylformamide could not be found in the literature. However, the similarity in the intrinsic viscosities of the two grades of polysulphone serves to confirm the molecular weight values for polysulphone P1700 and P3500 obtained directly from the literature. The intrinsic viscosity data also indicates, although not conclusively[a], that both polysulphone molecular weights are lower than that of the polyacrylonitrile.

[a] A large variation in intrinsic viscosity between two polymer types does not necessarily signify dissimilar molecular weights because K and α differ between polymers.

Polymer	[η] (dl/g)	K (dl/g)	α (--)	$\overline{M_w}$
Poly-acrylonitrile (P82)	1.443	2.43×10^{-4} [a]	0.75 [a]	107,500
Polysulphone (P1700)	0.267			35,400 [b]
Polysulphone (P3500)	0.291			38,600 [b]

[a] Ref [65]

[b] Ref [66]

Table 3.1 Polymer Intrinsic Viscosities and Molecular Weights

3.3.2 Behaviour of Spinning Dopes Under Shear

Tests were carried out using a computer managed Carri-Med Controlled Stress Rheometer. Each spinning dope was subjected to a range of shear rates covering those experienced during actual spinning. In order to achieve such elevated shear rates, in the region of 10,000 1/s (see section 5.1 for calculation of shear rates during spinning), the dopes were tested in a sample gap of 16 to 20 microns beneath a rotating 1 cm diameter flat plate. The tests were carried out at 25 ^{o}C.

Each sample was exposed to incrementally increasing shear stress, a period of constant shear stress and then incrementally decreasing shear stress. The corresponding shear rate of the sample was recorded during the test thus giving a standard flow curve. Test duration was in the order of 4 minutes. The rotational speed of the instrument was the limiting factor in all of the tests except for the most concentrated dopes of both the polysulphone and polyacrylonitrile when the instrument's maximum torque capability became limiting.

A curve fitting computer package was used to analyse the data. All of the dopes displayed classical shear thinning power law properties apart from the lowest concentration of polysulphone where the second Newtonian region prevailed.

For a fluid exhibiting Newtonian properties

$$\tau = \eta \dot{\gamma} \quad \text{----------} \quad 3.20$$

where τ = Shear stress

$\dot{\gamma}$ = Shear rate

η = Viscosity = Constant

For a fluid showing Power Law characteristics

$$\tau = k \dot{\gamma}^n \quad \text{----------} \quad 3.21$$

Thus $$\tau = \eta(\dot{\gamma})\ \dot{\gamma} \quad \text{----------} \quad 3.22$$

and $$\eta(\dot{\gamma}) = k \dot{\gamma}^{n-1} \quad \text{----------} \quad 3.23$$

where $\eta(\dot{\gamma})$ = Viscosity (apparent) which is dependent on shear rate

k and n are constants

If n>1 then fluid is shear thickening

If n<1 then fluid is shear thinning

None of the dopes exhibited time dependency during the period of peak stress (peak stress held for between 1 and 2 mins). This suggests that equilibrium prevailed at each increment during ascending shear stress. This is reinforced by the creep investigations where retardation

times were short in relation to the timescale of the current tests. On descending shear stress, flow curve hysteresis was frequently observed where apparent viscosities were lower than those on ascending shear. Viscoelastic effects may be the reason for this. The molecules become aligned on shearing and due to significant relaxation times, as suggested by the creep tests (relaxation times were found to be considerably higher than retardation times), a degree of orientation is maintained resulting in reduced apparent viscosities on descending shear.

Solvent leaching and evaporation from the dope during tests proved to be a problem on some occasions. However, perseverance and careful choice of test duration allowed consistent results to be obtained.

Details of the dopes tested and their properties under shear are given in **Table 3.2** and **Graphs 3.2 to 3.4**. The zero shear viscosities determined from the creep tests (section 3.3.5) are included here for completeness. No experimental points appear on **Graphs 3.3 or 3.4** because the data is continuously sampled by the rheometer.

As described in section 5.1, these dope characteristics are used to determine the actual velocity, shear rate and shear stress profiles as well as the pressure drop in the spinneret during the spinning runs.

Dope	Zero Shear Viscosity (Pa.s)	Behaviour (Shear Rate Range 500 - 10,000 1/s) (Units SI Based)
20% w/w Polysulphone(P1700) in Dimethylformamide	0.913	Newtonian $\tau = 0.427\ \dot{\gamma}$
30% w/w Polysulphone(P1700) in Dimethylformamide	9.491	Power Law $\tau = 53.7\ \dot{\gamma}^{0.665}$
40% w/w Polysulphone(P1700) in Dimethylformamide	102.6	Power Law $\tau = 508\ \dot{\gamma}^{0.586}$
30% w/w Polysulphone(P3500) in Dimethylformamide	19.19	Power Law $\tau = 150\ \dot{\gamma}^{0.586}$
15% w/w Polyacrylonitrile(P82) in Dimethylformamide	1.696	Power Law $\tau = 7.13\ \dot{\gamma}^{0.712}$
20% w/w Polyacrylonitrile(P82) in Dimethylformamide	9.453	Power Law $\tau = 35.4\ \dot{\gamma}^{0.662}$
25% w/w Polyacrylonitrile(P82) in Dimethylformamide	157.6	Power Law $\tau = 580\ \dot{\gamma}^{0.671}$

Table 3.2 Spinning Dope Behaviour Under Shear

Graph 3.2 Variation in Zero Shear Rate Viscosity with Concentration of Dope

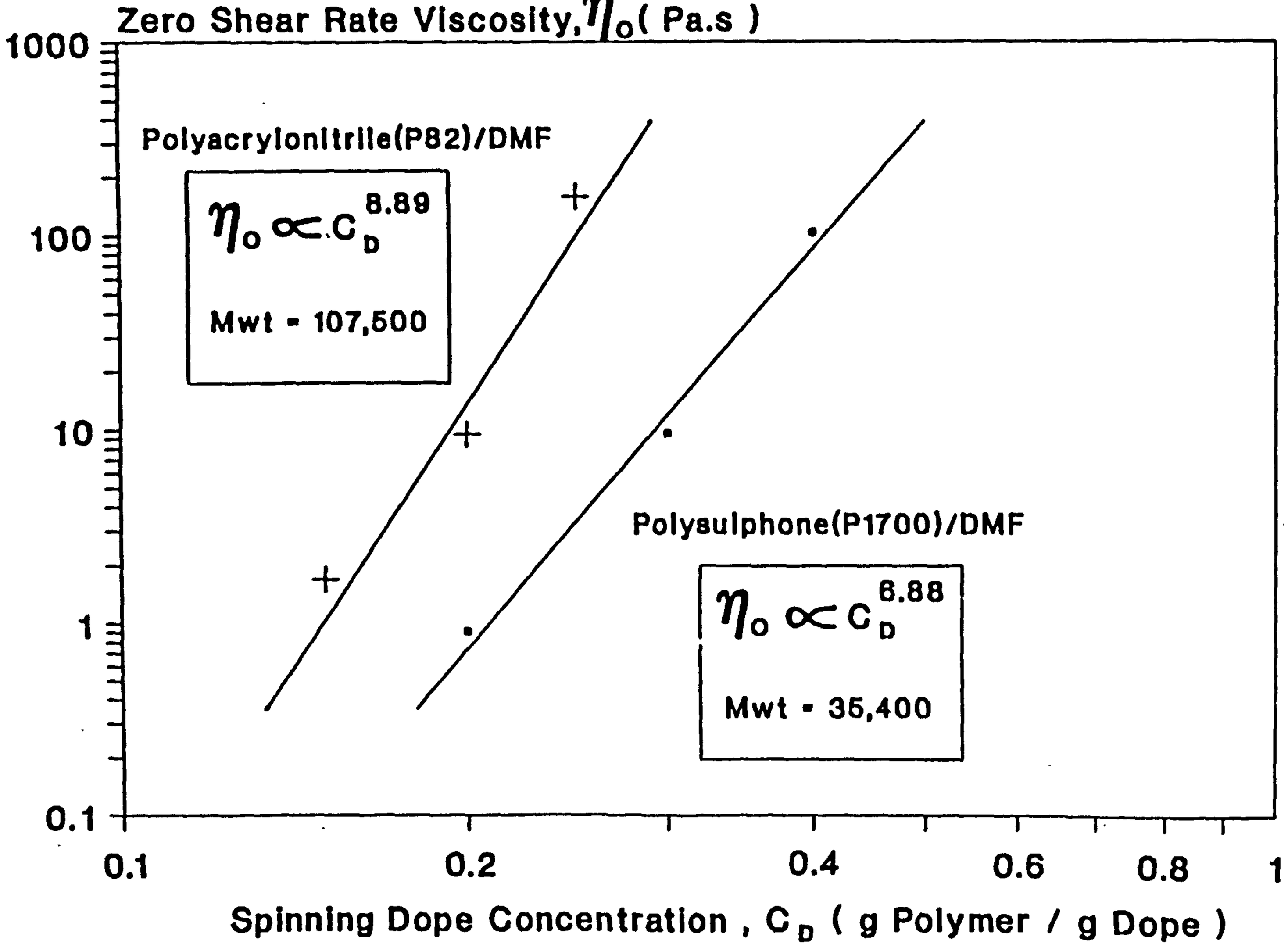

Graph 3.3 Behaviour of Polysulphone Dopes Under Shear

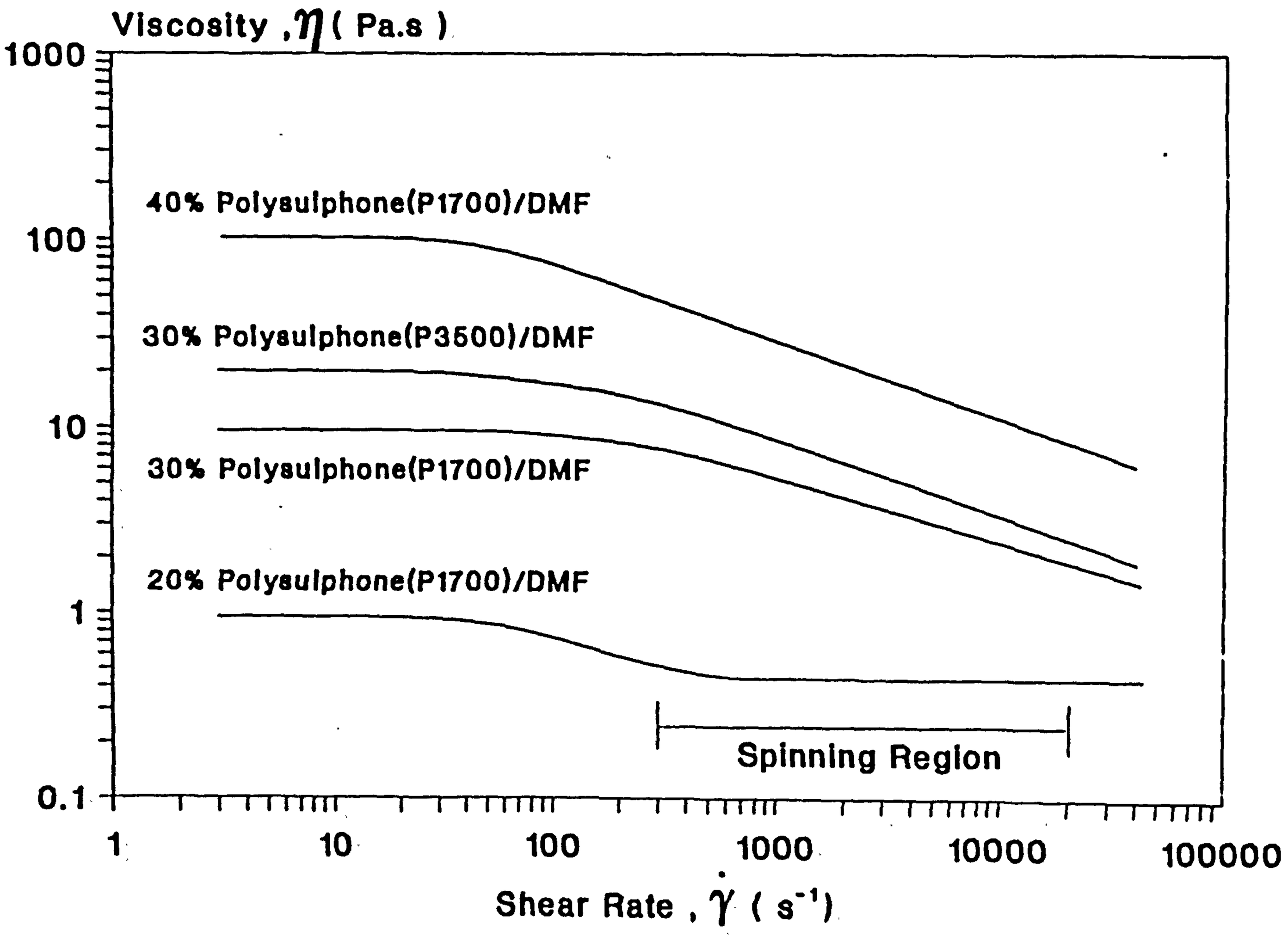

Graph 3.4 Behaviour of Polyacrylonitrile Dopes Under Shear

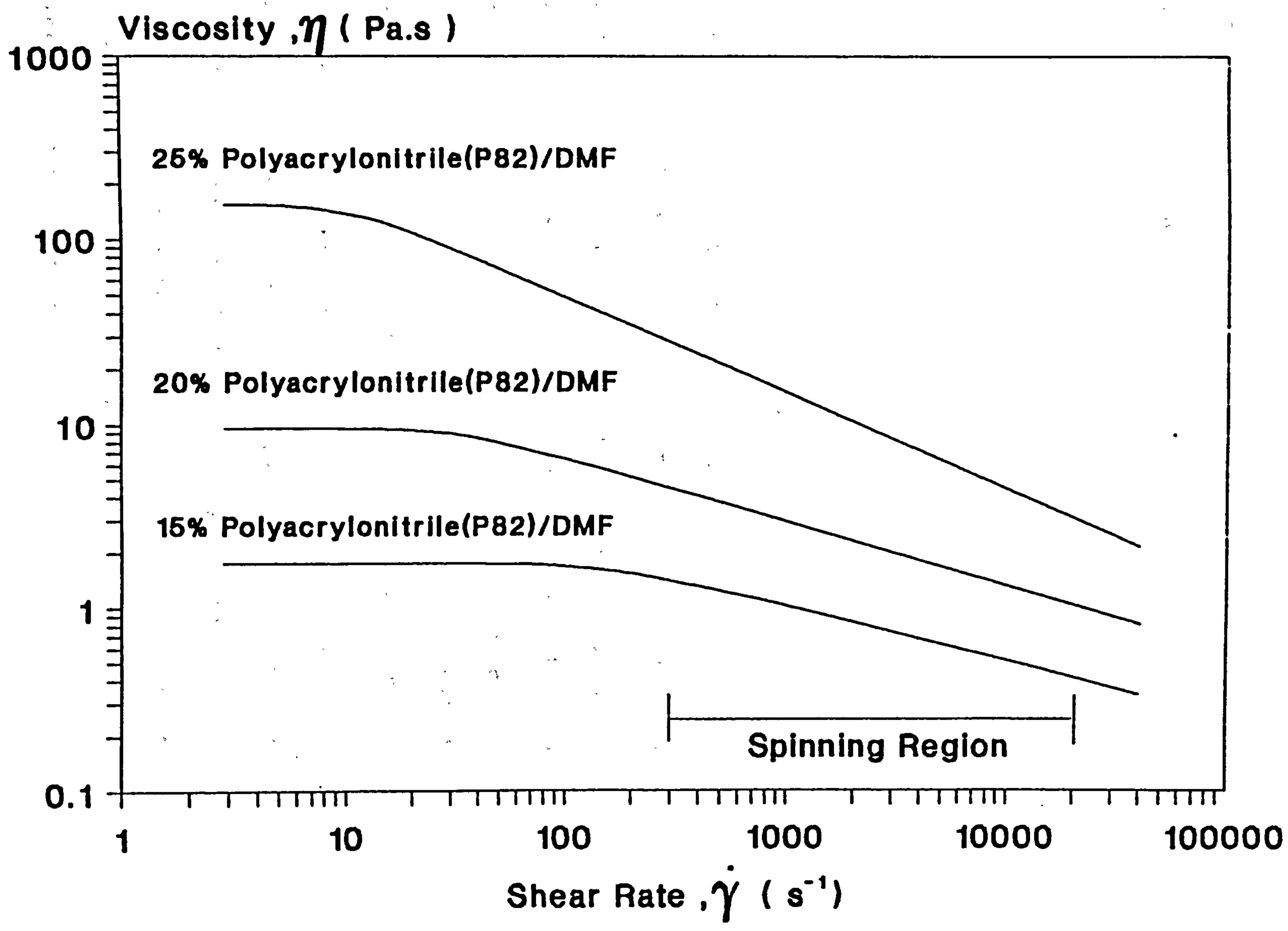

3.3.3 Behaviour of Spinning Dopes Under Elongation

In general, extensional viscosity, η_E is a function of extensional strain rate, $\dot{\epsilon}$, just as shear viscosity, η is a function of shear rate, $\dot{\gamma}$.

$$\sigma = \eta_E(\dot{\epsilon})\ \dot{\epsilon} \quad \text{----------} \quad 3.24$$

where σ = Tensile stress

If η_E increases with increasing $\dot{\epsilon}$ then the fluid is said to be "strain thickening" (c.f. shear thickening). Conversely, if η_E decreases with $\dot{\epsilon}$ then the fluid is "strain thinning" (c.f. shear thinning). However, it is difficult to achieve steady state conditions whilst investigating the response of a fluid under elongation. Under these circumstances measurement is limited to a transient elongational viscosity, $\eta_E(t,\dot{\epsilon})$, which is a function of t as well as $\dot{\epsilon}$. Values obtained for elongational viscosity are therefore specific to the particular experimental technique with respect to time effects. This goes some way to explain the inconsistencies in elongational viscosity results that frequently occur between research workers[67].

These difficulties do not normally occur in the measurement of shear viscosity, $\eta(\dot{\gamma})$ where steady state conditions of shear can be easily attained. Nevertheless, a study of $\eta_E(t,\dot{\epsilon})$ is still of considerable importance for the purposes of generally characterising a fluids behaviour under extension and allowing comparison of different fluids.

In contrast to the understanding of situations involving shear flow, the study of extensional flow is fairly new (beginning in the mid 1960's) and is still evolving. The principles of shear stress, shear rate and shear viscosity are mature and well appreciated whereas strain rate and axial stress in the context of elongational viscosity are less understood. It is therefore appropriate at this stage to describe the basic concepts involved in elongational flow.

The axial stress, $\sigma(x)$ at any point x along the length of a fluid filament undergoing extensional flow is given by

$$\sigma(x) = \frac{F(x)}{A(x)} \qquad \text{---------- } 3.25$$

Where **F(x)** is the resultant force or tension at that location in the filament (incorporates effect of gravity, surface forces, inertial effects and external drawing force).

A(x) is the cross sectional area of the filament.

The strain rate of the fluid, $\dot{\epsilon}(x)$ is defined as

$$\dot{\epsilon}(x) = \frac{\partial V(x)}{\partial x} \qquad \text{---------- } 3.26$$

where V(x) is the velocity of the filament

V(x) is simply evaluated from mass balance

$$V(x) = \frac{Q}{A(x)} \qquad \text{---------- } 3.27$$

where Q is the volumetric flowrate of the fluid

The time of elongation can also be stated

$$t = \int_0^x \frac{dx}{V(x)} \qquad \text{---------- 3.28}$$

as well as the total strain (Hencky strain), $\epsilon(x)$ experienced in the filament

$$\epsilon(x) = \int_0^t \dot{\epsilon}(x)\, dt \qquad \text{---------- 3.29}$$

$$= \int_0^t \frac{d\, V(x)}{dx}\, dt \qquad \text{from 3.26}$$

$$= \int_0^x \frac{d\, V(x)}{dx} \frac{dx}{V(x)} \qquad \text{from 3.28}$$

$$= \int_{V_o}^{V(x)} \frac{1}{V(x)}\, d\, V(x)$$

Thus $\epsilon(x) = \ln(\frac{V(x)}{V_o})$

$= \ln(JS)$

$= \ln(\frac{L}{L_o})$ ---------- 3.30

Where V_o is the initial speed of the filament at the onset of elongation.

L/L_o is the ratio of final to initial length of a fluid rod undergoing the equivalent degree of elongational deformation as the filament.

A full treatment of the kinematics of extensional flow can be found in the literature[68][69][70].

For the purposes of estimating the strain rate experienced during actual fibre spinning the following holds

$$\dot{\epsilon} = \frac{(WUS - LER)}{h_{gap}} \qquad \text{----------} \quad 3.31$$

but $$JS = \frac{WUS}{LER}$$

Thus $$\dot{\epsilon} = \frac{LER(JS - 1)}{h_{gap}} \qquad \text{----------} \quad 3.32$$

where h_{gap} is the height of gap the fibre passes through between spinneret and coagulation bath

LER is the linear extrusion rate of the fibre

and WUS is the fibre wind-up speed

A Carri-Med Elongational Viscometer as described by Ferguson and Hudson[69] was used to carry out the investigation of the spinning dopes under elongation. Test conditions such as extrusion rate, filament length and filament take-up velocity were altered and the resultant drawing force and filament dimensions recorded. From these parameters the strain rate, total strain, tensile stress and elongational viscosity can be determined at every stage along the filament length. However, from the viewpoint of obtaining a general measure of the dope's

response to extension, the average values of tensile stress, strain rate and elongational viscosity for each test, as described by Jackson et al[71] and Jones et al[72], are of more relevance and are reported here.

The experimental procedure was semi computer managed with the final data being processed by means of a menu driven computer package. The results of the tests, carried out at 20 ^{o}C, are shown in **Graphs 3.5** and **3.6** and **Table 3.3.** All of the dopes displayed strain thinning behaviour over the range of strain rates investigated.

A more detailed analysis of the individual conditions along the filament line during each of the tests would include considering the effect of total strain as opposed to the instantaneous strain at any point. Correlating elongational viscosity with total strain would have distinct advantages when considering tests, such as these, that occur over a short period of time and are transient in nature. Total strain, in such circumstances of unsteady state, is a more appropriate quantification of the degree of elongational deformation than strain rate. This would be especially pertinent when comparing elongational viscosity results produced from differing experimental procedures. However, for the purposes of this work, where a general assessment of the behaviour of each dope under elongation is adequate, concentrating on the average results of tensile stress, strain rate and elongational viscosity in each test is justifiable.

Graph 3.5 Behaviour of Polysulphone Dopes Under Elongation

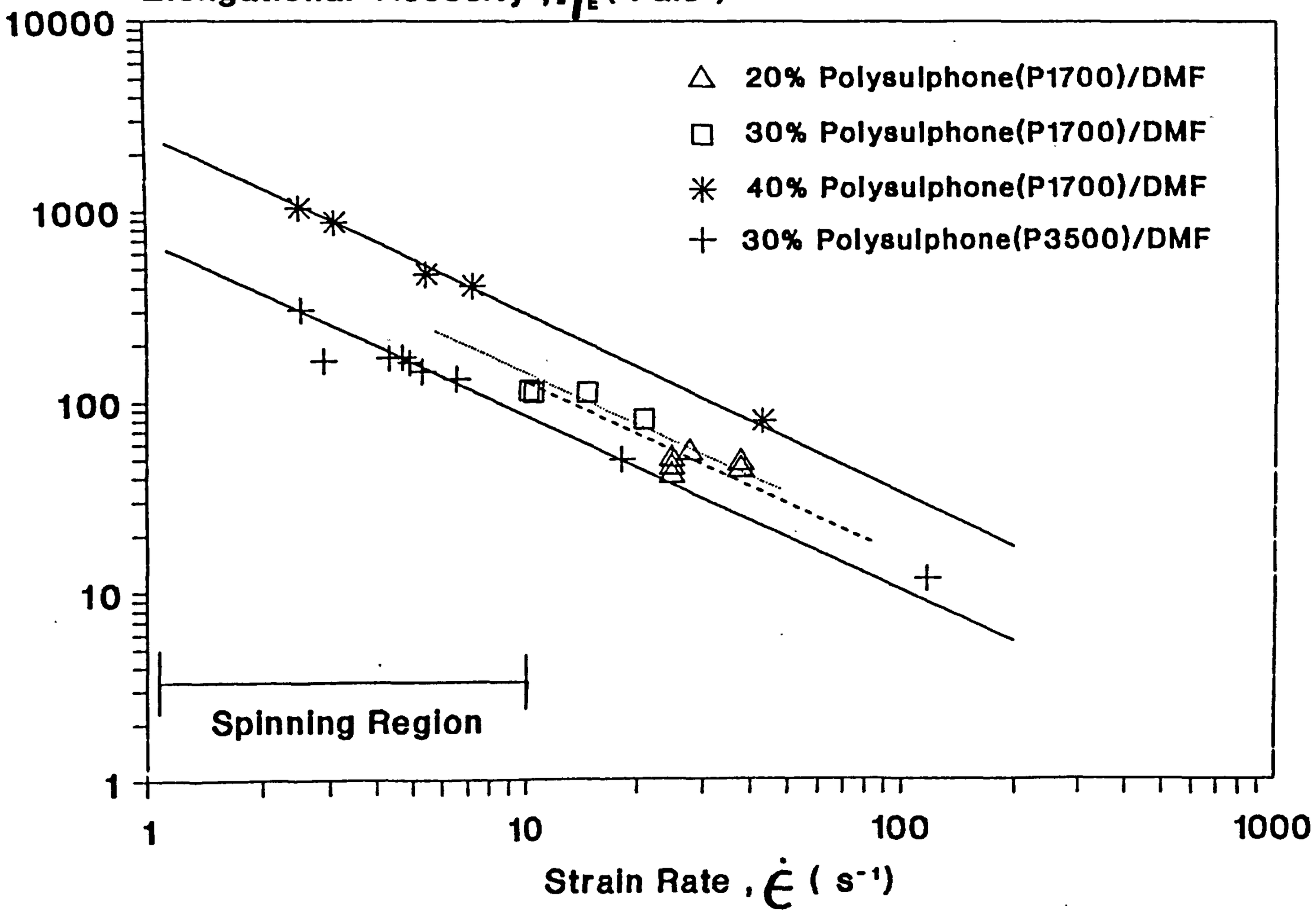

Graph 3.6 Behaviour of Polyacrylonitrile Dopes Under Elongation

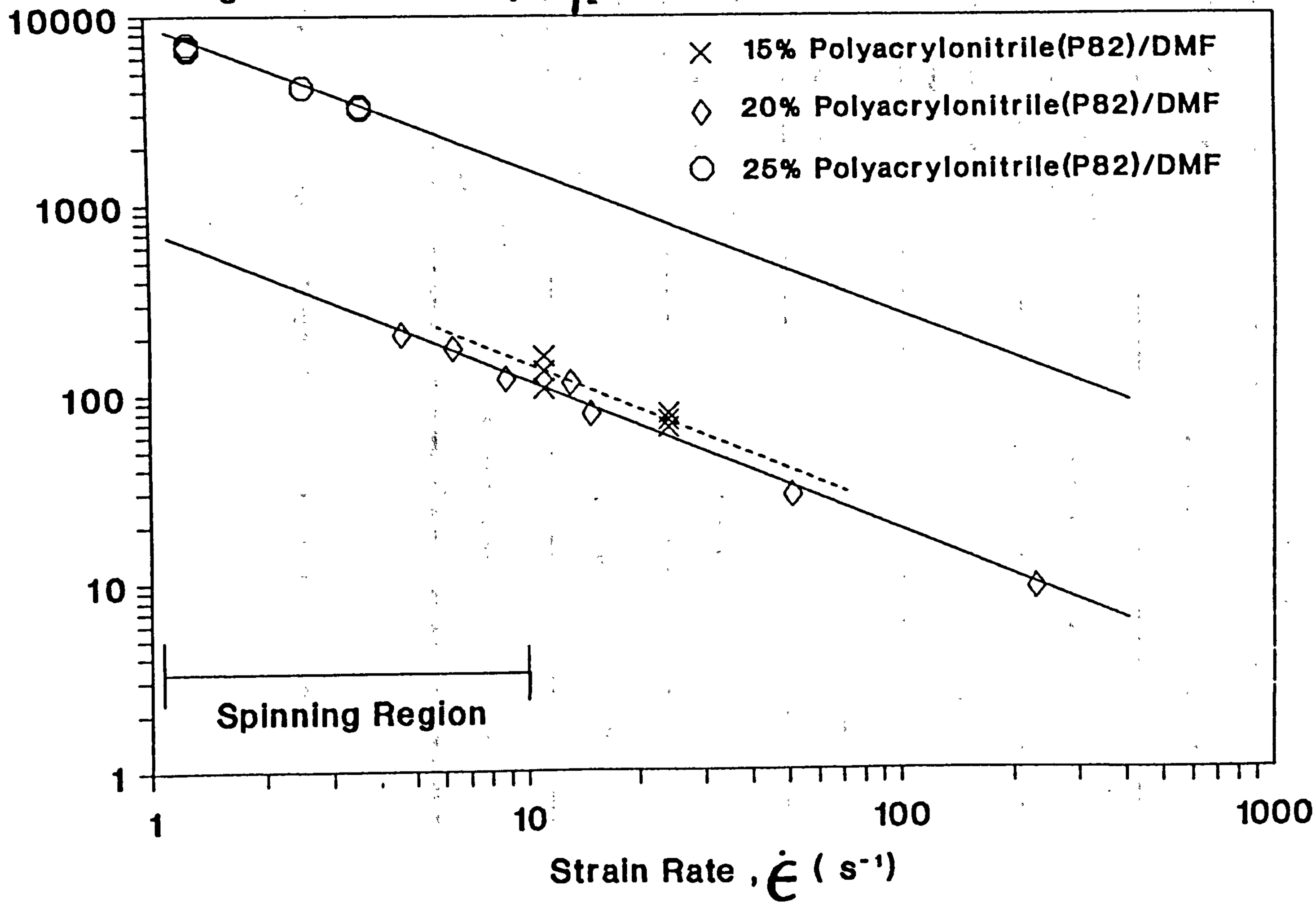

Dope	Behaviour (Strain Rate Range 1 - 200 1/s) (Units SI Based)
20% w/w Polysulphone(P1700) in Dimethylformamide	Strain Thinning $\sigma = 1150\ \dot{\epsilon}^{0.0775}$
30% w/w Polysulphone(P1700) in Dimethylformamide	Strain Thinning $\sigma = 1200\ \dot{\epsilon}^{0.0775}$
40% w/w Polysulphone(P1700) in Dimethylformamide	Strain Thinning $\sigma = 2510\ \dot{\epsilon}^{0.0775}$
30% w/w Polysulphone(P3500) in Dimethylformamide	Strain Thinning $\sigma = 700\ \dot{\epsilon}^{0.0775}$
15% w/w Polyacrylonitrile(P82) in Dimethylformamide	Strain Thinning $\sigma = 920\ \dot{\epsilon}^{0.180}$
20% w/w Polyacrylonitrile(P82) in Dimethylformamide	Strain Thinning $\sigma = 760\ \dot{\epsilon}^{0.180}$
25% w/w Polyacrylonitrile(P82) in Dimethylformamide	Strain Thinning $\sigma = 9000\ \dot{\epsilon}^{0.220}$

Table 3.3 Spinning Dope Behaviour Under Elongation

All dopes show a decrease in extensional viscosity with strain rate. This implies that the polymer solutions are not naturally spinnable. The question of "spinnability" can be explained by considering the fibre spinning process. It is of fundamental importance that the threadline is stable and does not snap. Tension along the threadline is chosen to avoid fracture under normal operating conditions. The main concern is with the propagation and magnification of small disturbances, which are to some extent unavoidable in a physical process of this nature. If, for whatever reason, a decrease in diameter occurs at any point in the filament then from continuity considerations velocity and hence strain rate are increased. If the dope is strain thinning, resistance to extension is reduced in the narrowed region, motion is accelerated and the filament breaks. This was reflected in the difficulty of early solid fibre dry jet wet spinning trials where fibre breakage was frequent.

This inherent "unspinnability" is counteracted in hollow fibre spinning by the fact that there is immediate coagulation from within on extrusion which gives the filament instant strength in the air gap prior to the coagulation bath. However, the hollow fibres still had a high breakage frequency at jet stretch ratios of greater than about two.

3.3.4 Comparison of Dope Response to Elongation and Shear

The Trouton ratio provides a comparison between the behaviour of a fluid under elongation and shear. This is important in processes which involve the two types of flow e.g. fibre spinning and also enhanced oil recovery.

The Trouton ratio is given by

$$T_R = \frac{\eta_E(\dot{\epsilon})}{\eta(\dot{\gamma})} \qquad \text{----------} \quad 3.33$$

For Newtonian fluids T_R=3, a result obtained by Trouton [73] as early as 1906.

The definition given in equation 3.33 is somewhat ambiguous since T_R depends on both $\dot{\epsilon}$ and $\dot{\gamma}$. Some correlation has therefore to be adopted to relate strain rate in extension and shear rate. To remove this ambiguity Jones et al[72] have proposed the following definition, which has become the convention, based on a simple analysis for an inelastic non-Newtonian fluid.

$$T_R = \frac{\eta_E(\dot{\epsilon})}{\eta(\sqrt{3}\dot{\epsilon})} \qquad \text{---------- 3.34}$$

i.e. in the denominator, the shear viscosity is evaluated at the shear rate numerically equal to $\sqrt{3}\dot{\epsilon}$.

Jones et al also show that ideally T_R=3 for all inelastic fluids and that any departure from this value indicates extent of viscoelasticity. The higher the T_R the greater the viscoelasticity of the fluid.

Taking equation 3.34 an expression that relates T_R directly with $\dot{\epsilon}$ can be derived.

$$T_R = \frac{K_E\,\dot{\epsilon}^{\,n_E-1}}{K\,(\sqrt{3}\dot{\epsilon})^{\,n-1}}$$

$$= \frac{K_E\,\dot{\epsilon}^{\,n_E-1}}{K\;3^{\frac{n-1}{2}}\;\dot{\epsilon}^{\,n-1}}$$

Thus $$T_R(\dot{\epsilon}) = 3^{\frac{1-n}{2}} \frac{K_E}{K} \dot{\epsilon}^{n_E-n} \quad \text{---------- 3.35}$$

where K and n are the power law constants

(K=η and n=1 for Newtonian behaviour)

and subscript E refers to elongation

Graphs 3.7 and 3.8 show that for all dopes the Trouton ratio decreases with increasing strain rate over the range tested. At the lowest strain rates Trouton ratios are high suggesting a significant degree of elasticity. Trouton ratios then rapidly fall which implies a decline in viscoelastic properties as strain rate progresses. This decline is less rapid with the most concentrated polyacrylonitrile dope, the fluid which exhibited greatest viscoelasticity in the creep and normal stress tests.

Graph 3.7 Trouton Ratios - Polysulphone Dopes

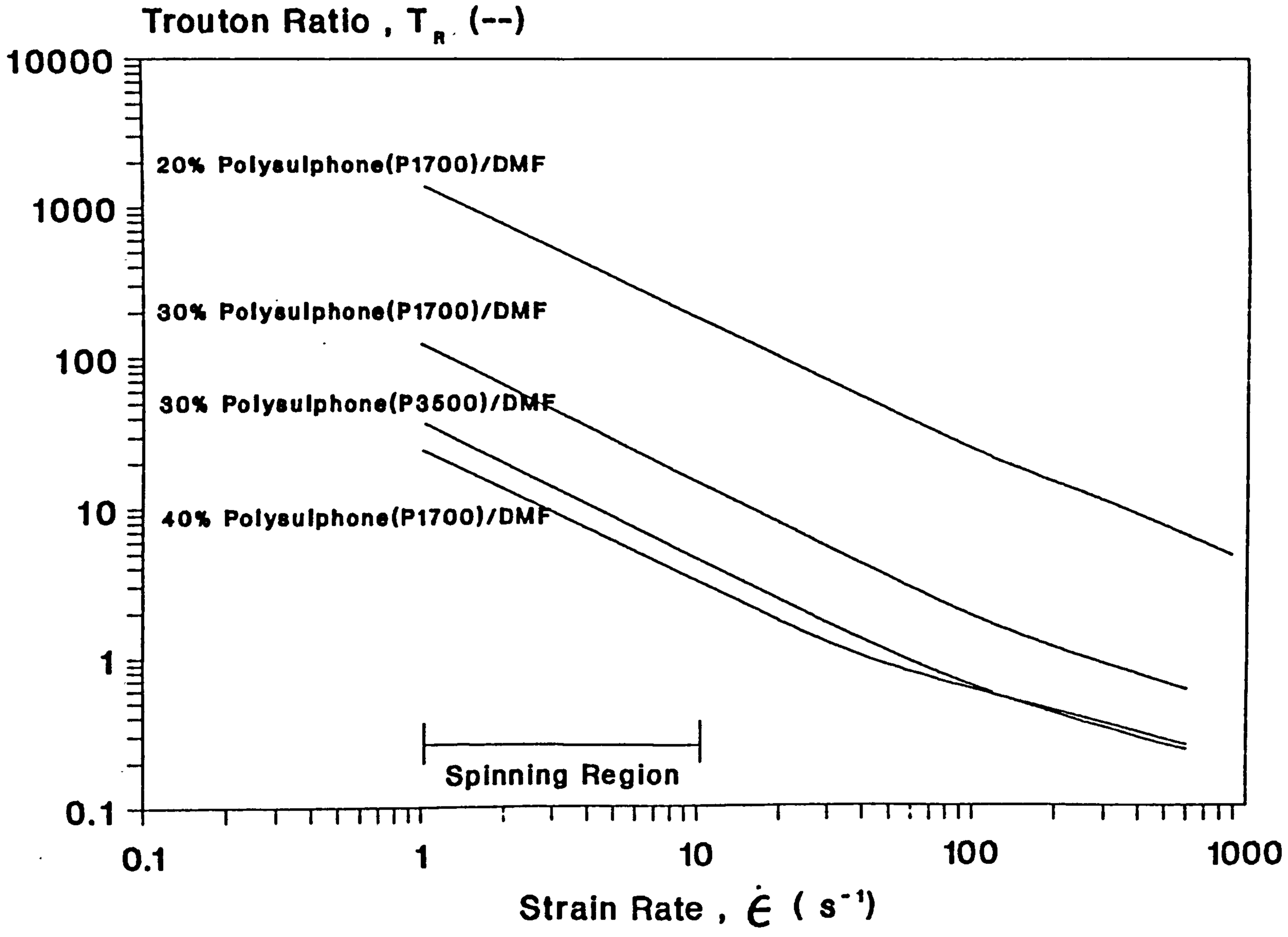

Graph 3.8 Trouton Ratios - Polyacrylonitrile Dopes

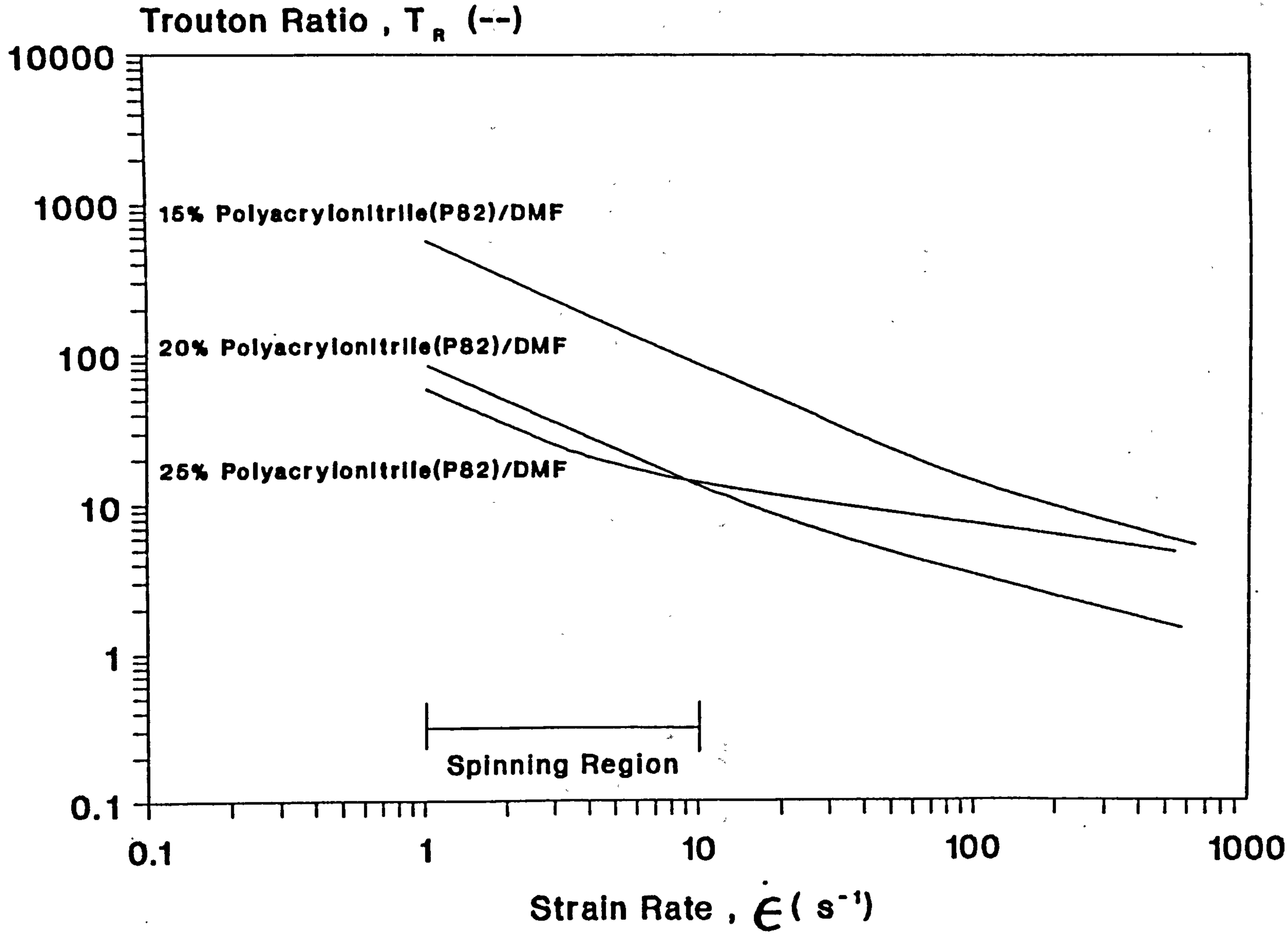

If the elongational viscosity tests had included very low strain rates ($< 10^{-3}\ s^{-1}$) then an initial increase in η_E with $\dot{\epsilon}$ due to elastic yield effects may have been observed. This would have been in line with current rheological modelling which suggests

$$\left.\frac{d\,\eta_E}{d\,\dot{\epsilon}}\right|_{\dot{\epsilon}\to 0} > 0 \qquad \text{---------- 3.36}$$

Finally, it is interesting to note that when the data referring to the individual conditions along the filament length (not presented here) is studied an initial increase in η_E with <u>total</u> strain ϵ <u>is</u> observed in almost all of the elongational viscosity tests carried out.

3.3.5 Creep Analysis of Spinning Dopes

The creep tests were carried out at 25 ^{o}C using a computer managed Carri-Med Controlled Stress Rheometer. Each spinning dope was subjected to a fixed shear stress appropriate to investigating the performance of the sample at low levels of deformation. The shear stress is instantaneously applied and the strain of the specimen with time is monitored. The stress is then released and any relaxation, reflected in negative strain or recoil, observed with time.

A purely viscous Newtonian response, **Figure 3.1** curve A, will result in an immediate linear increase in strain with time. On the cessation of stress at time t there will be no further movement. A purely elastic response, curve B, will show an instantaneous deflection in proportion to the applied stress (Hooke's law). Strain will then remain constant until stress removal, at which point full recovery will occur instantly.

A fluid exhibiting viscoelastic properties will respond in a manner depicted by curve C. After any instantaneous yield (initial elasticity) strain growth in the non-linear region is controlled by combined viscous and elastic effects. After all elastic yield is exhausted during this "retardation" period purely viscous flow then prevails. This is reflected in the linear (constant shear rate) region which corresponds to steady shear viscosity.

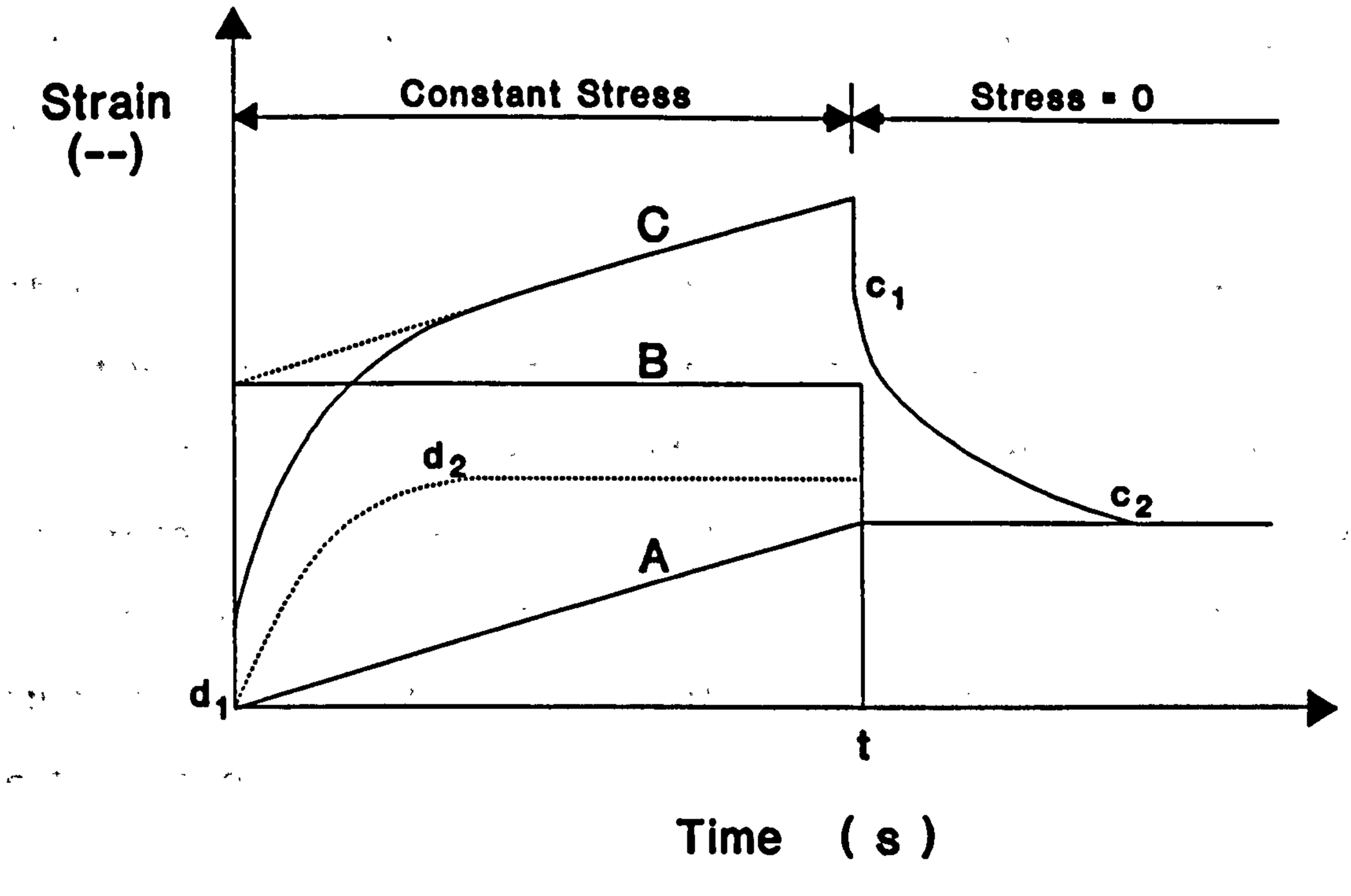

Figure 3.1 Ideal Creep Flow Behaviour

When stress is released elastic recovery will occur. The rate of recovery is again regulated by combined viscous and elastic effects. After any instantaneous recoil corresponding to the instantaneous yield the curve c_1 to c_2 follows a path equivalent to the inversion of the delayed elastic deformation d_1 to d_2. When elastic extension is recouped there is no further movement.

Strain growth is determined by the simultaneous progression of a series of strain increments each developing exponentially with time. Each increment is governed by viscous and elastic influences working in parallel and has a distinct retardation time which

quantifies the speed at which that strain interval is achieved. Similarly, relaxation times quantify the rate at which discrete increments of recovery are regained.

After each creep test retardation times, relaxation times and the strain increments to which they refer are produced by analysis of the strain-time data. The level of any instantaneous strain on loading or relaxation is also determined as well as the steady shear viscosity. This initial viscosity is also referred to as the zero shear rate viscosity.

The duration of each creep test was in the order of five minutes. The values of zero shear rate viscosity have already been recorded in **Table 3.2** and **Graph 3.2.**

The low and medium concentration dopes of both polymer types simply exhibited viscous flow behaviour on loading and relaxation i.e. elasticity in these dopes was undetected under the levels of strain tested. Strain levels can be no lower than those corresponding to the minimum torque capability and sampling resolution of the equipment: the more viscous a sample the lower the strain levels achievable. The low and medium concentration dopes were tested over a 0 to 2.5 strain range, the minimum reasonable.

The most concentrated polysulphone dope **(40% w/w P1700 in DMF)** was tested over a 0 to 0.1 strain range. Viscoelasticity was observed:

On loading (0.30 N/m^2):

Instantaneous yield strain 4.4 x 10^{-3}

Retardation time 6.64 secs in strain increment 4.2 x 10^{-3}

No strain recovery was detected on relaxation (very large relaxation time).

The most concentrated polyacrylonitrile dope **(25% w/w P82 in DMF)** clearly exhibited viscoelasticity. The following results were consistently obtained - samples were tested over a 0 to 2.0 strain range:

On loading (2.5 N/m^2):

No instantaneous yield

Retardation time 12 secs in strain increment 0.16

On relaxation:

Instantaneous relaxation strain 3.0 x 10^{-3}

Relaxation time 115 secs in strain increment 0.26

Relaxation time 12 secs in strain increment 0.10

A greater degree of viscoelasticity would be expected in the polyacrylonitrile dopes due to the higher molecular weight of the polymer, 107,500 compared to 35,400 for the polysulphone.

3.3.6 Normal Stress Analysis of Spinning Dopes

The normal stresses exhibited by the spinning dopes under shear were investigated using an R-16 Weissenberg Rheogoniometer with a 7.5 cm diameter cone and plate and a cone angle of 1^{o} 56 '. The main parameter of interest in such tests is the primary normal stress difference, N_1 which will simply be referred to as normal stress. The tests were carried out at $20^{o}C$.

The measurements were fraught with one particular problem: the solutions, especially the most concentrated, were reluctant to stay in the gap between the cone and plate. This ruined any investigation of the effect of shearing time or shear rate on normal stress as dope loss increased with both these variables. This problem was also experienced by Hudson and Ferguson[70]. Under these circumstances, the most reliable normal stress measurements correspond to low shear rates and low shearing times. A minimum shearing time of 0.5 mins was required to allow test equilibration.

Normal stresses were not detected in any of the polysulphone dopes or in the most dilute polyacrylonitrile dope. However, the **20% w/w PAN/DMF dope** did exhibit normal stresses, typically

Shear Rate	Time	Shear Stress	Shear Viscosity	Normal Stress	Recoverable Shear
1.0 s^{-1}	0.5 mins	11 Pa	11 Pa.s	30 Pa	1.4

The high concentration polyacrylonitrile dope (25% w/w PAN/DMF) gave by far the greatest normal stress values. The results are shown in **Table 3.4** and **Graph 3.9.** (The data points are fairly scattered and have been left out of Graph 3.9 to avoid congestion.)

	Time 0.5 mins			Time 1.0 mins		
Shear Rate $\dot{\gamma}$ (s^{-1})	Shear Stress τ (Pa)	Shear Viscosity η (Pa.s)	Normal Stress N_1 (Pa)	Shear Stress τ (Pa)	Shear Viscosity η (Pa.s)	Normal Stress N_1 (Pa)
0.34	51.3	151	62.5	53.4	157	140
1.06	187	176	1410	184	174	1710
2.12	280	132	3280	257	121	2060
2.12	267	126	2450	250	118	1430
5.33	462	86.6	3110	458	86.0	1910
10.63	792	74.5	2410	733	69.0	902
26.67	1227	46.0	2140	1013	38.0	1450
53.35	1430	26.8	2880	1056	19.8	1840
84.53	1023	12.1	2120	490	5.8	820
212.2			360			

Table 3.4 Normal Stress Data for 25% w/w PAN/DMF Dope

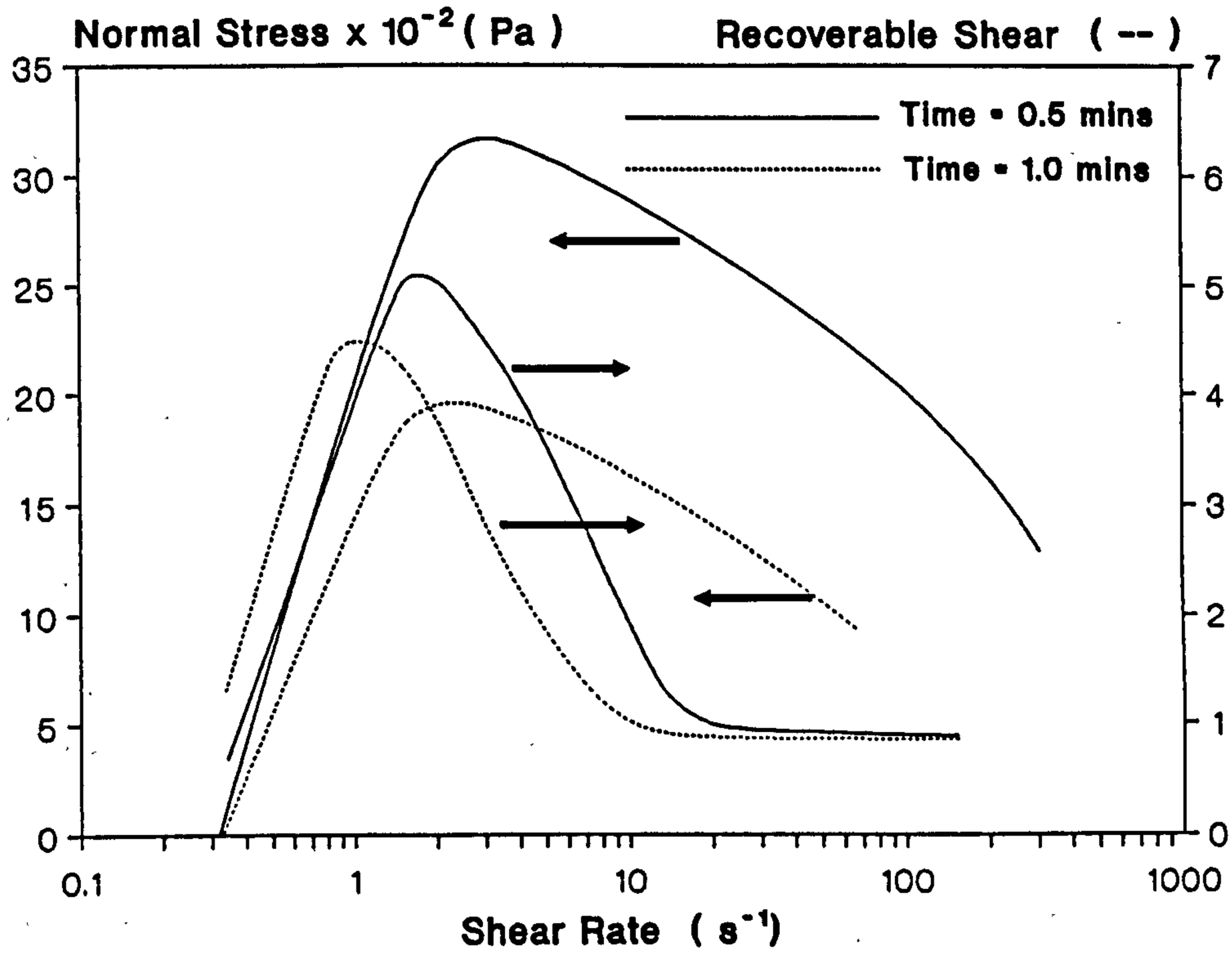

Graph 3.9 Normal Stress Data for 25% w/w PAN/DMF Dope

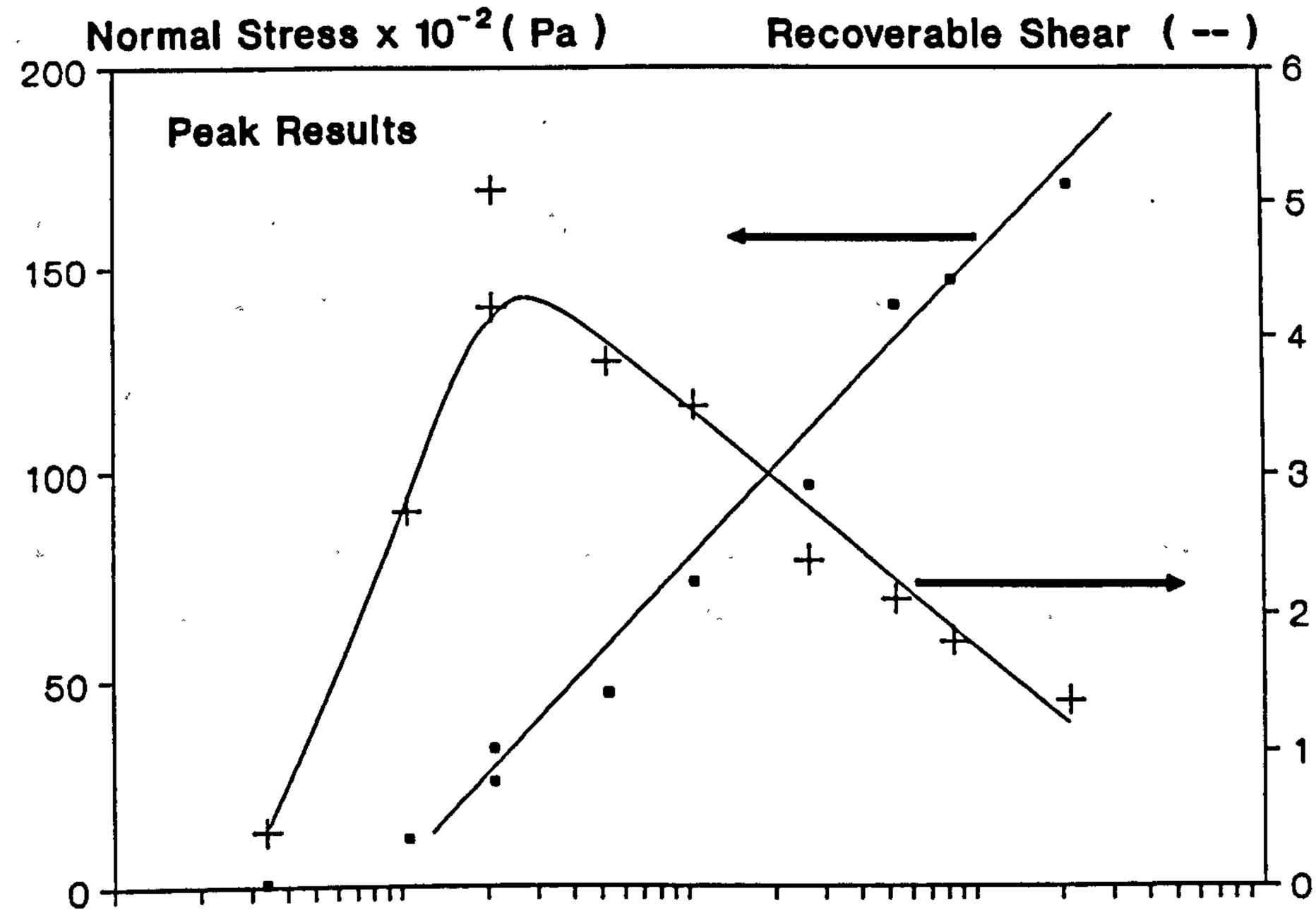

Graph 3.10 Peak Normal Stress Data for 25% w/w PAN/DMF Dope

After an initial increase, normal stress falls with shear rate due to increasing dope loss. It was impossible to test at shear rates of above 212.2 s^{-1}. Normal stress also decreases with shearing time again due to dope loss. However, the shear viscosity values obtained are in fair agreement with the flow curve given in **Graph 3.4.**

A clear increase in normal stress with shear rate can be seen if the peak results, obtained at the beginning of each test before equilibration, are studied. These results, shown in **Graph 3.10**, are of limited significance due to the fact that they are based on a sudden response but they do show the general trend of increasing normal stress with shear rate. The levelling off of N_1 at the higher shear rates (linear log plot) is again probably due to dope loss.

The reliable normal stress response of the **25% w/w PAN/DMF dope** is therefore limited to the following general statement:

Shear Rate	Time	Shear Stress	Shear Viscosity	Normal Stress	Recoverable Shear
1.0 s^{-1}	0.5 mins	170 Pa	170 Pa.s	1500 Pa	4.4

The ratio N_1 to τ is often taken as a measure of elasticity in a fluid. More specifically $N_1/(2\tau)$ is used and is called the recoverable shear. Values greater than 0.5 indicate significant viscoelasticity.

Recoverable shear values have been included in the results and they suggest that both the 20% and 25% polyacrylonitrile dopes are viscoelastic in nature.

3.4 Physical Properties of Fibres

3.4.1 Concept of Fibre Linear Density

At the beginning of this section it is appropriate to explain the concept of linear density, ρ_L. Linear density is the mass per unit length of the fibre (g/km or Tex) and is related to cross sectional area through fibre bulk density as described by equation 3.4. Linear density is of paramount importance because it standardises for the amount of solid material in the cross section of any sample regardless of porosity.

With non-porous entities cross sectional area can also be used as a basis of standardisation because in this case there is no porosity effect ($\rho_B = Const = \rho_P$). However, with non-porous samples where cross sectional area is difficult to measure or varying to some degree with length then working in terms of linear density is again preferred. This is seen in the textile industry where fibres are quantified in terms of Tex or dTex.

It is fairly obvious that measuring linear density is simply a matter of weighing a known length of fibre.

3.4.2 Fibre Dimensions and Porosity

The results shown in **Table 3.5** relate spinning conditions to fibre dimensions and porosity.

Run	C_D (g polymer/ g dope)	D.E.R. (cm^3/min)	J.S. (--)	d_O (mm)	d_L (mm)	ν_{Ideal} (--)	ν (--)	υ (--)
4.2	0.20	1.0	1.0	0.51	0.32	0.84	0.73	0.13
2.2	0.30	1.0	0.7	0.67	0.43	0.76	0.61	0.20
2.5		1.0	2.0	0.43	0.27		0.68	0.11
2.7		2.0	1.0	0.55	0.31		0.68	0.11
2.8		1.0	1.0	0.56	0.36		0.65	0.14
3.1	0.40	0.7	1.0	0.56	0.33	0.67	0.55	0.18
3.3		1.0	1.0	0.53	0.25		0.56	0.16

Table 3.5 Effect of Spinning Conditions on Fibre Dimensions and Porosity

Fibre outside diameters were measured using digital callipers (confirmed using a light microscope with calibrated graduated view lens) and lumen diameters determined from electron micrographs. Porosities were calculated from fibre dimensions and linear densities

(equation 3.6). Ideal porosity values are based on dope properties (equation 3.10) with contraction factors simply being evaluated from equation 3.11.

The contraction factor data shows that shrinkage invariably occurs on coagulation, porosity values decreasing from the ideal by between 10% and 20%. (Fibre dimensions also indicate shrinkage: when JS = 1 fibre cross sectional area is less than the extrusion area of the spinneret.)

It is worth briefly mentioning here that if contraction factor is related to fibre residence time in the coagulation bath (simply calculable from DER and JS knowing spinneret dimensions and bath length) some interesting suggestions emerge. At constant residence time, contraction factor increases with dope concentration. At constant dope concentration, contraction factor increases with residence time. Sophisticated explanations could be offered for these observations but would not be justified by the amount of data.

Primarily, fibre cross sectional area is independent of dope extrusion rate and only dependent on the jet stretch ratio (equation 3.12). However, the actual fibre lumen and outer diameters will depend on the water injection rate relative to the dope extrusion rate as well as on the jet stretch ratio (model equations 3.13 to 3.16).

Nevertheless, since the ratio of WIR to DER was kept constant throughout the spinning campaigns then fibre dimensions should also be purely dependent on JS. **Graphs 3.11** and **3.12** compare actual fibre dimensions with those predicted (d_o data extracted across all spinning runs).

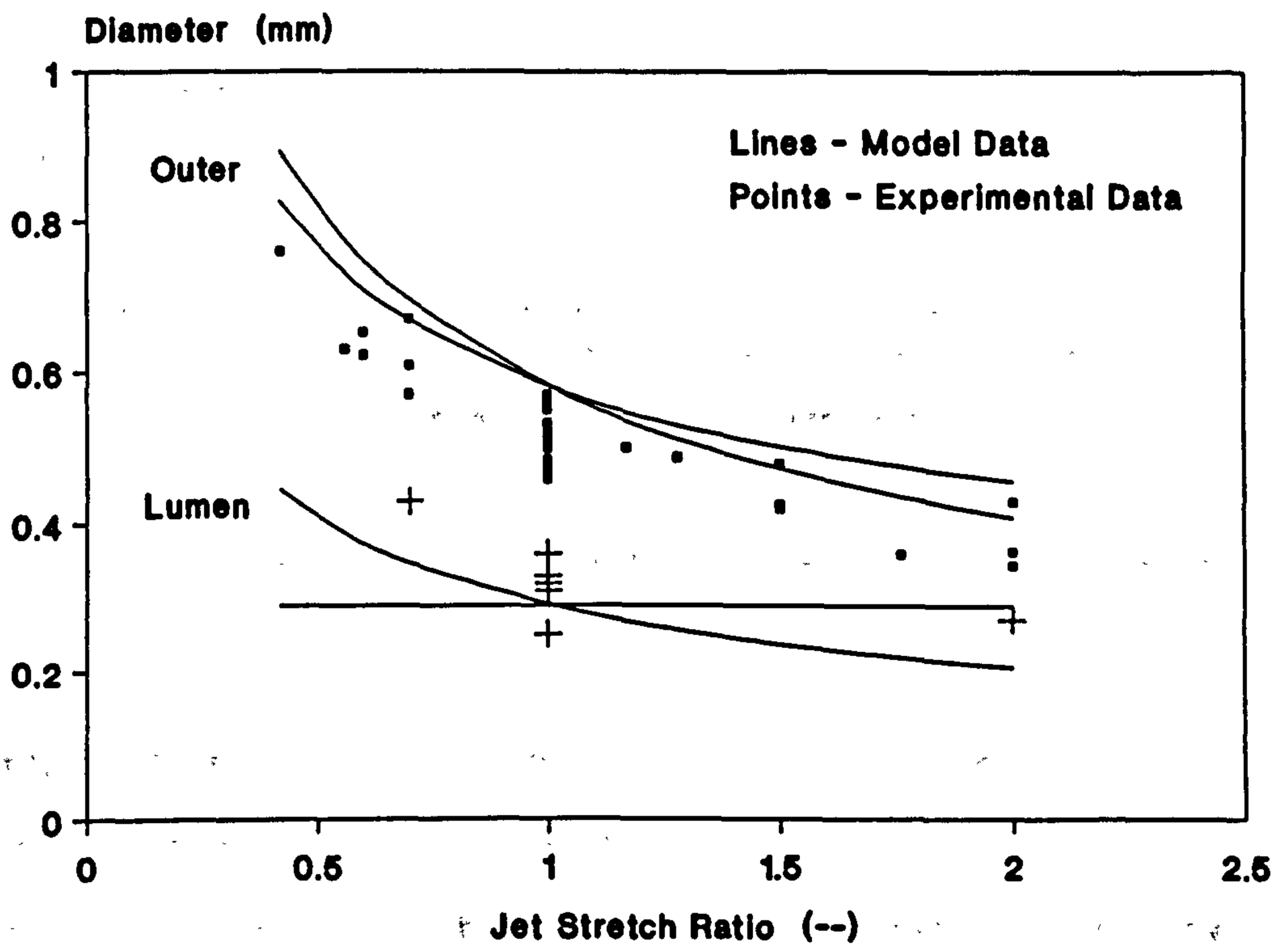

Graph 3.11 Effect of Jet Stretch on Fibre Dimensions

It can be seen from **Graph 3.11** that both fibre outer diameter and lumen diameter fall with increasing jet stretch as the model data predicts.

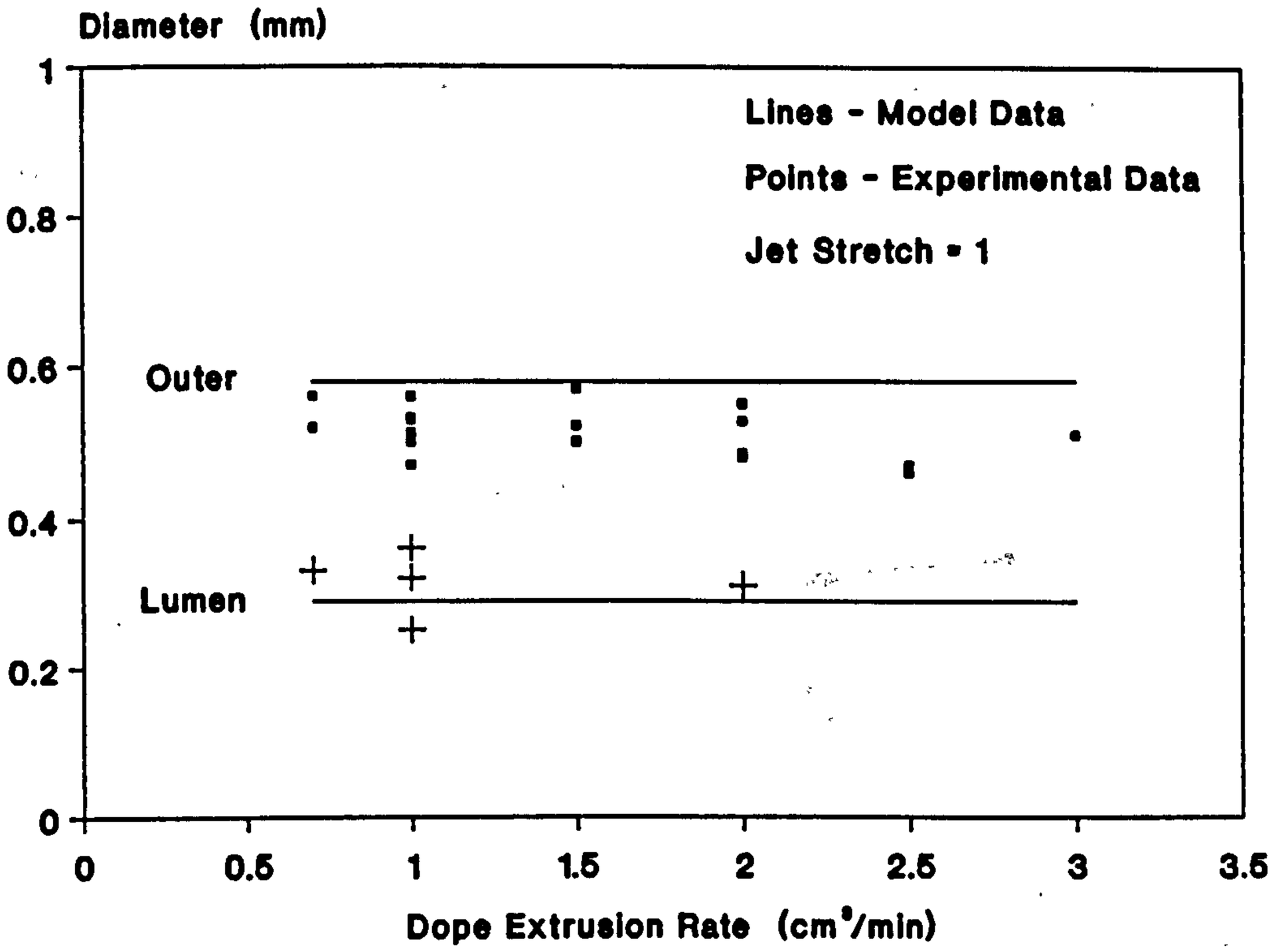

Graph 3.12 Effect of Dope Extrusion Rate on Fibre Dimensions

Graph 3.12 also shows good agreement between expected and actual dimensions with both outer and lumen diameters remaining constant with changing dope extrusion rate.

However, both graphs show that outer diameters seem to be slightly lower than those predicted and lumen diameters somewhat higher. This can be explained by the contraction effect. Contraction is greater on the outside of the fibre where coagulation is rapid. However, solvent build-up in the fibre lumen restricts coagulation from within. As a result the outer fibre wall is "pulled in" and the lumen wall "pulled up" giving the observed diameter shifts.

3.4.3 Tensile Properties of Fibres

Behaviour under elongation has been standardised with respect to fibre linear density, see section 3.4.1.

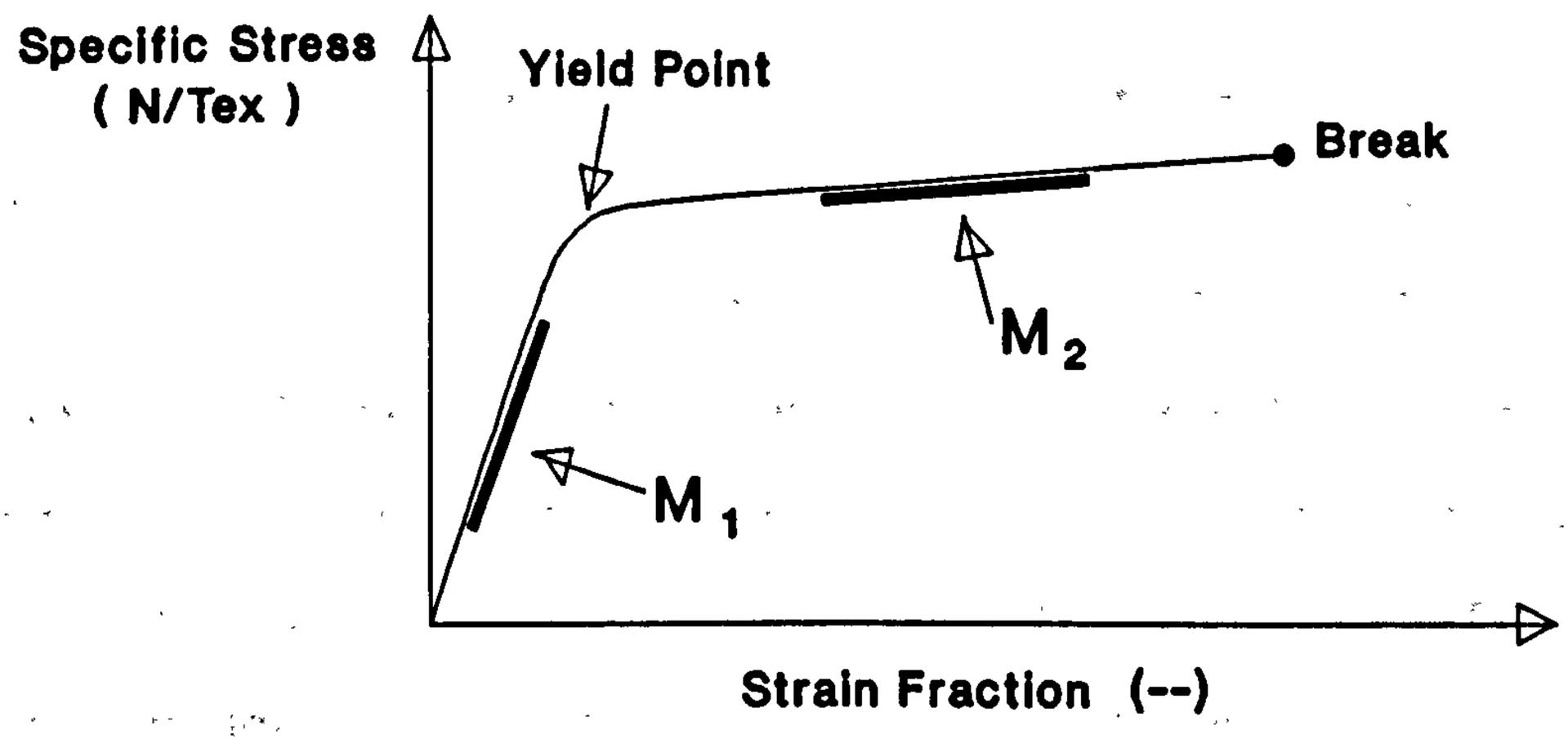

Figure 3.2 Typical Stress Strain Curve

Figure 3.2 shows a typical stress strain curve. The main parameters of interest are as follows:

1. $\textit{Fibre Strength ie Tenacity} = \textit{Specific Stress at Break} = \frac{\textit{Load at Break}}{\textit{Linear Density of Fibre}}$ $(\frac{N}{g/km}$ *ie* $\frac{N}{Tex})$

2. $\textit{First Modulus, } M_1 = \frac{\textit{Slope of Stress Strain Curve Before Yield Point}}{}$ $(\frac{N}{Tex})$

3. $\textit{Second Modulus, } M_2 = \frac{\textit{Slope of Stress Strain Curve After Yield Point}}{}$ $(\frac{N}{Tex})$

M_1 is a measure of resistance to extension before the elastic limit is reached.

M_2 is a measure of resistance to extension after yield i.e. after structure has been broken.

An Instron 1122 Materials Testing Instrument was used to carry out the tensile tests. The trials were carried out in a controlled environment laboratory (T = 20°C RH = 65%) where the fibre samples were allowed to condition prior to testing. Analysis of a particular fibre was considered complete when six samples had been tested successfully. A fibre gauge length of 40mm was used throughout.

Tables 3.6, 3.7 and **3.8** show the effect of spinning conditions on fibre tensile properties.

Run	D.E.R. (cm^3/min)	J.S. (--)	ρ_L (Tex = g/km)	At Breakage			M_1 (N/Tex)	M_2 (N/Tex)
				Load (N)	Tenacity (N/Tex)	Strain (%)		
4.1	1.0	0.7	58.9	1.448	0.02459	42.62	0.801	0.0181
4.2	1.0	1.0	41.3	1.122	0.02715	61.44	0.774	0.0132
4.3	1.0	2.0	20.4	0.556	0.02725	44.36	0.859	0.0166
4.4	2.0	1.0	40.7	1.106	0.02720	60.52	0.769	0.0132

Table 3.6 Effect of Spinning Conditions on Tensile Properties

C_D = 0.2 g polymer/g dope

Run	D.E.R. (cm^3/min)	J.S. (--)	ρ_L (Tex = g/km)	At Breakage			M_1 (N/Tex)	M_2 (N/Tex)
				Load (N)	Tenacity (N/Tex)	Strain (%)		
2.1	0.7	1.0	62.0	1.868	0.03013	55.12	1.042	0.0106
2.2	1.0	0.7	100.0	3.268	0.03268	87.10	0.999	0.0089
2.3	1.0	1.0	63.4	1.978	0.03119	62.98	1.052	0.0105
2.4	1.0	1.5	48.6	1.471	0.03026	51.21	1.005	0.0126
2.5	1.0	2.0	34.9	1.003	0.02875	43.87	1.031	0.0109
2.6	1.5	1.0	71.5	2.258	0.03159	65.48	1.032	0.0110
2.7	2.0	1.0	64.5	1.999	0.03100	56.58	1.059	0.0110
2.8	1.0	1.0	62.3	1.941	0.03116	63.84	1.050	0.0093
2.9	1.0	2.0	33.5	0.994	0.02968	48.60	1.033	0.0105
2.10	0.7	1.0	61.5	1.879	0.03055	76.90	0.995	0.0100

Table 3.7 Effect of Spinning Conditions on Tensile Properties

C_D = 0.3 g polymer/g dope

Run	D.E.R. (cm^3/min)	J.S. (--)	ρ_L (Tex = g/km)	At Breakage			M_1 (N/Tex)	M_2 (N/Tex)
				Load (N)	Tenacity (N/Tex)	Strain (%)		
3.1	0.7	1.0	90.3	2.867	0.03176	42.19	1.151	0.0102
3.2	1.0	0.7	134.3	4.324	0.03219	56.64	1.086	0.0080
3.3	1.0	1.0	93.2	2.995	0.03215	35.13	1.144	0.0116
3.4	1.0	1.5	62.6	2.082	0.03325	53.26	1.158	0.0081
3.5	1.0	2.0	50.7	1.680	0.03312	46.20	1.178	0.0077

Table 3.8 Effect of Spinning Conditions on Tensile Properties

C_D = 0.4 g polymer/g dope

Throughout the tests, not surprisingly, breaking load increases with linear density but it is the relative value i.e. tenacity that is more pertinent. Tenacity is a measure of the intrinsic strength of the solid polymer within a fibre. The results show no clear relationship between dope extrusion rate or jet stretch ratio with tenacity. However, the effect of dope concentration on intrinsic polymer strength is very interesting.

The same can be said for 1st and 2nd modulus i.e. the resistance to elongation offered by the polymer before and after yield. Again, there is no obvious correlation with DER or JS but the effect of dope concentration on M_1 and M_2 is striking.

In the case of strain (elongation at break) even with C_D no pattern readily emerges. The lack of variation in tenacity, M_1 and M_2 at fixed dope concentration makes any relationship between these variables and DER or JS difficult to discern. However, the above having been said, viewing the results in **Table 3.7** alone, a fall in tenacity and strain with JS (at constant DER) may be observable.

The distinct effect of dope concentration on tenacity, first modulus and second modulus can be seen in **Graphs 3.13** and **3.14.** Values at each dope concentration are based on average data from each spinning campaign.

Graph 3.13 shows that tenacity, or intrinsic polymer strength increases with concentration of spinning dope. This may be due to increased cohesion between polymer molecules as they become more densely packed on solidification. However, the two moduli are more relevant with respect to deducing polymer structure. These parameters do not depend on conditions of sudden fracture as is the case with tenacity but are reflective of polymer behaviour over a prolonged period of tensile stress.

It can be seen from **Graph 3.14** that M_1, the resistance of the polymer to elongation before yield i.e. stiffness, increases with C_D. The higher the dope concentration the greater the shear rate during spinning (dope power law index decreases with C_D - see **Table 3.2** and **Graph 5.2**) and hence greater orientation of polymer molecules occurs. Orientation coupled with greater cohesive forces may result in the increase in force required to stretch the material. However, after yield i.e. after structure is broken, the more aligned the molecules are the less resistance they offer to further elongation because they can "move over" each other easily. If the molecules are entangled they offer less resistance before yield due to "stretching capacity" but after yield they would in fact offer greater resistance to further elongation because they are less able to slide over each other. This is reflected in the reduction of M_2, resistance to elongation after yield, with dope concentration.

Graph 3.13 Fibre Tensile Properties
Effect of Dope Concentration on Tenacity

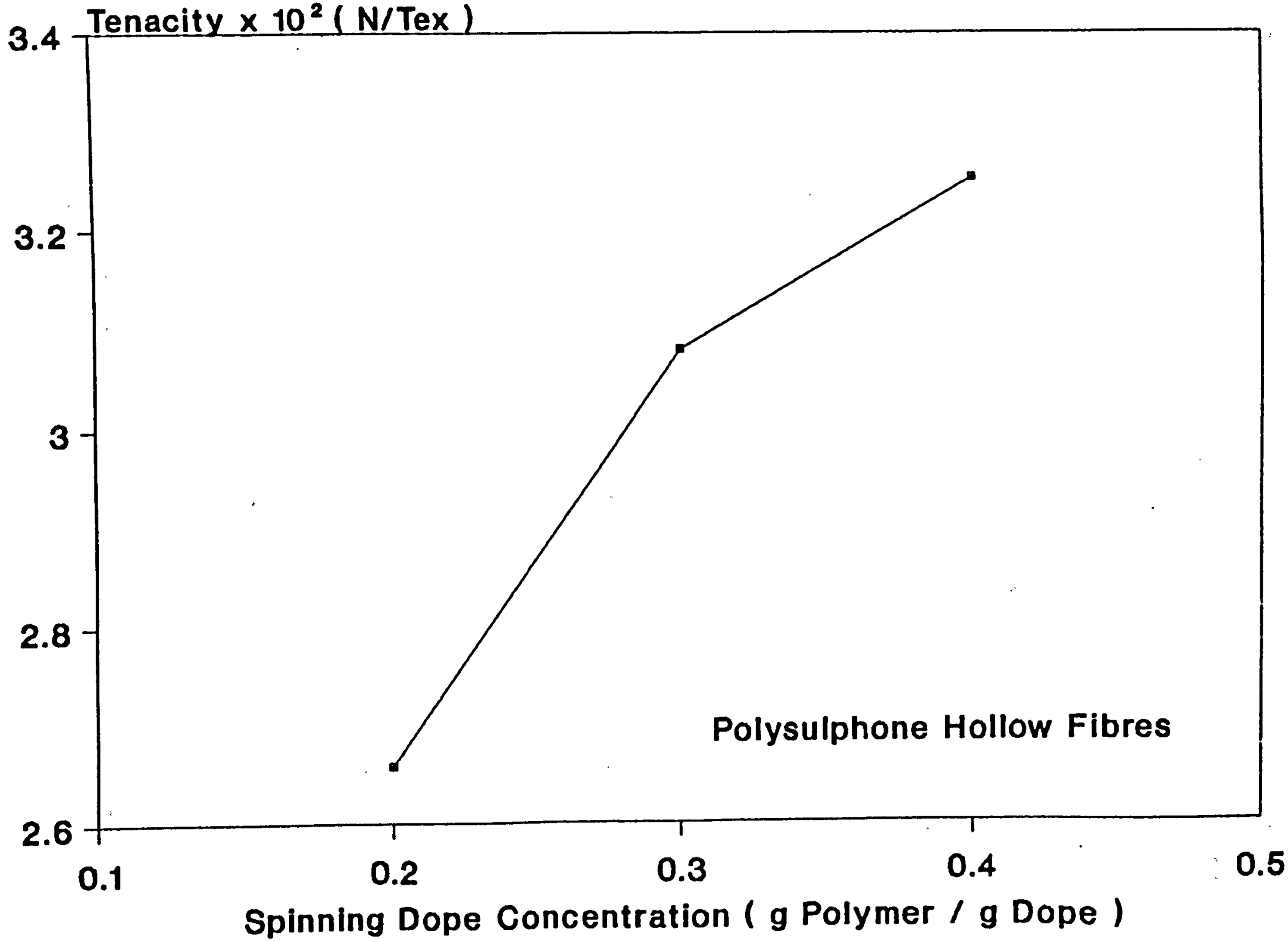

Graph 3:14 Fibre Tensile Properties
Effect of Dope Concentration on Modulus

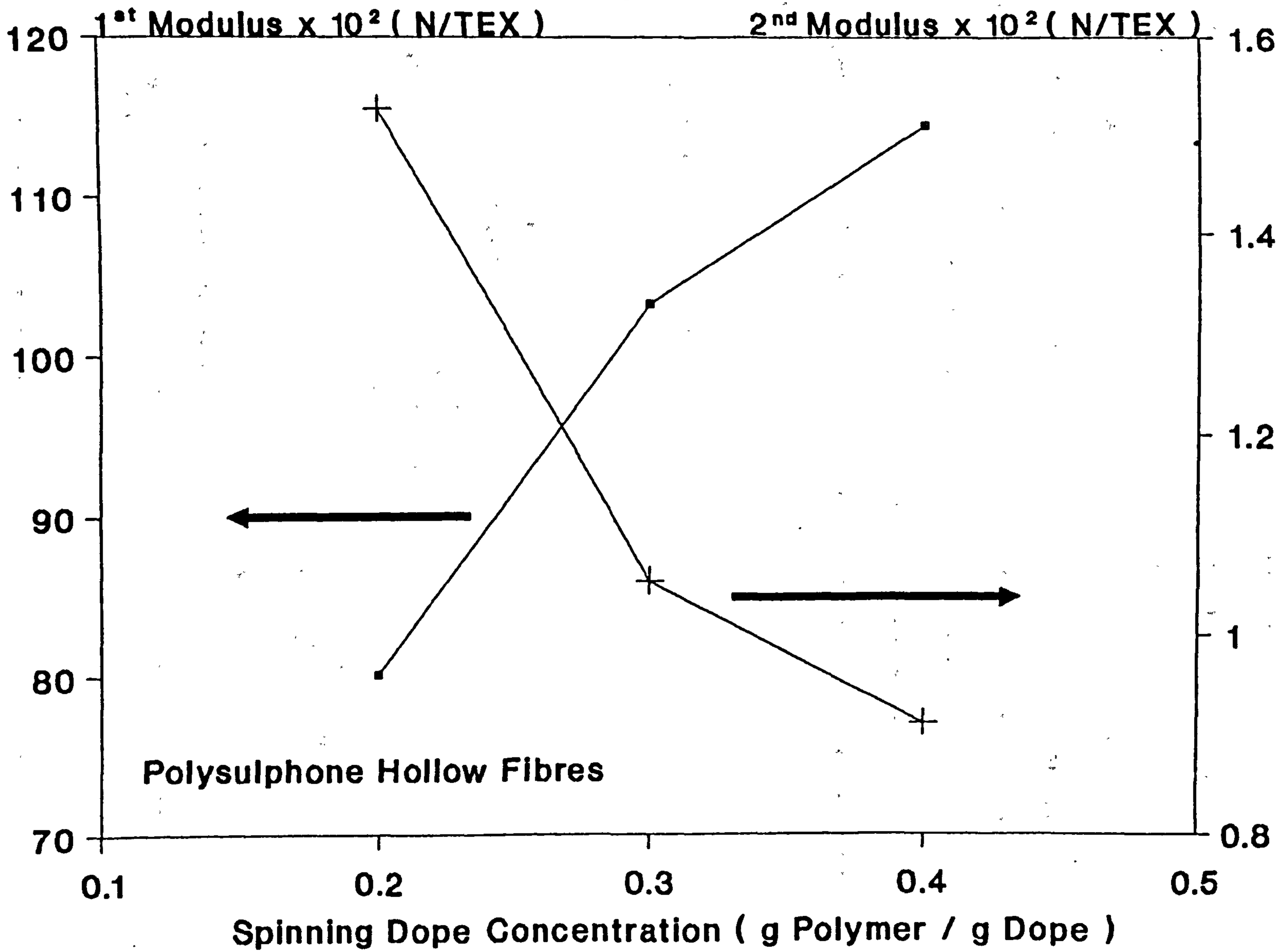

3.4.4 Integrity of Spinning Equipment and Techniques

As has already been seen, fibre dimensions are consistent with those anticipated as spinning variables are altered. Whilst this increases trust in the spinning process, dimensions are none-the-less under the influence of less quantifiable coagulation effects. Fibre linear density on the other hand is independent of the phase inversion process and as shown by equation 3.5 (determined solely by mass balance) should be inversely proportional to jet stretch and independent of dope extrusion rate at any particular dope concentration.

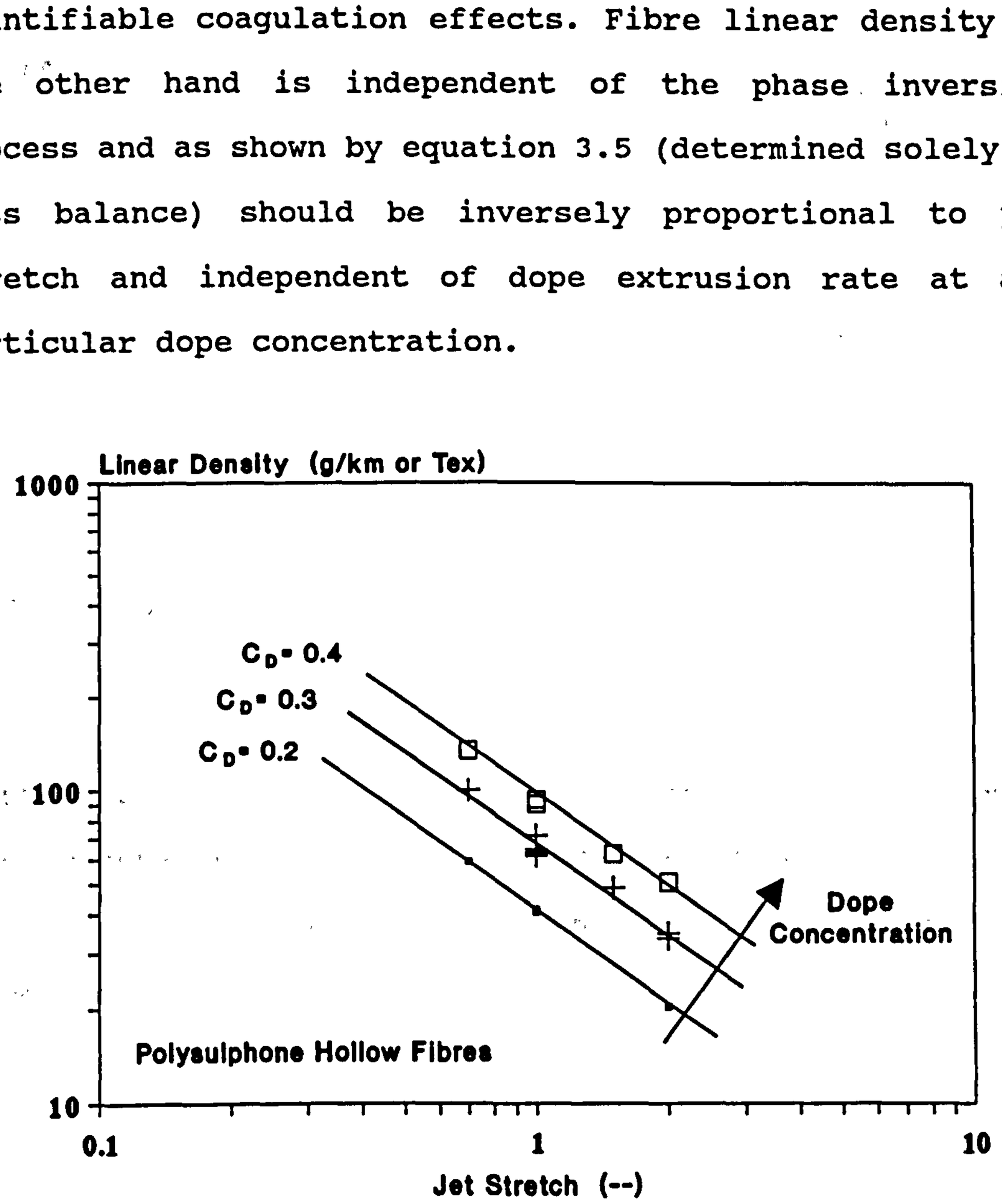

Graph 3.15 Effect of Jet Stretch on Linear Density

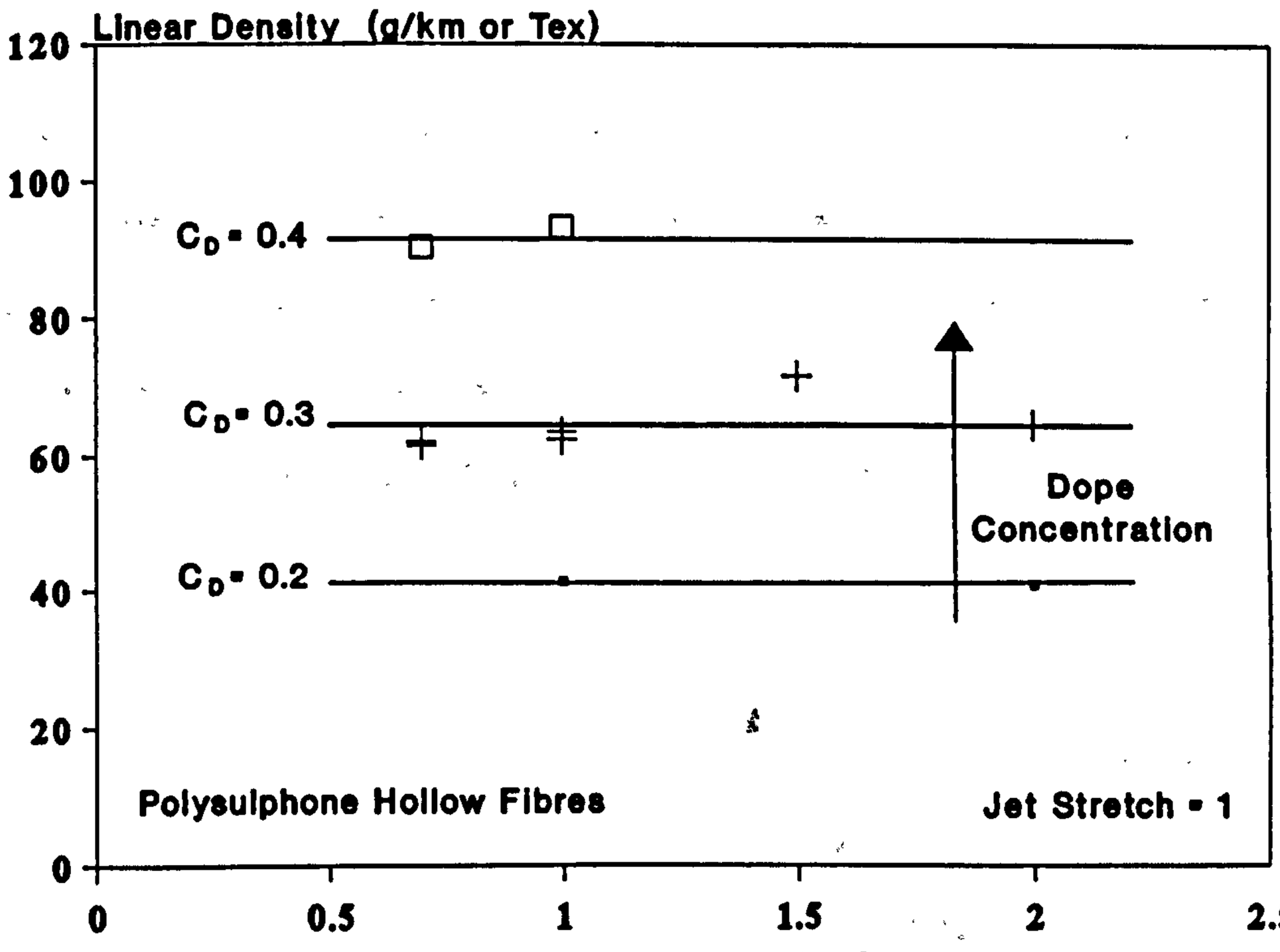

Graph 3.16 Effect of Dope Extrusion Rate on Linear Density

Graphs 3.15 and **3.16** show that experimentally linear density behaves entirely as expected and thus there can be a fair degree of confidence in the spinning apparatus and procedures.

3.4.5 Water Permeation Tests

Water permeation experiments were carried out at 25 °C using a selection of polysulphone hollow fibres covering the range of spinning dope concentrations. The fibres were quality checked by gas permeation prior to the tests. The gas permeation apparatus was modified for this work as shown in **Figure 3.3 (c.f. Figure 2.7)**.

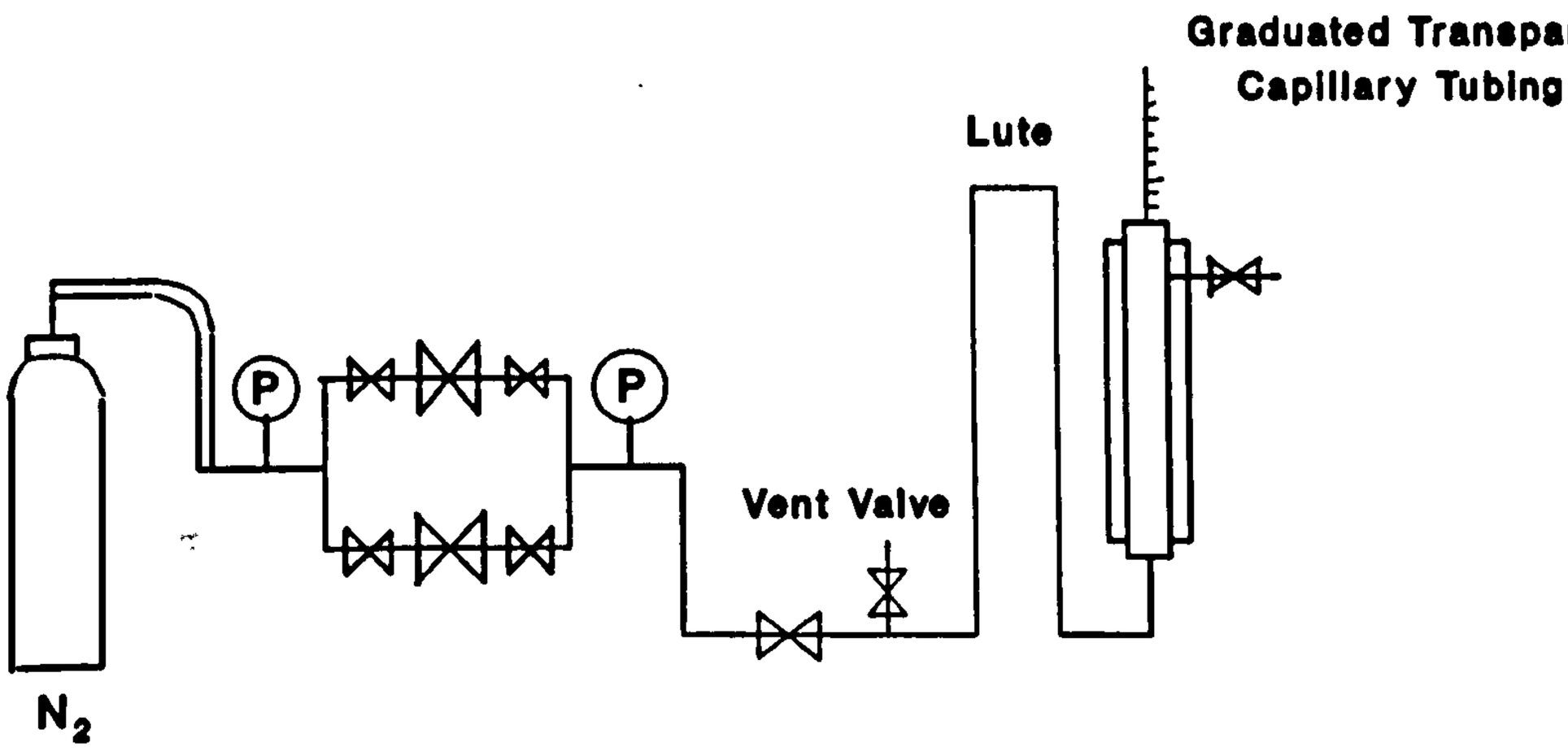

Figure 3.3 Hollow Fibre Water Permeation Apparatus

The permeation chamber was fully filled with water and the hollow fibre module fixed into position. A graduated length of transparent capillary tubing (ID 0.76 mm) was then attached vertically to the top of the fibre module

tube sheet. The chamber was then pressurised and the water permeation rate measured by timing the ascent of the water level in the capillary tubing.

Pore size and pore size distribution information can be deduced from the pressure water permeation rate profile of a membrane. The analysis is based on two physical laws:

1. Pressure drop over a curved surface balanced by surface tension according to Cantor's equation[74]

$$r = \frac{2\ \sigma_I \cos\theta}{\Delta P} \qquad \text{----------} \quad 3.37$$

where r = minimum pore radius 'opened' by pressure ΔP

σ_I = interfacial surface tension

θ = wetting angle

Equation 3.37 is commonly used in the standard bubble point technique[75] for fast membrane characterisation with respect to pore size. For water/air systems Cantor's equation can be simplified to[76]

$$r(nm) = \frac{1460}{\Delta P(bar)} \qquad \text{----------} \quad 3.38$$

2. Viscous flow (incompressible) in a capillary according to the Hagen-Poiseulle equation

$$Q = \frac{\pi r^4 \Delta P N_p A}{8 \eta L} \quad \text{---------- 3.39}$$

where Q = permeate flowrate

A = membrane area

N_p = number of 'opened' pores per unit area

η = viscosity

L = membrane thickness or thickness of active layer for asymmetric membranes

Theoretically the pressure water permeation rate profile should incorporate the full spectrum of pore sizes. A distinct minimum pressure required for flow corresponding to permeation through the largest pore size should be detected. The pressure at which no further pores are opened corresponding to complete Hagen-Poiseulle flow should also be identified i.e. the point at which the flow profile becomes linear with pressure and extrapolates through the origin. Between these two extremes both Hagen-Poiseulle flow and the progressive opening of new pores occurs. Thus by a stepwise graphical analysis of the full flow profile the pore size range (equation 3.38) and the number of pores or the pore size distribution (equation 3.39) can be evaluated. The method is clearly outlined by Kujawski et al[77] and Kesting[58].

The results of the water permeation tests are shown in **Graphs 3.17** to **3.19.** It can be seen that the analysis principles described above can only sensibly be applied to the hollow fibres spun from the 20% w/w and 30% w/w dopes where an increase in water permeation rate with pressure is observed. However, a full pore size distribution analysis for these membranes is impossible due to the fact that neither a minimum threshold pressure or a final pressure (where the graph tails off to become linear and extrapolates through the origin) is detected. The maximum pressure in each of the tests was limited by module failure when the water ruptures the membranes (witnessed by water gushing out from the top of the capillary tubing).

a.

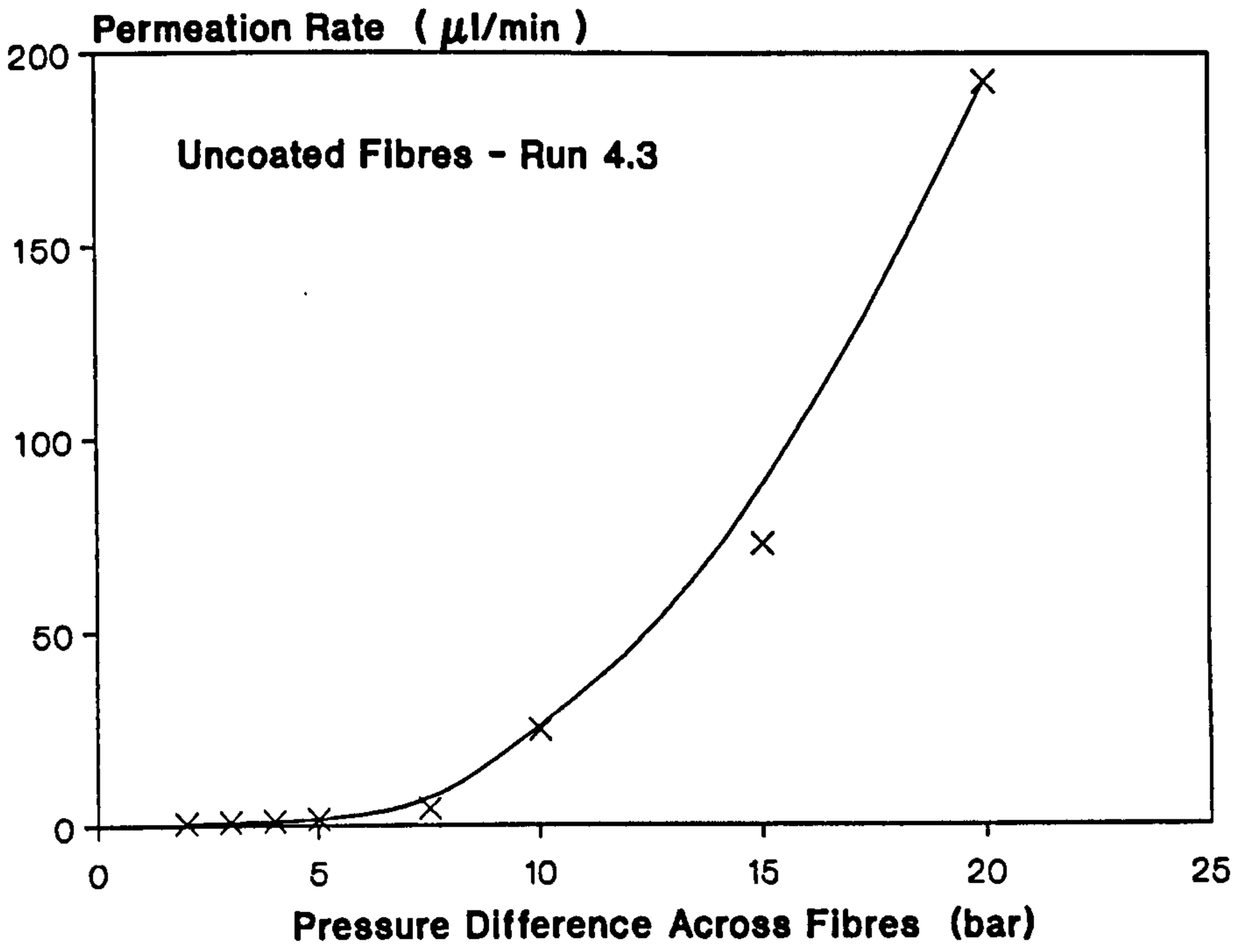

b.

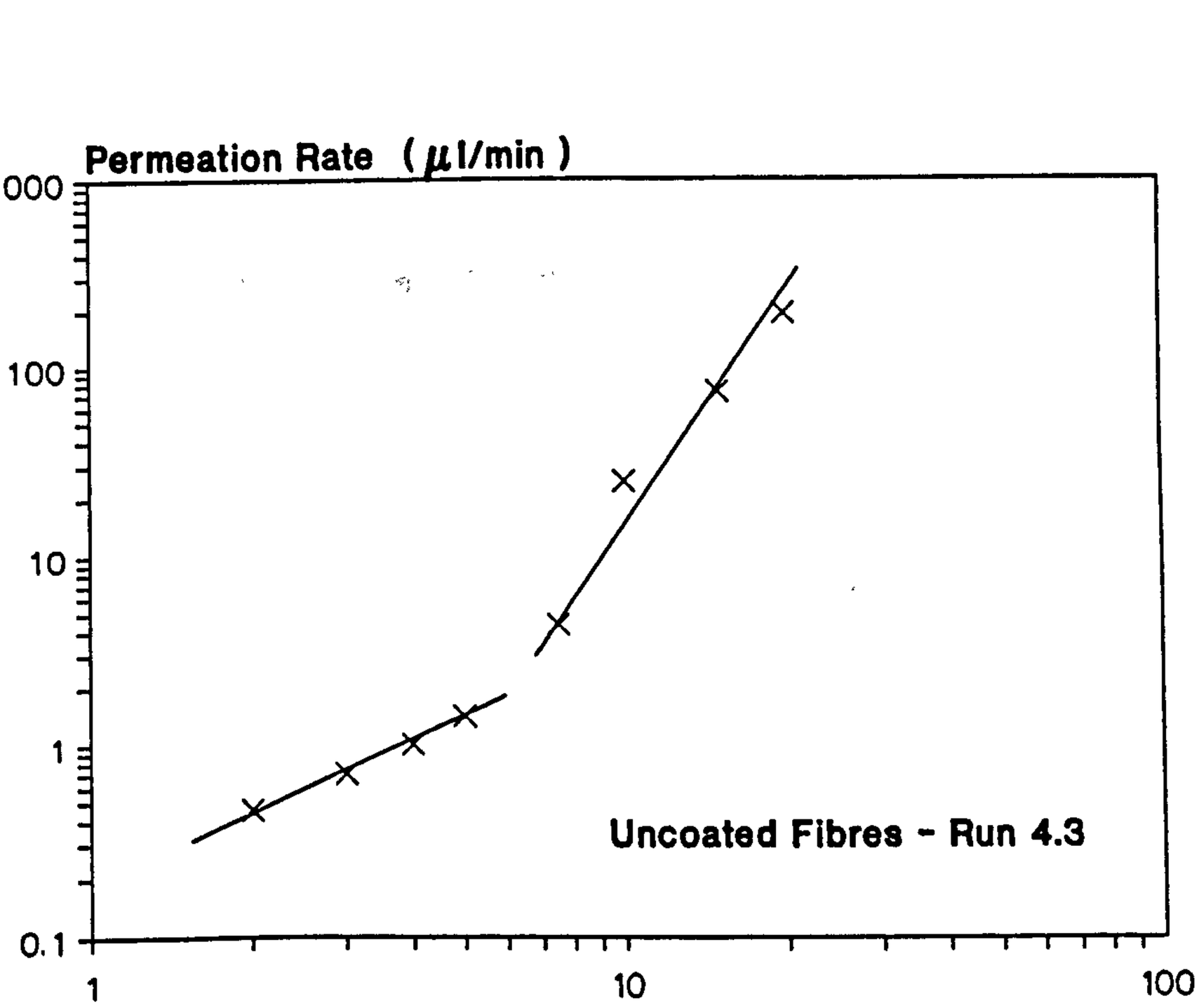

Graph 3.17 Water Permeation Tests - Polysulphone Fibres

Spinning Dope Concentration **20% w/w**

a.

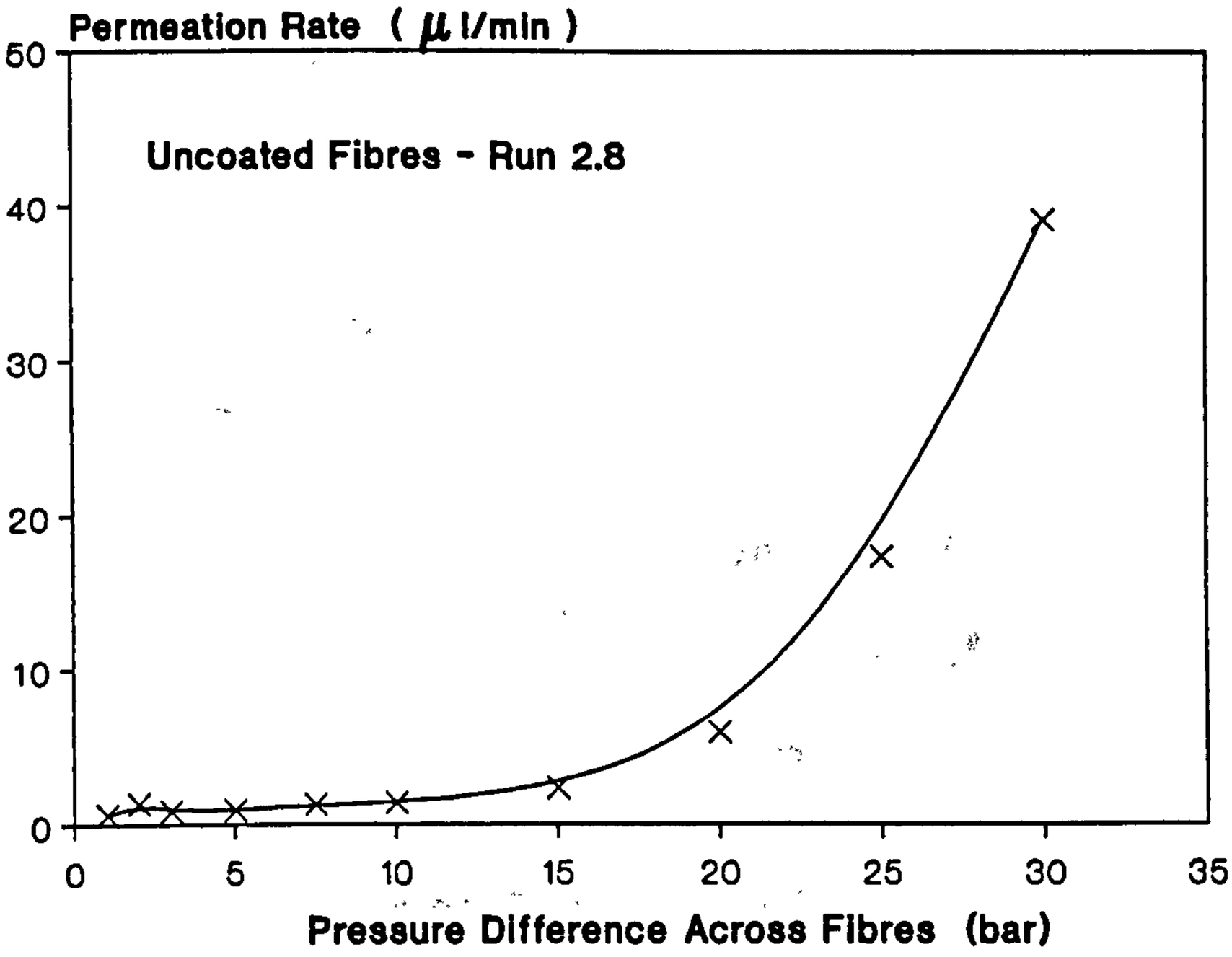

b.

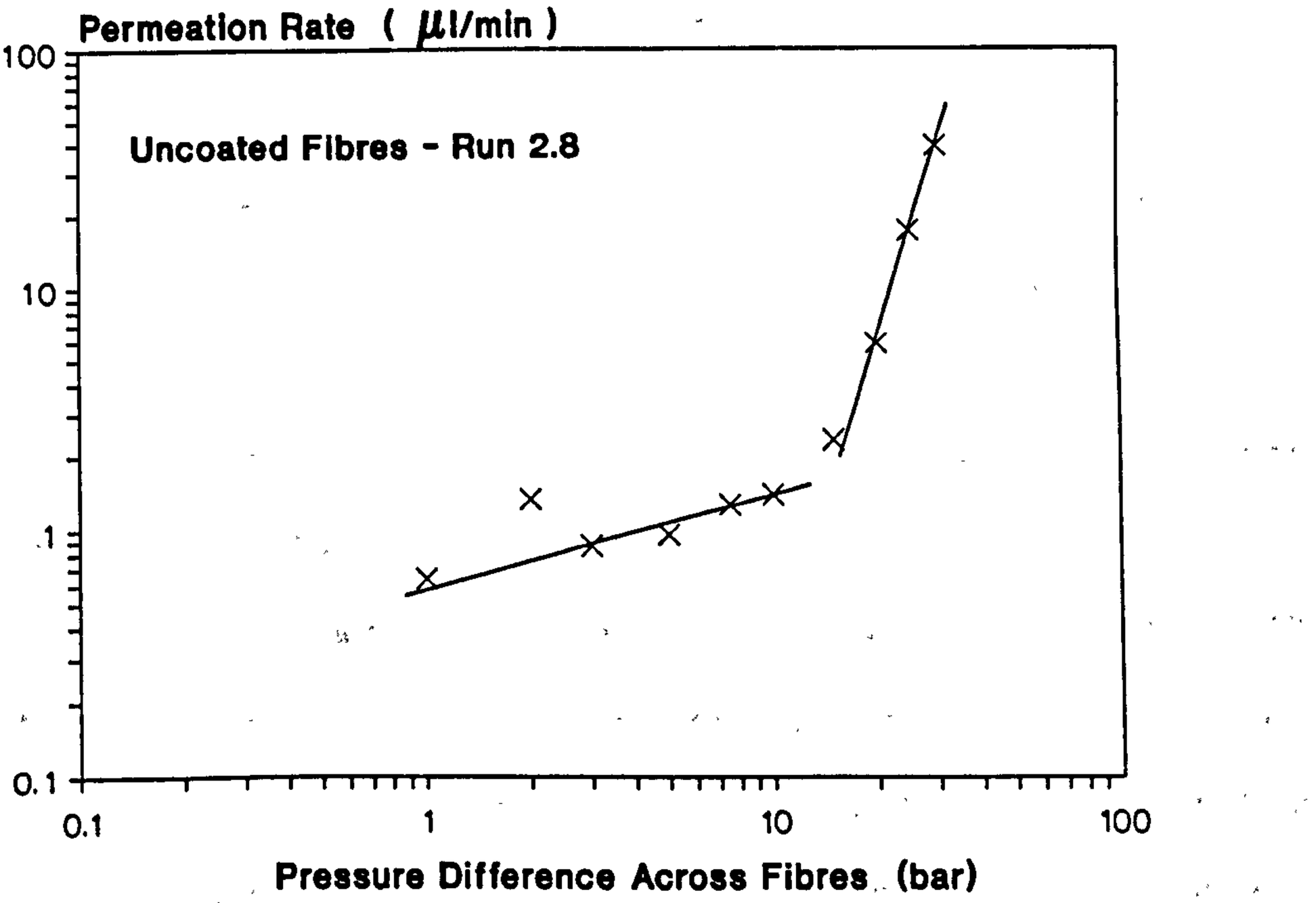

Graph 3.18 Water Permeation Tests - Polysulphone Fibres

Spinning Dope Concentration 30% w/w

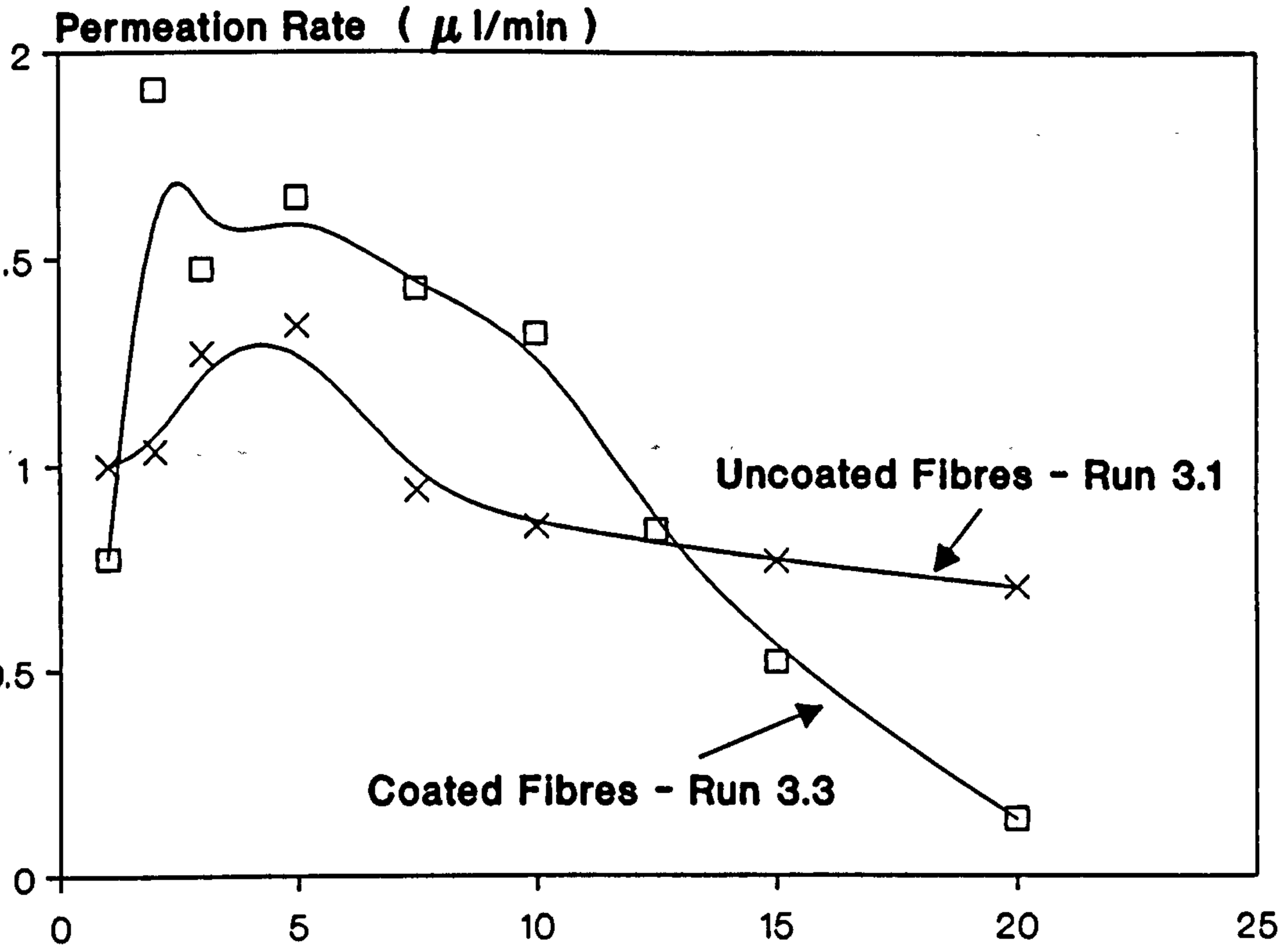

Graph 3.19 Water Permeation Tests - Polysulphone Fibres

Spinning Dope Concentration 40% w/w

In order to gain non-arbitrary pore size information regarding these two fibre types log log plots of the permeation results were carried out, shown in **Graphs 3.17b** and **3.18b**. Two distinct linear regions can be identified and the second steeper line can be assumed to indicate the serious development of pore flow. An overall pore size and ratio of pore number to pore length can be determined by considering the interval between the onset of pore flow and membrane failure represented by this second linear region. It is interesting and convenient that the pressure increase over the second region is approximately the same

for both fibre types (14bar and 15bar). Pore size is evaluated at the mean pressure of the interval using equation 3.38 and the ratio N_p/L is evaluated from equation 3.39 using the increase in flowrate over the interval. **Table 3.9** shows the results.

	Pore Radius (Å)	N_p/L (cm^{-2} $Å^{-1}$)
20% w/w Dope	1120	0.15
30% w/w Dope	650	0.16

Table 3.9 Pore Size and Structure Details from Water Permeation Tests - Polysulphone Hollow Fibres

The pore size of the 30% w/w spun membranes represented by Run 2.8 fibres is in good agreement with the corresponding value in **Table 3.10** calculated from the variation of gas permeability with pressure. **Table 3.9** like **Table 3.10** shows a decrease in pore size with increasing polymer concentration in the spinning dope.

The absolute values of pore size in **Table 3.9** will be overestimations of the actual average as they represent the large pores at one end of the pore size spectrum - module failure occurring before test completion. The contact angle at the water/air interface has been assumed to be zero which is unlikely. This would also contribute to an overestimation of pore size.

The failure pressure of 30 bar for the 30% w/w spun fibres **(Graph 3.18)** is in line with the nitrogen burst pressures (1st region failure) shown in **Table 3.11** for coated 30% w/w spun fibres.

The N_p/L values in **Table 3.9** are very similar. This suggests that if both spinning dope concentrations produce fibres with the same thickness of active layer (pore length) then pore numbers will be equal. There is little scope for further comment at this stage regarding the ratio of pore number to thickness of active layer. The gas transfer modelling described in section 5.2 seriously pursues such concepts and predicts the effect of spinning conditions on membrane structure in a fully quantitative manner. It only remains to be said that the N_p/L figures in **Table 3.9** are underestimations according to the gas transfer modelling even when the comparison is based on the area of surface pores, see **Table 5.6.** This is not unexpected as the water permeation tests were incomplete and hence pore number underestimated.

The water permeation results for the 40% w/w spun fibres shown in **Graph 3.19** are entirely as expected. These fibres spun from the most concentrated dope have the smallest pore sizes. The variation of gas permeability with pressure tests predict that these membranes have pore sizes of around 200 Å, as shown in **Table 3.10**, which would correspond to a flow pressure of 73 bar according to equation 3.38. (The electron microscope work indicates that pore sizes were actually smaller than 200 Å, section 5.2.2.) The fall in an already low water permeation rate with pressure in **Graph 3.19** is probably due to compression effects in the fibres. It is no surprise that the coated membranes show greater susceptibility to compression.

Finally one general point which regards the comparison of the molar flows of water and gases through the hollow fibres. The permeation results for the most permeable membranes (20% w/w spun) indicate that at equivalent pressures gaseous molar flux is typically 100 times greater than the molar flux of water. For the least permeable membranes (40% w/w spun) this factor approaches unity. As the fibres become solution diffusion controlled then the dependence of molar flux on the phase of the permeant is diminished.

3.4.6 Hollow Fibre Morphology - Electron Microscopy

Two electron microscopes were used: a Philips Scanning Electron Microscope Model 500 and a Jeol SEM Model 840 A. Hollow fibre samples 1-2 mm in length were cut using a fresh razor blade and mounted on sample stubs. These were then sputter coated with gold before being viewed with the electron microscope.

A gallery of the most significant electron micrographs is included in the pages following. No distinction in morphology was detected between the fibres spun at various levels of stretch and extrusion rate within any one particular dope concentration[a]. The electron micrographs are therefore presented purely according to the polymer concentration in the spinning solution.

It should be pointed out that the cross sections in **Figures 3.4** to **3.7** were chosen because they illustrate wall morphology well although they were atypical as far as hole symmetry is concerned. Fibres with centrally positioned lumens were used for quantitative measurements.

[a] The overall size of a fibre will obviously depend on the jet stretch ratio.

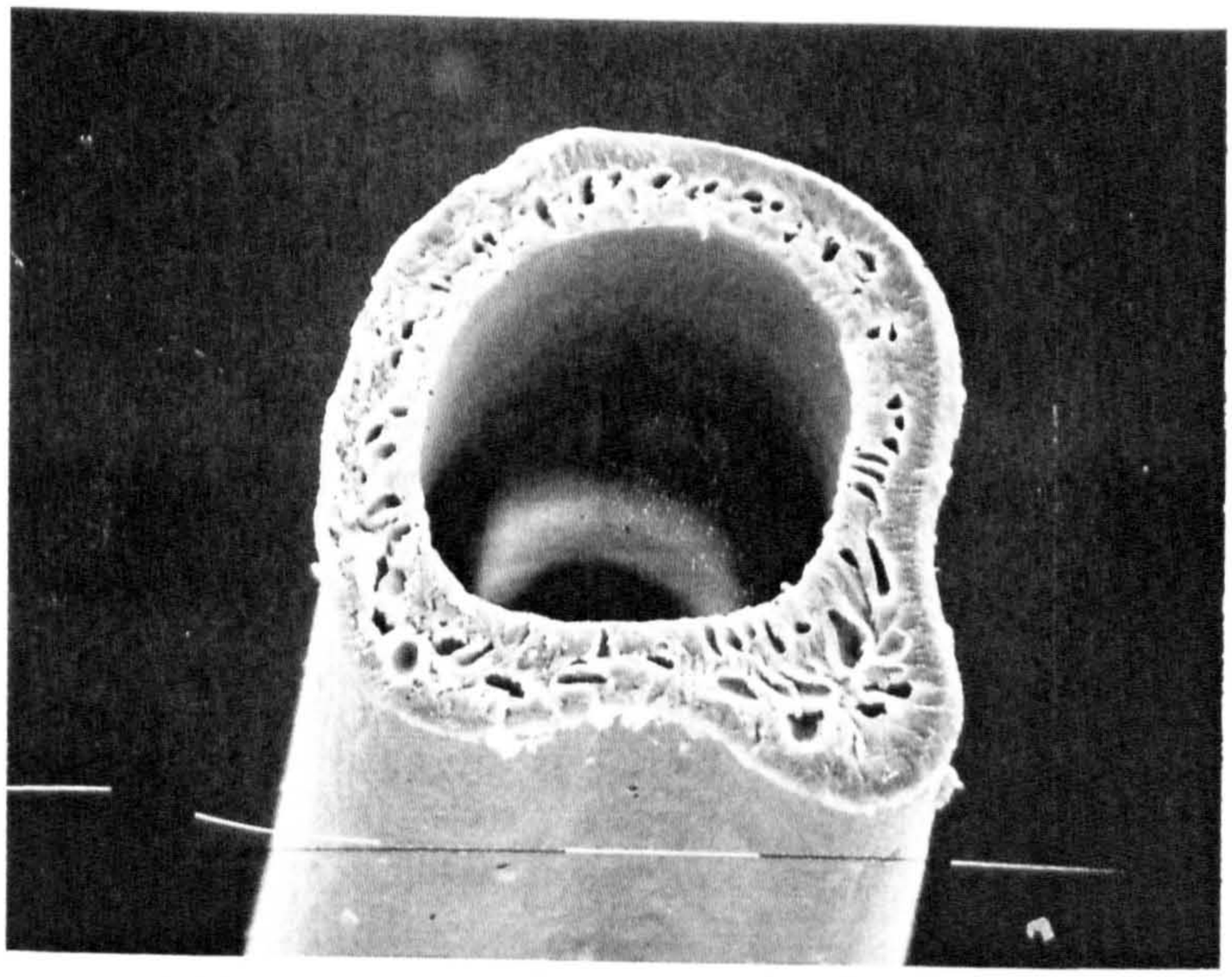

100 μm

Figure 3.4 Cross Section **Polysulphone** Hollow Fibre Dope **20% w/w** in Dimethylformamide **Magnification X 110**

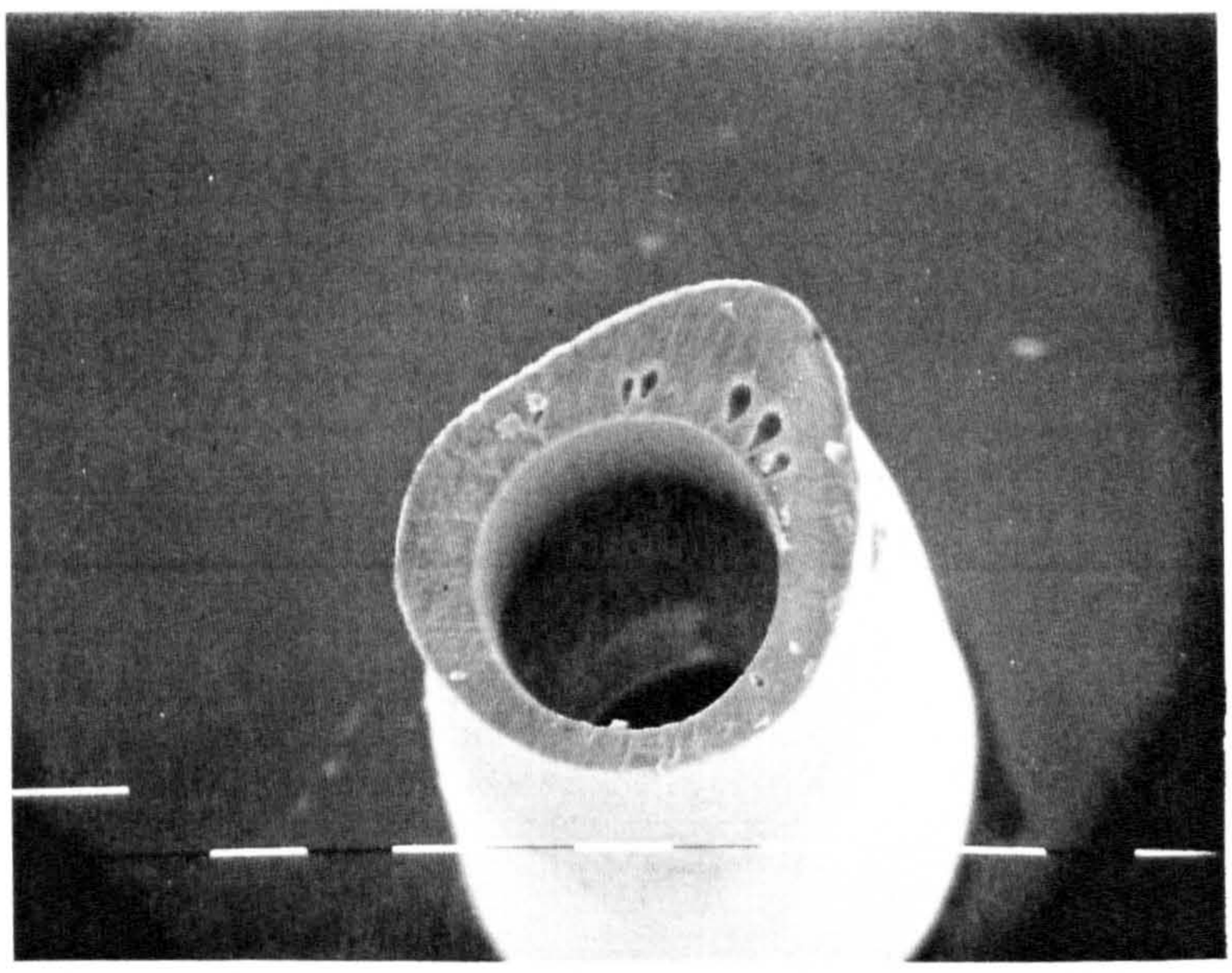

100 μm

Figure 3.5 Cross Section **Polysulphone** Hollow Fibre Dope **30% w/w** in Dimethylformamide **Magnification X 60**

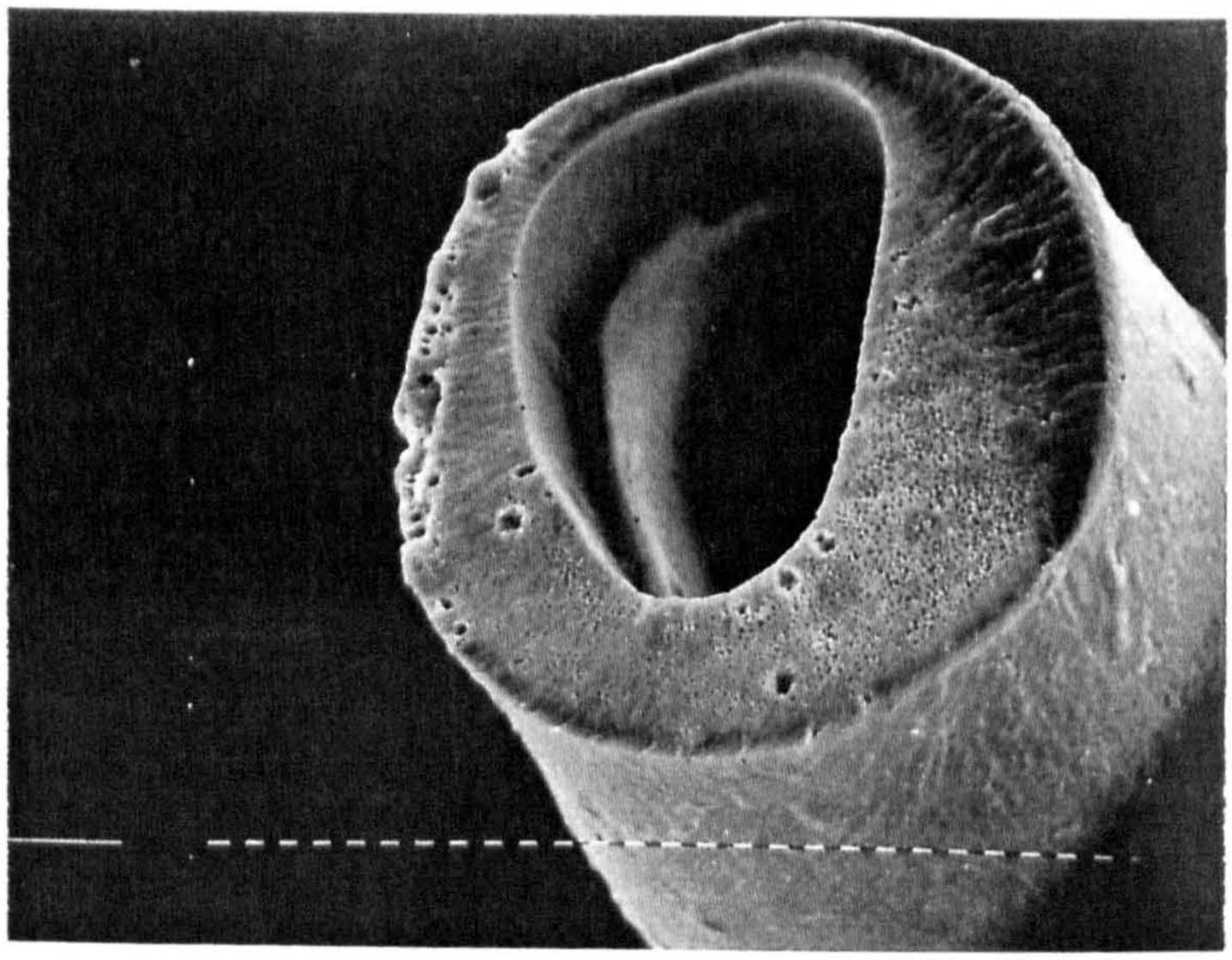

100 μm

Figure 3.6 Cross Section **Polysulphone** Hollow Fibre Dope **40% w/w** in Dimethylformamide **Magnification X 110**

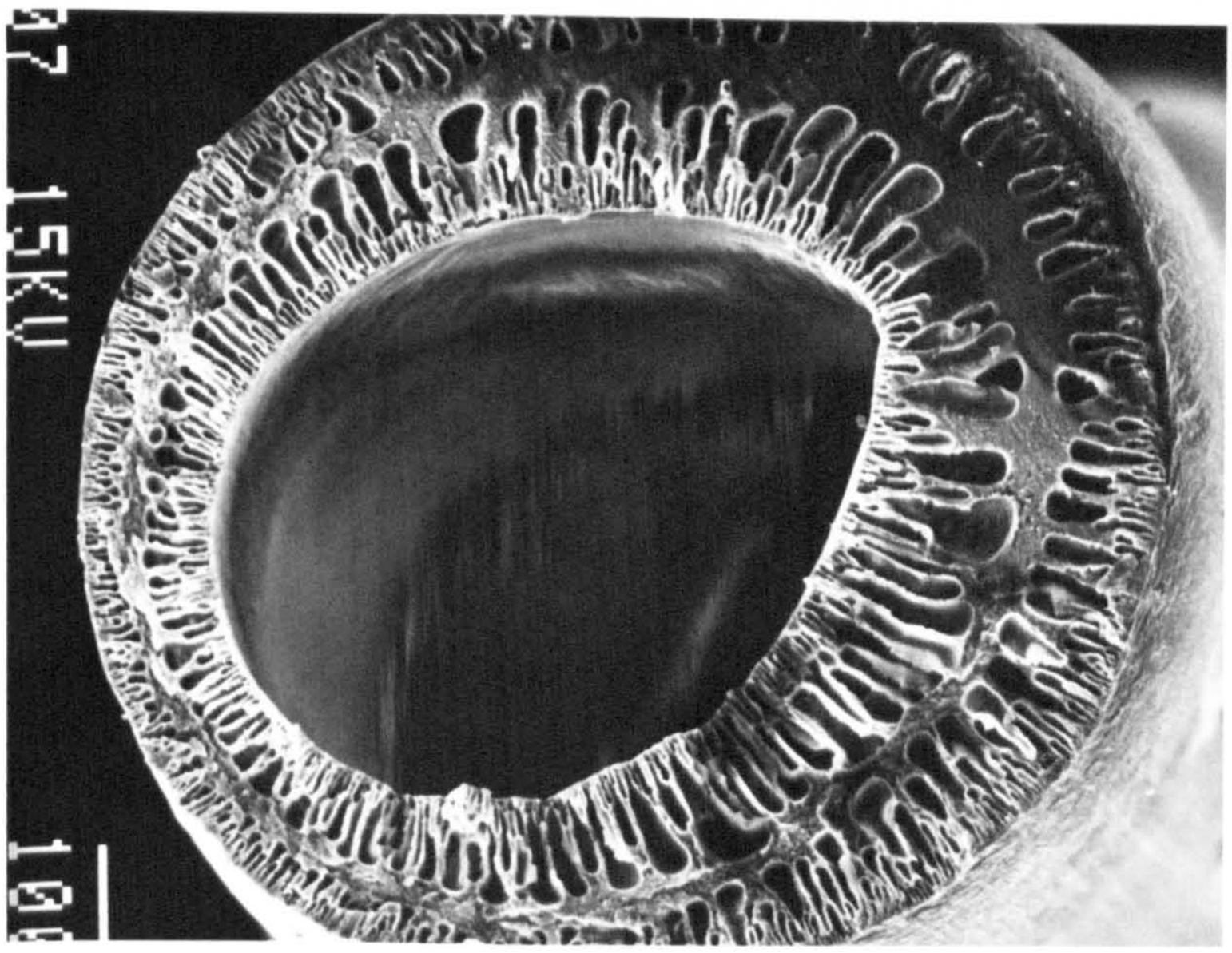

100 μm

Figure 3.7 Cross Section **Polyacrylonitrile** Hollow Fibre Dope **25% w/w** in Dimethylformamide **Magnification X 150**

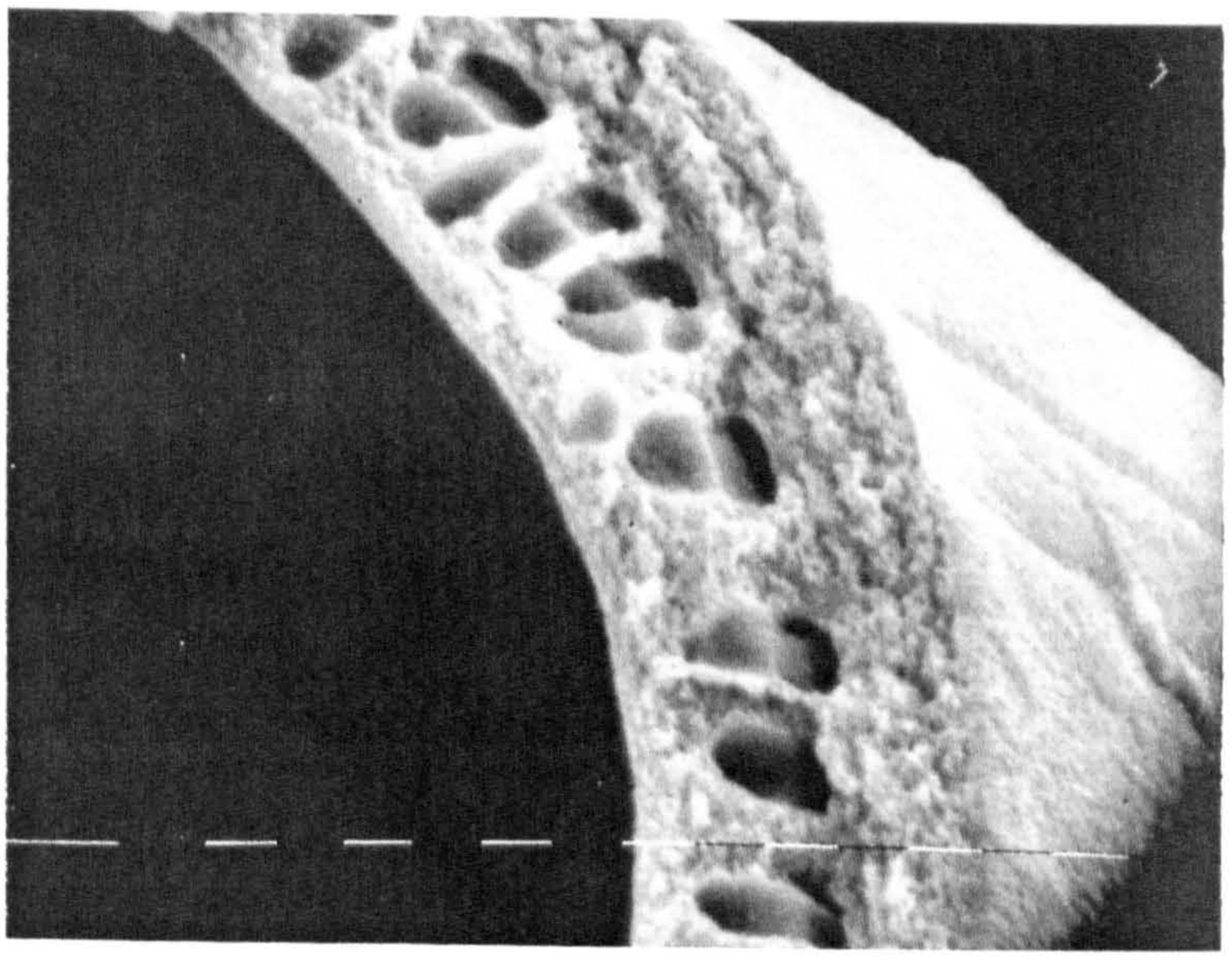

10 μm

Figure 3.8 Cross Section **Polysulphone** Hollow Fibre Dope **20% w/w** in Dimethylformamide **Magnification X 640**

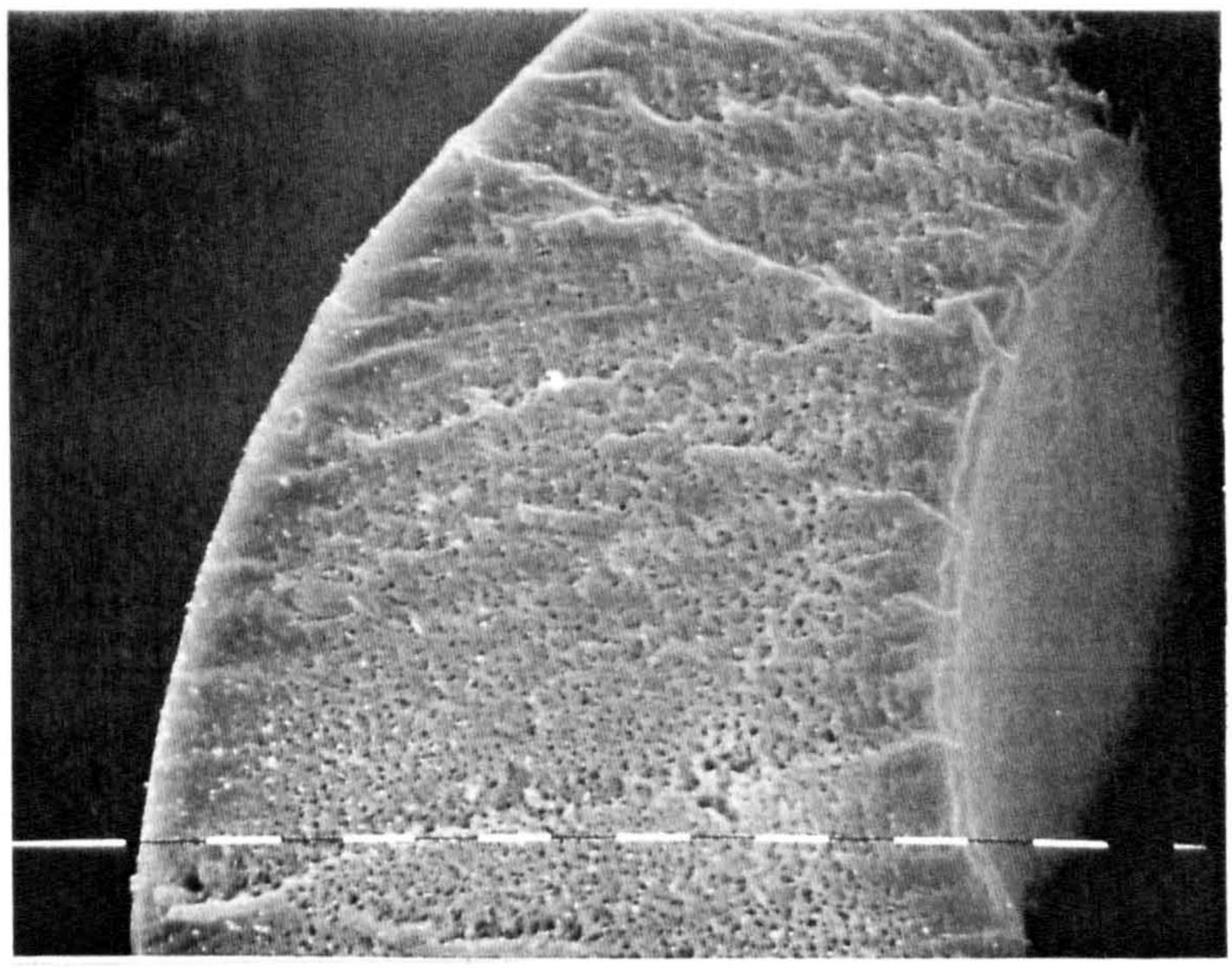

10 μm

Figure 3.9 Cross Section **Polysulphone** Hollow Fibre Dope **30% w/w** in Dimethylformamide **Magnification X 640**

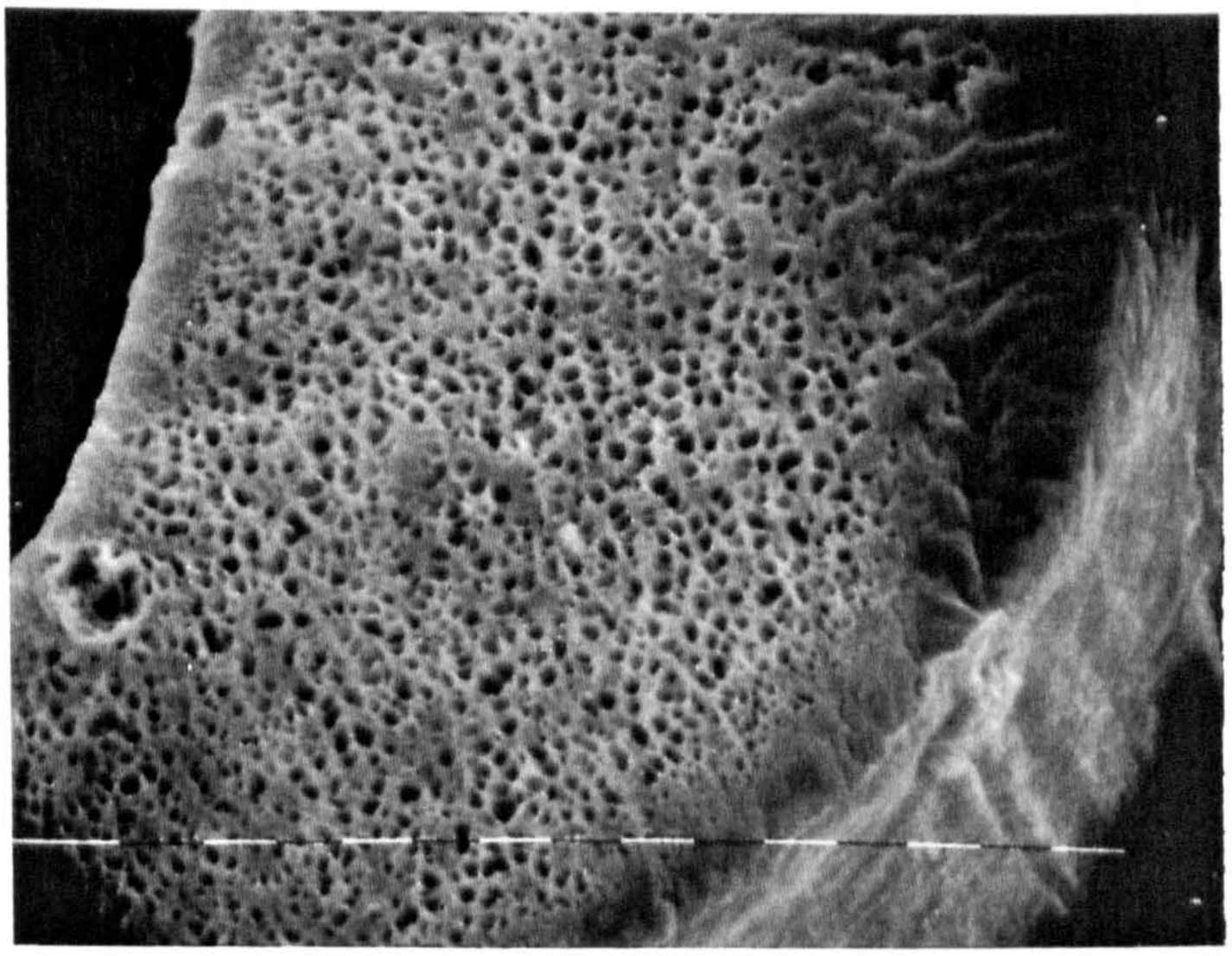

10 μm

Figure 3.10 Cross Section **Polysulphone** Hollow Fibre Dope **40% w/w** in Dimethylformamide **Magnification X 640**

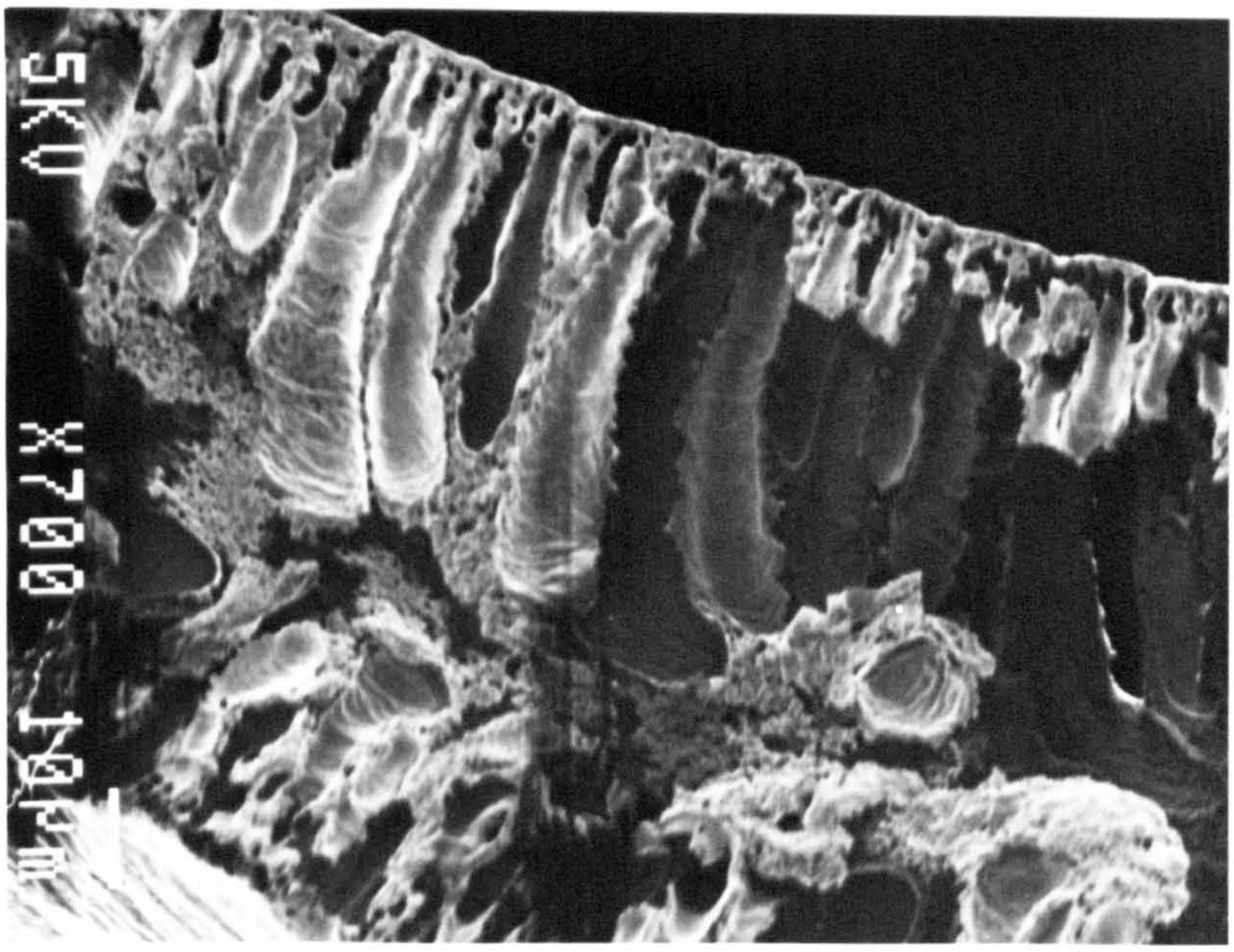

10 μm

Figure 3.11 Cross Section **Polyacrylonitrile** Hollow Fibre Dope **25% w/w** in Dimethylformamide **Magnification X 700**

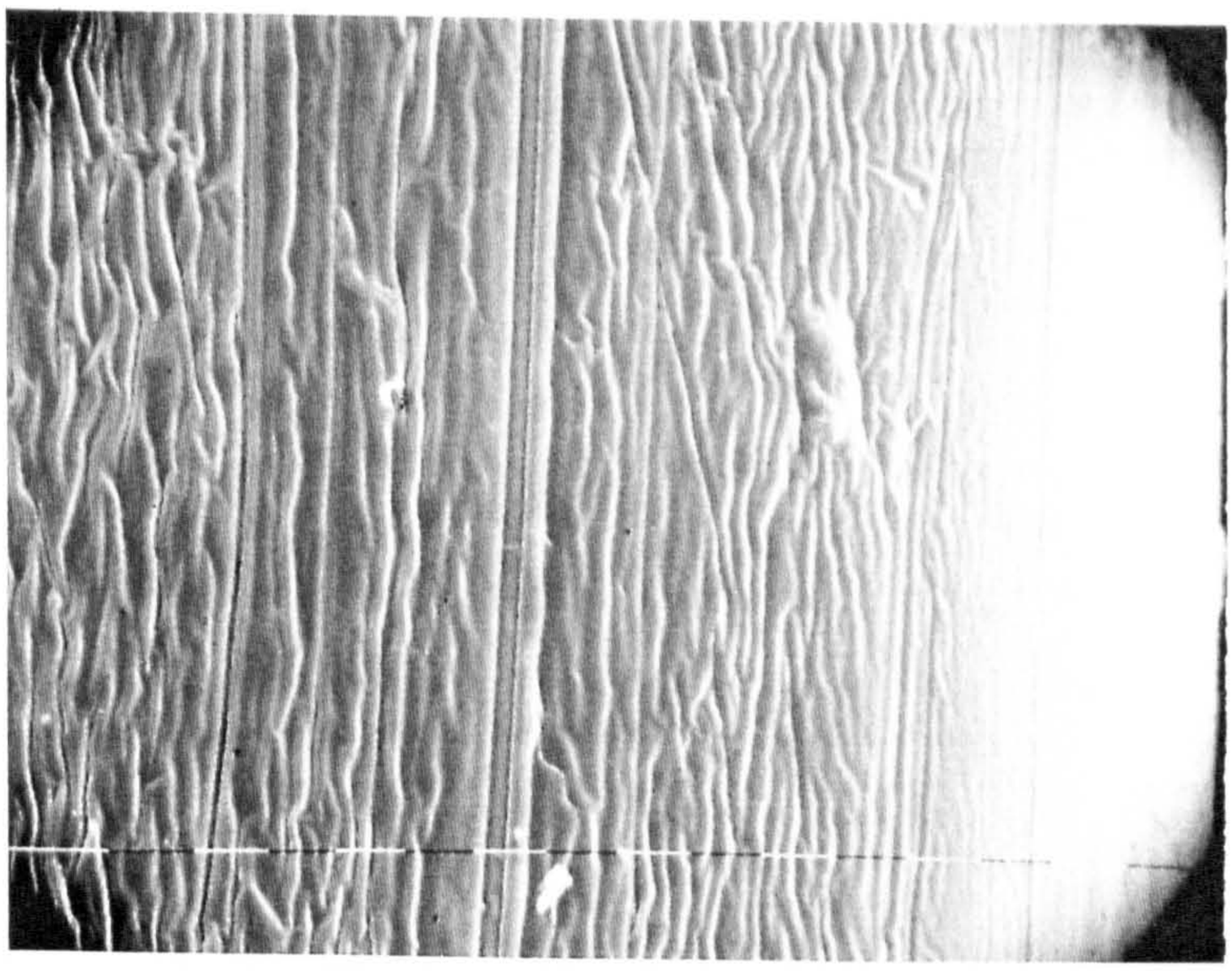

10 μm

Figure 3.12 Outer Wall **Polysulphone** Hollow Fibre Dope **20% w/w** in Dimethylformamide **Magnification X 640**

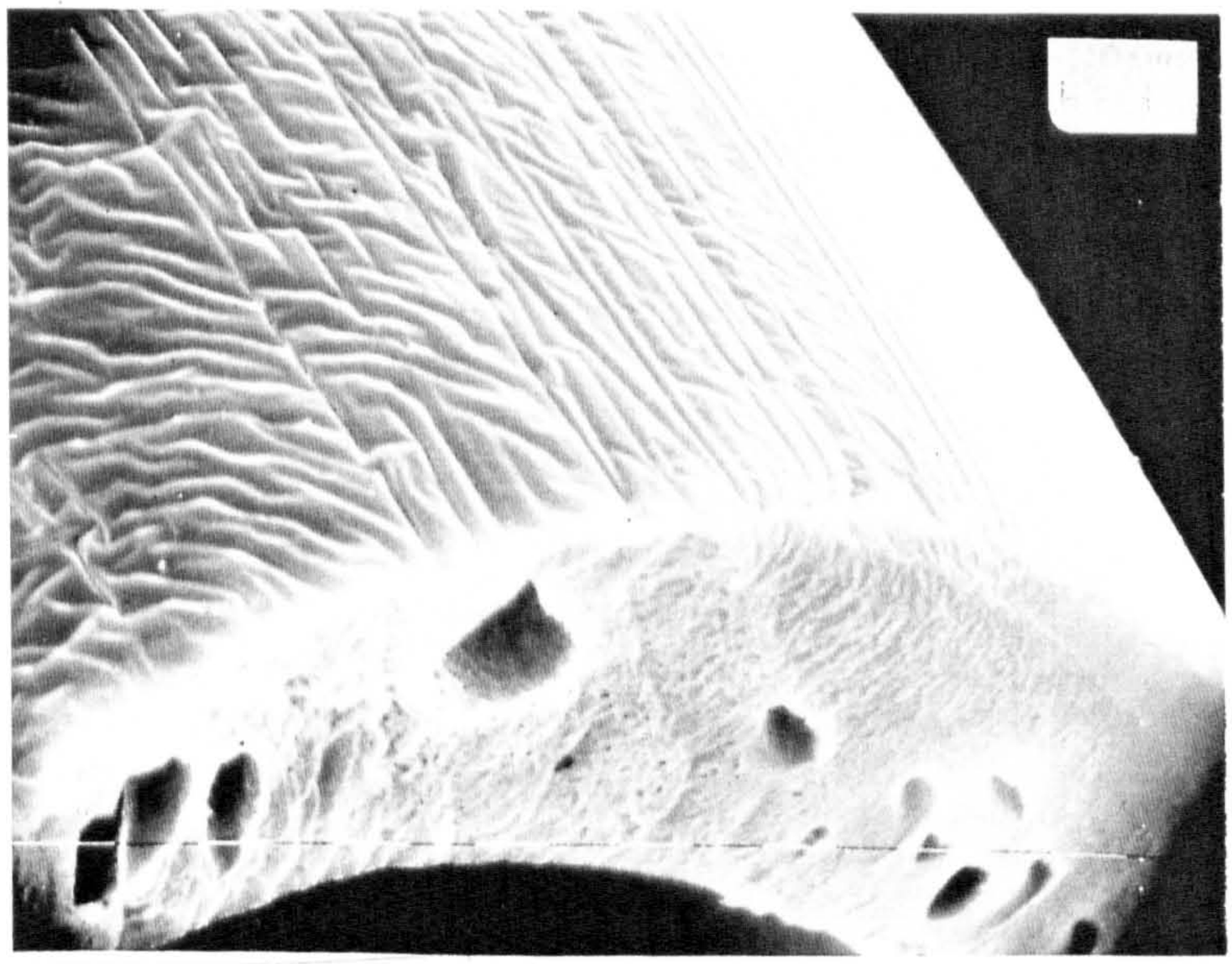

10 μm

Figure 3.13 Outer Wall **Coated Polysulphone** Hollow Fibre Dope **20% w/w** in Dimethylformamide **Magnification X 640**

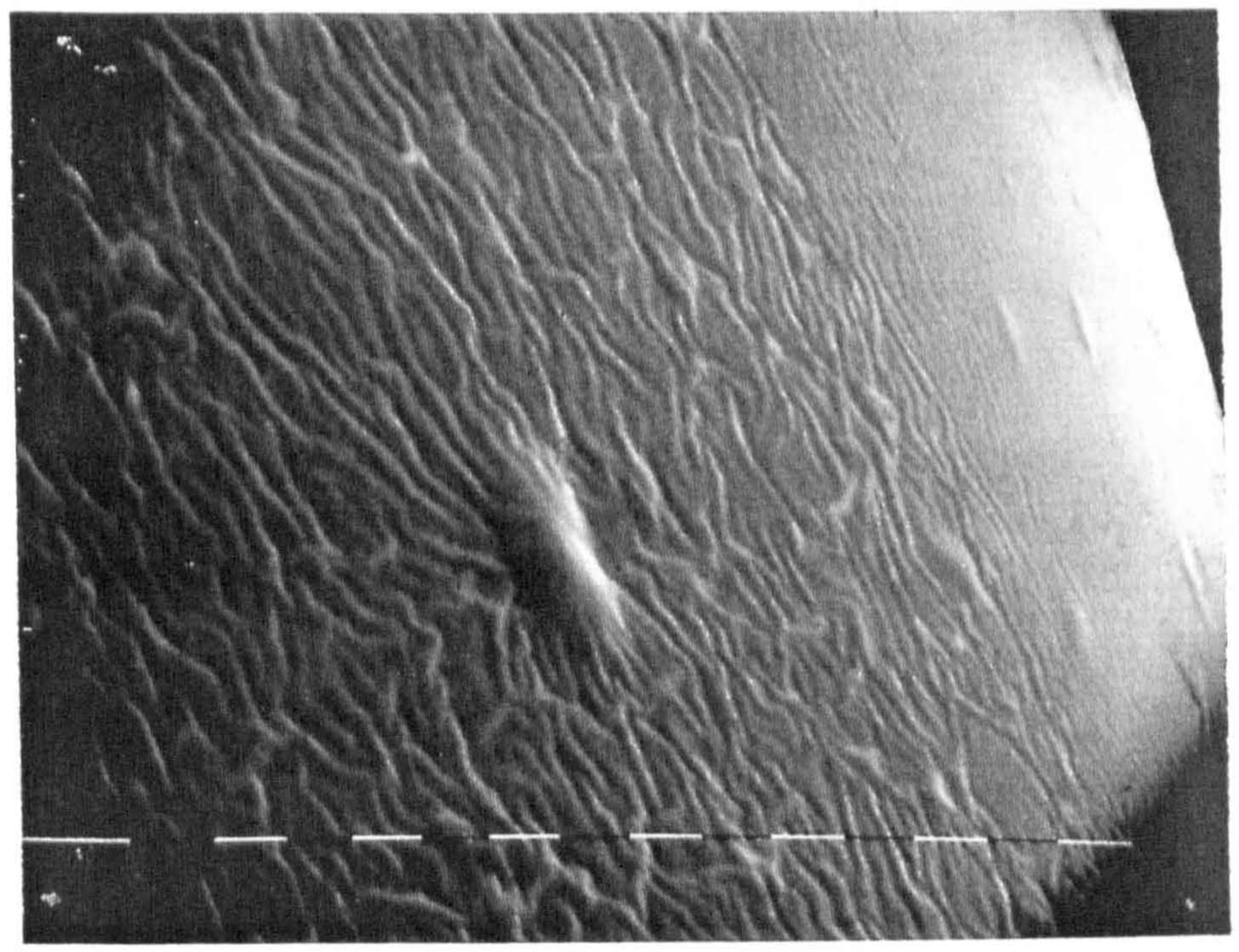

10 μm

Figure 3.14 Outer Wall **Polysulphone** Hollow Fibre Dope **40% w/w** in Dimethylformamide **Magnification X 640**

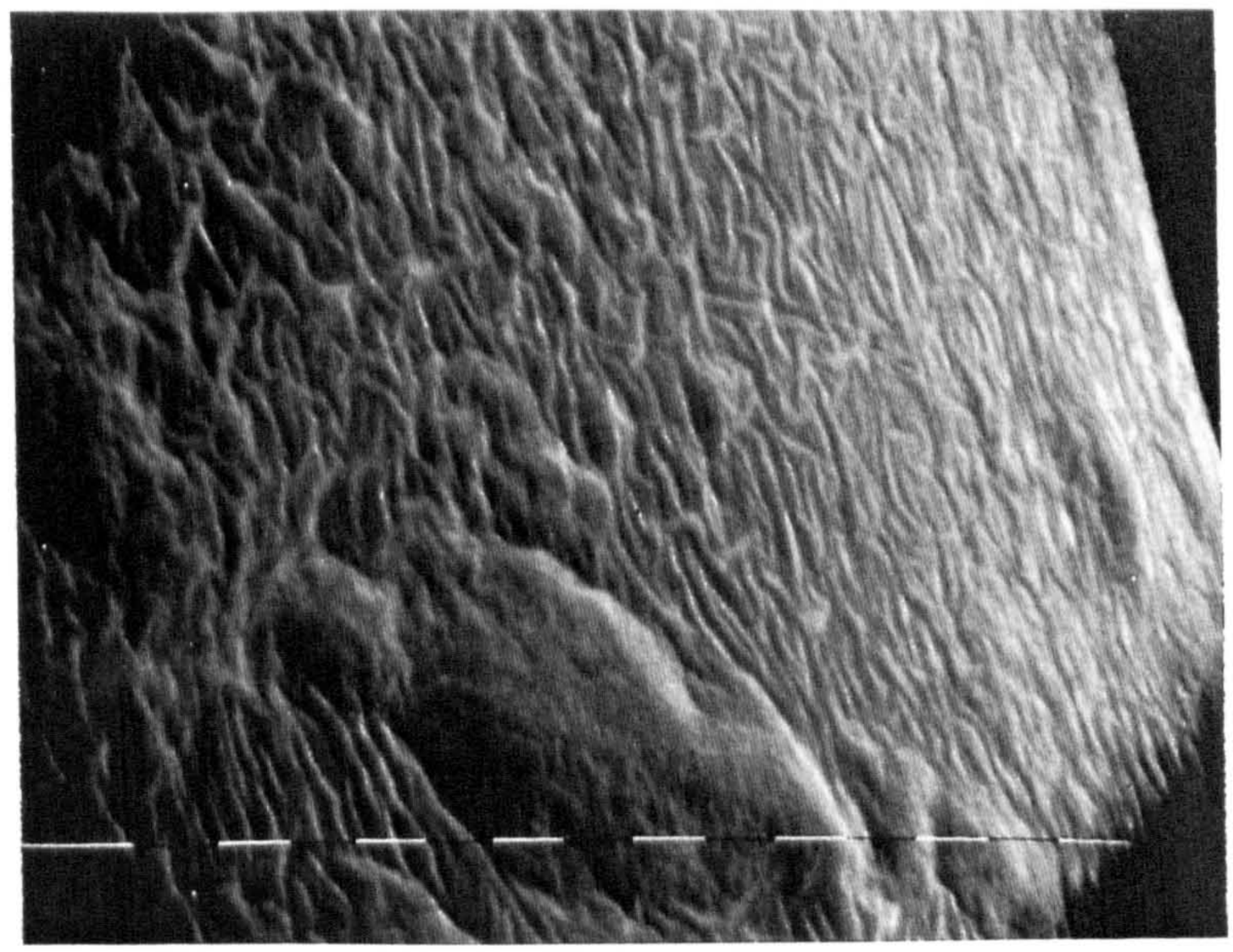

10 μm

Figure 3.15 Outer Wall **Coated Polysulphone** Hollow Fibre Dope **40% w/w** in Dimethylformamide **Magnification X 640**

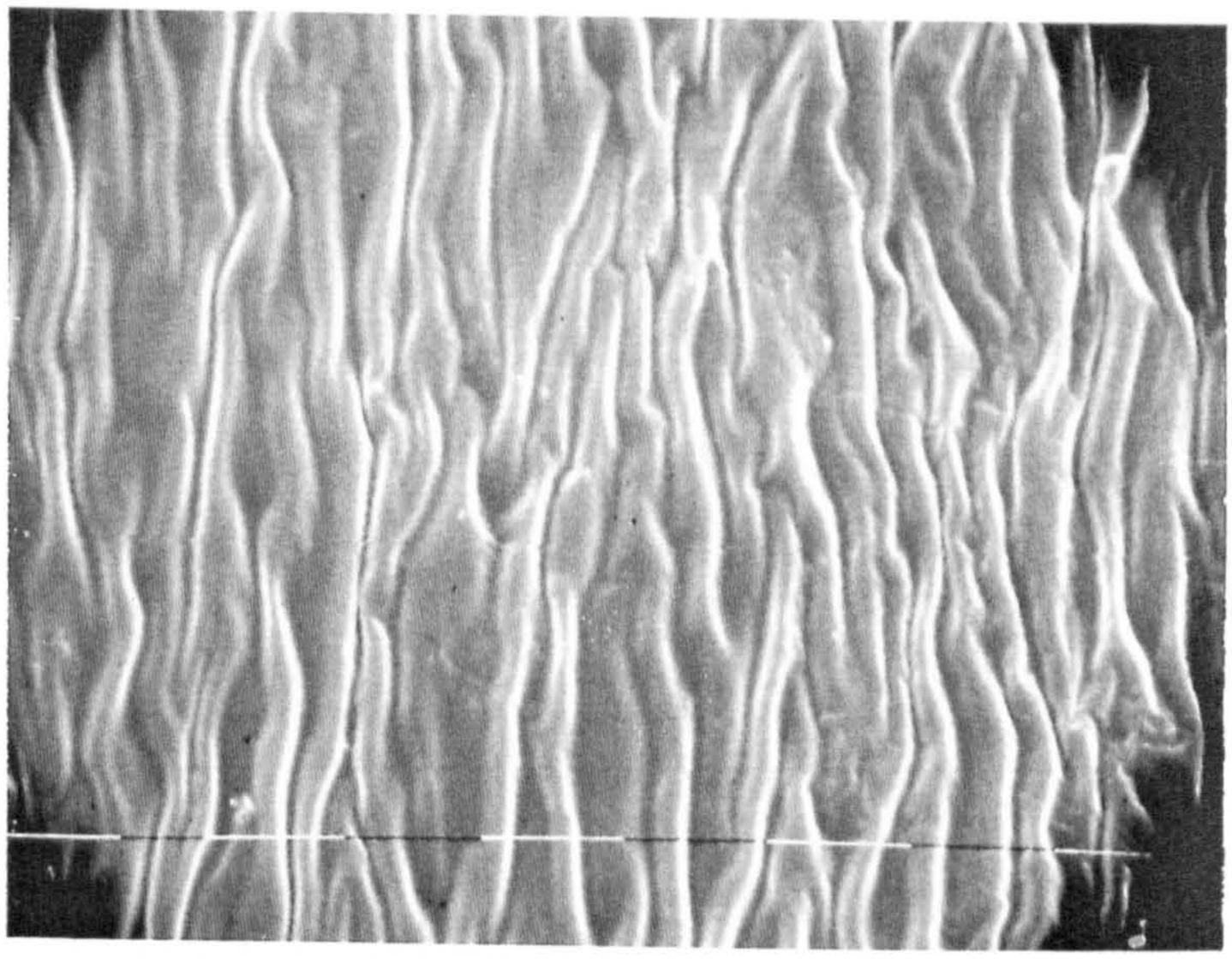

10 μm

Figure 3.16 Outer Wall **Polysulphone** Hollow Fibre Dope **20% w/w** in Dimethylformamide **Magnification X 1250**

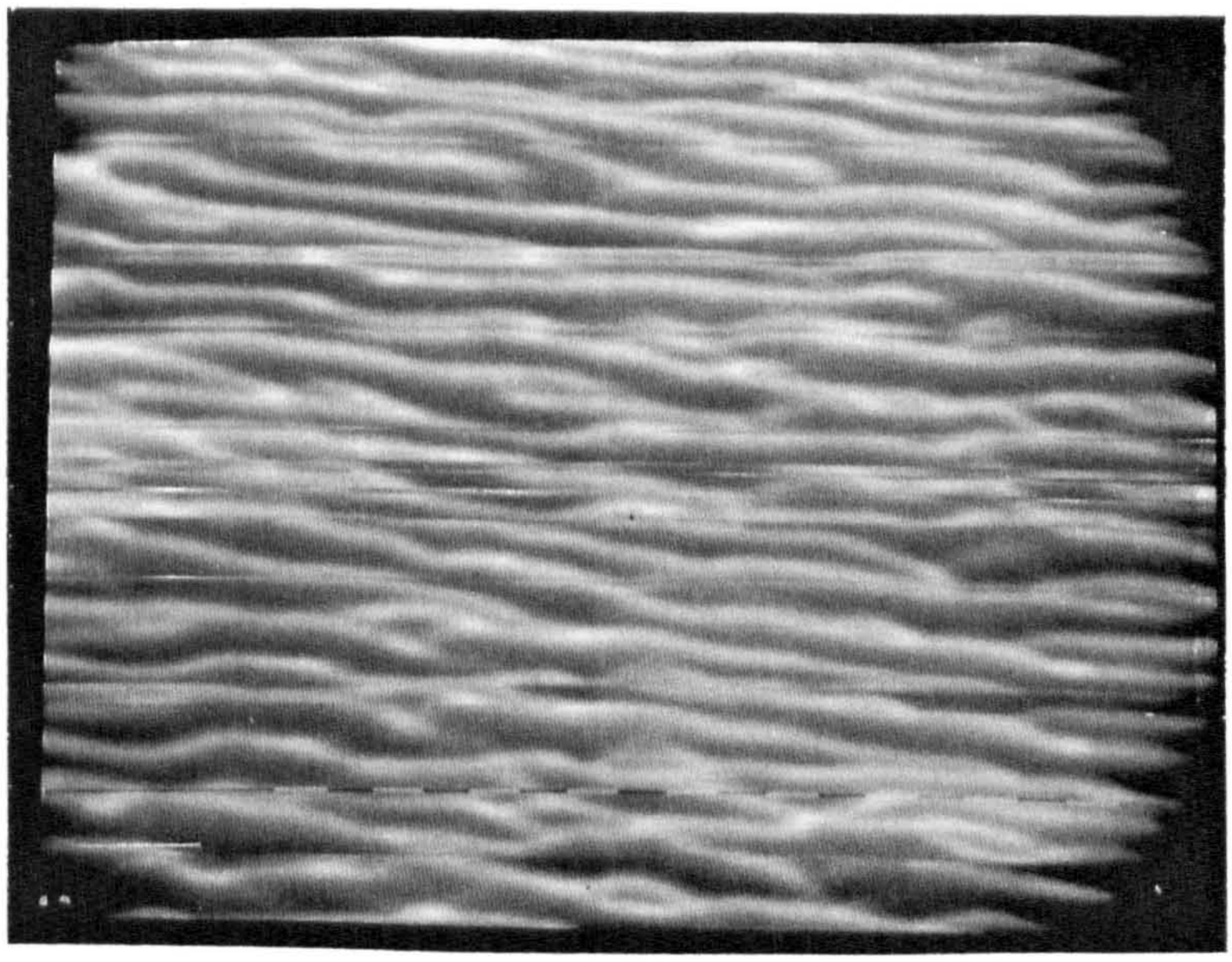

2 μm

Figure 3.17 Outer Wall **Polysulphone** Hollow Fibre Dope **30% w/w** in Dimethylformamide **Magnification X 5000**

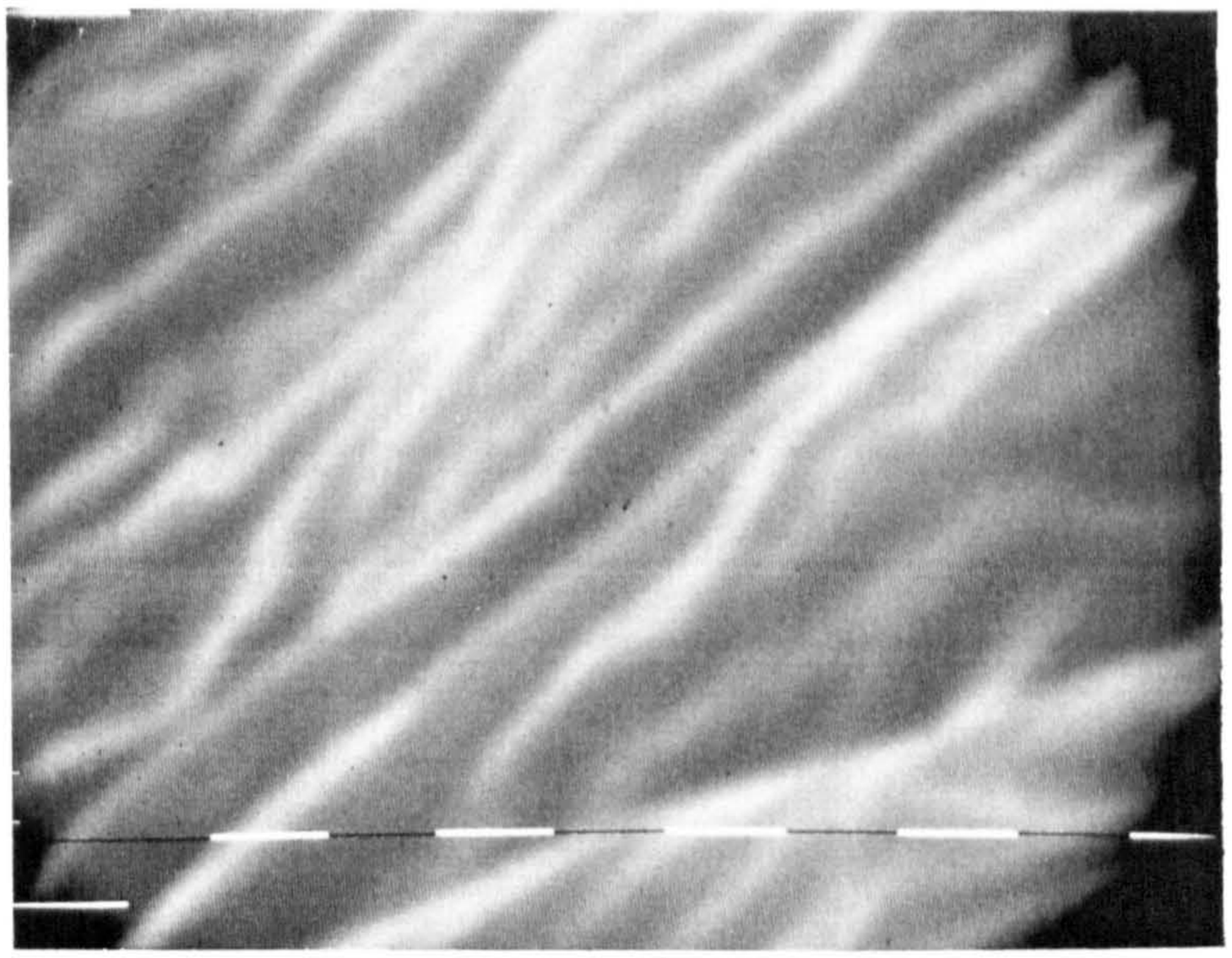

2 μm

Figure 3.18 Outer Wall **Polysulphone** Hollow Fibre Dope **40% w/w** in Dimethylformamide **Magnification X 10000**

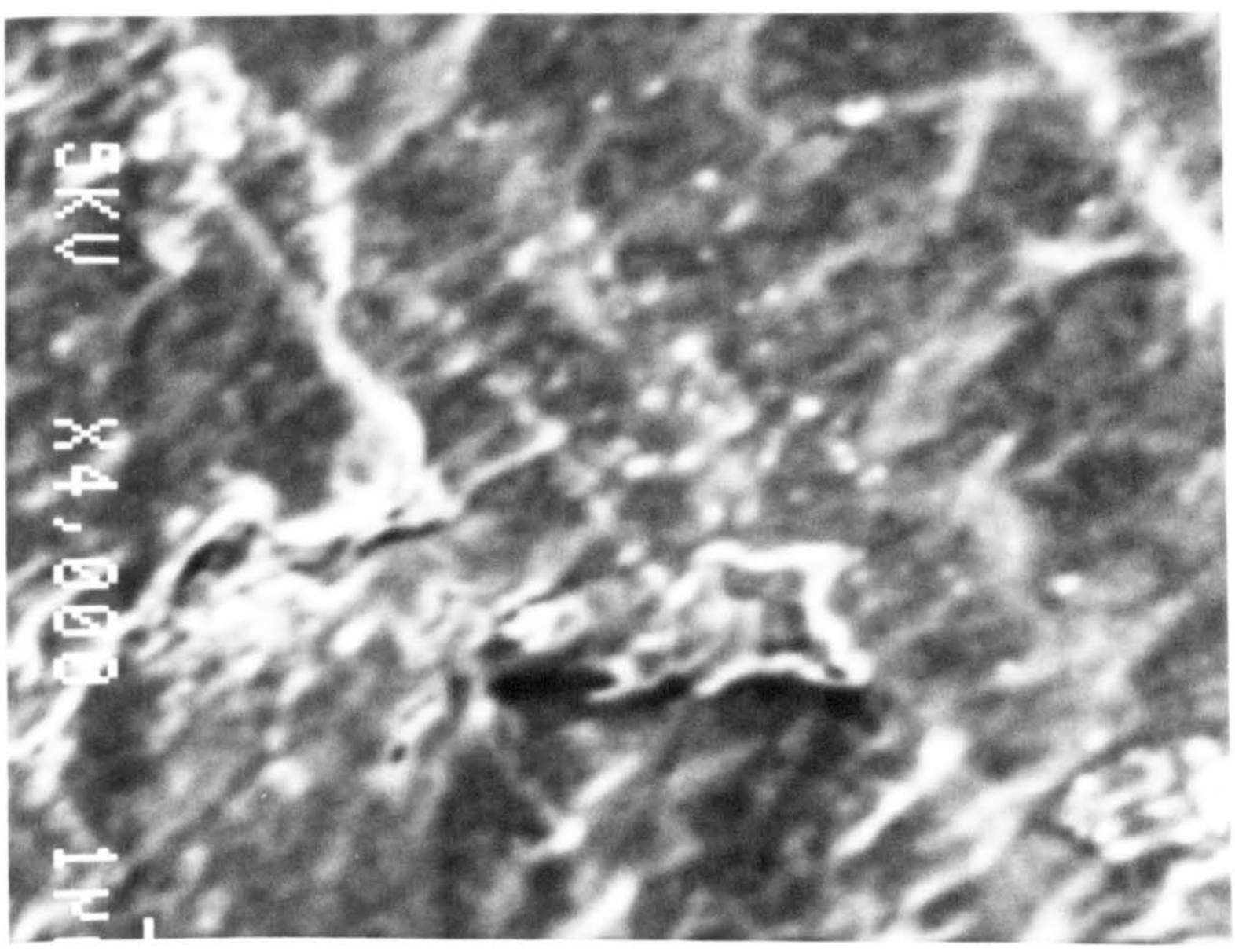

2 μm

Figure 3.19 Outer Wall **Polyacrylonitrile** Hollow Fibre Dope **25% w/w** in Dimethylformamide **Magnification X 4000**

Figures 3.4 to **3.7** show the full cross sections of the fibres spun from each of the spinning dopes. The first three electron micrographs show a reduction in macrovoids as polysulphone concentration in the dope increases to 40% w/w. Distinct regular inner and outer macrovoidal layers can be seen in **Figure 3.7.** This morphology was typical of the polyacrylonitrile fibres where the maximum spinnable dope concentration was 25% w/w.

Figures 3.8 to **3.11** show the asymmetric structure of the membranes: porous substructure and a dense relatively non-porous region at the fibre wall. Various pore structures can be observed. **Figure 3.10** shows the fibre with the least overall voidage fraction or porosity **(Table 3.5)** yet this membrane seems to have larger pores than the fibre spun from a more dilute polymer solution shown in **Figure 3.9.** This can be explained by considering pore number and size distribution. The 40% w/w spun fibre can be expected to have fewer pores and a highly dense layer of polymer at the outer wall can be identified. The polymer matrix in the porous region of this fibre may also be highly dense in nature. These comments are supported by the tensile tests. Tenacity, or the inherent strength of the polymer, and 1st modulus increase with increasing polymer concentration in the spinning dope **(Graphs 3.13** and **3.14).**

Figure 3.11 clearly shows the finger like macrovoidal structure of the polyacrylonitrile fibres. The macrovoids extend to a thin dense skin region at the fibre wall. **Figure 3.8**, the 20% w/w spun polysulphone fibre, also shows a macrovoidal structure but it is less ordered and co-exists with a significant microporous region. Again due to more subtle aspects of pore structure this membrane, although spun from a more dilute polymer solution, is less macroporous than the 25% w/w spun polyacrylonitrile fibre.

Figures 3.12 to **3.15** compare fibre outer walls before and after coating for 20% w/w and 40% w/w spun polysulphone hollow fibres. The presence of the coating is difficult to detect visually from the electron micrographs. This was also the case when viewing the cross sections of coated fibres. No silicone layer could be identified by eye.

Figures 3.16 to **3.19** show under high magnification the uncoated outer walls of fibres from each spinning dope. During the electron microscope work, no pores could be observed in any of the fibres even at magnifications of X 10000. Picture quality was compromised at high magnification.

Further consideration will be given to pore size and membrane structure in section 5.2 where gas transfer through the hollow fibres has been modelled.

3.5 Gas Permeation Tests

3.5.1 Basic Principles of Gas Permeation Measurements

Generally, the flux of a gas permeating a homogeneous membrane is directly proportional to the pressure difference across the membrane and inversely proportional to the membrane thickness such that

$$Q = \frac{\acute{P}}{L} A \Delta P \quad \text{---------- 3.40}$$

where Q = Volumetric flowrate of gas (STP)

A = Membrane area

ΔP = Pressure difference across membrane

L = Membrane thickness

The constant of proportionality or the permeability coefficient, $\acute{P}$ characterises a membrane with respect to gas transfer.

It is more appropriate when dealing with asymmetric membranes, as in this work, to characterise permeation performance by defining membrane permeability, P where

$$P = \frac{\acute{P}}{L} \quad \text{---------- 3.41}$$

thus

$$P = \frac{Q}{A \Delta P} \quad \text{----------} \quad 3.42$$

The selectivity, Ω of a membrane to any two gases, i and j, is simply the ratio of permeabilities

$$\Omega_j^i = \frac{P_i}{P_j} \quad \text{----------} \quad 3.43$$

If mixtures of two gases are tested then permeation measurements are based on the partial pressures of the permeating species. Thus equation 3.42 becomes

$$P_i = \frac{Q\, y_{ip}}{A\, (P_f\, y_{if} - P_p\, y_{ip})} \quad \text{----------} \quad 3.44$$

where y = Mole fraction

P = Pressure

Subscripts f and p refer to feed and permeate streams respectively

Selectivity is again simply the ratio of permeabilities but in addition the separation factor, α can be defined for gas mixture separations

$$\alpha_j^i = \frac{PP_{ip}/PP_{jp}}{PP_{if}/PP_{jf}} = \frac{y_{ip}/y_{jp}}{y_{if}/y_{jf}} = \frac{y_{ip}(1-y_{if})}{y_{if}(1-y_{ip})} \quad \text{-----} \quad 3.45$$

where PP = Partial pressure

The separation factor describes the actual separating efficiency of a system and is dependent on process parameters such as membrane module design and gas throughput. The selectivity, Ω is a measure of the inherent separating capabilities of the particular membrane and is sometimes referred to as the ideal separation factor. It can be shown that selectivity and separation factor are related thus

$$\alpha_j^i = \Omega_j^i \frac{1-(PP_{ip}/PP_{if})}{1-(PP_{jp}/PP_{jf})} \quad \text{----------} \quad 3.46$$

i.e. if $PP_f >>> PP_p$ for both species then $\alpha = \Omega$

3.5.2 Details of Gas Permeation Tests

The permeabilities of the hollow fibres from the various spinning campaigns were measured. The standard permeability test for general membrane assessment was carried out at a single chamber pressure, usually 5 barg. With some of the more permeable uncoated fibres the pressure was reduced to 2 barg to allow permeate flowrate measurement and prevent any overpressurization occurring in the permeate system. The pressure in the permeate line was usually negligible but may be noticeable (up to 0.5 barg) when gases pass through the automatic gas sampling valve of the gas chromatograph at high flowrate. In the gas mixture tests involving the least permeable membranes the chamber pressure was increased to 10 barg so as to reduce the equilibration time of the permeate composition in the gas sampling system.

The results of the permeability tests can be found in Appendix B. Details are given for uncoated and coated membranes tested with both pure gases and gas mixtures. Tests were carried out at 25 ^{o}C and permeabilities based on fibre outside area.

Non-routine permeability tests investigating the effect of chamber pressure and permeation time were also carried out. The results for these tests are included in sections 3.5.4 and 3.5.5 respectively.

3.5.3 Effect of Coating on Gas Permeation Properties

Two coating solution strengths were used: 3% w/w and 15% w/w silicone in hexane. **Graphs 3.20** and **3.21** show the effect of coating solution concentration on permeability and selectivity for hollow fibres spun from 40% w/w polysulphone(P1700) in dimethylformamide. The graphs indicate that there is no difference in the effects of the two coating strengths on fibre performance. The polysulphone fibres were considered to be fully coated after application of the 3% w/w silicone solution.

Most of the gas permeation research was based on polysulphone hollow fibres with much attention focusing on membranes spun from the 40% w/w dope. However, the permeation performance of hollow fibres spun from 25% w/w polyacrylonitrile in dimethylformamide was also investigated. Coating solution strength did effect the permeability of the PAN fibres and thus the results for these membranes shown in Chapter 4 make a distinction between the two coating concentrations.

Graph 3.20 Effect of Coating on Permeability Polysulphone Hollow Fibre Membranes

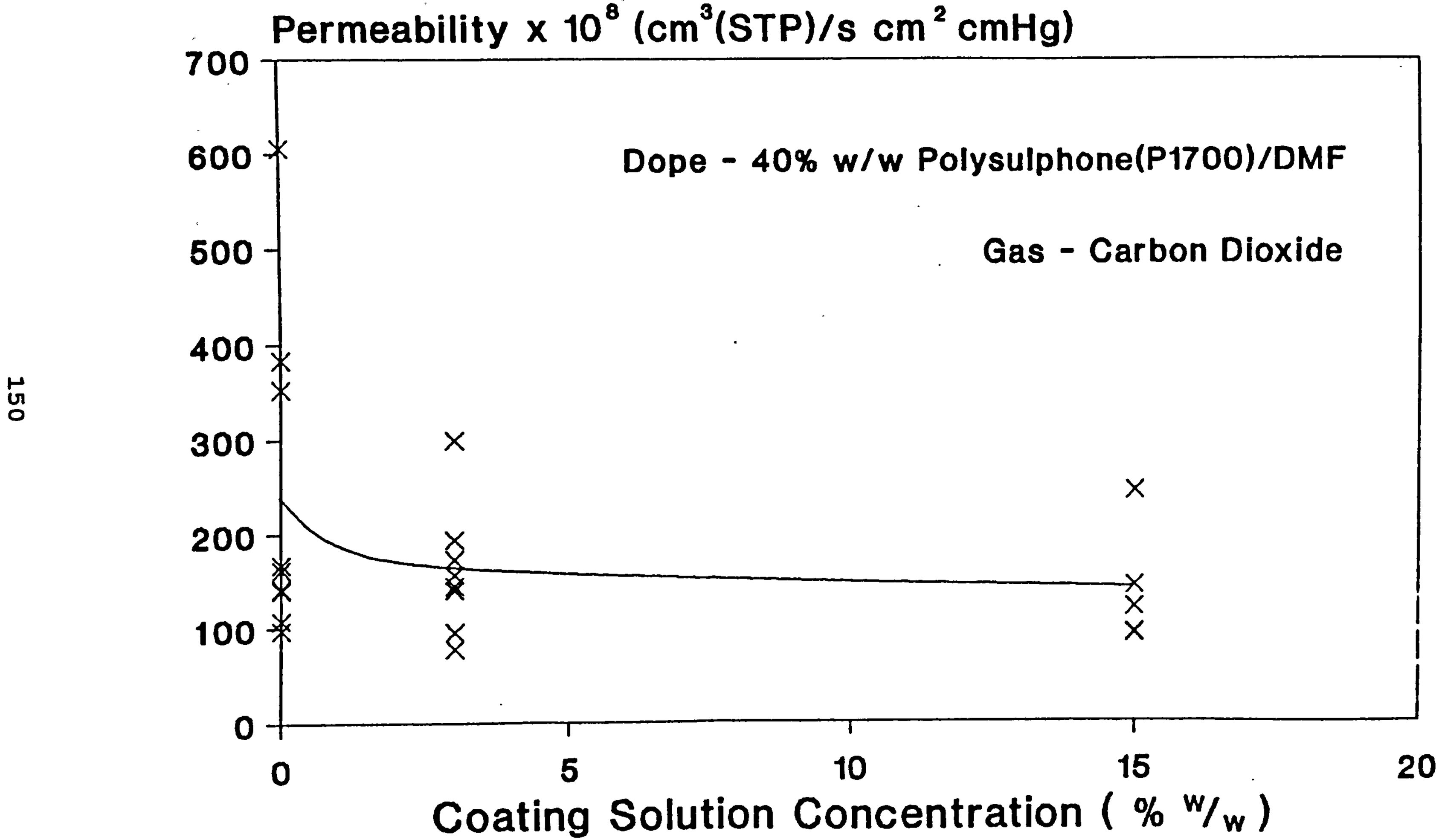

Graph 3.21 Effect of Coating on Selectivity
Polysulphone Hollow Fibre Membranes

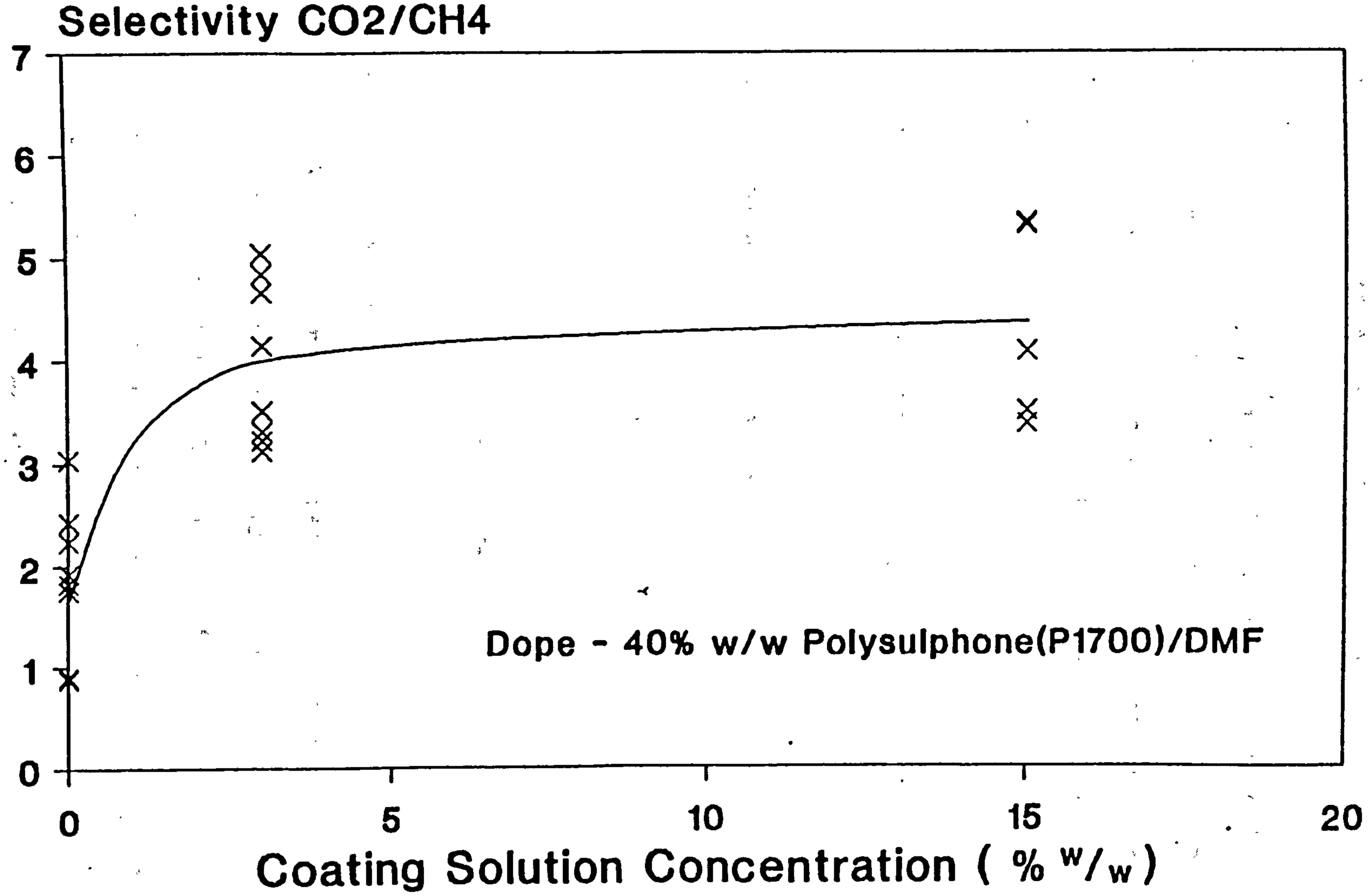

3.5.4 Effect of Pressure on Gas Permeation

3.5.4.1 Permeability Variation with Pressure

The effect of pressure on permeability was investigated using fibres from a selection of spinning runs. The permeability, P of a gas through a microporous membrane can be expressed as the sum of solution diffusion, Knudsen diffusion and viscous flow

$$P = \underbrace{\frac{\acute{P}}{L}}_{\text{Solution Diffusion}} + \underbrace{\frac{8}{3P_o}\left[\frac{RT}{2\pi}\right]^{\frac{1}{2}} \frac{A_P}{L}\, r\, M^{-\frac{1}{2}}}_{\text{Knudsen Diffusion}} + \underbrace{\frac{1}{8P_o}\,\frac{r^2}{\eta}\,\frac{A_P}{L}\left[\frac{P_f+P_P}{2}\right]}_{\text{Viscous Flow}} \quad \text{---- 3.47}$$

where r = Pore radius

A_P = Fraction of membrane area that is pores

L = Thickness of membrane active layer

M, η = Molecular weight, Viscosity of gas

$\acute{P}$ = Intrinsic permeability coefficient of polymer

P_o = Atmospheric pressure

R, T = Universal gas constant, Temperature

$\frac{P_f+P_P}{2} = P_{mean}$, the mean pressure across the membrane

If the solution diffusion term is assumed negligible then, as demonstrated by Yasuda and Tsai[78], the pressure permeability data can be used to estimate the average pore size of a microporous membrane. Equation 3.47 reduces to

$$P = Kn + Vs\ P_{mean} \quad \text{---------- 3.48}$$

where $$Kn = \frac{8}{3P_o}\left[\frac{RT}{2\pi}\right]^{\frac{1}{2}} \frac{A_p}{L}\ r\ M^{-\frac{1}{2}} \quad \text{----- 3.49}$$

and $$Vs = \frac{1}{8P_o}\ \frac{r^2}{\eta}\ \frac{A_p}{L} \quad \text{----- 3.50}$$

If P is plotted against P_{mean} then a straight line should be obtained. The intercept with the P axis yields Kn, the Knudsen flow component and the gradient gives Vs which indicates the viscous flow contribution.

The average pore size of the membrane can be evaluated by combining Kn and Vs

$$r = \frac{Vs}{Kn}\ \frac{64}{3}\left[\frac{RT}{2\pi}\right]^{\frac{1}{2}} \eta\ M^{-\frac{1}{2}} \quad \text{---------- 3.51}$$

Graphs 3.22 to **3.26** show the permeability pressure plots for the various fibres tested. **Table 3.10** gives the average pore size data.

Graph 3.22 Permeability Variation with Pressure Nitrogen Uncoated Fibres Campaign 2

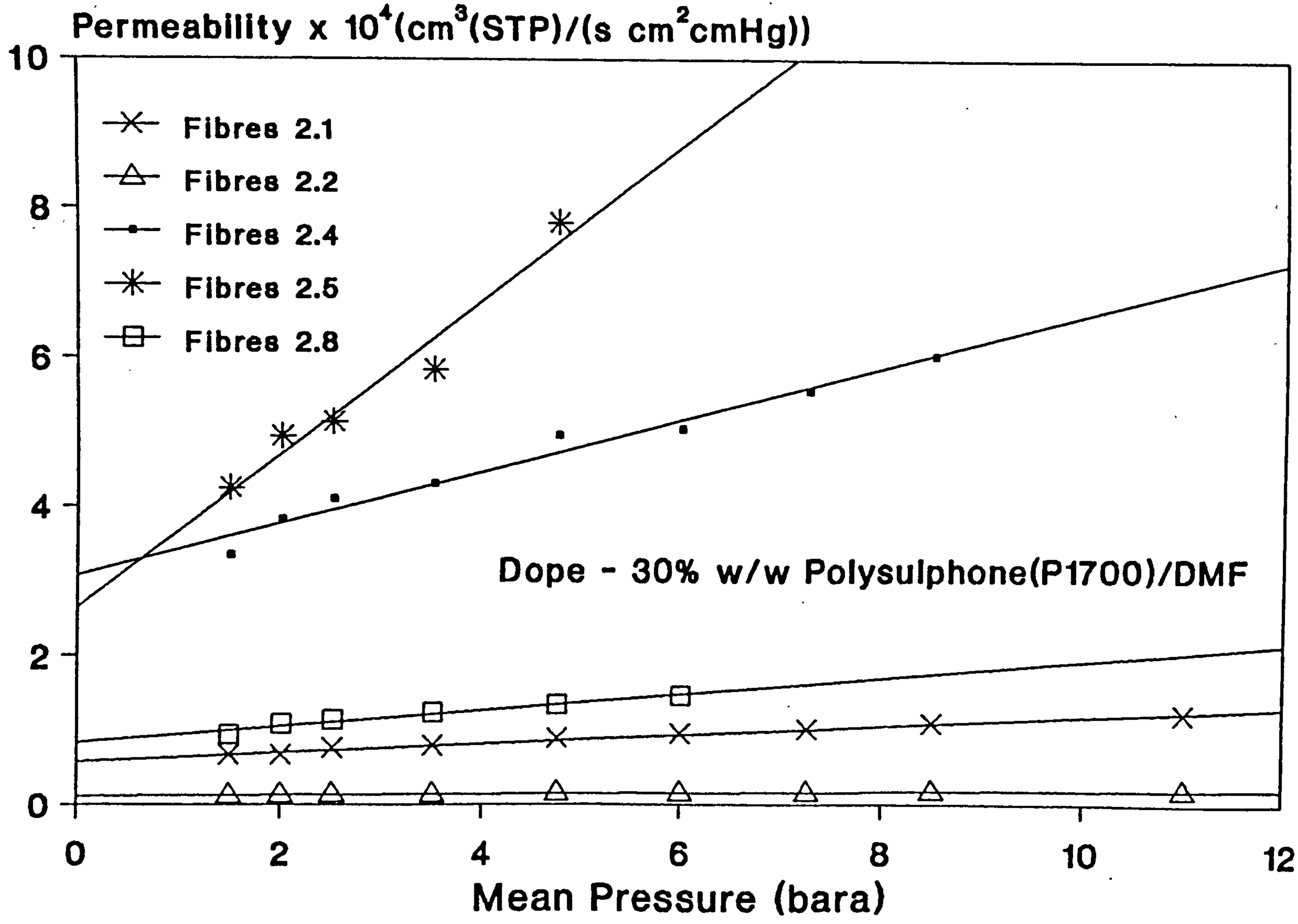

Graph 3.23 Permeability Variation with Pressure
Oxygen Uncoated Fibres Campaign 3

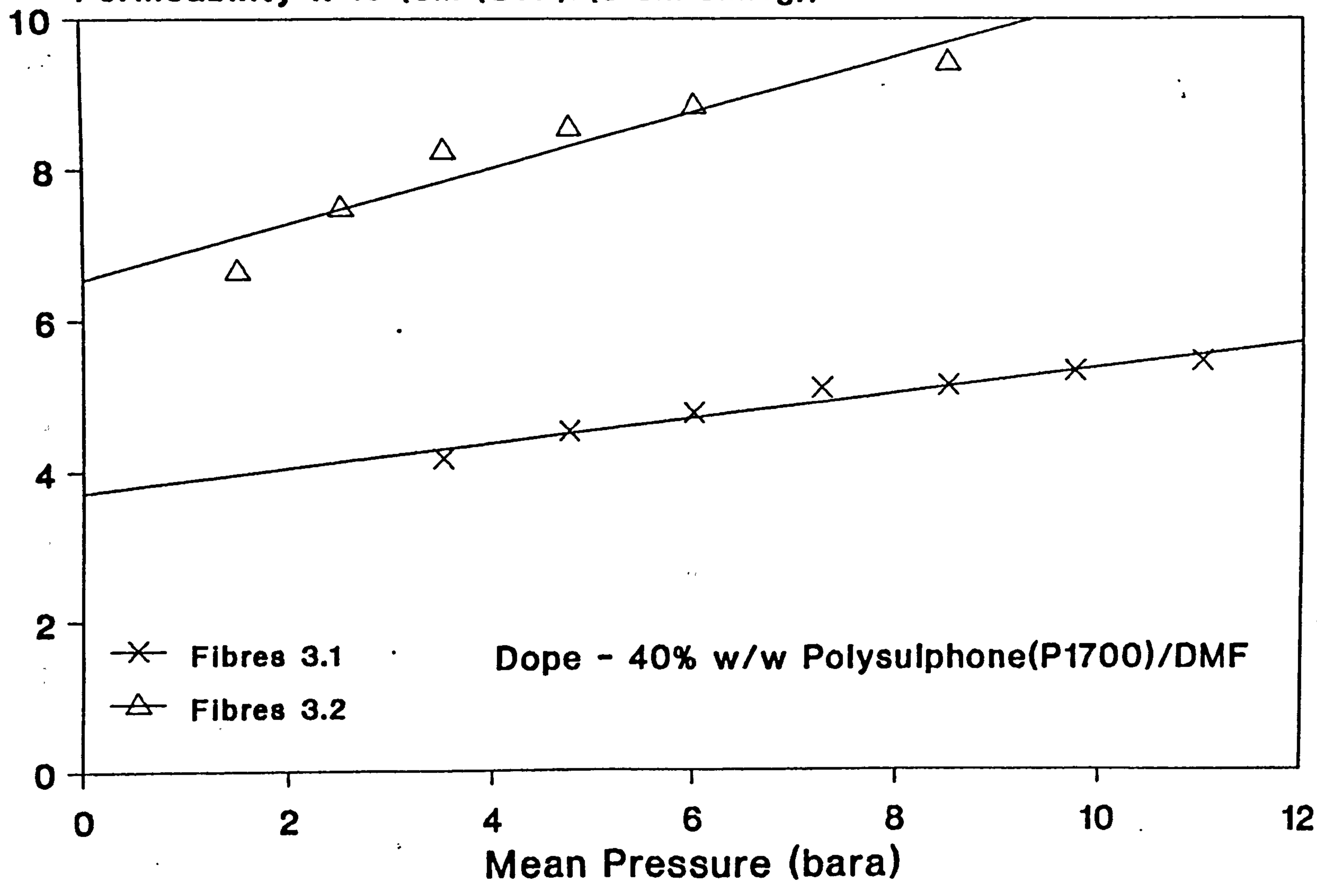

Graph 3.24 Permeability Variation with Pressure Nitrogen Uncoated Fibres Campaign 7

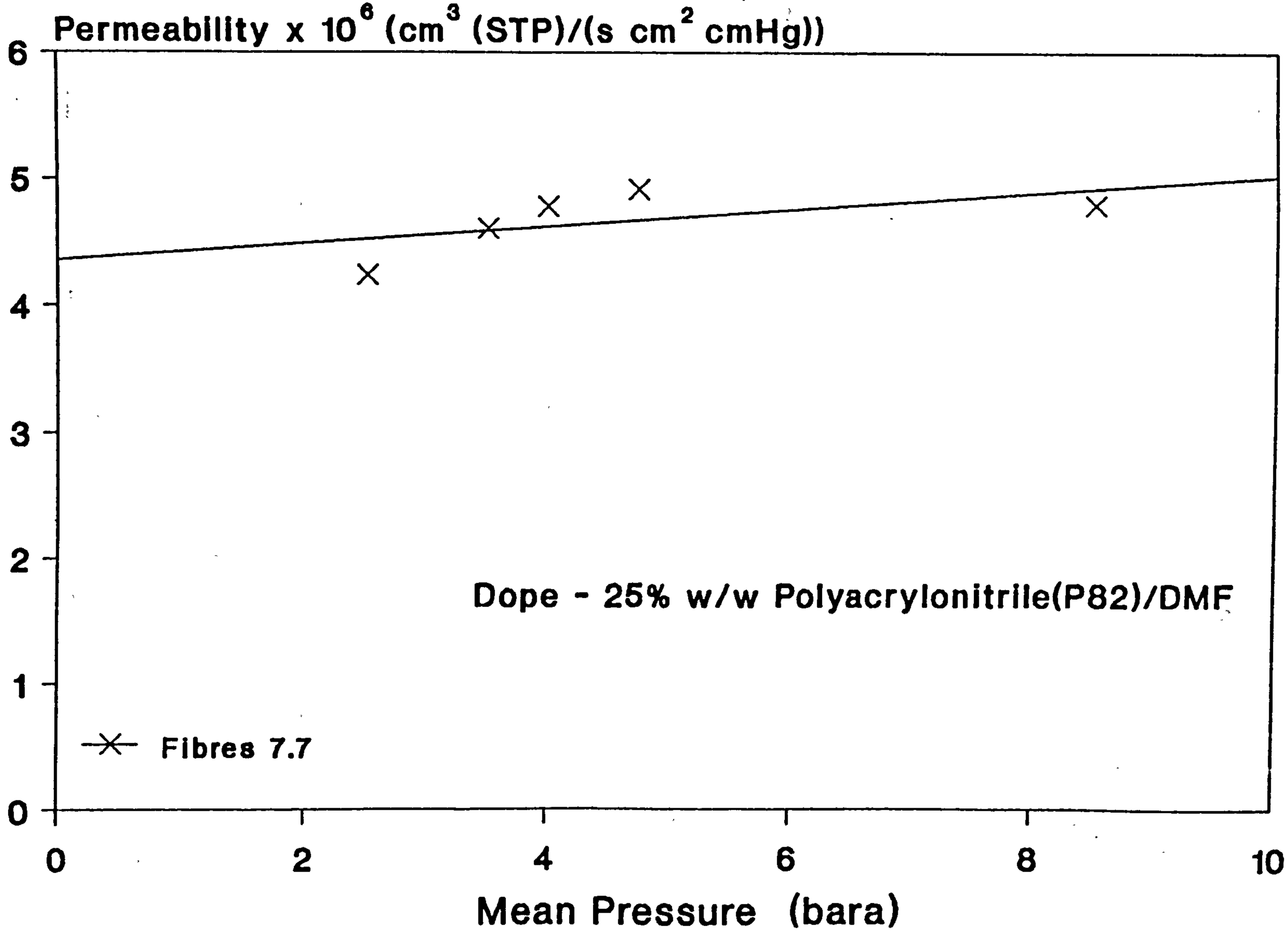

Graph 3.25 Permeability Variation with Pressure
Pure Gases Uncoated Fibres Run 2.2

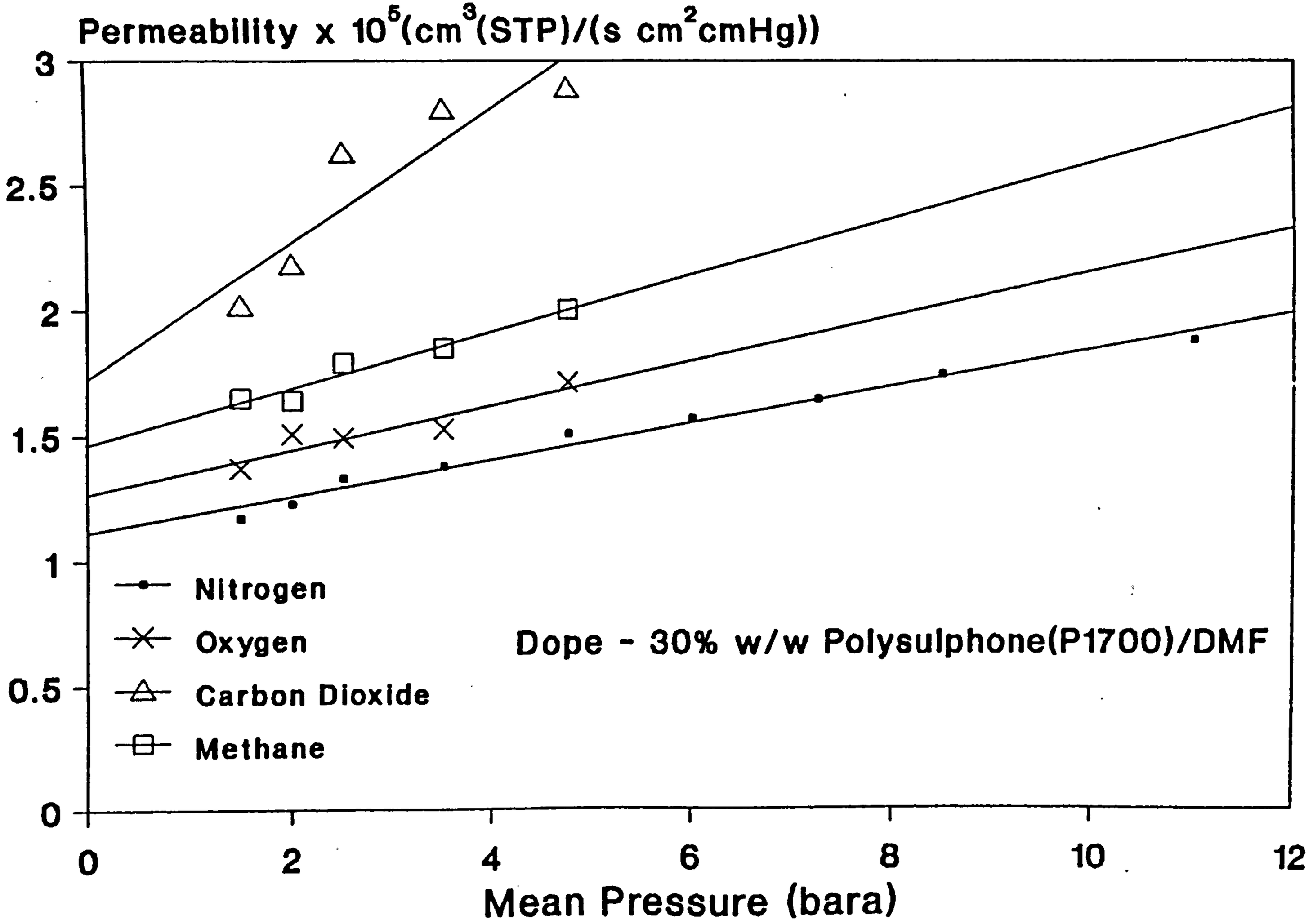

Graph 3.26 Permeability Variation with Pressure
Pure Gases Uncoated Fibres Run 2.4

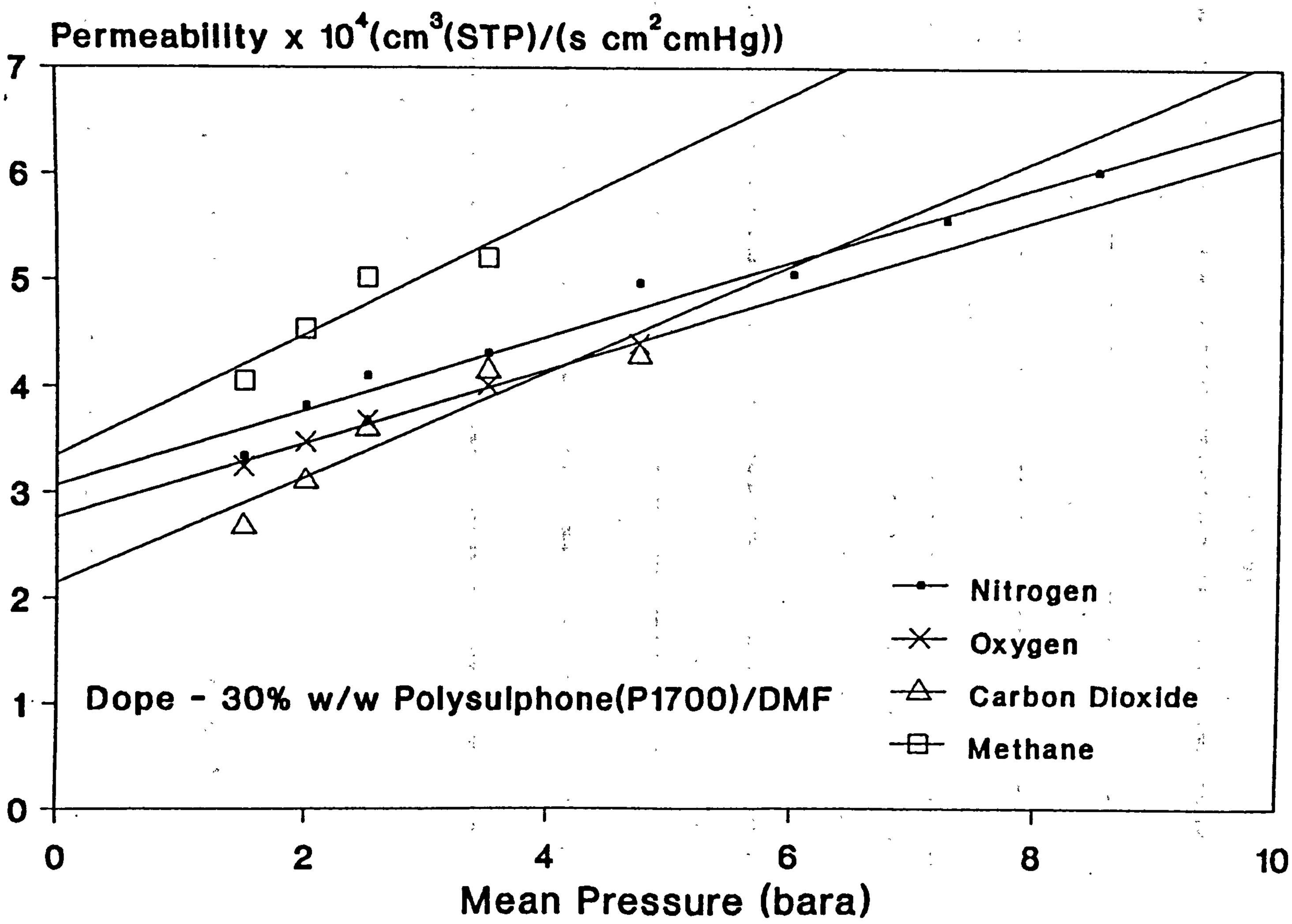

Fibre Run[a]	J.S. (--)	D.E.R. (cm^3/min)	Pore Radius (Ångstrom)	P_{CO_2}	$\Omega_{CH_4}^{CO_2}$
2.1	1.0	0.7	470	0.809	0.81
2.2	0.7	1.0	300	0.230	1.25
2.4	1.5	1.0	525	4.148	0.80
2.5	2.0	1.0	1800	6.369	0.66
2.8	1.0	1.0	610	1.287	0.73
3.1	1.0	0.7	200[b]	0.0097	3.03
3.2	0.7	1.0	260[b]	0.0167	2.42
7.7	1.0	2.5	68	0.0391	0.73

[a] Uncoated fibres

[b] Permeant gas O_2 all other pore sizes based on N_2

P = Permeability x 10^4 $\left(\frac{cm^3(STP)}{s\ cm^2\ cmHg}\right)$ (based on ΔP=5bar)

Ω = Selectivity (based on ΔP=5bar)

Table 3.10 Average Pore Size Data from Permeability Variation with Pressure

The pore size data obtained should be treated cautiously and viewed only as a guide. Solution diffusion terms have been neglected and the ratio of total pore area to pore length is taken to be the same in both the case of Knudsen diffusion and viscous flow. The fact that the two flow types are assumed to occur in pores of the same radius also casts doubt on the integrity of the pore size values. However, the general picture the results portray is clear: pore sizes are appropriate to microporous membranes.

Considering the pore size results for the polysulphone fibres in **Table 3.10**, based on **Graphs 3.22** and **3.23**, it can be seen that permeability decreases and selectivity increases with decreasing pore radius. **Graph 3.25** shows that for the fibres from Run 2.2 carbon dioxide is the fastest permeating gas indicating that solution diffusion is dominant. **Graph 3.26** relating to fibres from Run 2.4 illustrates Knudsen diffusion and viscous flow dominance with methane, the lightest and least viscous gas, having the greatest permeability.

The absolute values of pore size are especially dubious when relating to membranes showing solution diffusion dominance. This applies to fibres from Run 2.2 and in particular to fibres from Campaign 3.

The Campaign 3 fibres, spun from the most concentrated polysulphone dope (40% w/w), were found to have the smallest pore sizes of the polysulphone fibres. This is in association with a marked decrease in permeability and increase in selectivity over the Campaign 2 fibres which were spun from 30% w/w dope. A reduction in pore size with increasing polymer content in the casting solution was also found by Yasuda and Tsai [78].

In theory the value of pore radius should be independent of the permeant gas used in its determination. For a particular microporous membrane dominated by pore flow the Knudsen diffusion permeability term should be inversely proportional to the square root of the molecular weight of the permeating gas. The viscous flow permeability term should vary in inverse proportion to the viscosity of the permeant. These effects are shown in **Graph 3.26.**

The average pore size of the fibres from one polyacrylonitrile spinning run (Run 7.7) has also been included in **Table 3.10** based on the results shown in **Graph 3.24.** Judging by the 40% w/w spun polysulphone results the pore size value and selectivity of the polyacrylonitrile fibres seem small in relation to permeability. The extremely low intrinsic permeability of polyacrylonitrile polymer (thousands of times less than that of polysulphone) accounts for the poor selectivity at relatively low membrane permeabilities. The small pore

size may simply imply that the PAN fibres have a larger number of pores per unit area or smaller pore length (active layer thickness).

As pore size approaches a few hundred Ångstroms Knudsen flow dominates considerably. If pore size is estimated on the basis of the ratio of viscous flow to Knudsen diffusion components then it is possible to seriously underestimate smaller pore sizes due to the lack of gradient of the viscous flow contribution. **Graph 3.24** illustrates this point where the gradient of the permeability mean pressure plot could quite conceivably have been zero or even negative.

Parameters such as total pore area, pore length, number of pores and intrinsic polymer permeability coefficient could be considered using this technique. However, because of the simplifications and assumptions the current analysis is only appropriate for gaining a general indication of pore size.

A serious investigation of membrane structure is carried out in section 5.2 where gas transfer through membranes has been modelled. Concepts mentioned in the above discussion are addressed in earnest. Permeation resistances in series and parallel have been considered for both coated and uncoated hollow fibres. Details of membrane morphology have been deduced and related to spinning conditions.

3.5.4.2 Hollow Fibre Failure Under Pressure

Coated hollow fibre membranes from Campaign 2 (spinning dope - 30% w/w Polysulphone(P1700)/DMF) were tested to failure with nitrogen as the permeant gas. Two regions of failure were identified:

1. At medium pressures - burst or blow through,
   a sudden increase in permeate flowrate is detected.

2. At high pressures - fibre collapse,
   a distinct decrease in permeability occurs, the permeate flowrate levelling off with pressure.

The results of the fibre failure tests are given in **Graph 3.27** and **Table 3.11.**

The significance of such failure tests is not entirely clear. Permeability and hence lumen pressure will affect the differential pressure or stress on the fibre wall. (In these tests however, a simple calculation predicts that lumen pressures will not exceed 0.1 bar and are therefore insignificant.) In the first failure region silicone plugs which block surface pores are perhaps dislodged depending on pore size and shape. The fibre polymer itself may rupture also causing blow through depending on the thickness of the outer active layer or the strength of the highly porous substructure of the membrane wall.

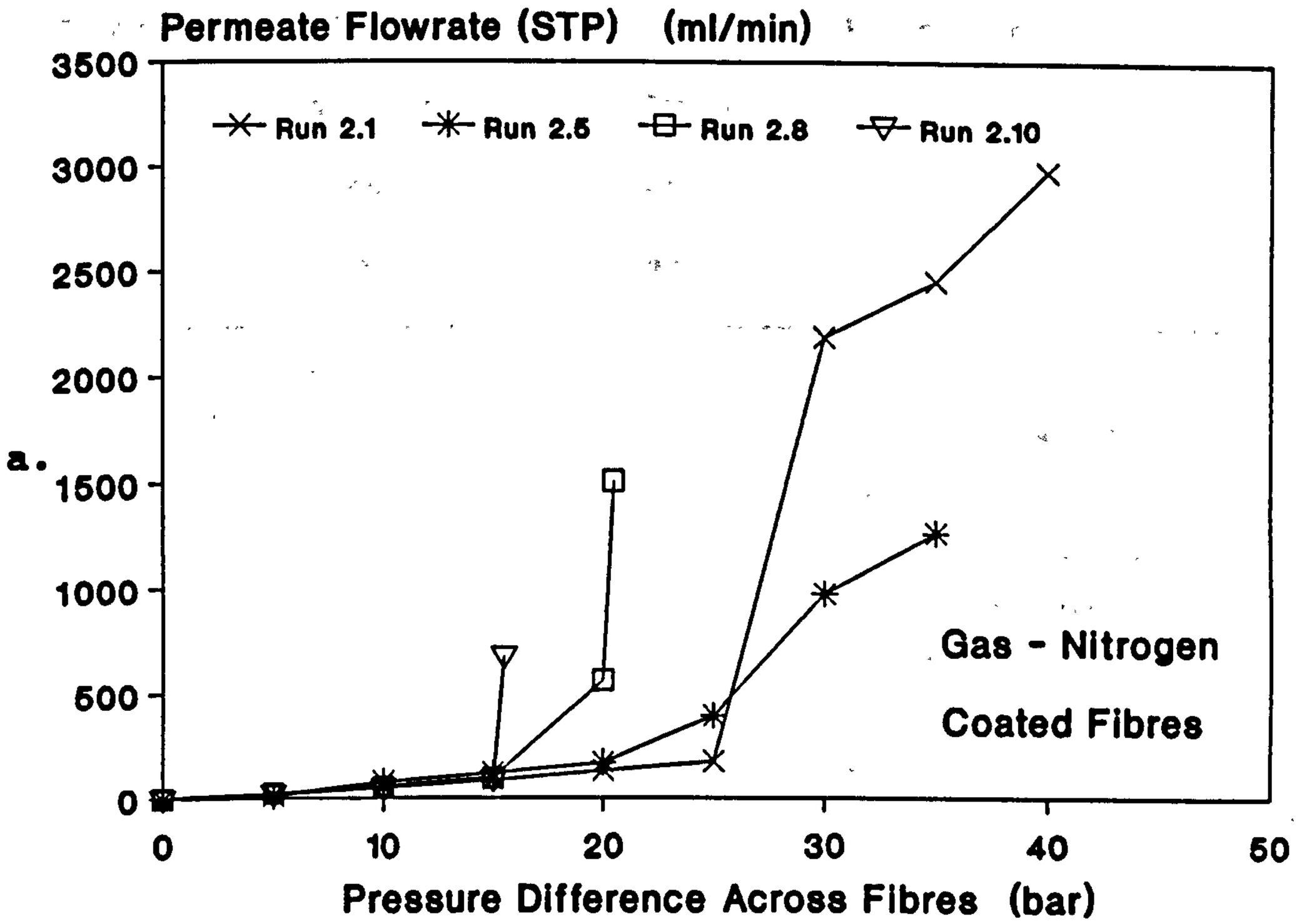

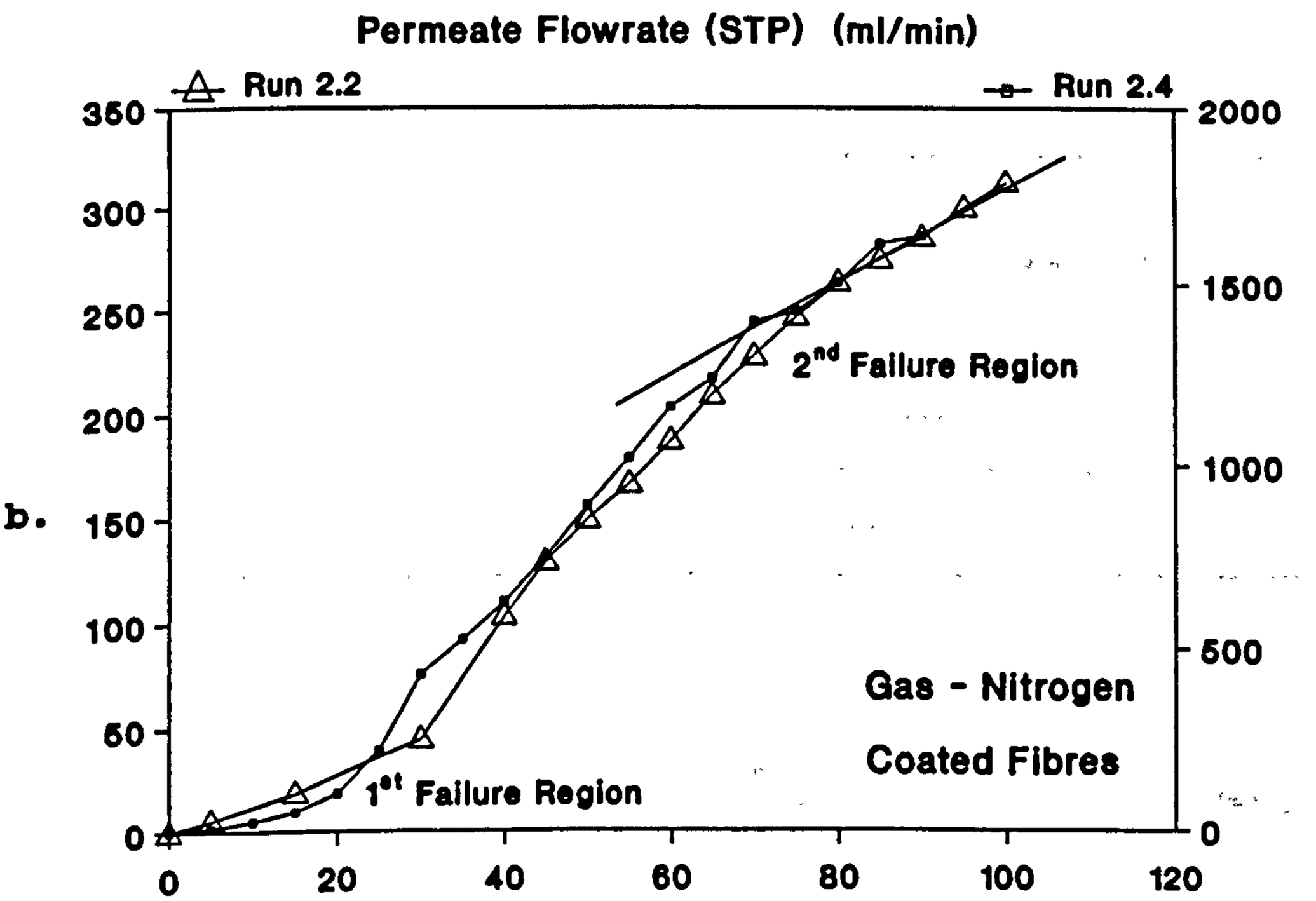

Graph 3.27 Hollow Fibre Failure Under Pressure

Fibre Run[a]	1st Region Failure Pressure (bar)	2nd Region Failure Pressure (bar)	Fibre Module Inspection After Test	P_{N_2}
2.1	25-30		Collapse only partial - fibres still open.	0.260
2.2	30-40	80-85	All fibres collapsed i.e. flattened. No fibre collapse in tube sheet.	0.059
2.4	20-30	70-75	"	0.146
2.5	20-25		"	0.176
2.8	15-20		Collapse only partial - fibres still open.	0.302
2.10	15-20		Collapse only partial - fibres still open.	0.261

[a] Coated fibres

$$P = \text{Permeability} \times 10^4 \left(\frac{cm^3\,(STP)}{s\ cm^2\ cmHg} \right) \quad \text{(based on } \Delta P = 5 \text{bar)}$$

Table 3.11 Hollow Fibre Failure Under Pressure

When the results in **Table 3.11** and **Table 3.10** are viewed together it can be seen that the fibres from spinning runs 2.1, 2.2 and 2.4 have the smallest pore sizes and also withstand the greatest pressures before blow through or bursting occurs. This may be due to increased stability of the silicone plugs in the pores or simply a result of greater fibre strength. It is interesting to note that the fibres from run 2.2 which show the greatest resistance to pressure have the smallest pore size, greatest linear density, greatest tenacity **(Table 3.7)** and probably the lowest porosity (void volume fraction) **(Table 3.5)** of all the fibres tested to failure.

At high pressures the fibres will tend to collapse causing the second failure region which was detected with the least permeable membranes. **Graph 3.27** also indicates that fibre failure may be sudden or progressive.

These tests were carried out with fibres spun exclusively from 30% w/w polysulphone dope. However, judging by fibre properties such as pore size, linear density, tenacity and porosity, it is reasonable to assume that resistance to failure under pressure will increase with increasing spinning dope concentration.

3.5.5 Effect of Time on Gas Permeation

In some of the polysulphone hollow fibre permeation tests involving CO_2 there was evidence of a slight decrease in permeation rate with time. No effect was observed with any of the other gases. Two fibre runs which showed signs of exhibiting this drift were examined in long term permeation tests. The results are shown in **Graph 3.28.** It can be seen that for both fibre types permeability drops by approximately 40% before approaching steady state after 3 hours.

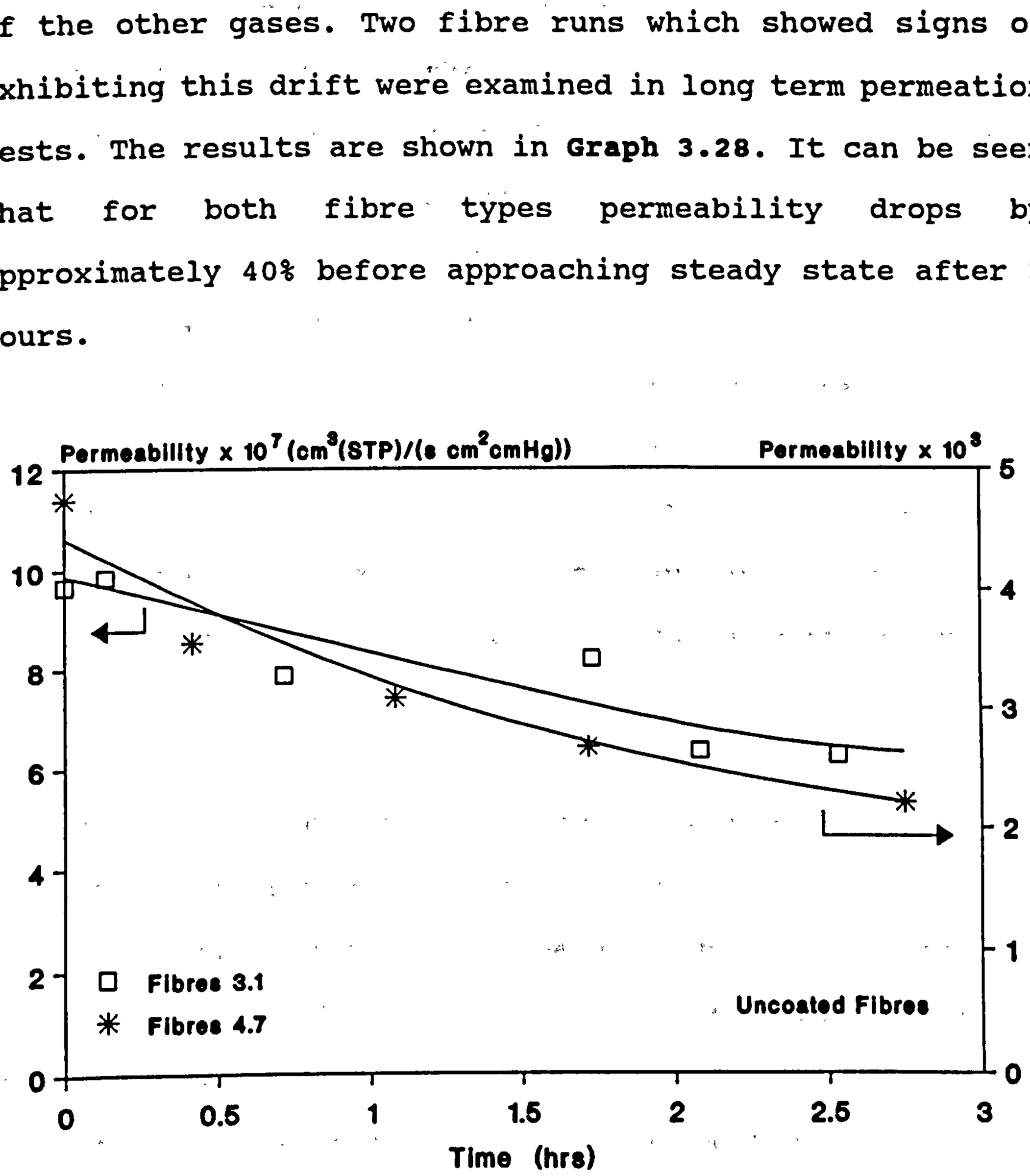

Graph 3.28 Effect of Time on CO_2 Permeability Polysulphone Hollow Fibres

The decrease in permeability was reversible as the fibres regained their original permeability levels after a recovery period of a few days.

This CO_2 time effect is of little concern as the time delay involved in the permeation measurements was negligible (a few minutes) in all of the polysulphone tests but for one scenario: investigations involving gas mixtures and fibres spun from 40% w/w dope. The study of CO_2/CH_4 gas mixture permeation through these low permeability fibres was the only situation at risk of suffering from time effects because of the lengthy equilibration period necessary for the permeant in the automatic gas sampling valve of the gas chromatograph (up to 4 hours). Although permeability was measured immediately, effects may manifest themselves in decreased selectivity values in comparison to pure gas measurements.

There is some evidence of this. Gas mixture CO_2/CH_4 selectivities are lower than those based on pure gases for the two most selective coated fibre batches from Campaign 3 - see Appendix B **Tables B7** and **B8**. However, it must be said that there is no evidence of CO_2/CH_4 selectivity drop in the remaining coated fibres nor in any of the uncoated Campaign 3 fibre measurements - **Tables B5** and **B6**. Nevertheless, due to concern over this potential phenomenon CO_2/CH_4 gas mixture tests involving 40% spun

polysulphone hollow fibres were limited to Campaign 3 and attention directed mainly on pure gas studies for these membrane types.

No time effects were observed with any of the gases in the polyacrylonitrile hollow fibre permeation studies. **Graph 3.29** which shows the influence of time on N_2 permeability for Run 7.7 fibres is entirely typical.

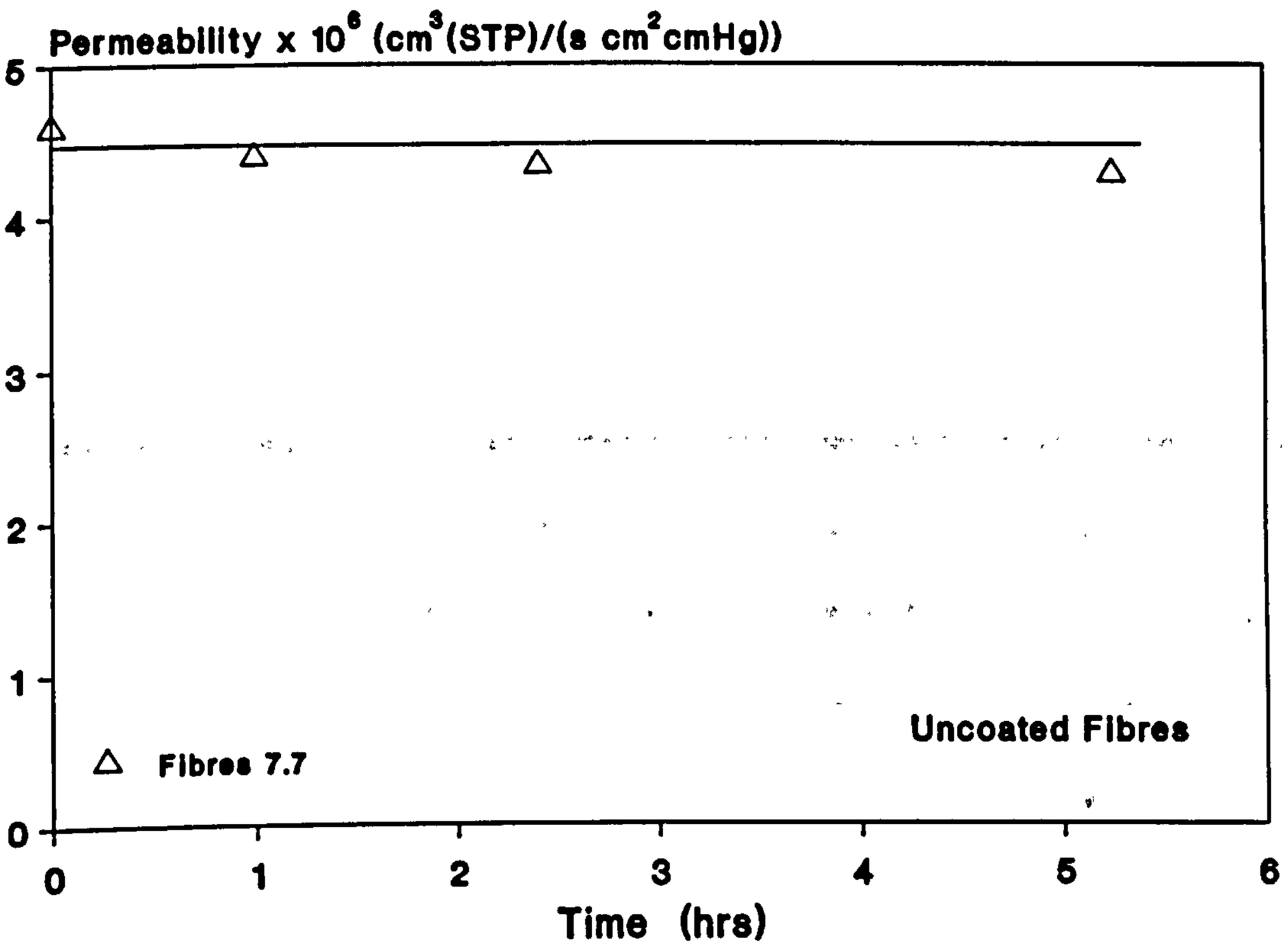

Graph 3.29 Effect of Time on N_2 Permeability Polyacrylonitrile Hollow Fibres

The automatic permeate flowrate measurement system was particularly useful in these tests. Flowrates were automatically recorded by computer.

Chapter 4 Results Relating Spinning Conditions to Hollow Fibre Gas Permeation Performance

The primary objective of this work was to endeavour to understand the science of spinning hollow fibre membranes for gas separation. As explained in section 3.2, key spinning variables were identified to allow the rheological aspects of fibre formation to be considered. The following set of graphs, extracted from the results in Appendices 1 and 2, shows the principal effects of spinning conditions on permeability and selectivity for uncoated and coated fibres.

Initially the effect of polymer concentration in the spinning dope was investigated. The results are shown in **Graphs 4.1** and **4.2**. Values at each dope concentration are based on average data from each spinning campaign. The 40% w/w spun polysulphone fibres, because of their superior separation characteristics in the raw uncoated state, were targeted for studying the effect of jet stretch and dope extrusion rate on fibre performance.

Graphs 4.3 to **4.6** show the influence of jet stretch and dope extrusion rate on hollow fibre gas permeation. The overall trends are based on lines of best fit through the complete data set in any particular graph. Where necessary a distinction has been made between spinning campaigns only in order to confirm the direction of the overall trend. In some cases the individual slopes of the pairs of points from distinct campaigns are steeper than or offset from the overall trend. Gas permeation performance is

sensitive to the slightest alterations in the character of surface pores. The delicate nature of the membrane surface also results in susceptibility to random pinholes or imperfections. Thus subtle alterations in process conditions, practical procedures or handling in spinning, washing, drying, potting-up, coating or gas permeation testing inevitably cause variations in the separation performance of the hollow fibres. In these circumstances the data sets from the separate campaigns are encouraging because they consistently confirm the direction of the overall trends but their individual gradients and positions which are based on only two data points should be viewed cautiously.

It was necessary to define a discrete overall trend line in order to extract data for the gas permeation modelling work. The effect of the various spinning conditions on fine details of fibre structure are deduced in the light of the gas permeation trends.

Graphs 4.3a and **4.3b** show that permeability increases with increasing dope extrusion rate for both uncoated and coated fibres. Not surprisingly selectivity decreases with increasing dope extrusion rate for uncoated membranes as shown in **Graph 4.4a**. However, the result for the coated fibres is striking. It can be seen from **Graph 4.4b** that selectivity actually increases with increasing dope extrusion rate once the membranes have been coated.

Coating takes care of fibre imperfections or surface pores and allows the intrinsic separating properties of the membrane polymer itself to dominate.

Graphs 4.5a and **4.5b** show that permeability increases with increasing jet stretch for both uncoated and coated fibres. It is evident from **Graphs 4.6a** and **4.6b** that increasing jet stretch results in decreasing selectivity for coated as well as uncoated fibres.

Graphs 4.7 and **4.8** show the effect of spinning conditions on the gas permeation performance of fibres spun from the most concentrated polyacrylonitrile dope. No correlation involving jet stretch or dope extrusion rate was found. As a consequence the permeability and selectivity results for the polyacrylonitrile fibres have been given as bar charts. The conditions of each spinning run are included at the base of each bar set. As explained in section 3.5.3 a distinction has been made between the two coating strengths. **Graph 4.8** shows that selectivity is consistent and poor for these fibres. Even the lowest permeability fibres (the lowest permeabilities of all the fibres in this work) shown in **Graph 4.7**, exhibit no significant superiority over the other polyacrylonitrile fibres in terms of selectivity.

Graph 4.1 *Effect of Dope Concentration on Permeability*
Polysulphone Fibres

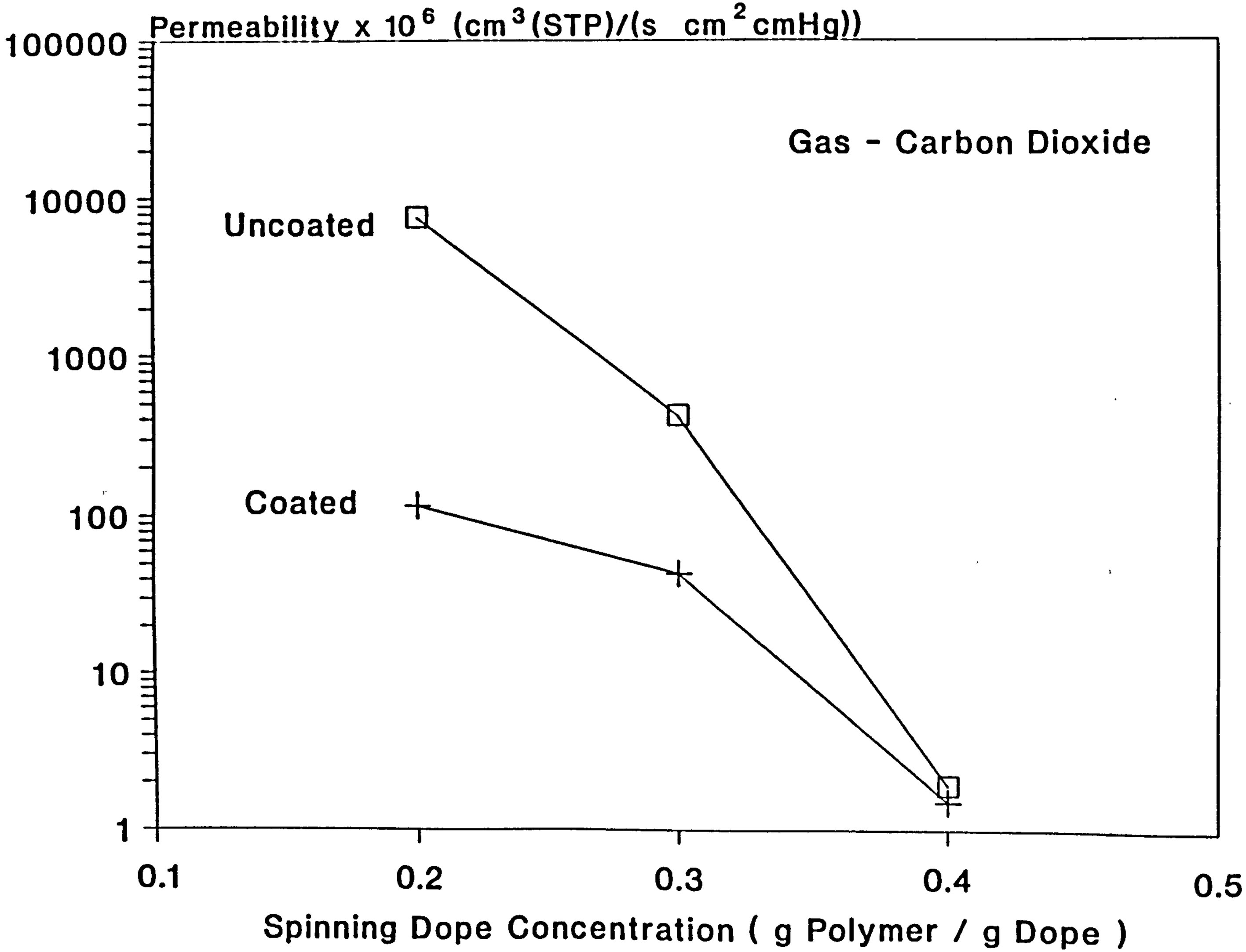

Graph 4.2 Effect of Dope Concentration on Selectivity
Polysulphone Fibres

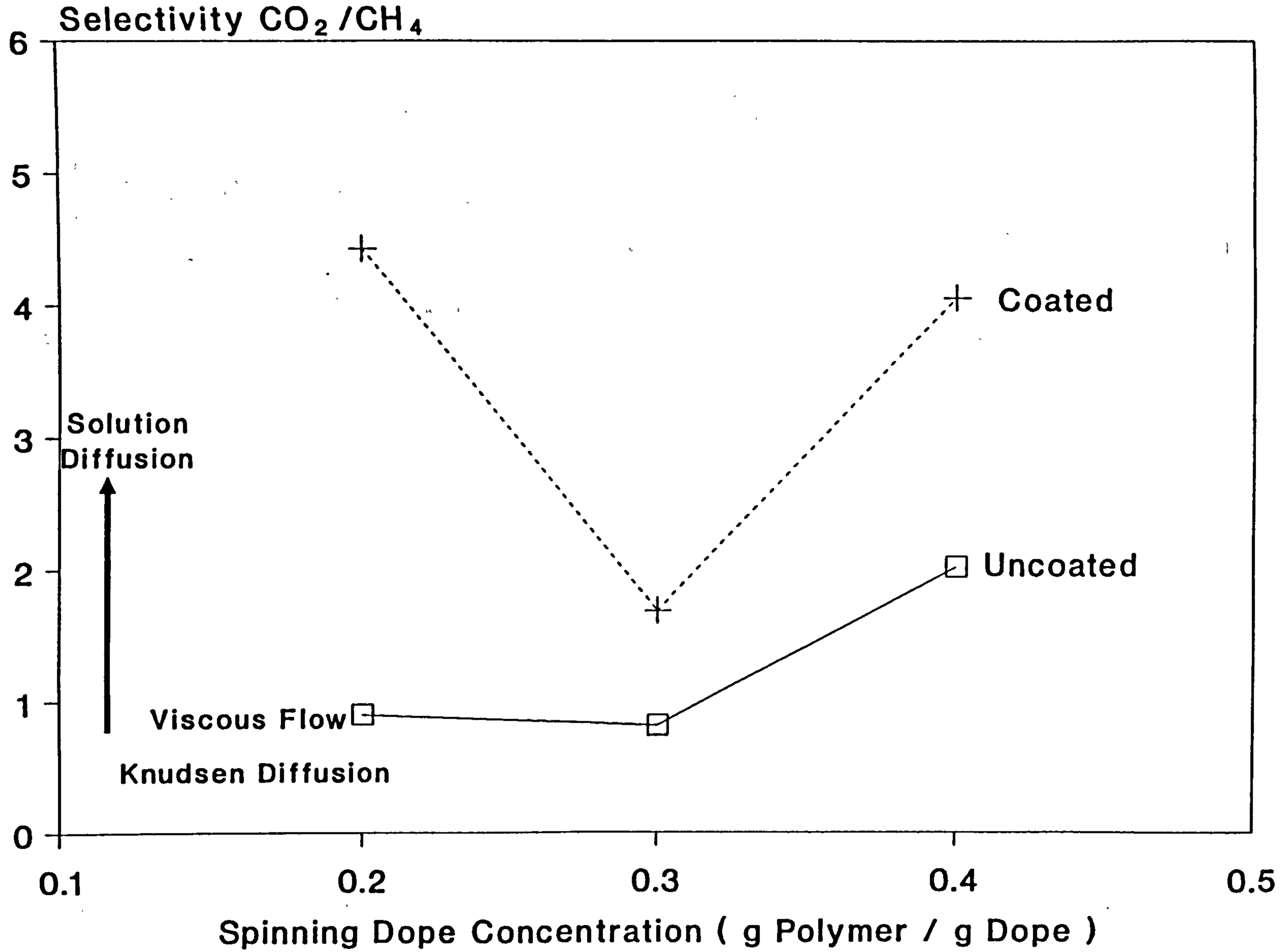

Graph 4.3a Effect of Dope Extrusion Rate on Permeability Uncoated Polysulphone Fibres

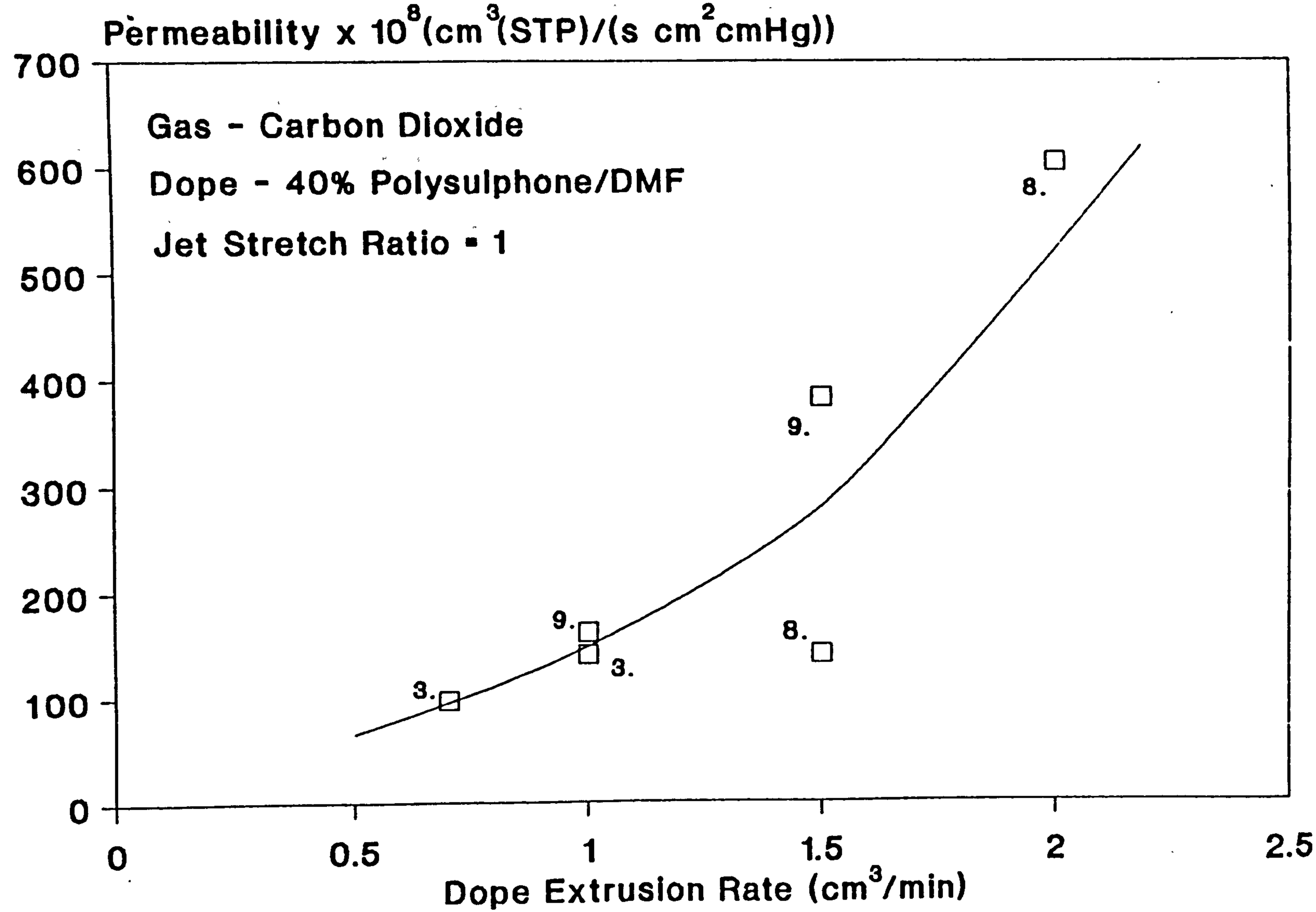

Graph 4.3b Effect of Dope Extrusion Rate on Permeability
Coated Polysulphone Fibres

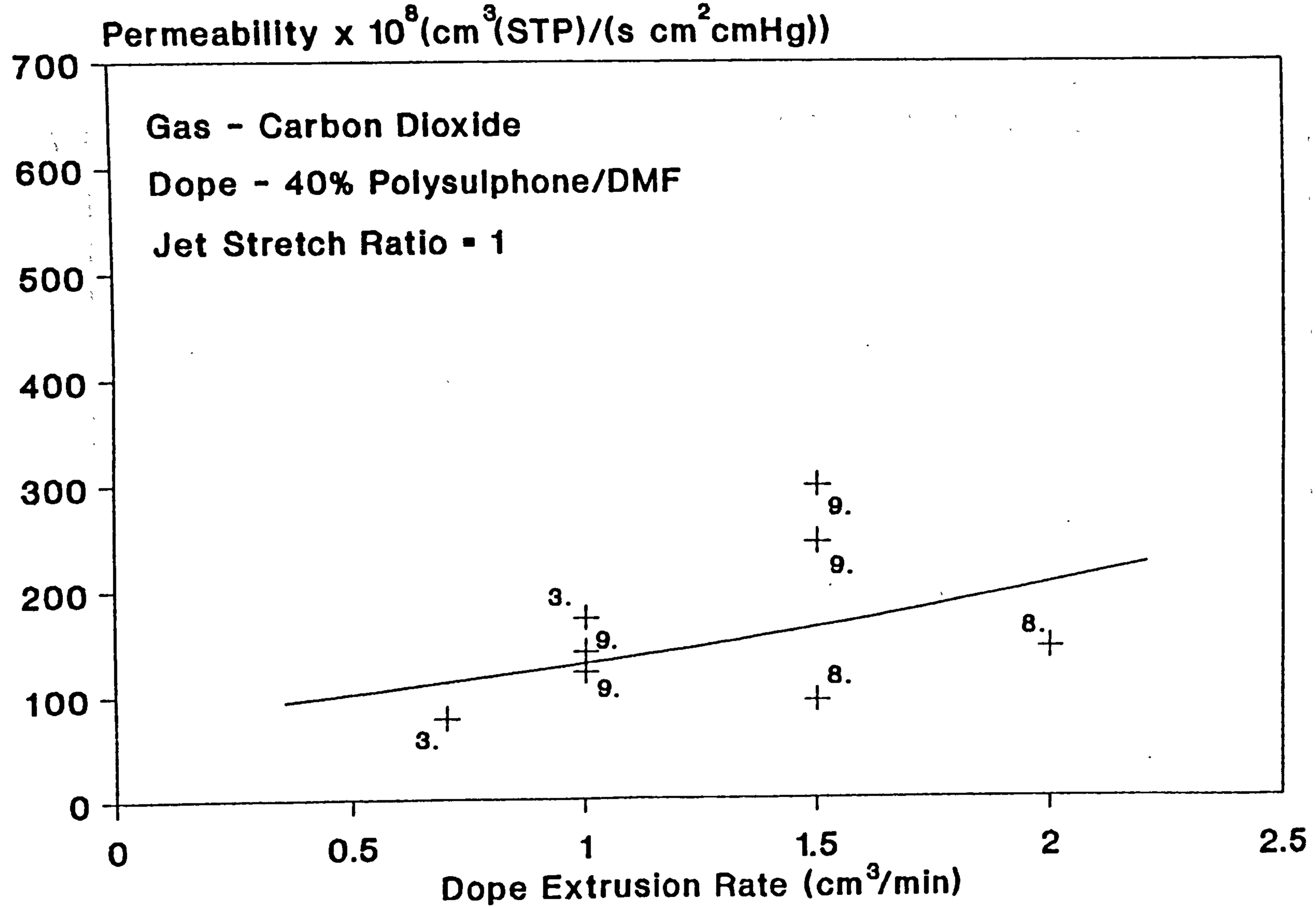

Graph 4.4a Effect of Dope Extrusion Rate on Selectivity
Uncoated Polysulphone Fibres

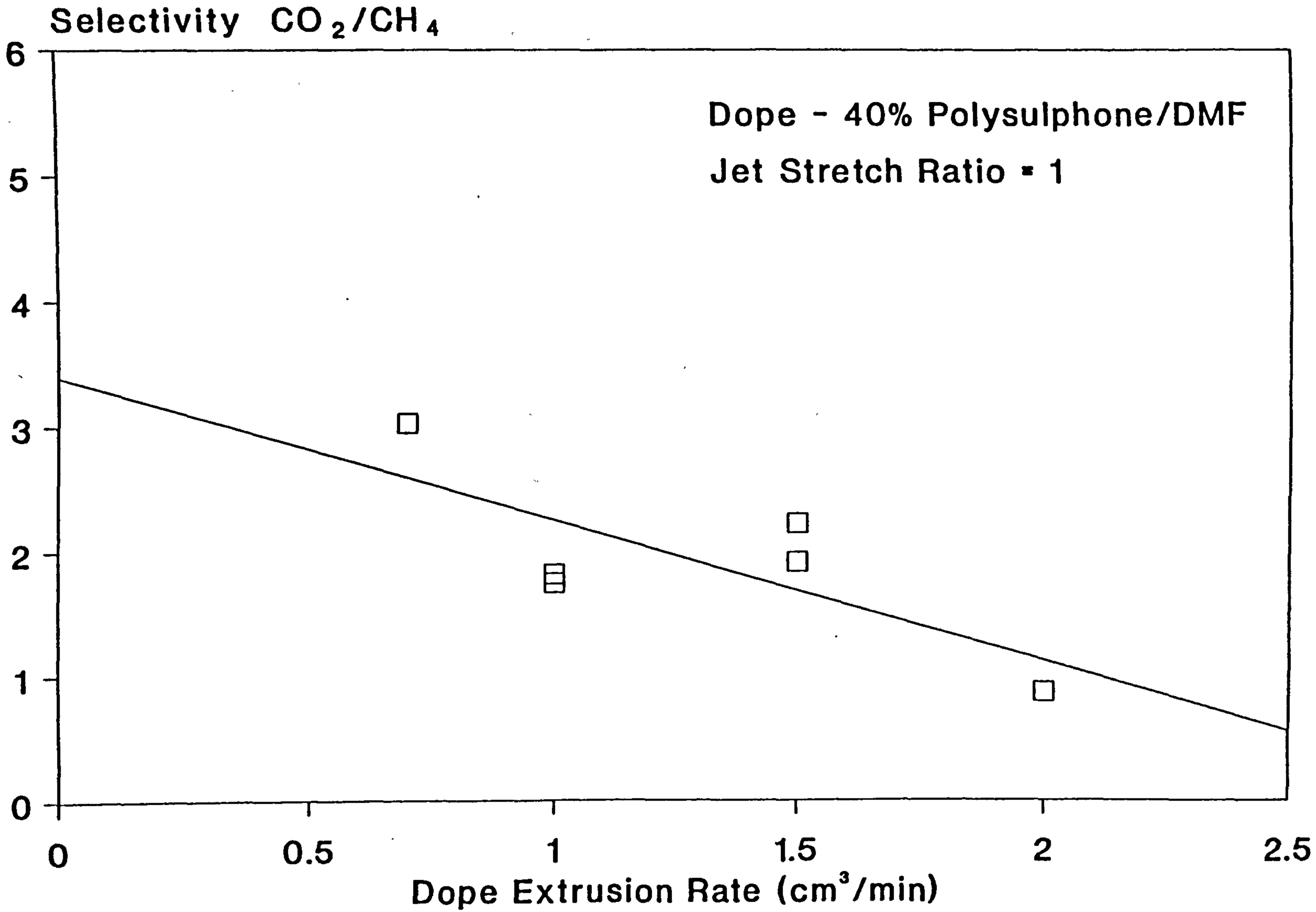

Graph 4.4b Effect of Dope Extrusion Rate on Selectivity Coated Polysulphone Fibres

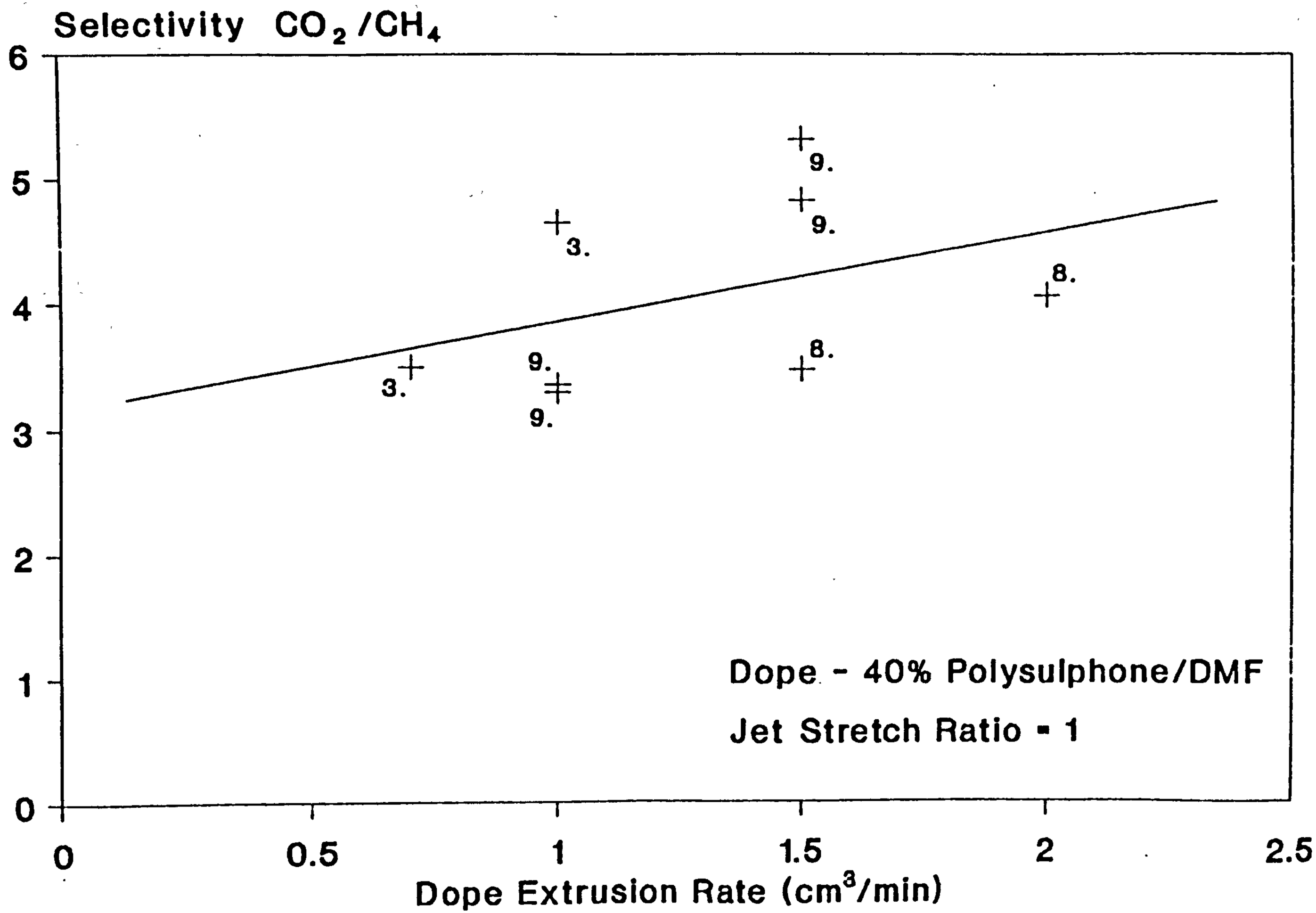

Graph 4.5a Effect of Jet Stretch on Permeability
Uncoated Polysulphone Fibres

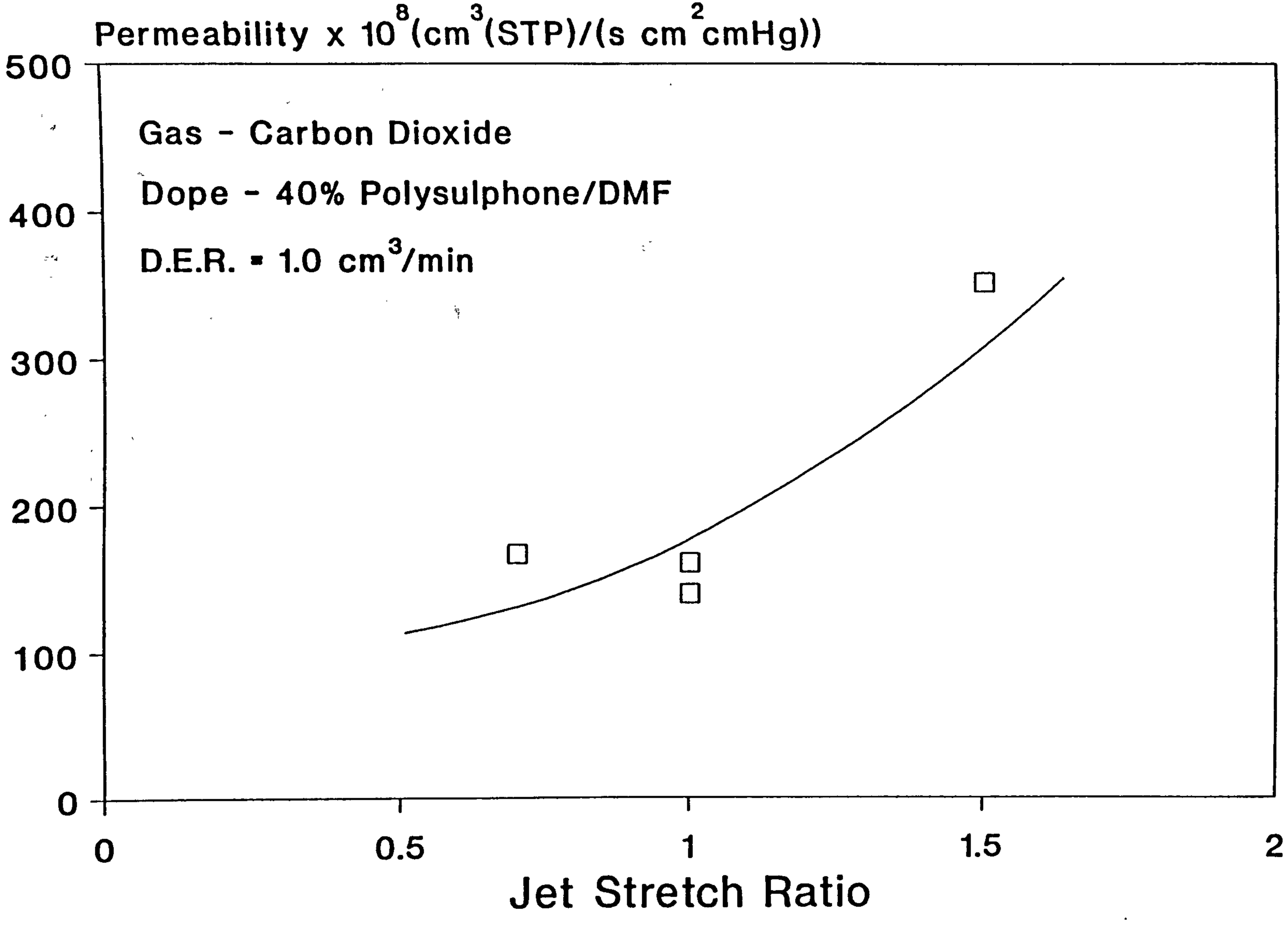

Graph 4.5b Effect of Jet Stretch on Permeability
Coated Polysulphone Fibres

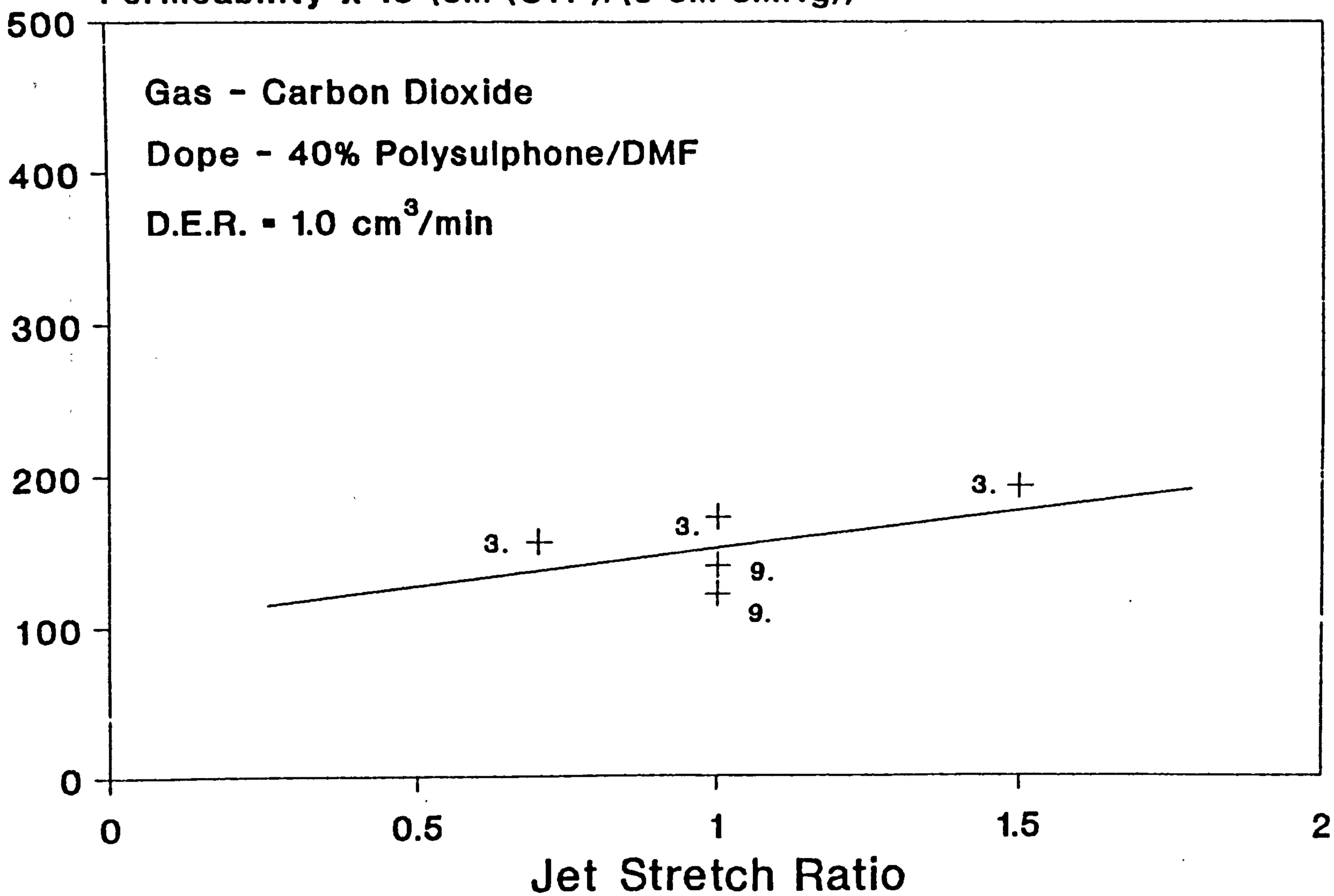

Graph 4.6a Effect of Jet Stretch on Selectivity
Uncoated Polysulphone Fibres

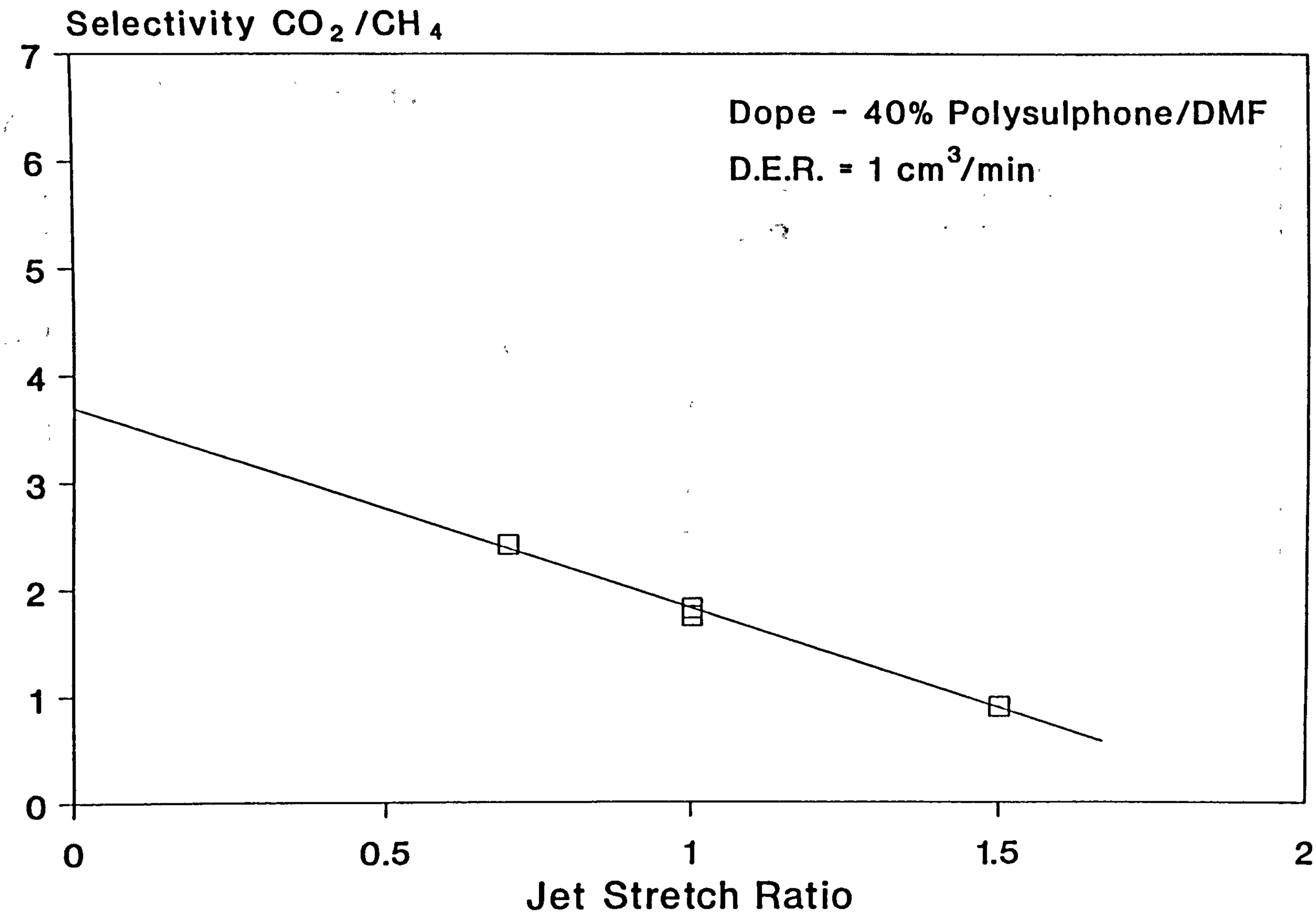

Graph 4.6b Effect of Jet Stretch on Selectivity Coated Polysulphone Fibres

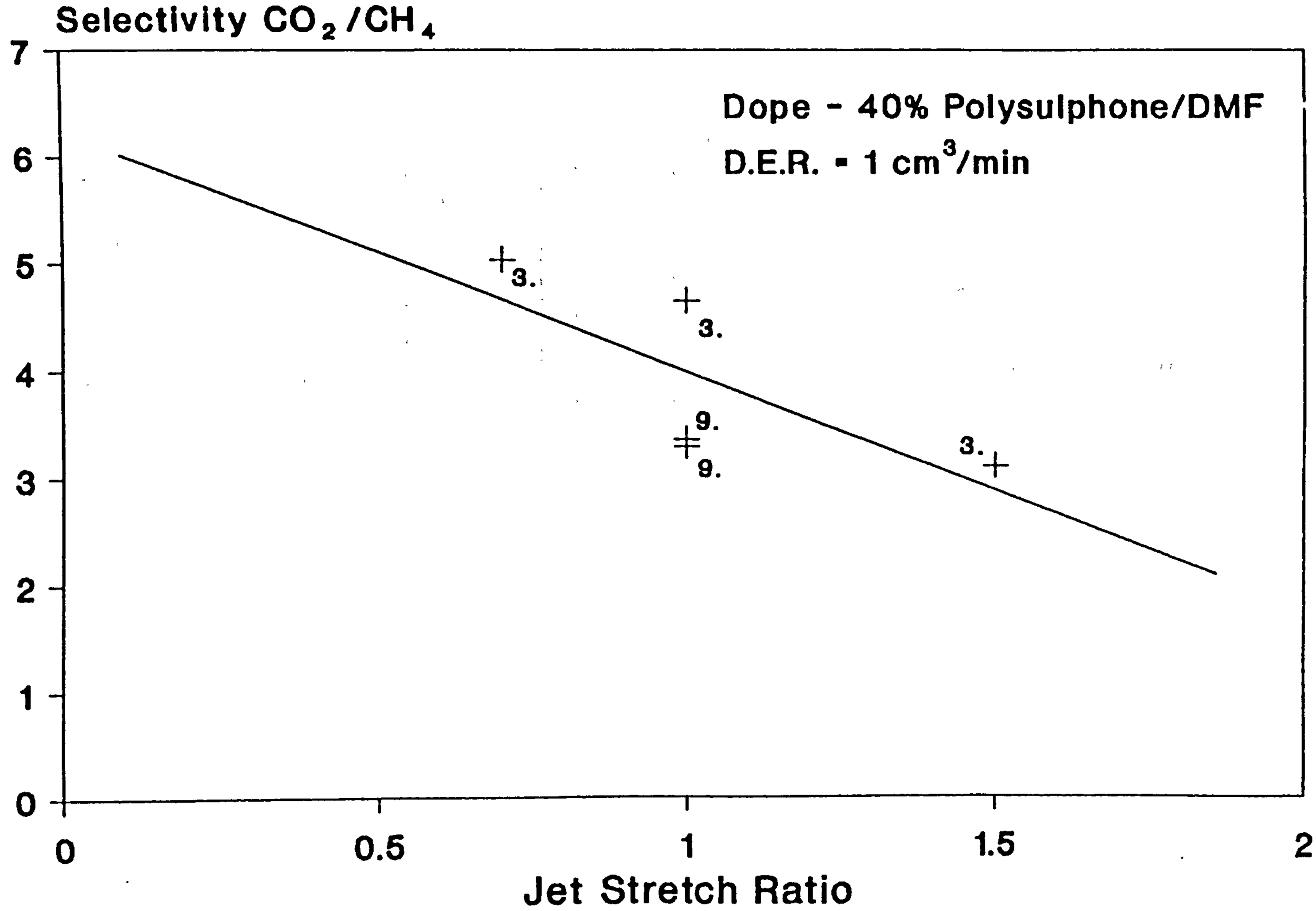

Graph 4.7 Effect of Spinning Conditions on Permeability Polyacrylonitrile Fibres

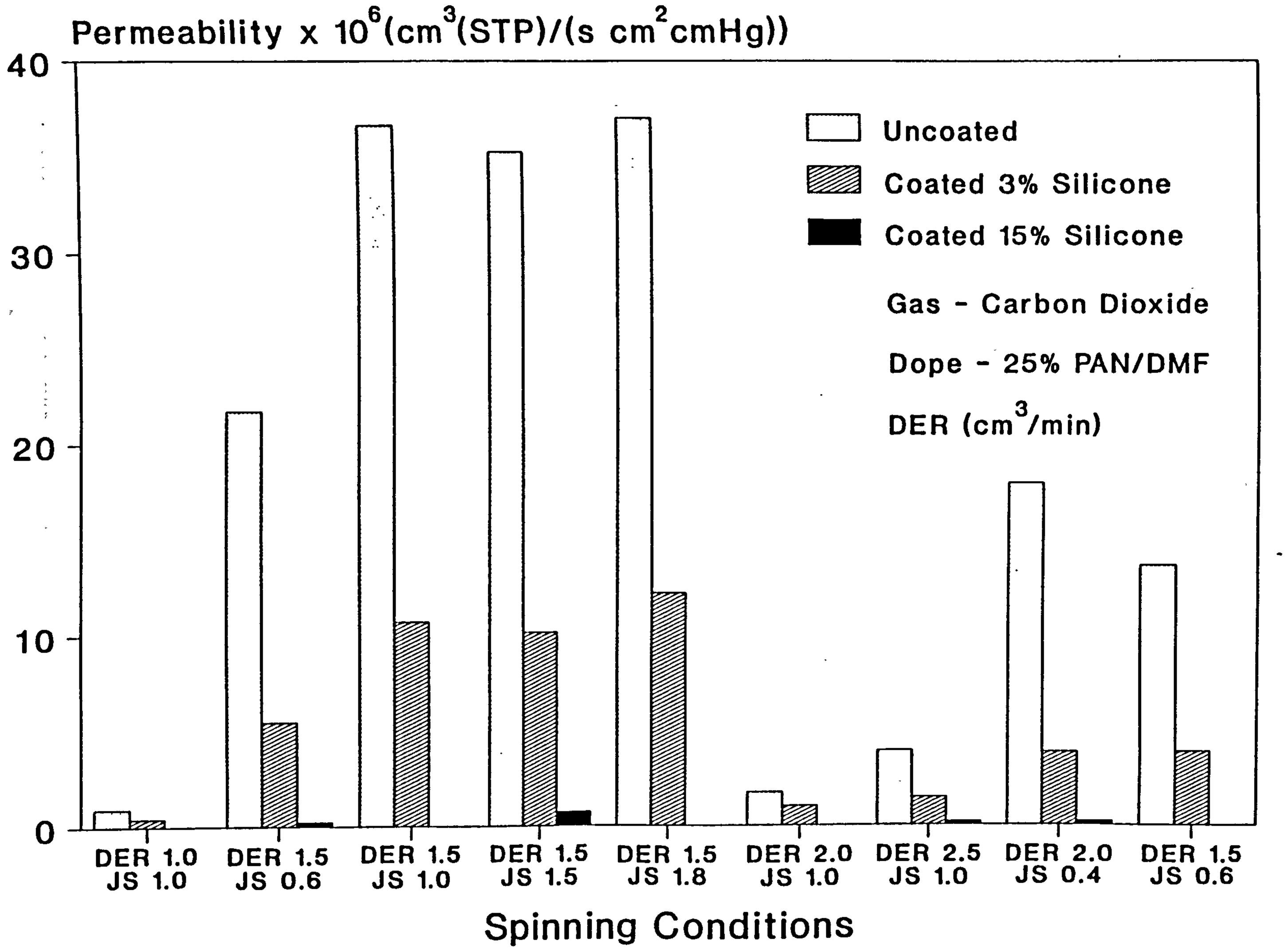

Graph 4.8 Effect of Spinning Conditions on Selectivity
Polyacrylonitrile Fibres

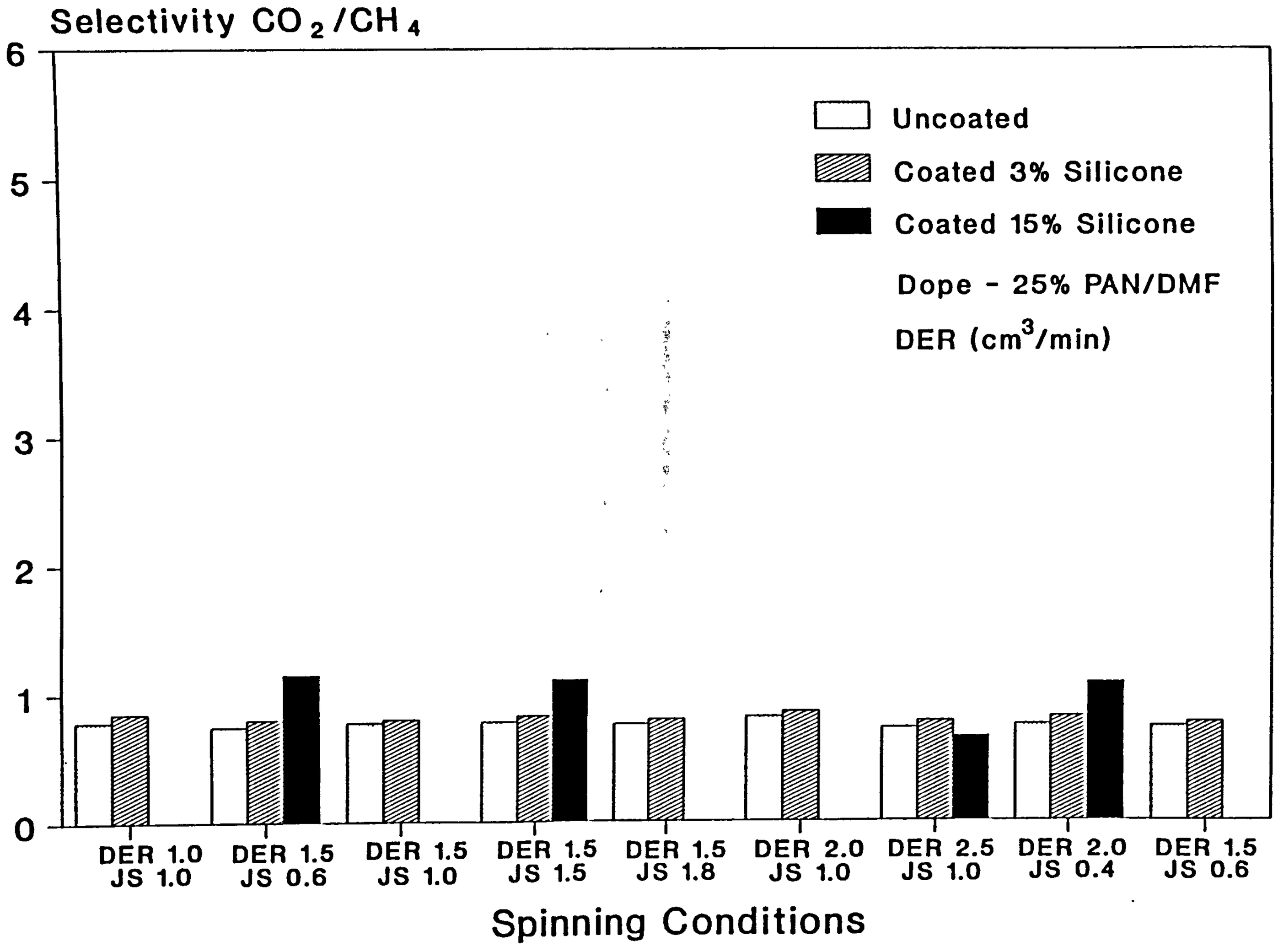

Chapter 5 Modelling

5.1 Rheological Modelling of Extrusion Through Spinneret

5.1.1 Basic Flow Equations by Force Balance

The flow in the spinneret during fibre spinning is always laminar. A Reynolds number of 0.5 is typical. All of the material presented here is based on laminar flow.

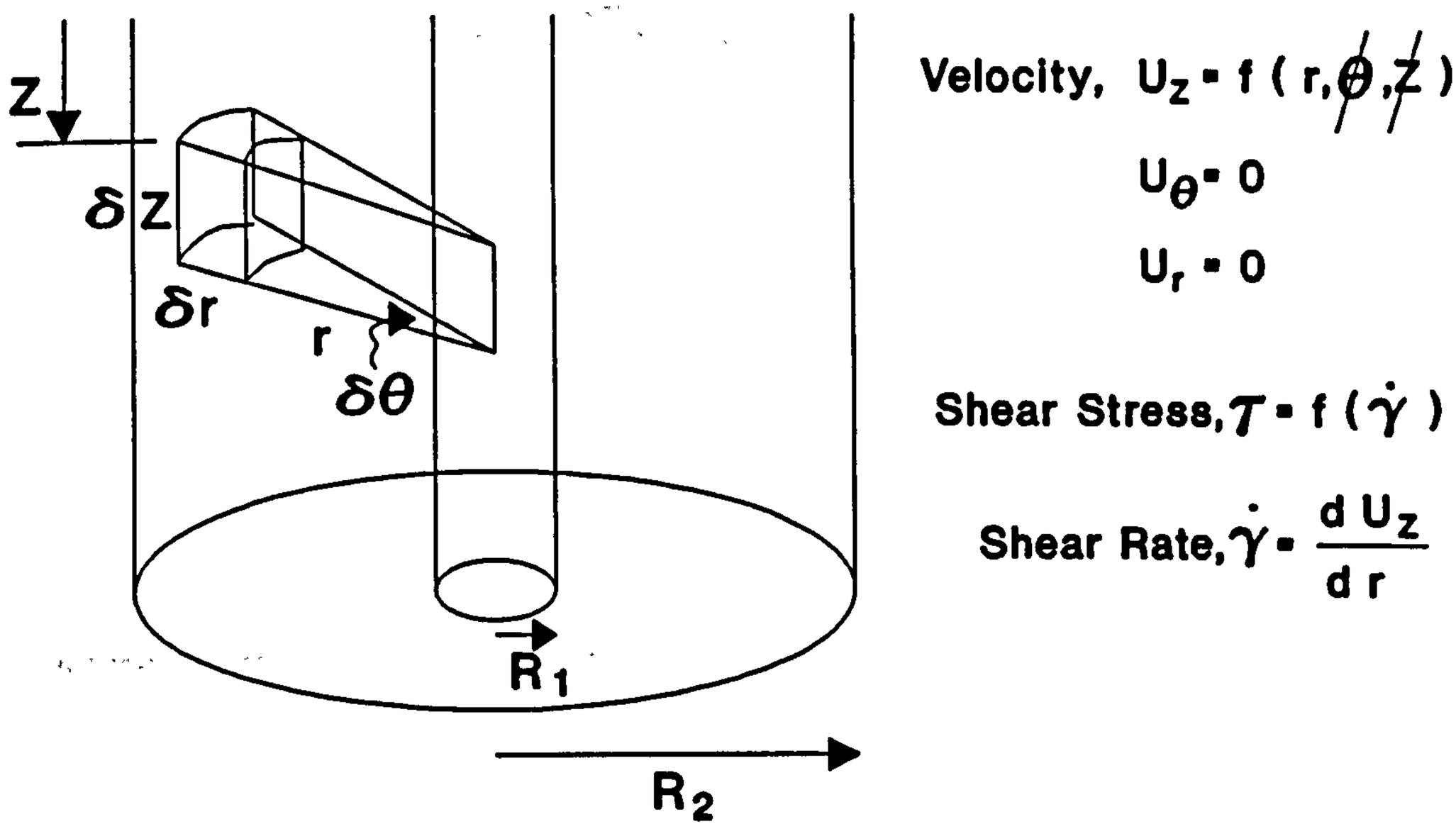

Figure 5.1 Element of Fluid in Spinneret Annulus

Force Balance Over Element in Z Direction (Figure 5.1)

Viscous Forces + Pressure Forces + Body Forces = 0

$$\therefore -\tau\Big|_{r} r\delta\theta\delta Z + \tau\Big|_{r+\delta r} (r+\delta r)\delta\theta\delta Z$$

$$+ P\Big|_{Z} r\delta\theta\delta r - P\Big|_{Z+\delta Z} r\delta\theta\delta r + \rho g r\delta\theta\delta r\delta Z = 0$$

$$\therefore -\tau\Big|_r r\delta\theta\delta Z + (\tau\Big|_r + \frac{d\tau}{dr}\delta r)(r+\delta r)\delta\theta\delta Z$$

$$+ P\Big|_Z r\delta\theta\delta r - (P\Big|_Z + \frac{dP}{dZ}\delta Z) r\delta\theta\delta r + \rho g r\delta\theta\delta r\delta Z = 0$$

multiplying out and removing negligible terms gives

$$\tau + \frac{d\tau}{dr}r - \frac{dP}{dZ}r + \rho g r = 0$$

$$\therefore \frac{d(r\tau)}{dr} = r(\frac{dP}{dZ} - \rho g) \qquad \text{----------} \quad 5.1$$

integrating w.r.t. r gives

$$\tau = \frac{r}{2}(\frac{dP}{dZ} - \rho g) + \frac{K_1}{r} \qquad \text{----------} \quad 5.2$$

where K_1 = Constant

Equation 5.2 is a general expression from which flow conditions for particular circumstances are derived.

For a Newtonian fluid, $\tau = \eta \frac{dU_z}{dr}$

where η = Const = Viscosity.

For a power law fluid, $\tau = K(\frac{dU_z}{dr})^n$

where K and n are power law constants.

In the case of a plain circular pipe,

$\tau = 0$ at $r = 0$ thus $K_1 = 0$

$U_Z = 0$ at $r = R$,

flow conditions can be analytically derived for both Newtonian and power law fluids.

In the case of a concentric annulus i.e. the spinneret,

r at $\tau = 0$ is not obvious and $K_1 \neq 0$

$U_Z = 0$ at $r = R_1$

$U_Z = 0$ at $r = R_2$,

flow conditions can be analytically derived only for Newtonian fluids giving

$$\frac{dP}{dZ} = \left(\frac{8Q\,\eta}{\pi} \frac{1}{\frac{(R_2^2-R_1^2)^2}{\ln(\frac{R_2}{R_1})} - (R_2^4-R_1^4)} \right) + \rho g \quad \text{---------- 5.3}$$

where Q = Volumetric flowrate

$$U_z = \frac{2Q}{\pi} \frac{\frac{(R_2^2-R_1^2)\ln(\frac{R_2}{r})}{\ln(\frac{R_2}{R_1})} - (R_2^2-r^2)}{\frac{(R_2^2-R_1^2)^2}{\ln(\frac{R_2}{R_1})} - (R_2^4-R_1^4)} \quad \text{---------- 5.4}$$

$$\dot{\gamma} = \left(\frac{8Q}{\pi} \frac{1}{\frac{(R_2^2-R_1^2)^2}{\ln(\frac{R_2}{R_1})} - (R_2^4-R_1^4)} \right) \left(\frac{r}{2} + \frac{(R_2^2-R_1^2)}{4r\ln(\frac{R_1}{R_2})} \right) \quad \text{---- 5.5}$$

and $$\tau = \eta\,\dot{\gamma} \quad \text{---------- 5.6}$$

Equation 5.5 can be used to give an initial estimation of the shear rates occuring during spinning. The equation shows that typically shear rates of up to 10,000 s^{-1} are experienced. The investigation of the spinning dopes under shear using the Carri-Med rheometer (section 3.3.2) must therefore cover this shear rate range. The rheological measurements showed that the dopes behaved as power law fluids **(Table 3.2)**. Thus the problem of flow of a power law fluid through a concentric annulus must be solved if the actual extrusion conditions during the spinning runs are to be determined.

The equations of flow relating to a power law fluid through an annulus cannot be derived analytically. The problem has been addressed by a number of workers[79][80]. Hanks and Larsen[81] in 1979 were the first to present a full non-empirical solution valid for all values of the flow behaviour index n (not just reciprocal integers as in previous cases).

The following section describes the solution to this flow problem. Principles elucidated by Hanks and Larsen proved very helpful. A fairly sophisticated computer program was written in order to solve the flow equations and give the conditions in the spinneret during extrusion. The computer program employs a trial and error solution involving numerical integration.

5.1.2 Flow of a Power Law Fluid in a Concentric Annulus

The basic flow equation has been derived

$$\tau = \frac{r}{2}\left(\frac{dP}{dZ}-\rho g\right) + \frac{K_1}{r} \qquad \text{----------} \quad 5.2$$

The constant K_1 can be represented by defining r_o as the radius at which $\tau = 0$ thus

$$K_1 = -\frac{r_o^2}{2}\left(\frac{dP}{dZ}-\rho g\right)$$

and

$$\tau = \frac{1}{2}\left(\frac{dP}{dZ}-\rho g\right)\left(r-\frac{r_o^2}{r}\right) \qquad \text{----------} \quad 5.7$$

For a power law fluid

$$\tau = K\dot{\gamma}^{n} = k\left(\frac{dU_z}{dr}\right)^{n} \qquad \text{----------} \quad 5.8$$

Combining equations 5.7 and 5.8

$$dU_z = \left(\frac{1}{2K}\left\{\frac{dP}{dZ}-\rho g\right\}\left\{r-\frac{r_o^2}{r}\right\}\right)^{\frac{1}{n}} dr \qquad \text{----------} \quad 5.9$$

Normalising equation 5.9 w.r.t. R_2 and collecting constants

$$dU_z = K_2 \left(\frac{\lambda^2}{\xi} - \xi\right)^{\frac{1}{n}} d\xi \qquad \text{---------- 5.10}$$

where $\xi = \frac{r}{R_2}$,

$$\lambda = \frac{r_o}{R_2}$$

and $K_2 = R_2 \left(\frac{R_2}{2K}\{\rho g - \frac{dP}{dZ}\}\right)^{\frac{1}{n}}$ ---------- 5.11

From equation 5.10

defining the standardised velocity, $u_z = \frac{U_z}{K_2}$ ----- 5.12,

defining the aspect ratio of the annulus, $\sigma = \frac{R_1}{R_2}$

and using the boundary condition $u_z = 0$ at $\xi = \sigma$

$$u_z\Big|_\xi = \int_\sigma^\xi \left(\frac{\lambda^2}{\xi} - \xi\right)^{\frac{1}{n}} d\xi \qquad \sigma \le \xi \le \lambda \qquad \text{---------- 5.13}$$

From equation 5.10

using the boundary condition $u_z = 0$ at $\xi = 1$

$$u_z\Big|_\xi = \int_\xi^1 (\xi - \frac{\lambda^2}{\xi})^{\frac{1}{n}} d\xi \qquad \lambda \leq \xi \leq 1 \qquad \text{---------- 5.14}$$

Combining equations 5.13 and 5.14 gives the following expression which is solved numerically for λ by trial and error.

$$\int_\sigma^\lambda (\frac{\lambda^2}{\xi} - \xi)^{\frac{1}{n}} d\xi - \int_\lambda^1 (\xi - \frac{\lambda^2}{\xi})^{\frac{1}{n}} d\xi = 0 \qquad \text{---------- 5.15}$$

Evaluating λ which represents the radius at which $\tau = 0$ is the crux of the problem. Once λ is found the flow conditions are easily determined.

The standardised velocity profile in the annulus is evaluated numerically from equations 5.13 and 5.14.

Using the velocity profile data the standardised volumetric flowrate, q can in turn be numerically determined since

$$q = \int_0^1 \xi \; u_z\Big|_\xi \; d\xi \qquad \text{----------} \quad 5.16$$

(c.f. $Q = 2\pi \int_{R_1}^{R_2} r \; U_z \; dr$)

The actual volumetric flowrate through the annulus is given by

$$Q = 2\pi \; R_2^2 \; K_2 \; q \qquad \text{----------} \quad 5.17$$

K_2 can be evaluated for any particular volumetric flowrate from equation 5.17. The pressure drop through the annulus is then calculated from equation 5.11.

The actual velocity profile is determined from equation 5.12 and the shear stress profile from equation 5.7. Finally, the shear rate profile is evaluated from equation 5.8.

5.1.3 Flow Conditions in the Spinneret

A computer program was written to carry out the procedure described in the previous section. Appendix D contains a listing of the program and the program itself is included for demonstration purposes.

Input to Program :

Inner Radius of Annulus

Outer Radius of Annulus

Length of Annulus

Dope Power Law Index

Dope Power Law Constant

Density of Dope

Dope Extrusion Rate i.e. Volumetric Flowrate

Output from Program :

Radius at Zero Stress and Corresponding Maximum Velocity

Pressure Drop Across Spinneret

Velocity Profile

Shear Stress Profile

Shear Rate Profile

Flow conditions in the spinneret during the spinning runs were evaluated. **Table 5.1** shows a typical data file produced by the program.

The main results provided by the extrusion model are presented in **Graphs 5.1 to 5.8.**

Inner Radius of Annulus .165 (mm)
Outer Radius of Annulus .3 (mm)
Spinneret Length 1.25 (mm)
Power Law Index .584 (--)
Power Law Constant 508 (Based on SI units)
Dope Density 1 (g/cm3)
Dope Extrusion Rate 1 (cm3/min)

Radius at Zero Stress 0.2278 (mm)
Maximum Velocity 11.6246 (cm/s)

Pressure Drop Across Spinneret 12.9629 (bar)

Radius (mm)	Velocity (cm/s)	S.Stress (N/m2)	S.Rate (1/s)
0.1650	0.0000	77569	5488
0.1677	1.4165	73543	5009
0.1704	2.7076	69600	4558
0.1731	3.8804	65736	4134
0.1758	4.9420	61948	3734
0.1785	5.8991	58232	3359
0.1812	6.7579	54585	3007
0.1839	7.5247	51004	2677
0.1866	8.2054	47487	2369
0.1893	8.8057	44029	2081
0.1920	9.3310	40630	1814
0.1947	9.7867	37286	1566
0.1974	10.1781	33995	1336
0.2001	10.5100	30755	1126
0.2028	10.7876	27564	933
0.2055	11.0156	24420	758
0.2082	11.1988	21322	601
0.2109	11.3418	18267	461
0.2136	11.4495	15254	339
0.2163	11.5264	12281	234
0.2190	11.5773	9346	146
0.2217	11.6071	6450	78
0.2244	11.6210	3589	28
0.2271	11.6245	763	2
0.2298	11.6274	2030	11
0.2325	11.6201	4790	47
0.2352	11.6006	7519	101
0.2379	11.5643	10218	171
0.2406	11.5073	12887	254
0.2433	11.4261	15529	349
0.2460	11.3176	18143	456
0.2487	11.1789	20731	573
0.2514	11.0073	23293	700
0.2541	10.8004	25831	835
0.2568	10.5557	28344	979
0.2595	10.2710	30835	1131
0.2622	9.9443	33303	1290
0.2649	9.5737	35749	1457
0.2676	9.1571	38175	1630
0.2703	8.6929	40579	1810
0.2730	8.1793	42964	1996
0.2757	7.6148	45330	2187
0.2784	6.9976	47676	2385
0.2811	6.3264	50005	2588
0.2838	5.5998	52316	2796
0.2865	4.8162	54610	3009
0.2892	3.9744	56887	3227
0.2919	3.0731	59148	3450
0.2946	2.1111	61393	3677
0.2973	1.0871	63623	3909
0.3000	0.0000	65837	4145

Table 5.1 Flow Conditions in Spinneret

Dope 40% w/w Polysulphone(P1700) in DMF

Dope Extrusion Rate 1.0 cm^3/min

Graph 5.1 Velocity Profiles in Spinneret Polysulphone(P1700) Dopes

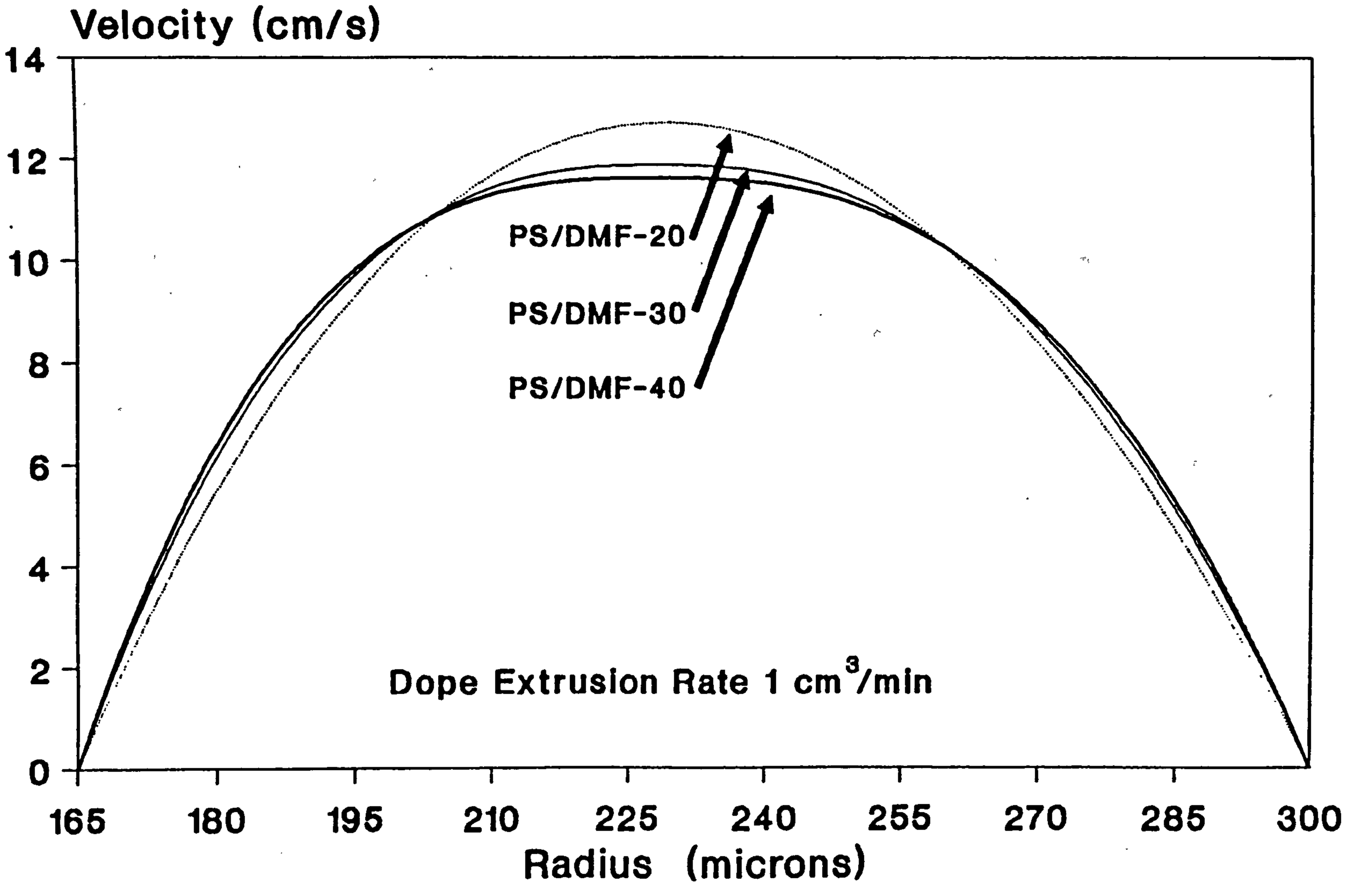

Graph 5.2 Shear Rate Profiles in Spinneret Polysulphone(P1700) Dopes

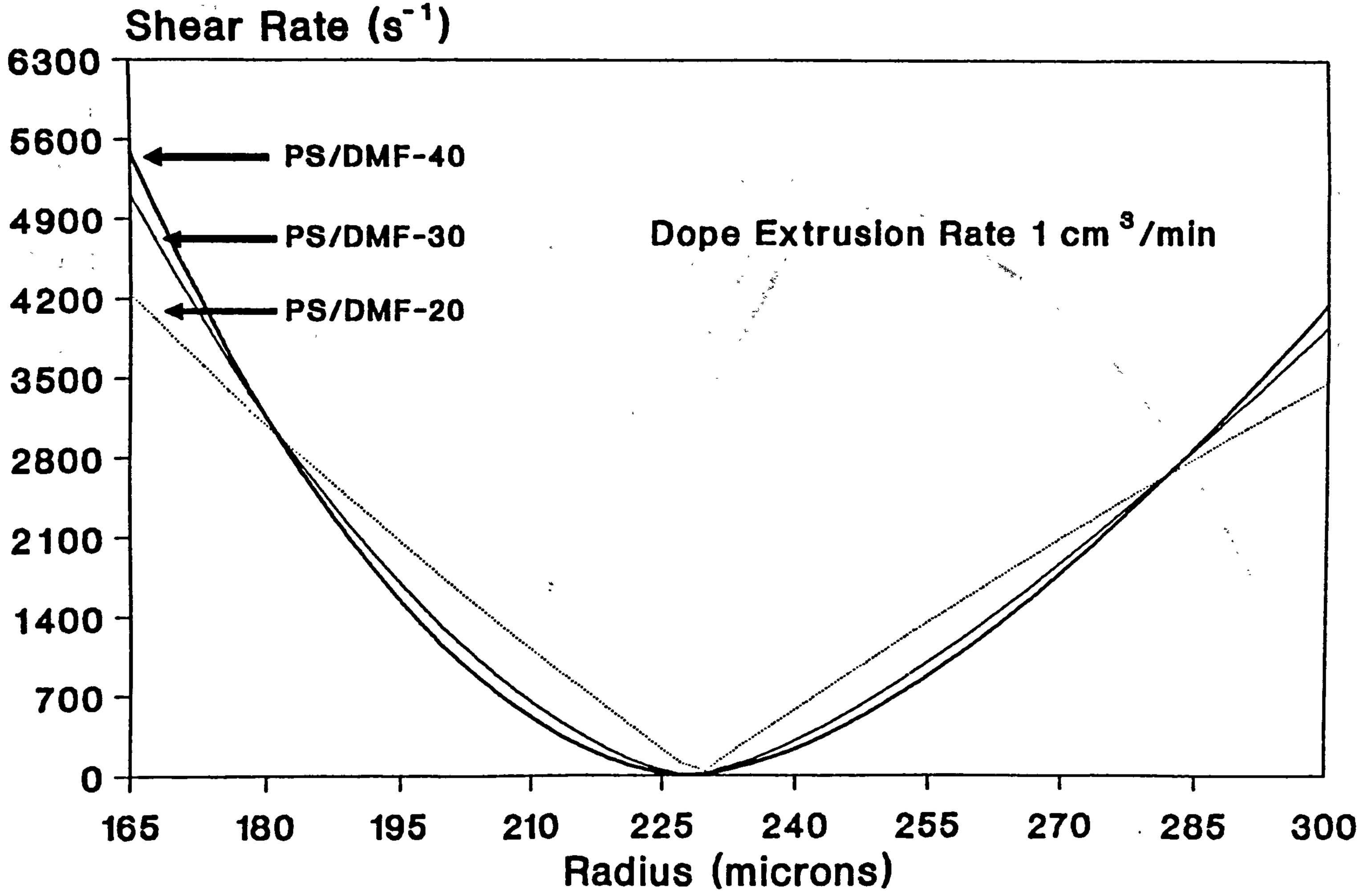

Graph 5.3 Velocity Profiles in Spinneret Polyacrylonitrile Dopes

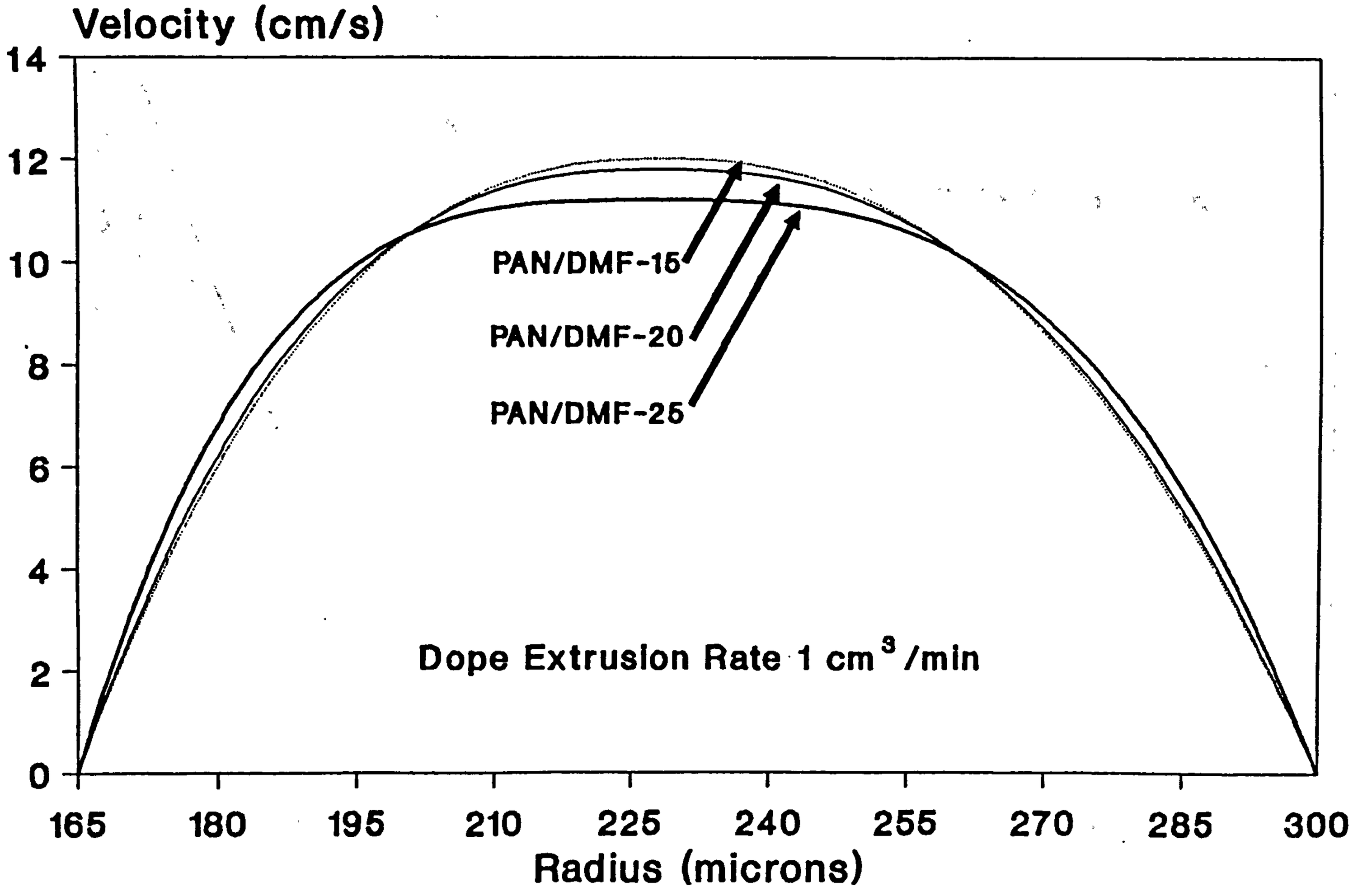

Graph 5.4 Shear Rate Profiles in Spinneret Polyacrylonitrile Dopes

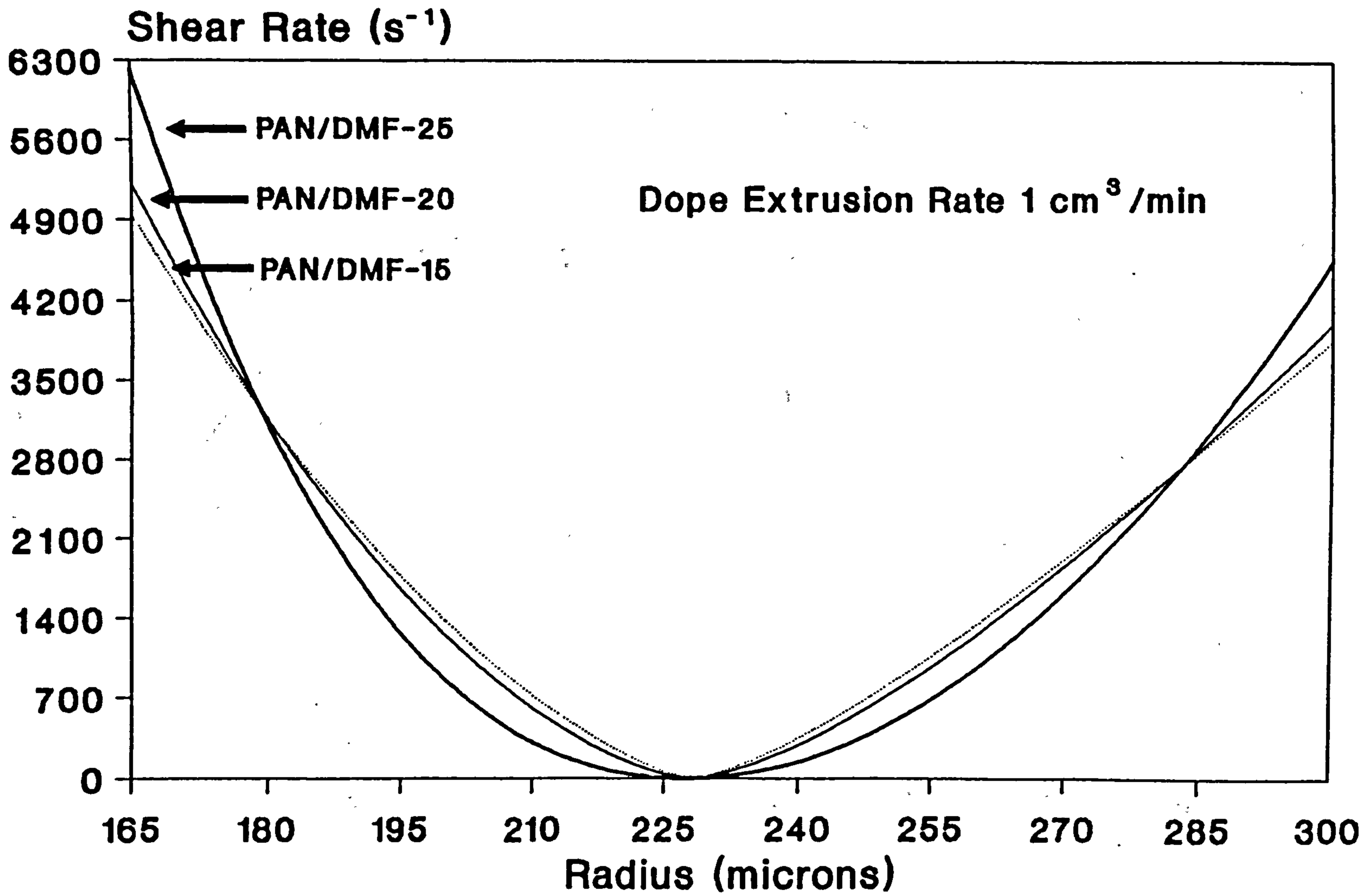

Graph 5.5 Velocity Profiles in Spinneret
Dope 40% w/w Polysulphone(P1700) in DMF

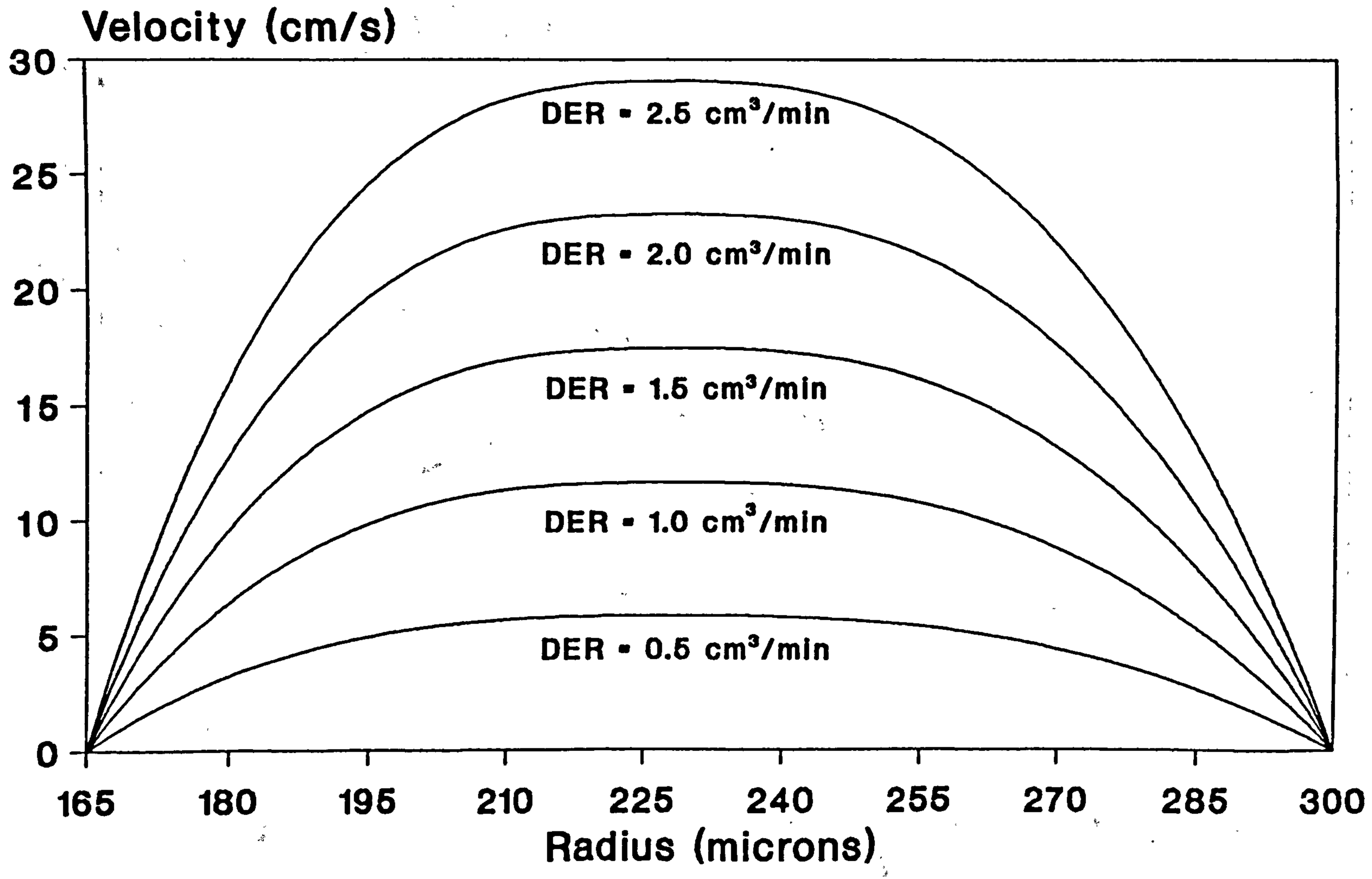

Graph 5.6 Shear Rate Profiles in Spinneret
Dope 40% w/w Polysulphone(P1700) in DMF

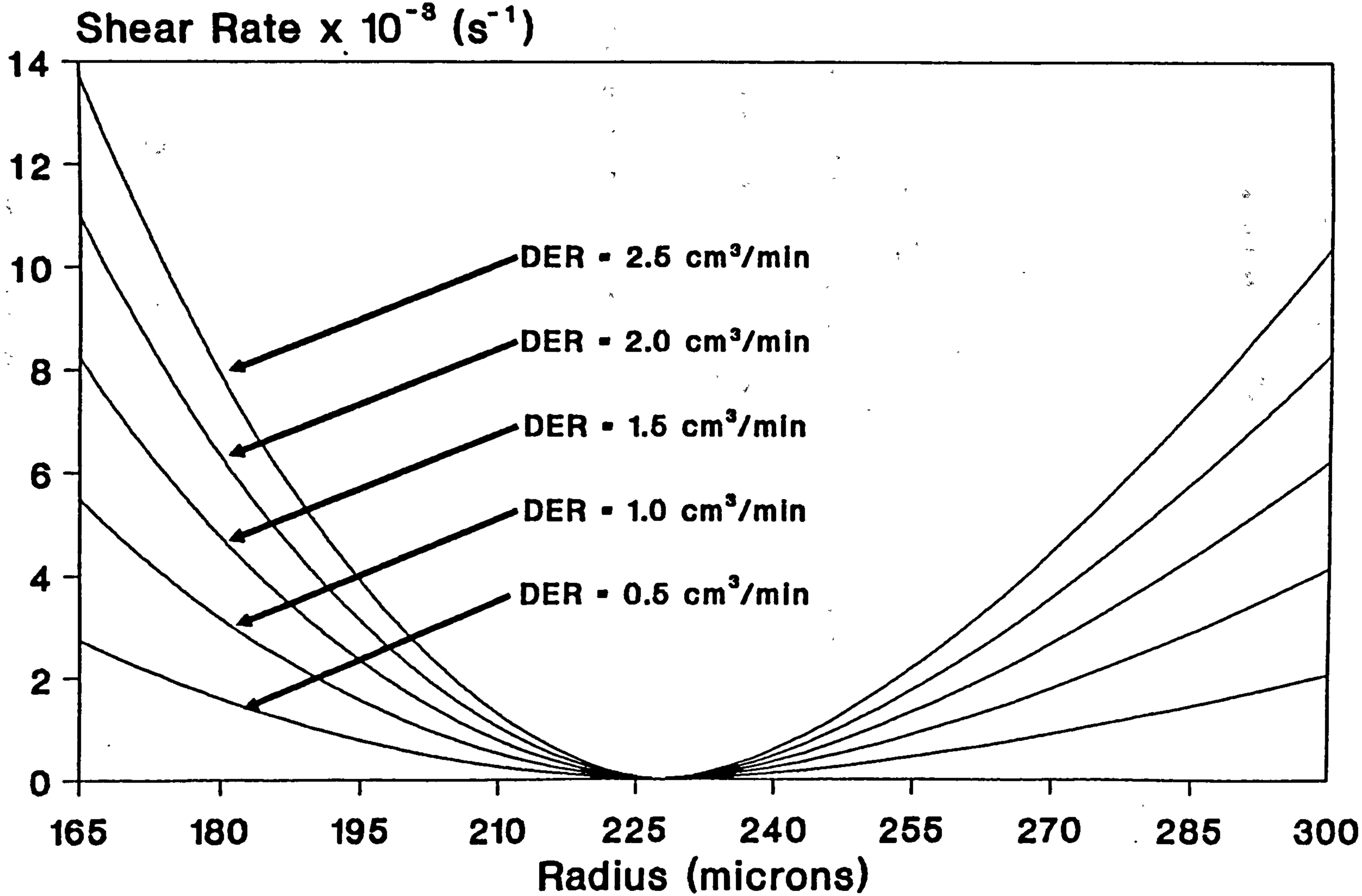

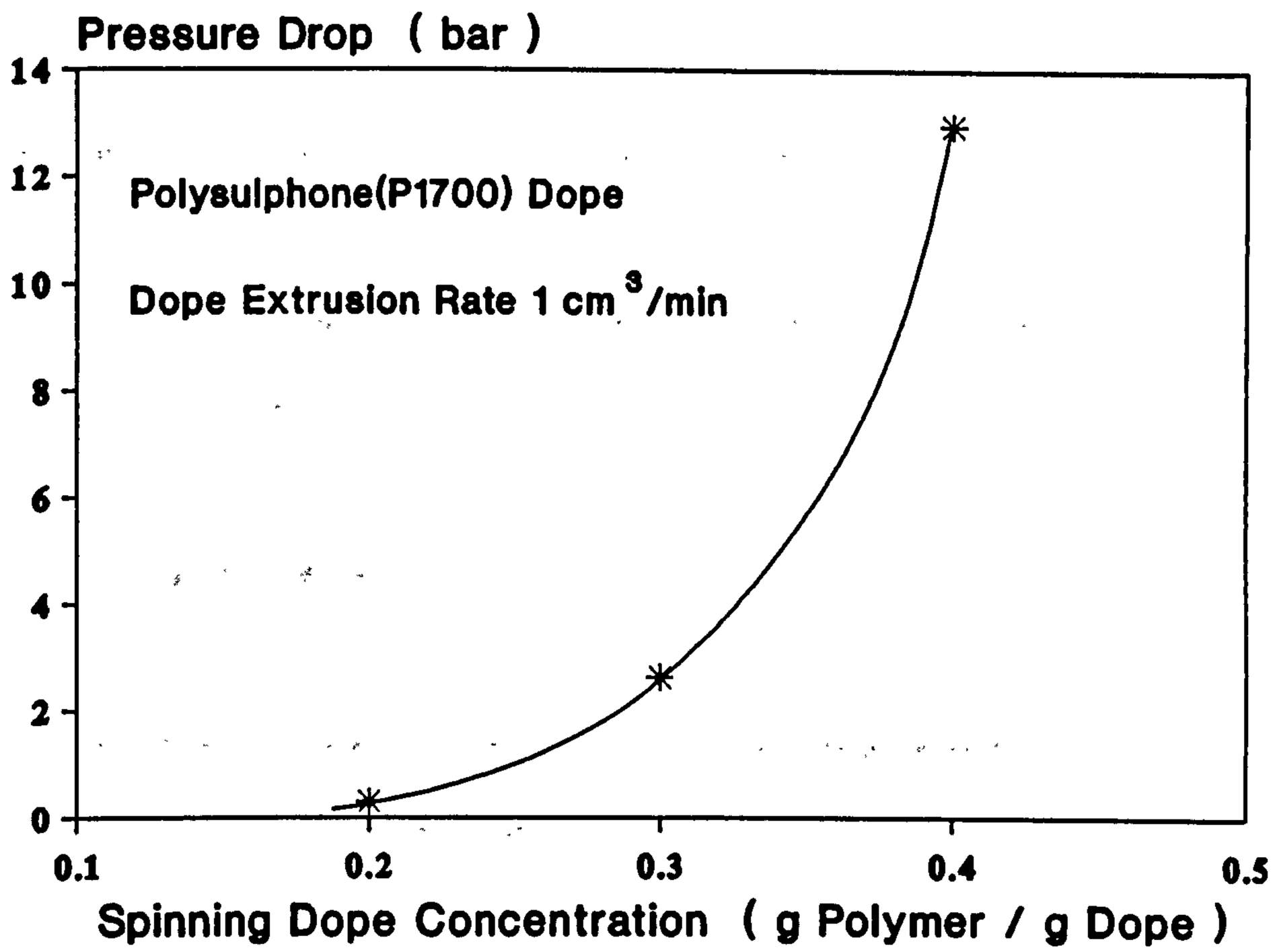

Graph 5.7 Pressure Drop Across Spinneret
Effect of Dope Concentration

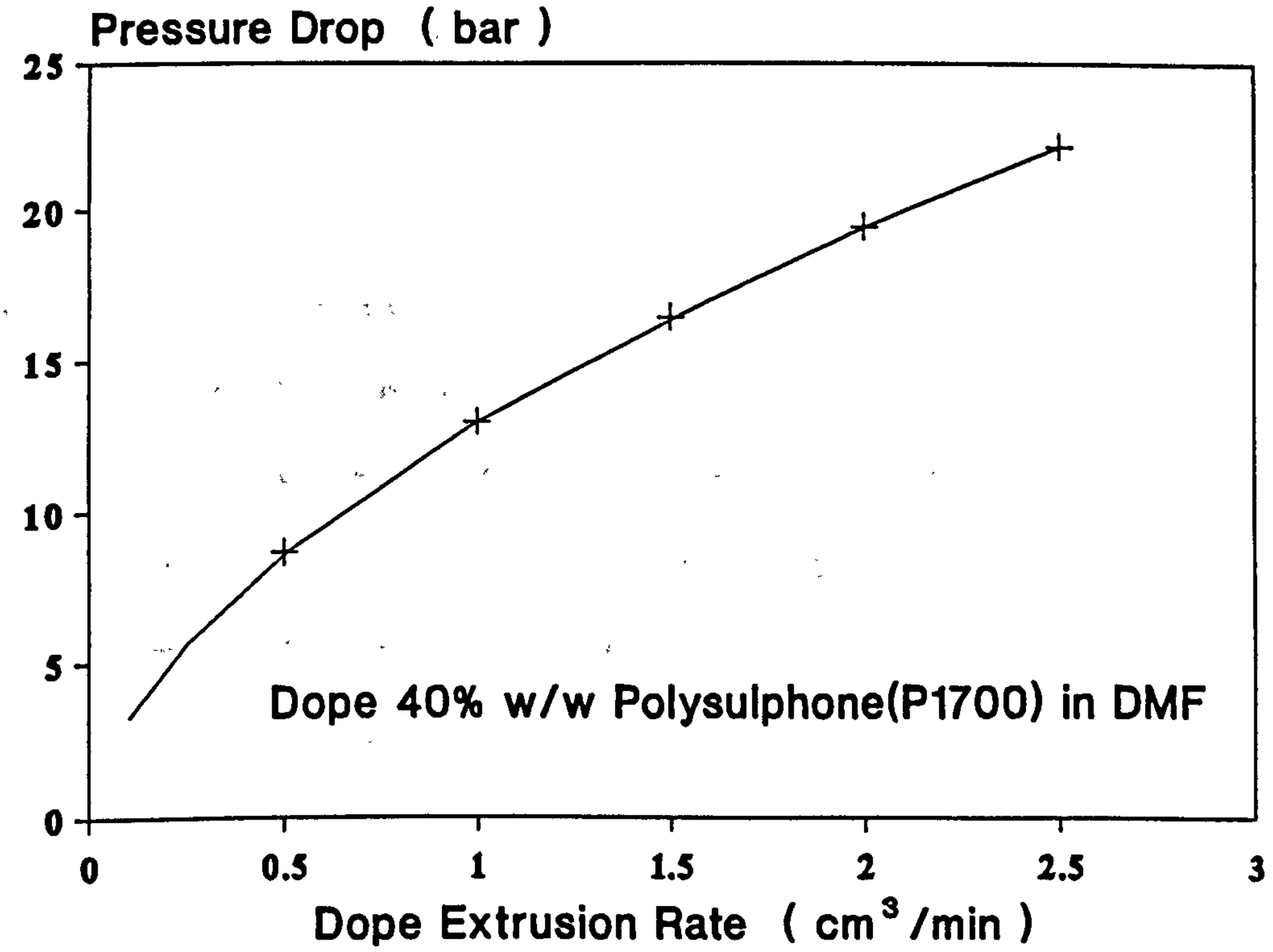

Graph 5.8 Pressure Drop Across Spinneret
Effect of Dope Extrusion Rate

5.2 Gas Permeation Modelling

5.2.1 Pore Size and Flow Mechanisms.

Gas transfer through membranes is governed by three major flow mechanisms:

1. Solution Diffusion

Solution diffusion occurs when the membrane is completely non-porous. Gas transfer is controlled by the intrinsic permeation properties of the polymer material

$$Q = \frac{DS}{L} A \Delta P = \frac{\acute{P}}{L} A \Delta P \quad \text{---------- 5.18}$$

where Q = Molar gas flowrate

A = Membrane area

ΔP = Pressure difference across membrane

L = Thickness of membrane active layer

D,S = Diffusivity and solubility of gas in polymer

$\acute{P}$ = Intrinsic permeability coefficient of polymer

2. Knudsen Diffusion

This type of flow occurs when the Knudsen number[82]

$$\frac{\lambda}{r} > 10$$

where λ is the mean free path of the gas molecule

r is pore radius

For Knudsen diffusion [83][84]

$$Q = \frac{8}{3}\left[\frac{1}{2\pi RTM}\right]^{\frac{1}{2}} \frac{r}{L} A_p A \Delta P \quad \text{-----} \quad 5.19$$

where A_p = Fraction of membrane area that is pores

M = Molecular weight of gas

R,T = Universal gas constant, Temperature

3. Viscous Flow

Viscous flow occurs when the Knudsen number[82]

$$\frac{\lambda}{r} < 0.01$$

and for viscous flow [83]

$$Q = \frac{r^2}{8RT} \frac{1}{L\,\eta} \left[\frac{P_f + P_p}{2}\right] A_p\, A\, \Delta P \quad \text{-----} \quad 5.20$$

where η = Viscosity of gas

$\frac{P_f + P_p}{2} = P_{mean}$, the mean Pressure across the membrane

The viscosity of a gas is essentially independent of pressure. It can be shown from kinetic theory that

$$\eta = \left[\frac{MRT}{\pi^3}\right]^{\frac{1}{2}} \frac{1}{N\, d_m^2} \quad \text{----------} \quad 5.21$$

where N = Avogadro's number

d_m = Molecular diameter

Also from kinetic theory, the mean free path of a gas molecule is given by

$$\lambda = \frac{RT}{\sqrt{2}\ \pi\ P\ N\ d_m^2} \quad \text{----------} \quad 5.22$$

where P = Pressure of gas

Important properties of gases and polymers are included in **Tables 5.2** and **5.3.** Values of viscosity were taken from the literature and molecular diameters evaluated from equation 5.21. Mean free paths were calculated from equation 5.22.

Gas	Molecular Weight M	Viscosity η 25 °C (Ns/m^2)	Molecular Diameter d_m (Å)	Mean Free Path λ 25 °C, 1 atm (Å)
CO_2	44	15	4.6	446
CH_4	16	11	4.1	551

Table 5.2 Physical Properties of Gases

Polymer	$\acute{P}_{CO_2}$	$\acute{P}_{CH_4}$	$\Omega_{CH_4}^{CO_2}$
Polysulphone	0.45[a]	0.016	28[a]
Polyacrylonitrile	0.00018[b]	0.000001[c]	180
Dimethyl- Silicone	325[d]	95[d]	3.4

[a] Ref [85]

[b] Ref [86]

[c] extracted from Refs [39][50]

[d] Ref [87]

$\acute{P}$ = Intrinsic Permeability Coefficient x 10^9 $\left(\frac{cm^3\,(STP)\,cm}{s\ cm^2\ cmHg}\right)$

Ω = Intrinsic Selectivity

Table 5.3 Intrinsic Permeation Properties of Polymers

Between the extremes of Knudsen diffusion and viscous flow, that is when $10 > \lambda/r > 0.01$, there lies the complex transition region where the flow changes character progressively from Knudsen to viscous. Flow in this region has been described by Present and de Béthune[88]. According to Dushman[89] even when $\lambda/r = 1$, 85% of the total flow occurs by Knudsen diffusion. The value of λ depends on molecular diameter which in turn depends on the material property used in its determination. Values in **Table 5.2** originate from gas viscosities but had they been based on Van der Waals' co-volume then the mean free paths would almost double[90][91]. The mean free path varies inversely with pressure. For the purposes of predicting pore sizes and flow regimes it would seem most appropriate to base λ on the mean pressure across the membrane, typically 3.5 bara in this work. This reduces λ values based at 1 atm by a factor of 3.5. All things considered the following pore sizes corresponding to the different flow regimes are estimated from the Knudsen number conditions:

Pore Radius	**Flow Regime**
Non-porous	Solution diffusion
$r < 30$ Å	Knudsen diffusion
$r = 300$ Å	85% Knudsen diffusion
$r > 30000$ Å	Viscous flow

From equations 5.19, 5.20 and 5.21 the ratio of flows based on Knudsen diffusion and viscous flow for a particular pore size is given by

$$\frac{Q_{Viscous}}{Q_{Knudsen}} = \frac{3\sqrt{2}\,\pi^2\,N\,d_m^2\,P_{mean}}{64\,RT}\,r \qquad \text{-----} \quad 5.23$$

under the conditions of this work this conveniently reduces to

$$\frac{Q_{Viscous}}{Q_{Knudsen}} = 1 \times 10^{-3}\,r$$

where r is in Ångstroms

Equation 5.23 shows that at a pore radius of 1000 Å gas flowrates based on Knudsen diffusion and viscous flow are equal. The implications of this result with respect to the pore size/flow regime intervals shown above are not entirely clear without further analysis. For the purposes of the current work it will be assumed that up to a pore radius of 1000 Å Knudsen diffusion adequately describes flow.

Figure 5.2 summarises the complete pore size and flow mechanism spectrum.

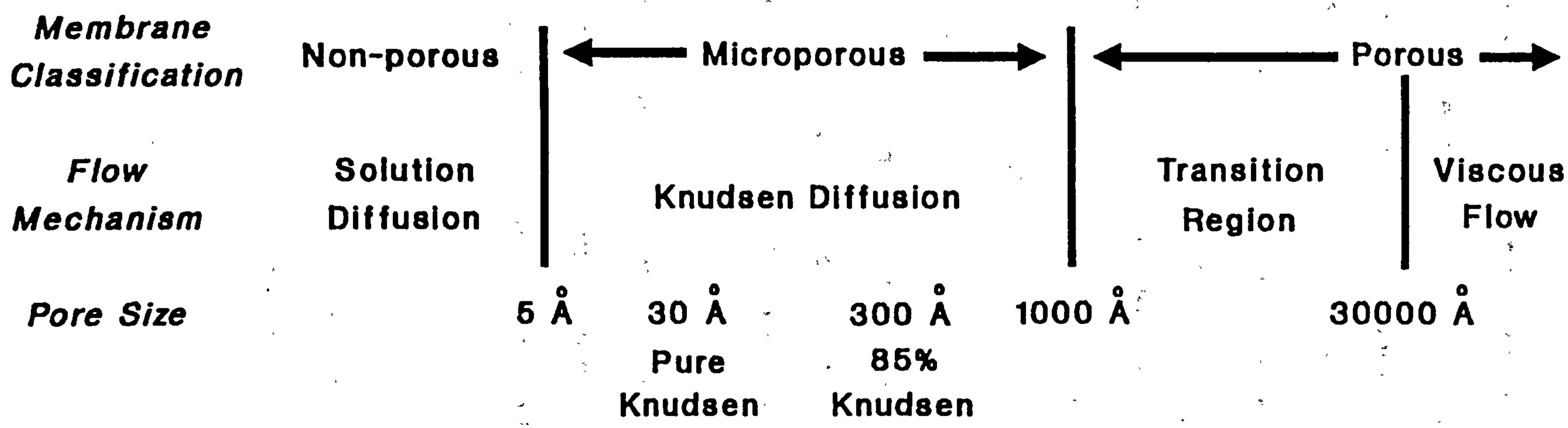

Figure 5.2 Pore Size and Gas Flow Mechanism Spectrum

5.2.2 Resistance Modelling of Gas Permeation

The principles of applying flow resistances in series and parallel in order to describe gas permeation through asymmetric membranes have been outlined by Henis and Tripodi[31][39]. They predicted that a membrane useless for gas separation due to surface pores or imperfections could in fact exhibit gas separation properties akin to the intrinsic capabilities of the polymer material once coated with silicone. Henis and Tripodi applied the resistance approach to typical membrane morphologies and made assumptions as to the nature of the deposition of the coating material (eg thickness of silicone layer and pore penetration depth). They then predicted the performance of these hypothetical coated membranes.

In this work the resistance approach is applied to the actual uncoated and coated permeation properties of the spun hollow fibres in order to deduce details of membrane morphology.

As has already been shown the permeation of a gas through a membrane can be described by the general flow equation

$$Q = P\ A\ \Delta P \quad \text{----------} \quad 3.42$$

The flow mechanisms discussed in the previous section can be represented by permeability expressions

$$P_{Solution\ Diffusion} = \frac{\acute{P}}{L} \quad \text{----------} \quad 5.24$$

$$P_{Knudsen\ Diffusion} = \frac{8}{3}\left[\frac{1}{2\pi RTM}\right]^{\frac{1}{2}} \frac{r}{L} A_p \quad \text{-----} \quad 5.25$$

$$P_{Viscous\ Flow} = \frac{r^2}{8RT} \frac{1}{L\eta} P_{mean} A_p \quad \text{-----} \quad 5.26$$

Analogous to the flow of electricity the resistance to permeation, R can be defined as

$$R = \frac{1}{P A} \quad \text{----------} \quad 5.27$$

In the electron microscope work (section 3.4.6) no pores could be identified in the fibres at magnifications of up to X 10000. This suggests that generally the membranes have pore sizes of less than 100 Å as shown below

Magnification X 10000

Resolution of naked eye 0.2 mm

$\therefore d_{pore} < 0.2mm / 10000$

$\therefore r_{pore} < 100$ Å

Pore flow was assumed to be exclusively Knudsen.

Figure 5.3 illustrates the resistances and corresponding fibre structures from which permeation equations were derived.

Uncoated Fibres:

$$\frac{1}{R_{Overall}} = \frac{1}{R_{Polymer}} + \frac{1}{R_{Knudsen}}$$

from equations 5.24, 5.25 and 5.27

$$P_{Overall}\, A = \frac{\acute{P}_{Polymer}}{L_o} A_{Polymer} + \frac{8}{3} \frac{1}{\sqrt{2\pi RTM}} \frac{r}{L_o} A_p\, A \quad \text{---- 5.28}$$

Coated Fibres:

$$R_{Overall} = R_{\substack{Silicone \\ Layer}} + \frac{1}{\frac{1}{R_{Polymer}} + \frac{1}{R_{\substack{Silicone \\ Plug}} + R_{Knudsen}}}$$

from equations 5.24, 5.25 and 5.27

$$\frac{1}{P_{Overall}\, A} = \frac{L_s}{\acute{P}_s\, A} + \frac{1}{\frac{\acute{P}_{Polymer}}{L_o} A_{Polymer} + \frac{1}{\left[\frac{L_p}{\acute{P}_s\, A_p\, A}\right] + \left[\frac{3}{8}\sqrt{2\pi RTM}\, \frac{(L_o - L_p)}{r\, A_p\, A}\right]}} \quad \text{---- 5.29}$$

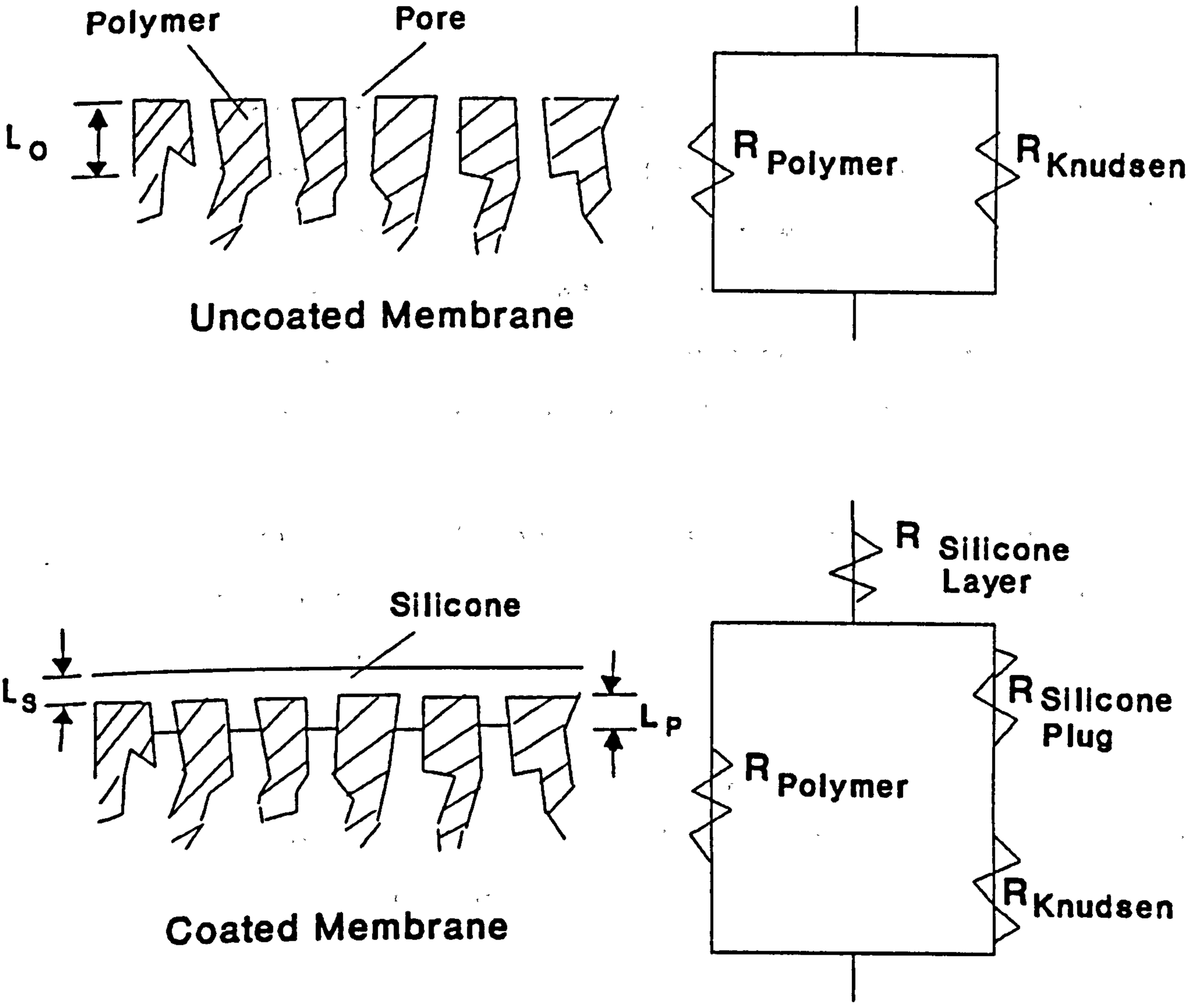

L_o Thickness of active layer

L_s Thickness of silicone layer

L_p Pore penetration depth

Figure 5.3 Resistance Modelling - Gas Transfer Through Asymmetric Membranes

It was found that $A_p << 1$ and hence $A_{Polymer} = A$

Also $L_p << L_o$

On coating the resistance offered by the outer silicone layer was negligible. Even for the most permeable (least resistance) coated fibres (20% w/w spun) a silicone layer 1 μm thick is required to exert 10% of the overall resistance. The electron microscope work indicated that coating thicknesses are easily less than 1 μm.

From equations 5.28 and 5.29 and taking into account the above observations the following set of model equations can be established.

The equations were solved by computer using actual hollow fibre permeabilities. 'TK Solver' an equation solving software package was utilised.

$$P_{\substack{Overall\ CO_2 \\ Uncoated}} = \frac{\acute{P}_{Polymer\ CO_2}}{L_o} + \frac{8}{3}\frac{1}{\sqrt{2\pi RTM_{CO_2}}}\frac{r}{L_o}A_p \qquad 5.30$$

$$P_{\substack{Overall\ CH_4 \\ Uncoated}} = \frac{\acute{P}_{Polymer\ CH_4}}{L_o} + \frac{8}{3}\frac{1}{\sqrt{2\pi RTM_{CH_4}}}\frac{r}{L_o}A_p \qquad 5.31$$

$$P_{\substack{Overall\ CO_2 \\ Coated}} = \frac{\acute{P}_{Polymer\ CO_2}}{L_o} + \frac{1}{\left[\frac{L_p}{\acute{P}_{s\ CO_2}\ A_p}\right]+\left[\frac{3}{8}\sqrt{2\pi RTM_{CO_2}}\ \frac{L_o}{r\ A_p}\right]} \qquad 5.32$$

$$P_{\substack{Overall\ CH_4 \\ Coated}} = \frac{\acute{P}_{Polymer\ CH_4}}{L_o} + \frac{1}{\left[\frac{L_p}{\acute{P}_{s\ CH_4}\ A_p}\right]+\left[\frac{3}{8}\sqrt{2\pi RTM_{CH_4}}\ \frac{L_o}{r\ A_p}\right]} \qquad 5.33$$

$$\frac{P_{\substack{Overall\ CO_2 \\ Uncoated}}}{P_{\substack{Overall\ CH_4 \\ Uncoated}}} = \Omega^{CO_2}_{CH_4}\ Uncoated \qquad 5.34$$

$$\frac{P_{\substack{Overall\ CO_2 \\ Coated}}}{P_{\substack{Overall\ CH_4 \\ Coated}}} = \Omega^{CO_2}_{CH_4}\ Coated \qquad 5.35$$

Resistance Model Equations

5.2.3 Effect of Spinning Conditions on Fibre Structure

5.2.3.1 Effect of Dope Extrusion Rate

permeability and selectivity data was extracted from the overall trends given in **Graphs 4.3** and **4.4.** The data was inserted into the resistance model equations allowing the effects of dope extrusion rate on membrane structure to be determined.

In the analysis, based on 40% w/w spun polysulphone hollow fibres, the thickness of the active layer was assumed constant. This is in accordance with the electron microscope work where no distinction in structure, and in particular active layer thickness, was visually detected between fibres within one dope concentration. (This statement is based on magnifications of up to X 4000 where the active layer could be clearly distinguished from the rest of the fibre cross section.)

The intrinsic selectivity of the polysulphone polymer was found to increase with dope extrusion rate. The standard literature figure of 28 in favour of CO_2 over CH_4 was used as an anchor to represent the lowest intrinsic selectivity value.

Pore size was also found to increase with dope extrusion rate. (The results of the permeability variation with pressure tests shown in **Table 3.10** for the 30% w/w fibres at constant JS support this trend.) It was decided to base the results on a maximum pore radius of 100 Å as suggested by the electron microscopy. The ratio of silicone penetration depth to pore radius was established at this pore size and assumed constant at a value of 0.521.

The model results relating membrane structure to dope extrusion rate are shown in **Table 5.4.**

D.E.R. cm^3/min	Polysulphone Intrinsic Selectivity CO_2/CH_4	Total Pore Area cm^2/cm^2	Pore Radius Ångstrom	Pore Number $1/cm^2$	Distance Between Pores Ångstrom
1.0	28.1	$1.25x10^{-6}$	38.0	$2.76x10^{6}$	$6.02x10^{4}$
1.33	33.1	$1.55x10^{-6}$	54.3	$1.67x10^{6}$	$7.74x10^{4}$
1.67	38.1	$2.12x10^{-6}$	73.2	$1.26x10^{6}$	$8.91x10^{4}$
2.0	43.3	$3.13x10^{-6}$	100.0	$1.00x10^{6}$	$10.01x10^{4}$

Dope = 40% w/w Polysulphone in Dimethylformamide
Jet Stretch Ratio = 1

Thickness of Active Layer = **4.31×10^{4} Ångstrom or 4.31 micron**
On Coating - Silicone Penetration Depth : Pore Radius = **0.521**

Gas Transport by Solution Diffusion and Knudsen Diffusion

Table 5.4 Effect of Dope Extrusion Rate on Fibre Structure

5.2.3.2 Effect of Jet Stretch Ratio

Permeability and selectivity values were obtained from the overall trends in **Graphs 4.5** and **4.6.** The model calculations are based on the DER 1 JS 1 fibres having the standard literature intrinsic selectivity of 28 as established in the dope extrusion rate analysis.

The results relating membrane structure to jet stretch ratio are shown in **Table 5.5.** The increase in pore size with JS is supported by the permeability variation with pressure results for the 30% w/w fibres at constant DER recorded in **Table 3.10.**

J.S.	Polysulphone Intrinsic Selectivity CO_2/CH_4	Total Pore Area cm^2/cm^2	Pore Radius Ångstrom	Pore Number $1/cm^2$	Distance Between Pores Ångstrom
0.75	27.1	$1.06x10^{-6}$	40.0	$2.10x10^{6}$	$6.89x10^{4}$
1.0	28.1	$1.42x10^{-6}$	46.4	$2.10x10^{6}$	$6.90x10^{4}$
1.25	27.7	$2.03x10^{-6}$	59.3	$1.84x10^{6}$	$7.38x10^{4}$
1.5	20.9	$3.00x10^{-6}$	78.0	$1.57x10^{6}$	$7.98x10^{4}$

Dope = 40% w/w Polysulphone in Dimethylformamide
Dope Extrusion Rate = 1.0 cm^3/min

Thickness of Active Layer = **3.86 x 10^4 Ångstrom or 3.86 micron**
On Coating - Silicone Penetration Depth : Pore Radius = **0.521**

Gas Transport by Solution Diffusion and Knudsen Diffusion

Table 5.5 Effect of Jet Stretch Ratio on Fibre Structure

5.2.3.3 Effect of Dope Concentration

Permeabilities and selectivities were taken from **Graphs 4.1** and **4.2**. Pore size was found to increase with decreasing polymer content in the spinning dope and values were primarily based on a maximum pore radius of 100 Å. However, for the fibres spun from the 20% w/w and 30% w/w dopes, highly permeable in comparison to the 40% w/w spun fibres, an additional pore size term of radius 1000 Å was introduced. This was necessary to enable the resistance modelling to produce results that accurately represented the permeation properties of these fibres.

The model results relating membrane structure to dope concentration are shown in **Table 5.6.**

The effects will be considered in the overall discussion of results but for the moment it is worth noting the values of active layer thickness. It can be seen from **Table 5.6** that the 40% w/w and 30% w/w spun fibres are predicted to have a similar active layer thickness of 3-4 microns, much higher than the value of 0.14 micron for the 20% spun fibres. This would seem to be confirmed by the electron micrographs. **Figures 5.4** and **5.5** show distinct active layers of appropriate thickness for 40% and 30% fibres. No such discrete layer can be identified in the high voidage 20% fibres as shown in **Figure 3.8.**

Dope Concentration % w/w	Thickness of Active Layer Angstrom	Total Pore Area cm^2/cm^2	Pore Radius (I) Angstrom	Pore Number (I) $1/cm^2$	Distance Between Pores (I) Angstrom	Pore Radius (II) Angstrom	Pore Number (II) $1/cm^2$	Distance Between Pores (II) Angstrom
20	0.14×10^4	148×10^{-6}	100.0	43.1×10^6	1.52×10^4	1000	3.87×10^4	50.8×10^4
30	3.00×10^4	136×10^{-6}	75.5	62.2×10^6	1.27×10^4	1000	7.84×10^4	35.7×10^4
40	4.31×10^4	1.25×10^{-6}	38.0	2.76×10^6	6.02×10^4			

Dope = Polysulphone in Dimethylformamide

Intrinsic Selectivity of Polysulphone Polymer CO_2/CH_4 = **28**
On Coating - Silicone Penetration Depth : Pore Radius = **0.521**

Gas Transport by Solution Diffusion and Knudsen Diffusion

Table 5.6 Effect of Dope Concentration on Fibre Structure

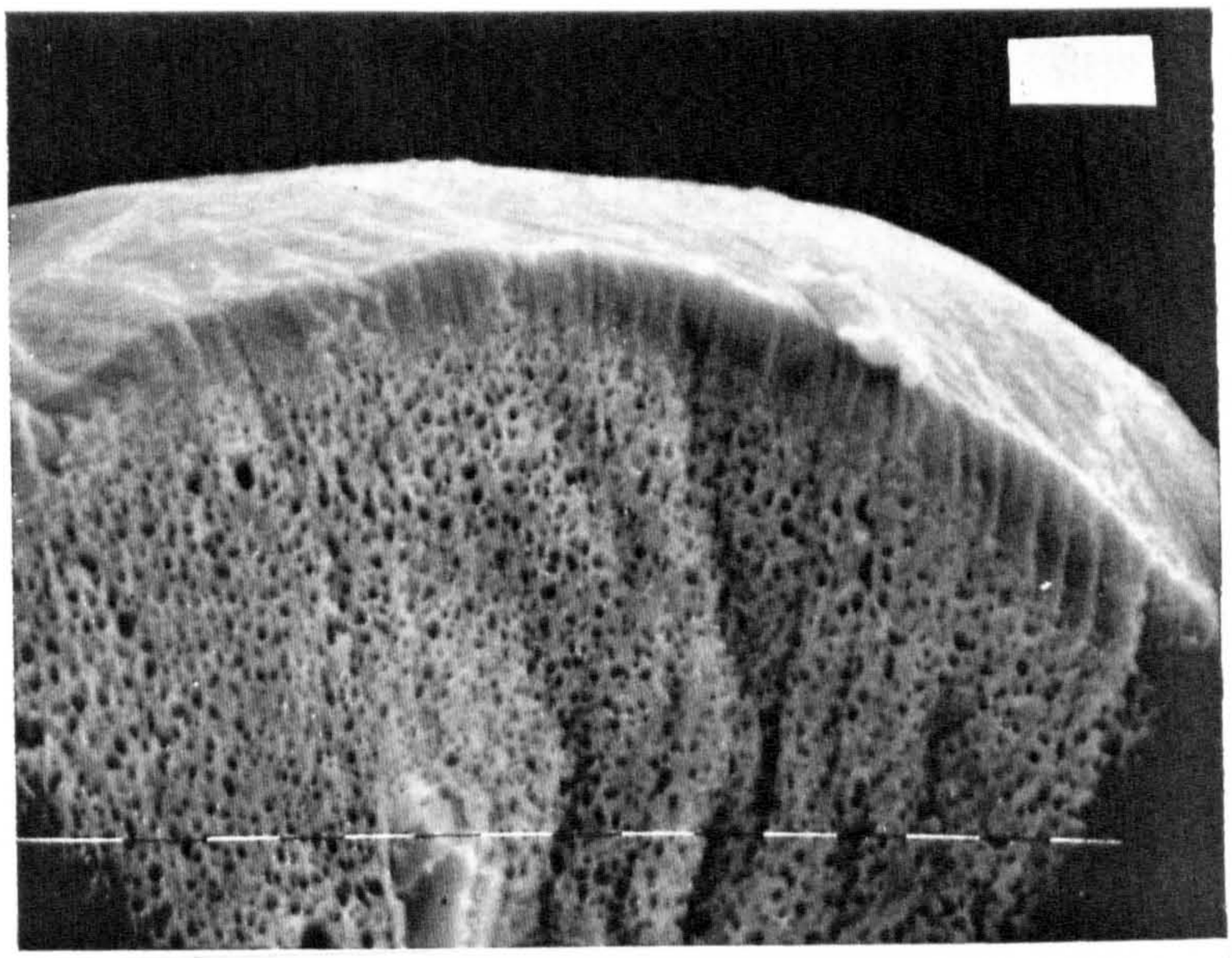

a. 10 μm

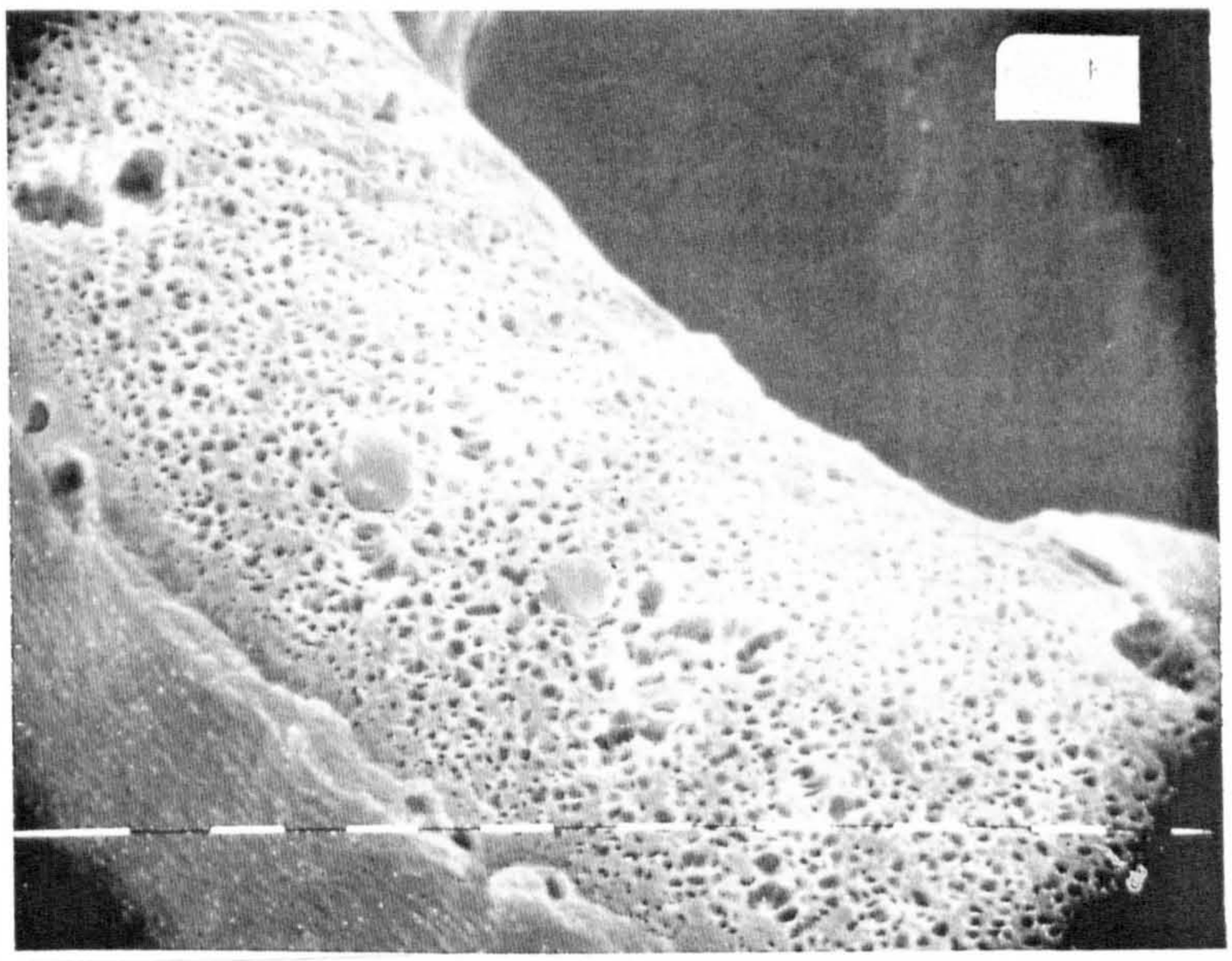

b. 10 μm

Figure 5.4 Cross Section **Polysulphone** Hollow Fibres
Dope **40% w/w** in Dimethylformamide
Magnification X 640

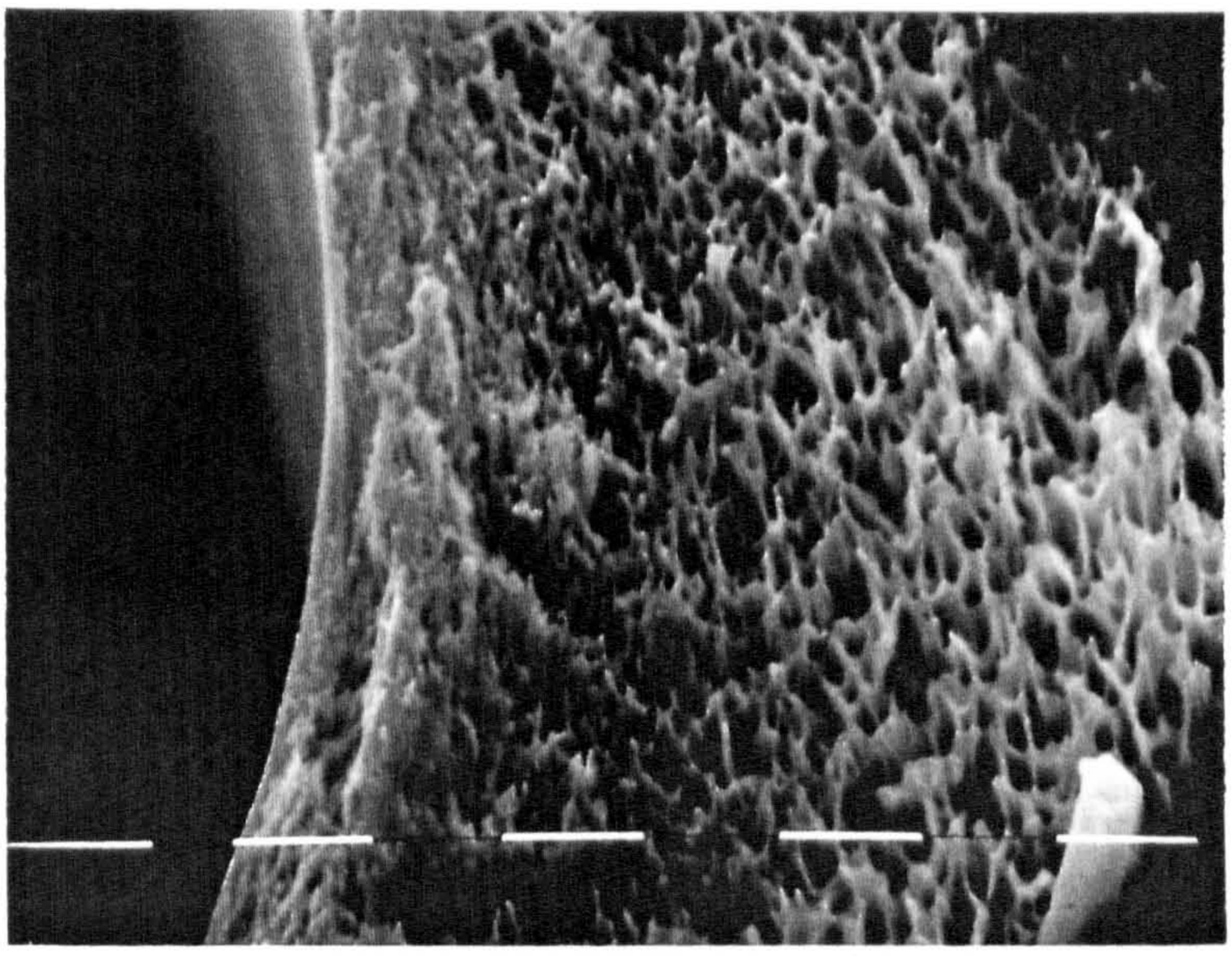

10 μm

Figure 5.5 Cross Section **Polysulphone** Hollow Fibre Dope **30% w/w** in Dimethylformamide
Magnification X 1250

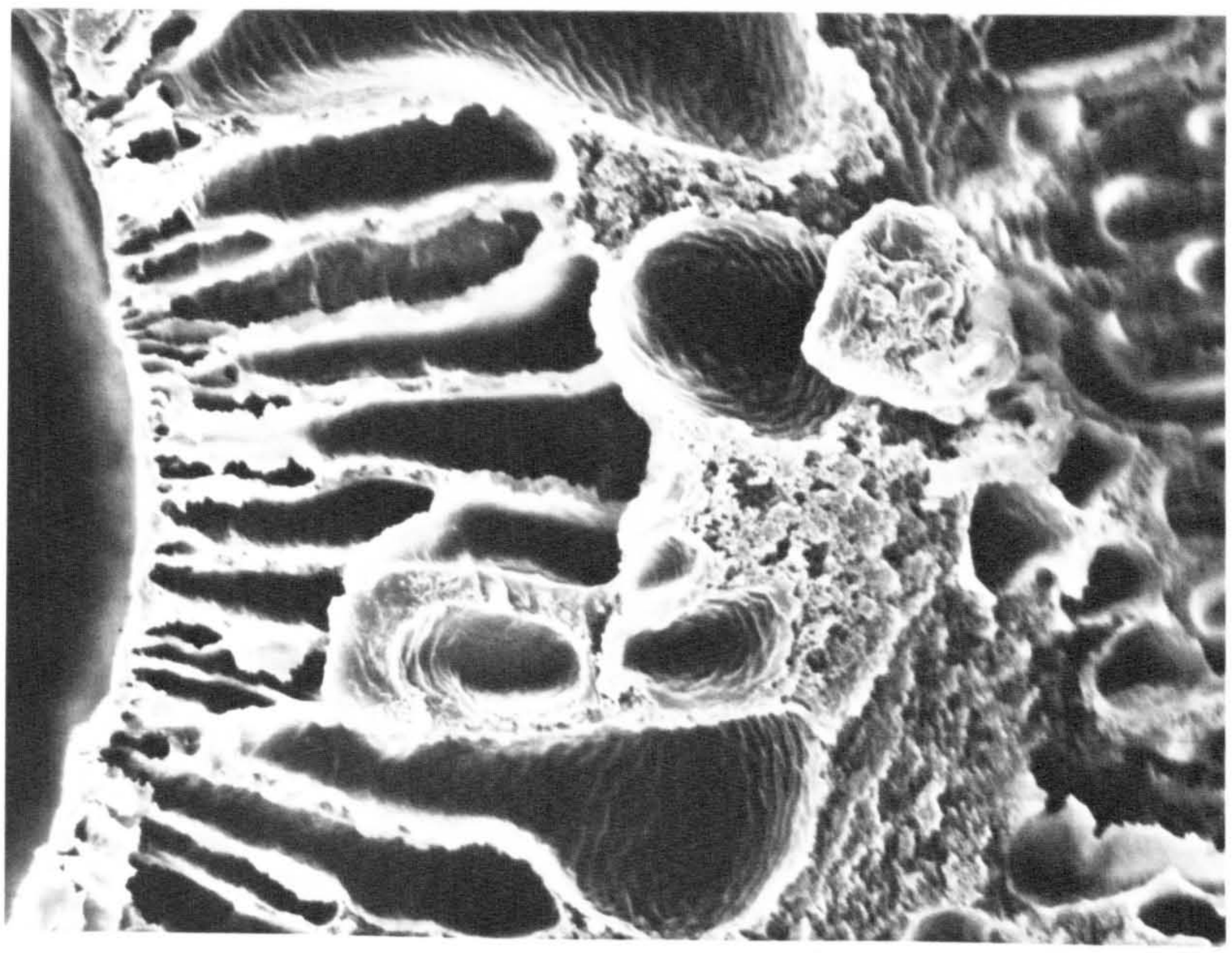

10 μm

Figure 5.6 Cross Section **Polyacrylonitrile** Hollow Fibre Dope **25% w/w** in Dimethylformamide
Magnification X 850

5.2.3.4 Polyacrylonitrile Hollow Fibres

Polyacrylonitrile fibres were spun from one dope concentration (25% w/w). The permeation results given in **Graphs 4.7** and **4.8** show no clear correlation with dope extrusion rate or jet stretch ratio. The permeability of the PAN membranes exhibited significant dependence on coating solution strength but selectivity values were consistently poor, doggedly remaining at around unity.

Polyacrylonitrile has a high intrinsic selectivity of 180 (CO_2/CH_4) compared to 28 for polysulphone. However, polyacrylonitrile has an extremely low intrinsic permeability, thousands of times less than that of polysulphone. The figures are shown in **Table 5.3**. As a result PAN membranes require to have an extremely thin and imperfection free active layer in order for the high inherent selectivity of the polymer to be realised at sufficient permeate fluxes. Henis and Tripodi[39] have predicted that even for very thin (0.1 micron) fully silicone sealed active layers ($L_p = L_o$) an increase in surface porosity from 10^{-6} to 10^{-4} will cause a drastic decrease in the selectivity of PAN membranes. A drop would occur from 29% to 0.4% of the intrinsic selectivity of the polymer. In the case of polysulphone membranes the decline would only be from 82% to 76% of the intrinsic selectivity. Also, the permeation rates are 100 times greater through the polysulphone membranes.

The sensitivity of the PAN membranes to surface imperfections may explain the wide variation in the permeabilities of the hollow fibres **(Graph 4.7)**. The fact that the permeability of the PAN membranes is affected by coating solution strength is also indicative of their high dependence on flow through channels rather than diffusion through the low permeability polyacrylonitrile polymer in the membrane wall itself.

With these inherent properties of the PAN polymer it is no surprise that the selectivities shown in **Graph 4.8** are disappointing. Even in the least permeable membranes (the lowest permeabilities of all the fibres in this work) flow through the solid highly selective polymer is still insufficient for selectivity to climb above unity. Silicone penetration depth as a fraction of total pore length is insufficient for the silicone to cause a rise in selectivity. The Knudsen flow through the remainder of the open pore remains dominant.

As a consequence of the above, modelling the permeation performance of the polyacrylonitrile hollow fibres on the basis of selectivity becomes trivial. However, some knowledge can be gained by simply considering permeability. Such an analysis was carried out on the two sets of PAN fibres representing the extremes of the permeability range. The results are shown in **Table 5.7.**

	PAN Fibres	
	DER 1.5 JS 1.5	DER 2.5 JS 1.0
Total Pore Area cm^2/cm^2	2.3×10^{-5}	3.1×10^{-6}
Pore Radius Ångstrom	100	82
Pore Number $1/cm^2$	7.3×10^{6}	1.4×10^{6}
Distance Between Pores Ångstrom	3.7×10^{4}	8.3×10^{4}
Coated 3% Silicone L_p/r	0.521	0.521
Coated 15% Silicone L_p/r	10.0	6.8

Dope = 25% w/w Polyacrylonitrile in Dimethylformamide

Thickness of Active Layer = **2.1×10^{4} Ångstrom**
or 2.1 micron

Gas Transport by Solution Diffusion (Through Silicone Plugs) and Knudsen Diffusion

Table 5.7 Structure of Polyacrylonitrile Fibres

In the case of the least permeable PAN coated hollow fibres the active layer thickness would still have to be as low as 1000 Å (0.1 micron) if flow through the solid polymer was to contribute to a mere 10% of the total flux. It is clear that exploiting the separation potential of PAN membranes is not without difficulty.

With respect to the accuracy of the predicted PAN membrane structures, it is encouraging to see that **Figure 5.6** indicates an active layer thickness in the region of 2 micron.

5.2.4 Effect of Coating on Membrane Performance

It was shown in section 5.2.2 that the resistance offered by the outer layer of silicone was negligible. For polysulphone membranes with typical surface porosities (10^{-5}) the silicone layer has to be some 20 times thicker (more for PAN) than the active layer of the membrane before its effect becomes at all significant. In the resistance arrangement depicted in **Figure 5.3** any influence of the outer layer of silicone is actually detrimental to the membrane performance, decreasing both permeability and selectivity. The critical parameter in terms of improving selectivity is the depth to which the silicone penetrates the pores, L_p.

However this resistance approach, as suggested by Henis and Tripodi[31][39], may be an over simplification when considering the effect of the silicone. **Figure 5.7** shows a revised resistance model for a coated membrane. The model yields exactly the same set of permeation equations as shown in section 5.2.2

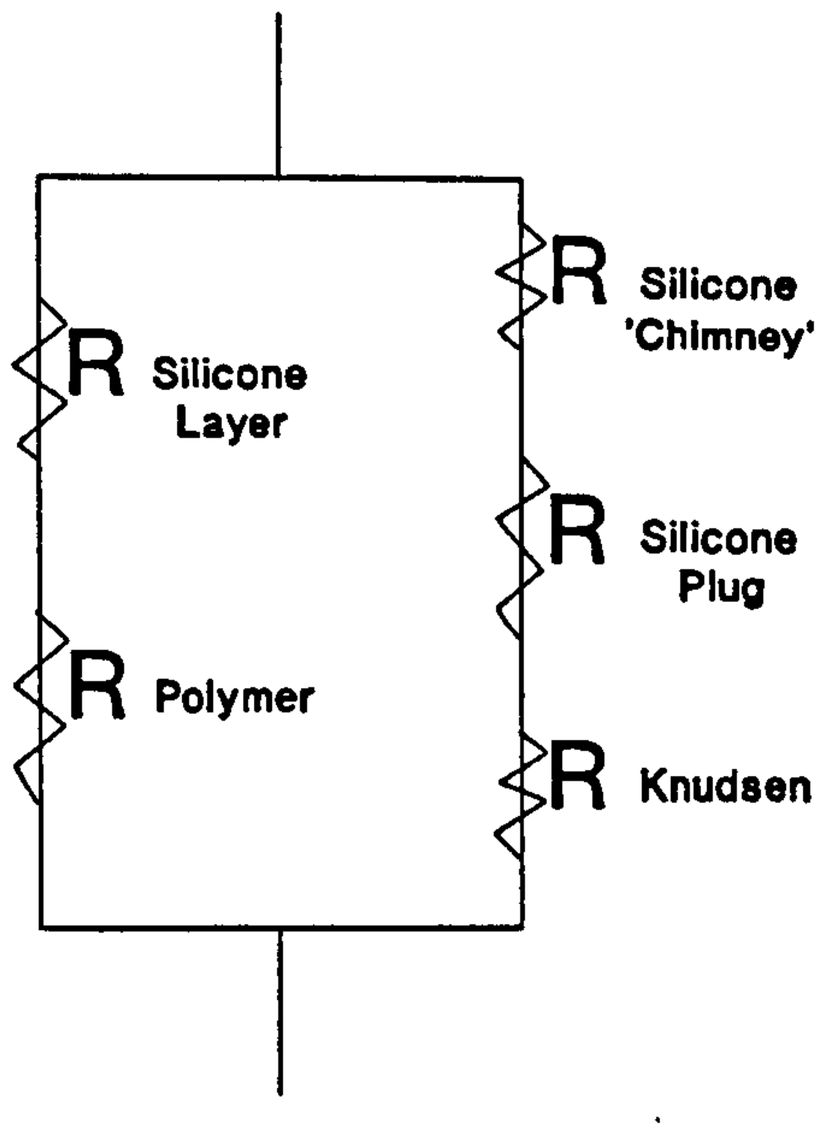

Figure 5.7 Revised Resistance Model

apart from one distinction: the L_p term becomes $(L_p + L_s)$. This basically says that the silicone 'chimney' in the outer silicone layer above the pore plus the penetration depth contributes to the resistance to pore flow. In reality the true effect of the silicone probably lies somewhere between the two resistance models, coating layer thickness contributing significantly to improved selectivity but probably not to the degree of a simple summation with penetration depth. **Figure 5.8** attempts to illustrate these variations in the resistance modelling.

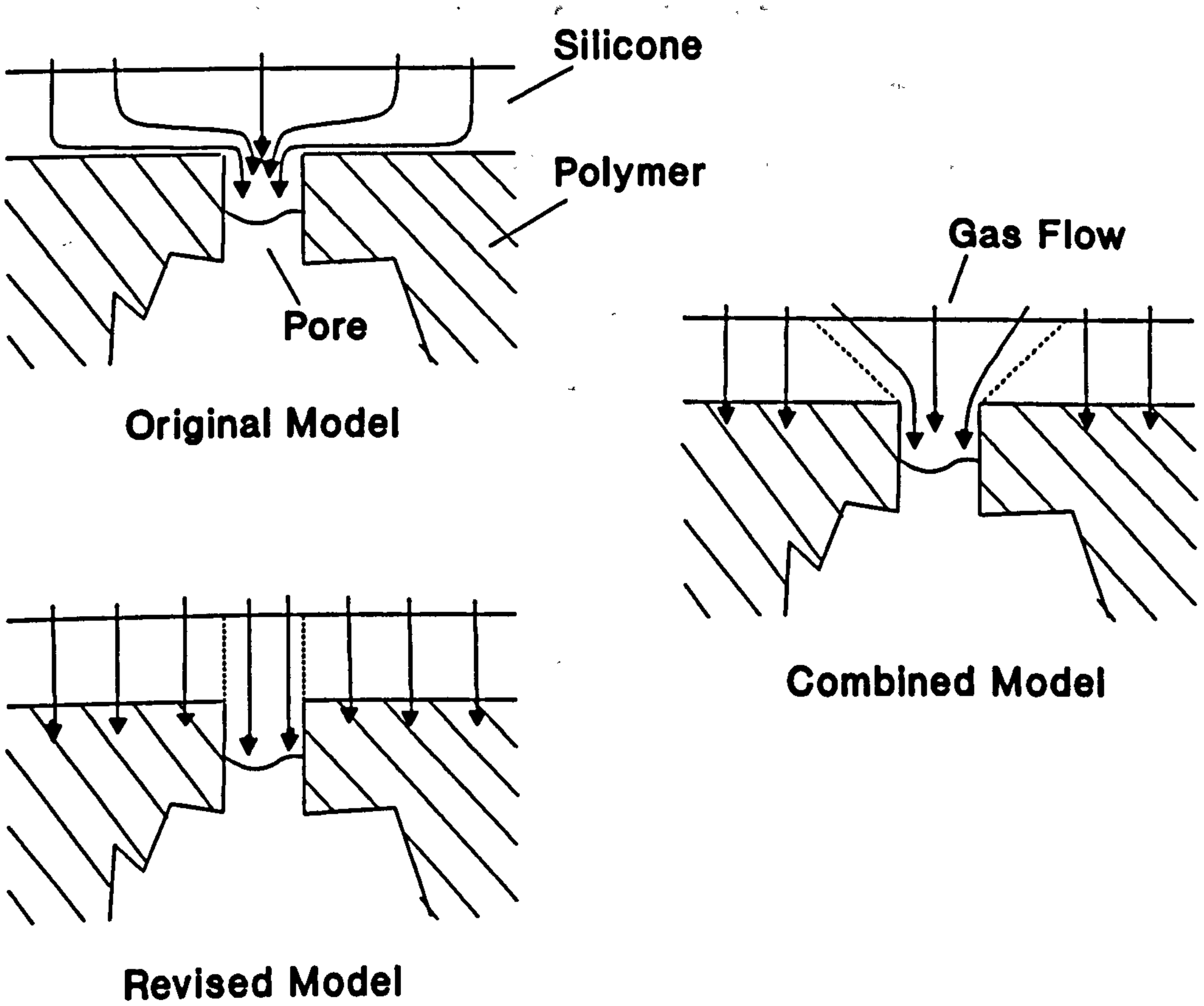

Figure 5.8 Variations in Resistance Modelling

This improved knowledge is inconsequential with regard to the deduction of membrane structure as in section 5.2.3. However, the fresh interpretation of the 'L_p' term brings greater liberty when considering improvements in coating. No longer is increased selectivity limited to that corresponding to full pore penetration ($L_p = L_o$) since the influence of the outer layer of silicone is also advantageous. The effect of improved silicone coating can be studied by freely increasing the 'L_p' term.

For the purposes of the following investigations, the 'L_p' term, which combines penetration depth and the influence of the outer silicone layer, will simply be called 'coating height'. The absolute interpretation of the coating height with respect to actual penetration depth and coating thickness is unclear but the necessity for lengthy unrealistic penetration depths is removed.

5.2.4.1 Improved Coating and the Effect of Dope Extrusion Rate

Graphs 5.9 to **5.11** show the influence of coating height on fibres spun at increasing dope extrusion rate. It can be seen from **Graph 5.9** that after a certain coating height (0.05 micron) little further decrease in permeability is experienced. **Graphs 5.10a** and **5.10b** show an initial rapid improvement in selectivity (increasing to about 30) as coating height builds up to 0.15 micron. However, in order to approach maximum selectivity corresponding to the intrinsic selectivity of the polymer, there requires to be a significant increase in coating height from 0.15 micron to above 1.0 micron. **Graphs 5.10a** and **5.10b** also reflect the increase in the intrinsic selectivity of the polymer with increasing dope extrusion rate.

A maximum efficiency region can be identified: between coating thickness 0.05 and 0.15 micron selectivity rapidly increases from roughly 20 to 30 with no permeability penalty.

The continuing improvement in selectivity after permeability has stabilised is indicated in **Graph 5.11** where the permeability selectivity plots approach the horizontal after about selectivity 20.

Graph 5.9 Permeability Response to Improved Coating at Various Dope Extrusion Rates

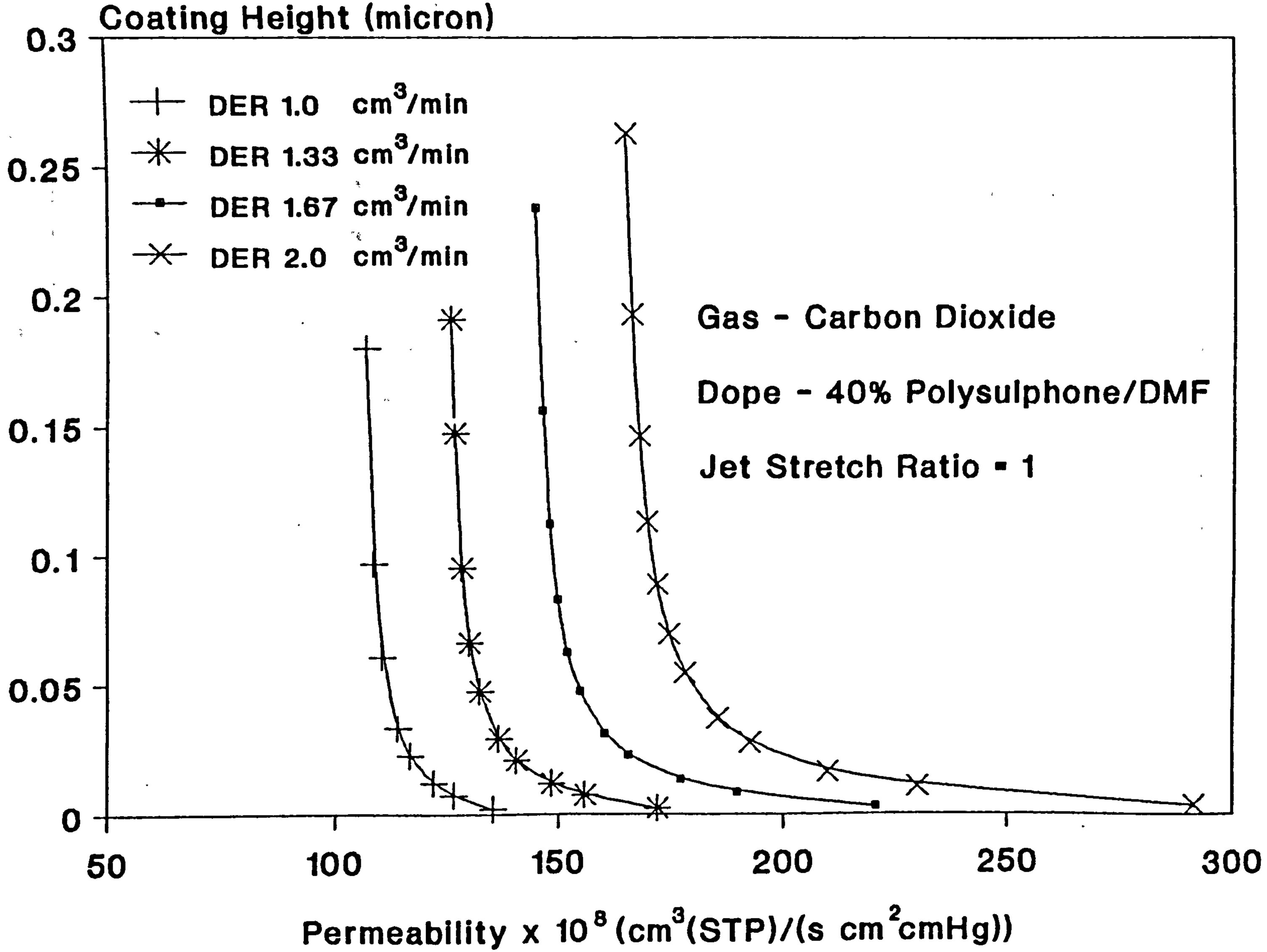

Graph 5.10a Selectivity Response to Improved Coating at Various Dope Extrusion Rates

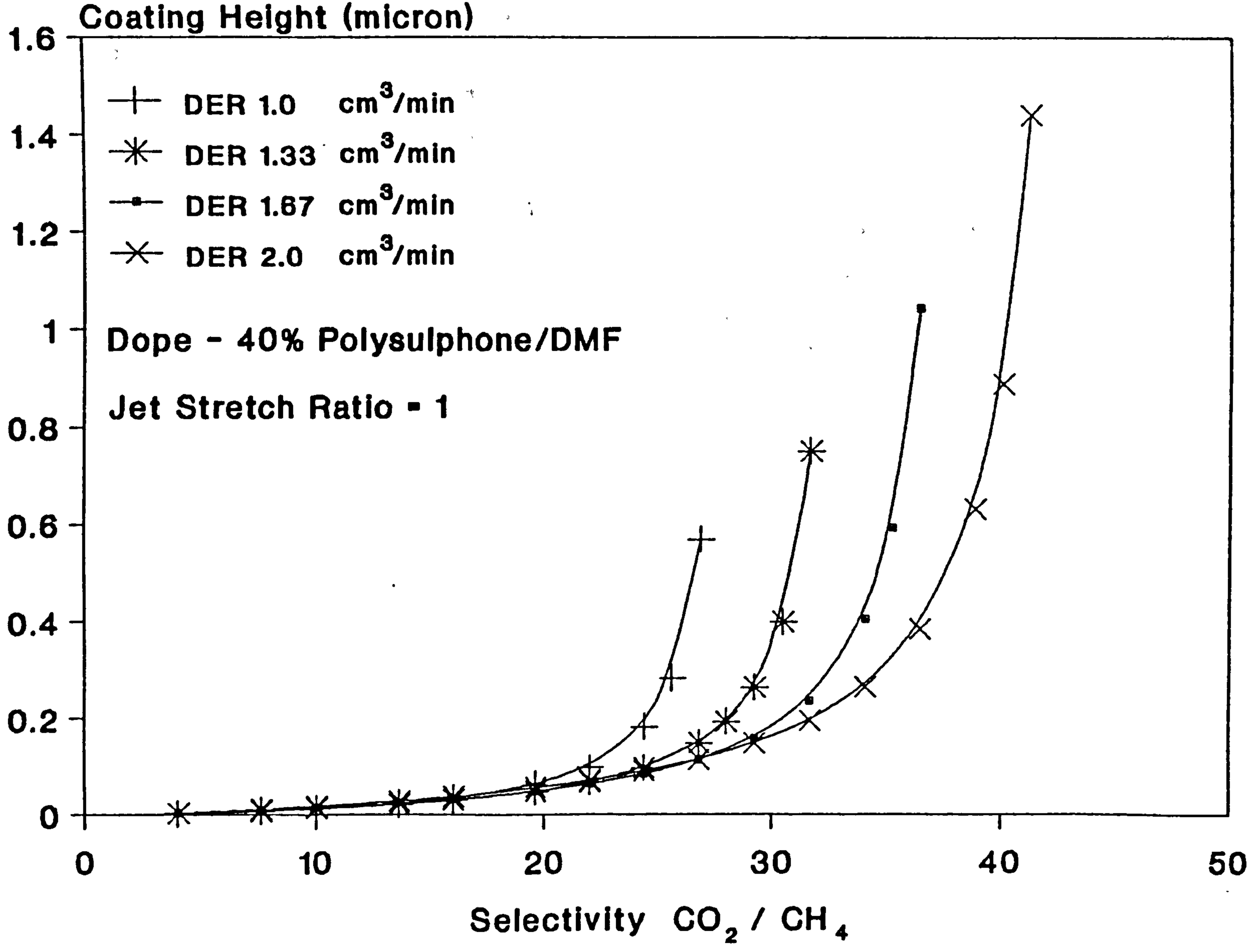

Graph 5.10b Selectivity Response to Improved Coating at Various Dope Extrusion Rates

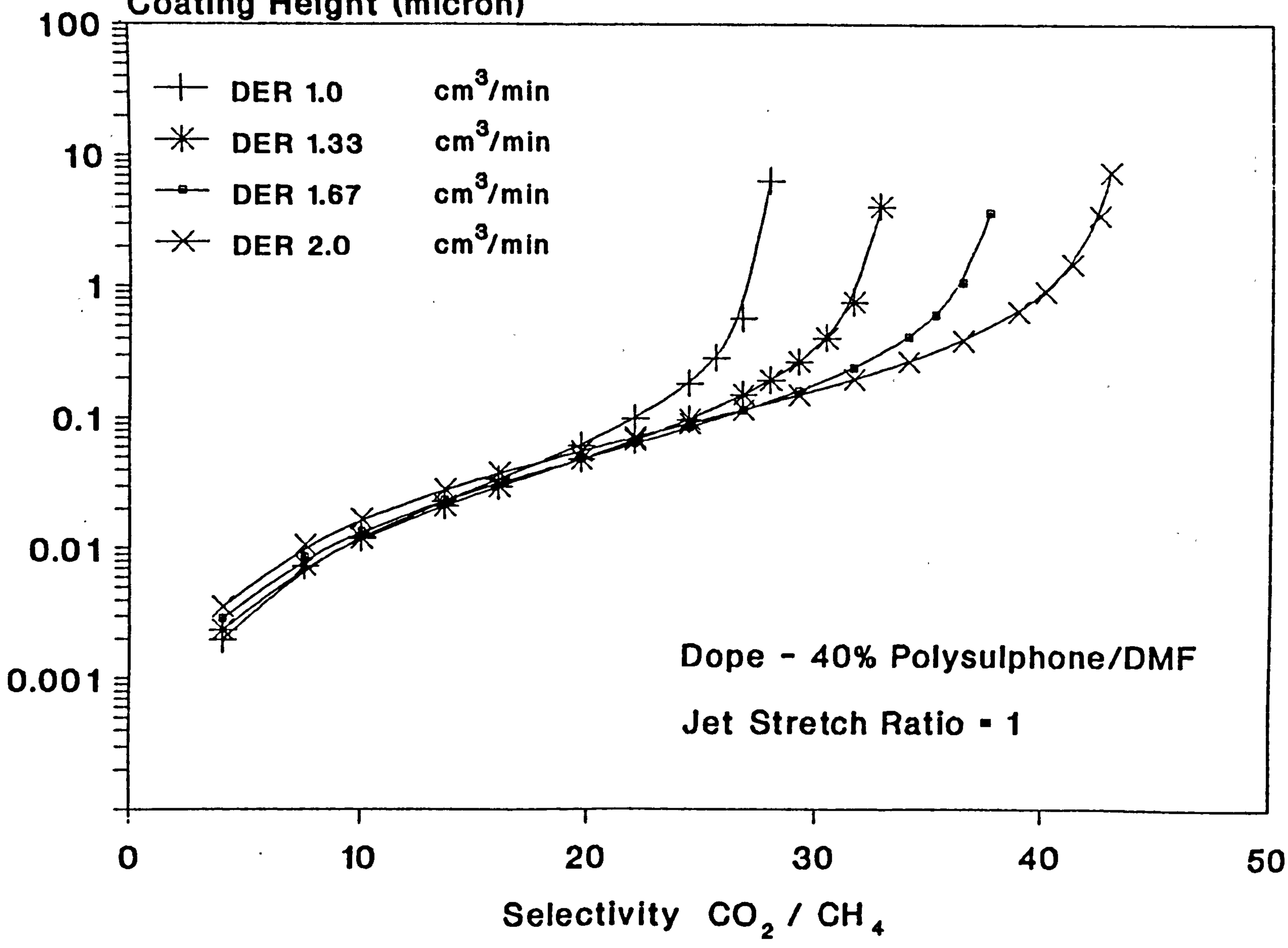

Graph 5.11 Variation of Permeability with Selectivity as a Result of Improved Coating at Various Dope Extrusion Rates

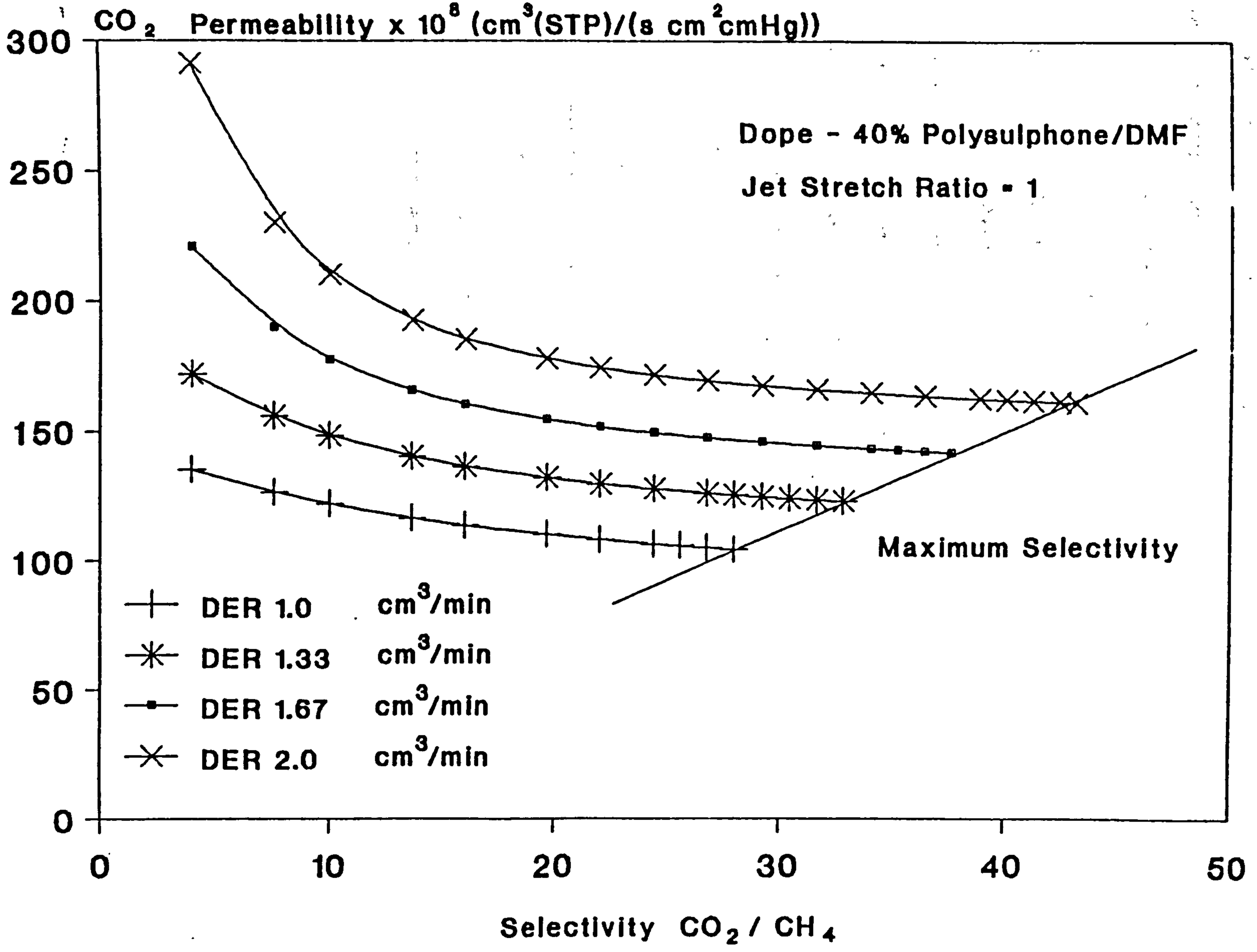

5.2.4.2 Improved Coating and the Comparison of Hollow Fibres from Various Workers

The effect of increasing coating height was investigated for polysulphone fibres spun at the various dope concentrations. The analysis was also carried out on hollow fibres typical of those from two other groups of workers: McIntyre, University of Leeds and Smolders, University of Twente. The results should only be viewed in the context of the current comparison and any absolute interpretation should be avoided. Pore size was simply assumed to be 100Å and intrinsic selectivity assumed to be 28 for all membranes. The modelling was carried out on this basis.

A description of the various fibre types including the main structural details obtained from the modelling is given in **Table 5.8.** **Graphs 5.12** and **5.13** show the influence of coating height on the permeation properties of the membranes.

	Shilton - 20	Shilton - 30	Shilton - 40	M^{c}Intyre[a]	Smolders[b]
Polymer	Polysulphone UDEL P1700	Polysulphone UDEL P1700	Polysulphone UDEL P1700	Polysulphone UDEL P3500	Poly- ethersulphone Victrex 200P
Solvent	DMF	DMF	DMF	95:5 FP:F[c]	93:7 NMP:PA[d]
Dope Concentration	20% w/w	30% w/w	40% w/w	30%w/w	30% w/w
Measured Uncoated P_{CO_2}	700000	40000	190	100000	2000
Measured Uncoated $\Omega_{CH_4}^{CO_2}$	0.7	0.7	2.2	0.7	1.0
Measured Coated P_{CO_2}	10000	5000	150	7000	800
Measured Coated $\Omega_{CH_4}^{CO_2}$	4.5	2.0	4.1	10	20
L_o (micron)	0.14	3.0	4.3	0.1	0.6
A_p (cm^2/cm^2)	250×10^{-6}	330×10^{-6}	0.5×10^{-6}	26×10^{-6}	3×10^{-6}
Silicone Coating	Dow Corning 200/1000cs	Dow Corning 200/1000cs	Dow Corning 200/1000cs	Dow Corning Sylgard 184	Dow Corning Sylgard 184

Pure water as coagulant

[c] FP 1-Formylpiperidine, F Formamide

[d] NMP N-methyl-2-pyrrolodine, PA Polyalcohol

P = Permeability x 10^{6} $\left(\frac{cm^3\,(STP)}{s\ cm^2\ cmHg}\right)$

Ω = Selectivity

Table 5.8 Details of Polysulphone Hollow Fibre Membranes from Various Workers

[a] Ref [36]

[b] Ref [41]

Graph 5.12 Selectivity Response to Improved Coating
Comparison of Polysulphone Hollow Fibres from Various Workers

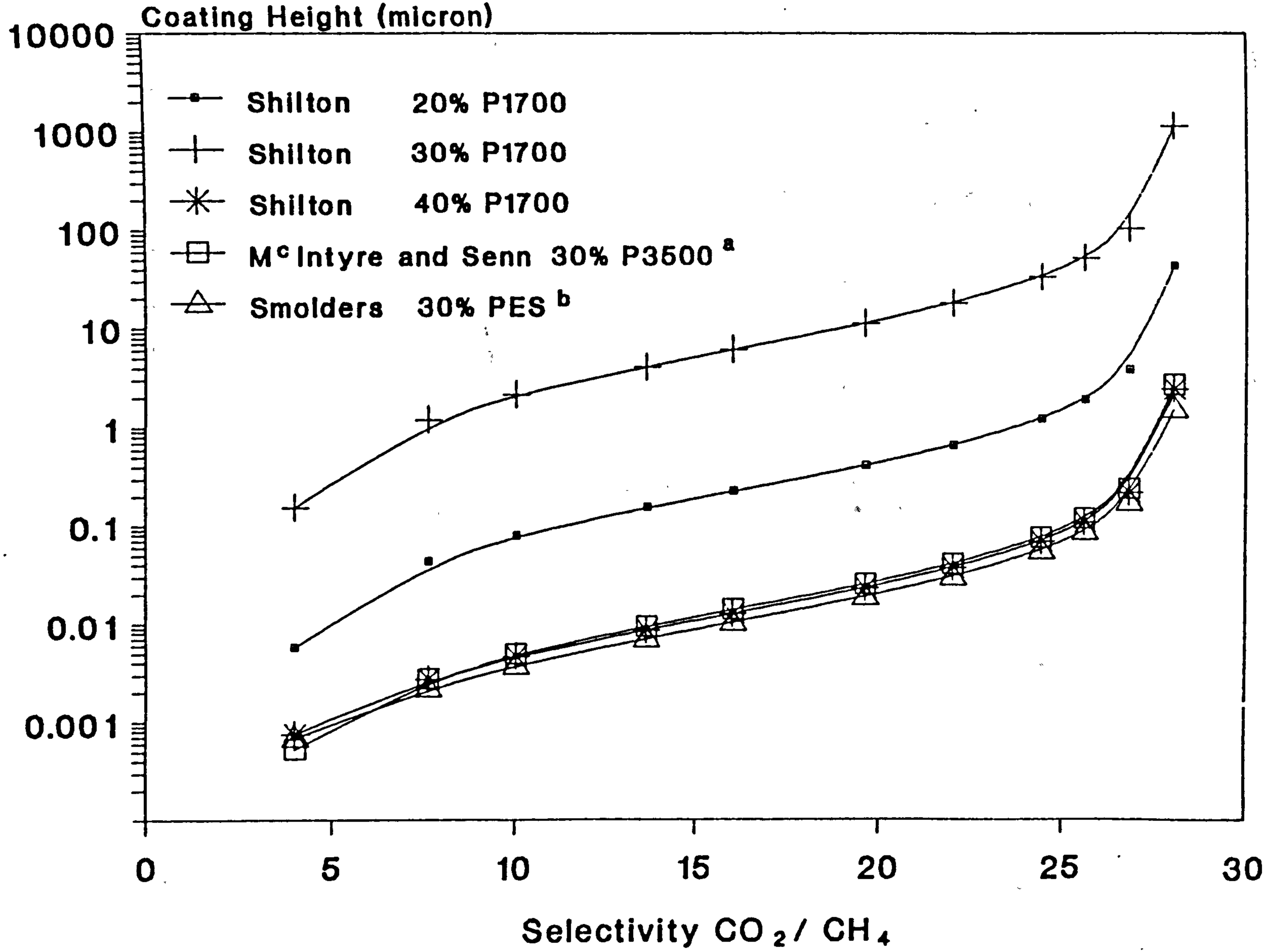

Graph 5.13 Permeability Response to Improved Coating
Comparison of Polysulphone Hollow Fibres from Various Workers

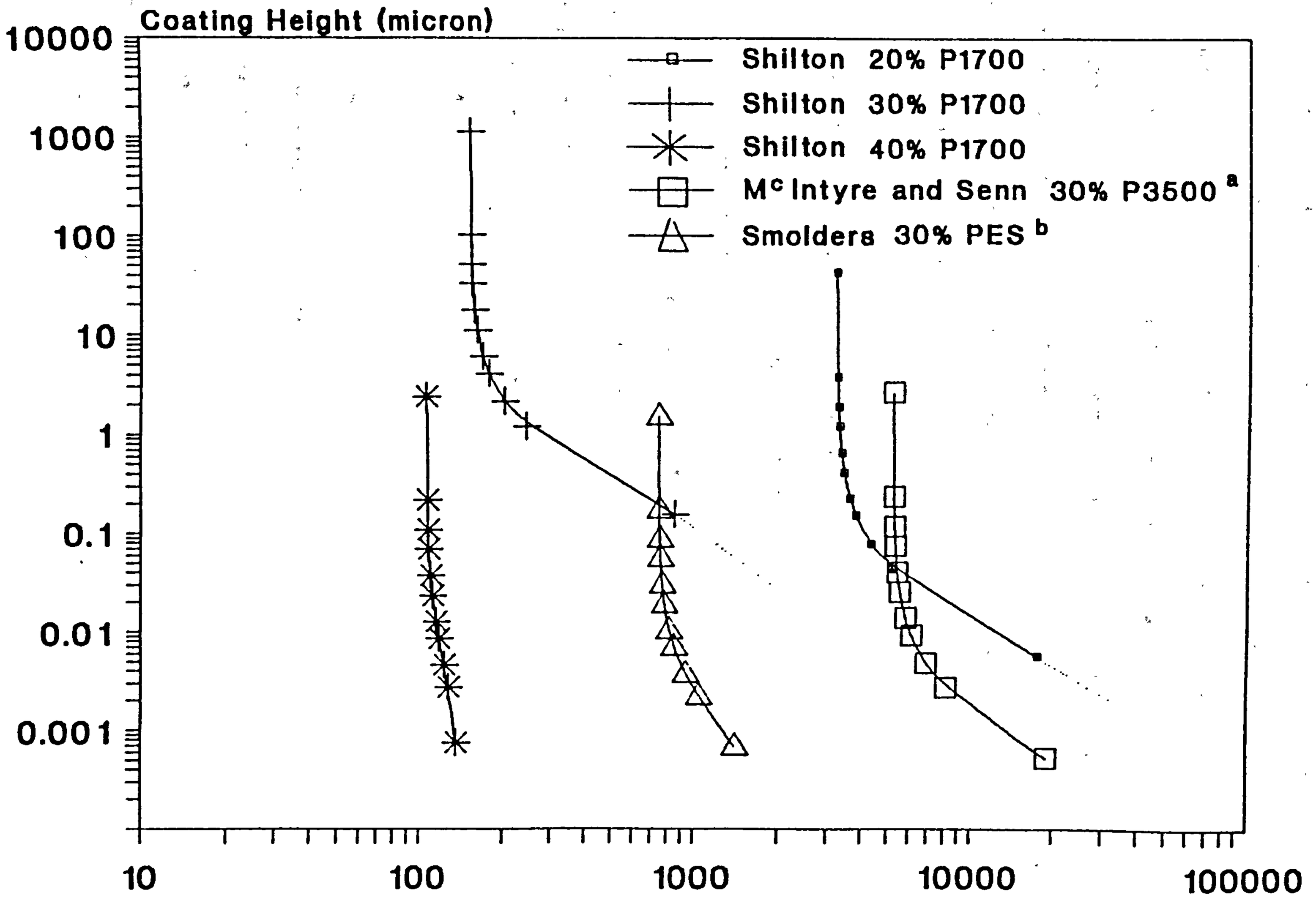

Graph 5.12 shows a rapid rise in selectivity with increasing coating height for all the membranes. The final upturn in the plots represents the final sudden increase in coating height required to achieve maximum selectivity. The 30% home spun P1700 fibres require a large coating height if reasonable selectivity is to be achieved. It is no surprise that these membranes exhibited the lowest coated selectivities (**Graph 4.2**). The 20% fibres due to their thinner active layer require less coating height to attain selectivity.

It is striking that the other three fibre types should all lie on the same plot, requiring the least coating heights for selectivity. **Table 5.8** shows that high selectivities were in fact achieved by the M^{c}Intyre and Smolders groups who both used the Sylgard 184 coating system. It is probable that a marginal increase in the coating effectiveness would significantly boost the selectivities of the 40% spun fibres.

The dependence of selectivity on coating height decreases with decreasing thickness of active layer and decreasing surface porosity. Thus the product of L_o and A_p gives a measure of the reliance of selectivity on coating height. The product of the L_o and A_p values in **Table 5.8** correspond to the position of the plots in **Graph 5.12**.

Permeability increases with decreasing thickness of active layer and increasing surface porosity, the quotient A_p/L_o therefore indicating permeability. The L_o and A_p values in **Table 5.8** reflect the differing permeabilities of the fibres shown in **Graph 5.13.**

The morphological variation in the 30% spun fibres can be attributed to the differing dope solvents and possibly to the differing polysulphone grades. The latter point is more pertinent regarding the fibres from the Smolders group but probably less so in the case of the two UDEL polysulphones where molecular weights are similar **(Table 3.1).**

Finally, **Graph 5.12** indicates that to obtain a selectivity of 4-5, the 20% spun fibres require a coating height 5-8 times greater than that necessary for the 40% spun fibres. This increased coating level was actually achieved in the 20% fibres, indicated by **Graph 4.2**, as a result of their greater pore size **(Table 5.6)** and hence increased silicone penetration depth. The home spun 30% fibres because of similar pore characteristics would have a coating level akin to the 20% fibres but as suggested by **Graph 5.12** and confirmed in **Graph 4.2** this only corresponds to a selectivity of about 2 for these fibres.

Chapter 6 Discussion of Results

6.1 General Discussion of Results

This is intended to be an overall discussion covering the main aspects of this work. Much of the content draws on the substantial discussion of results already given at the 'local level'.

At this stage it is worth emphasising the basis of the spinning variables; dope extrusion rate, DER and jet stretch ratio, JS. When investigating DER it is important to keep JS constant in order to allow the effects of shear in the spinneret to be studied independently. Similarly, when altering JS, DER should remain fixed permitting the influence of elongation alone to be considered. Varying dope flowrate without altering wind-up speed results in a combined variation of DER and JS which leads to an empirical approach. The study of rheological effects with a view to understanding the process of fibre formation must make the clear distinction between DER and JS. Also, in the analysis of the spinning process with respect to fibre dimensions, linear density and porosity (void volume fraction) it is necessary to appreciate the autonomy of these two key spinning variables.

By carrying out a mass balance over the spinning line primary spinning variables and the basic physical properties of the resultant hollow fibres can be interrelated. Fundamentally, hollow fibre dimensions (outer and lumen diameter) are simply dependent on the area of the

spinneret, water injection rate, DER and JS and as such can be effectively predicted. However, as discussed previously, more subtle effects involving contraction on coagulation do influence fibre dimensions to some degree resulting in a slight but observable diameter shift against the predicted values.

It is fairly obvious that fibre porosity will decrease with increasing polymer concentration in the spinning dope and in the ideal case (which assumes no filament volume change on solidification) is easily calculated from dope properties. Porosity provides a convenient method of quantifying the degree of fibre contraction. The contraction factor is defined as the fractional drop in porosity from the ideal to the actual. The contraction factor data illustrated that shrinkage invariably occurs on coagulation, porosity values decreasing from the ideal by between 10 and 20%. At constant fibre residence time in the coagulation bath an increase in contraction factor with increasing dope concentration was noticed.

It is no surprise that linear density (mass/unit length) and hence fibre breaking load increase with increasing dope concentration at any particular JS. However, the tensile properties standardised on the basis of polymer content (linear density) are of greater interest. Tenacity, a measure of the intrinsic strength of the solid polymer within the fibre, increases with dope concentration . This result coupled with the increase in contraction factor may

indicate that polymer molecules become more densely packed with greater cohesion on coagulation as polymer content in the dope increases. As will be discussed later, the thickness of the dense active layer of the fibres increases with dope concentration.

The first modulus, M_1, reflecting the resistance of the polymer to elongation before yield, increases with dope concentration whereas M_2, the resistance after yield, actually decreases with increasing C_D. An explanation involving polymer orientation and cohesive forces between molecules has been offered for this.

physical properties such as porosity, tenacity and moduli are representative of the overall nature of the hollow fibres and exhibit clear correlations with dope concentration. Subtle effects due to varying JS or DER tend to be lost in such parameters. This was also witnessed in the electron microscope work where distinctions in morphology between fibres spun from various dope concentrations were clearly identifiable but variations due to JS and DER were not visually recognised.

JS and DER relate to fine matters such as polymer orientation in the surface skin layer of the membrane and the nature of the surface pores. These aspects are of critical importance in determining the gas separation potential of hollow fibres. The effects of JS and DER are thus only really made manifest in the gas permeation tests.

Clearly dope concentration itself will have a major influence on gas permeation properties. The thickness of the active layer of the membrane and the order of magnitude of the surface porosity (fraction of membrane surface area that is pores) are determined by the concentration of the spinning dope. The general level of coating required to achieve selectivity and the permeability of the fibres are largely established by the dope concentration but there is opportunity for the development of the potential selectivity of the membrane by virtue of JS and DER. To investigate the influence of these two key variables a rheological perspective must be adopted.

Considerations such as composition and temperature of the coagulation bath or the use of solvent additives in the spinning dope have been successfully addressed elsewhere [36][41] with a view to improving fibre morphology and gas separation performance. Studies of this nature target the phase inversion process and coagulation conditions. However, the difficulty of relating alterations in coagulation conditions to gas permeation properties due to the complexity of the solidification process inevitably results in these studies tending to the empirical.

This work has attempted to differentiate between rheological influences and those of phase inversion. The wider influence of dope concentration which relates to the phase inversion process has been mentioned and must be considered but it is the study of JS and DER at fixed C_D

that carries more potential for an increased understanding of the science of spinning hollow fibre membranes. This program of research has considered the rheological implications of JS and DER and has predicted the structure and polymer characteristics of the resultant membranes in the light of gas separation properties.

Spinning dopes were studied under shear rates representative of those experienced during actual spinning. All dopes showed classical shear thinning behaviour with the exception of the lowest concentration of polysulphone which exhibited the second Newtonian region. The power law index decreased with increasing polymer concentration in both the polysulphone and polyacrylonitrile dopes. From the rheological data the flow characteristics of the various dopes in the spinneret were determined under the conditions of extrusion.

Maximum shear rates occur at the walls of the spinneret and increase in direct proportion to the dope extrusion rate. It was demonstrated that at equivalent dope extrusion rates, shear rate also increases with increasing dope concentration: the decrease in power law index results in a flattening of the velocity profile and the velocity gradient increases at the spinneret walls. Obviously there is a considerable increase in shear stress and pressure drop with increasing dope concentration due to the rise in viscosity.

When tested under elongation, all of the dopes displayed strain thinning behaviour. As explained, such a decrease in extensional viscosity with strain rate indicates inherent 'unspinnability'. This was reflected in the difficulty of early solid fibre dry jet wet spinning trials where fibre breakage was frequent. Lack of spinnability is counteracted in hollow fibre extrusion by the immediate coagulation from within. However, breakages were still frequent when hollow fibres were spun at jet stretch ratios greater than about two.

The Trouton ratio relates the behaviour of the spinning dopes under elongation and shear, values greater than three indicating viscoelasticity. Trouton ratios were high for all dopes at low strain rates suggesting a considerable degree of elasticity. The ratio then drops which implies a decline in viscoelastic properties as strain rate progresses. However, over the strain rates experienced during spinning, the Trouton ratios reflect viscoelastic behaviour for all dopes.

Under creep, viscoelastic behaviour was not detected in the low and medium concentration dopes of both polysulphone and polyacrylonitrile. The minimum strain levels that could be tested (dependent on sample viscosity) were not sufficiently low for these dopes to exhibit elastic behaviour under creep. However, viscoelasticity was detected in the most concentrated dopes of both polymer types.

As described, normal stress measurements proved difficult because of sample loss. Nevertheless, normal stresses were detected in the medium and high concentration polyacrylonitrile dopes. Recoverable shear values indicated significant viscoelasticity in these dopes.

In all of the circumstances that indicate viscoelasticity; degree of shear thinning (power law index), rate of decline of Trouton ratio with strain rate, creep analysis and normal stress measurement, viscoelastic behaviour was more obvious in the polyacrylonitrile dopes. This would be as expected due to the higher molecular weight of the polymer, 107,500 compared to 35,400 for the polysulphone.

The polysulphone hollow fibres exhibited vastly superior gas separation properties in comparison to those spun from polyacrylonitrile. As has been discussed, it is the extremely low intrinsic permeability of the polyacrylonitrile polymer that results in the consistently poor performance of these membranes. As a consequence, the investigation of the effect of spinning conditions on gas separation performance mainly focused on polysulphone fibres.

Permeability was found to decrease with increasing dope concentration. Coating obviously reduced permeability and the effect was more marked with fibres spun at low dope concentration. Before coating the 20% and 30% spun polysulphone fibres exhibited poor selectivities, those

associated with Knudsen diffusion or pore flow dominance. The 40% spun membranes did show solution diffusion properties achieving selectivities of over 2 in favour of CO_2 over CH_4. After coating the fibres from all three dope concentrations exhibited solution diffusion selectivities. The 20% and 40% spun fibres showed values between 4-5 but the selectivities of the 30% fibres were disappointing, barely reaching 2.

These results are explained by the gas transfer modelling work. Thickness of membrane active layer, L_o increases with increasing C_D whilst total pore area on the membrane surface, A_p decreases with increasing dope concentration. Coated fibre selectivities increase with decreasing pore area but decrease with increasing thickness of active layer because of limitations regarding silicone penetration depth. As a result the product of A_p and L_o largely controls selectivity; a thin active layer and low pore area corresponds to a high selectivity. The 30% spun fibres have both a thick active layer and a large pore area causing the poor selectivity of these membranes in comparison to those spun from the other two dope concentrations.

permeability increases with increasing pore area and decreasing thickness of active layer. Permeability decreases with increasing dope concentration because the ratio A_p/L_o decreases.

The gas transfer modelling, water permeation tests and variation of permeability with pressure measurements all show that pore size decreases with increasing dope concentration. (Coated fibre selectivity values have some degree of sensitivity with regard to pore size; coating height increasing with increased pore size by virtue of the resultant increased silicone penetration depth. This finer effect finally accounts for the similarity in the selectivities of the 40% and 20% spun fibres. For any one fibre type an increase in selectivity due to increased coating height is always accompanied by a decrease in permeability.)

The 40% spun membranes, because of their superior separation characteristics in the raw uncoated state, were targeted for studying the effects of jet stretch and dope extrusion rate on fibre performance.

permeability increases and selectivity decreases with increasing jet stretch ratio for both uncoated and coated fibres. These results can be explained by morphological variations in the membranes as suggested by the gas transfer modelling. As jet stretch increases both pore area and pore size increases. The most interesting effect from a purely rheological standpoint is the apparent decrease in the intrinsic selectivity of the solid polymer as jet stretch increases. The elongational viscosity tests carried out on the spinning dopes indicated reluctance to stretching flow. This lack of molecular cohesion under

elongation may result in an unfavourable molecular structure, with respect to selectivity, on polymer solidification.

The effect of dope extrusion rate on fibre structure and hence gas permeation performance provided the most interesting results of this work. Permeability increases with increasing DER for both coated and uncoated fibres. Not surprisingly, selectivity decreases with increasing DER for uncoated membranes but the selectivity result for the coated membranes is striking. Selectivity as well as permeability increases with dope extrusion rate once the fibres have been coated. The gas permeation modelling showed that pore area and pore size increase with DER accounting for the rise in permeability. However, it is the substantial increase in the intrinsic selectivity of the solid polymer that is sufficient to actually cause an increase in selectivity with increasing DER even at the generally low coating penetration levels.

The dope extrusion rate results can be related to the rheological behaviour of the spinning dopes under shear. All dopes exhibited shear thinning behaviour. It could be suggested that as the shear rates in the vicinity of the spinneret wall increase due to increasing DER, the polymer molecules become more aligned. It is this enhanced orientation that may be the cause of the improving intrinsic selectivity of the polymer with increasing DER.

Viscoelastic effects would certainly explain the presence of a highly orientated skin region. Coagulation occurs rapidly on extrusion and thus structure is 'frozen' into the fibre wall before relaxation can take place. Further coagulation of the relaxed core by diffusion results in the differing morphology between skin and core. This is a well documented phenomenon with respect to textile fibre spinning[59].

The effect of coating height (combination of silicone penetration depth and thickness of outer silicone layer) on membrane performance was investigated using the gas transfer modelling techniques. The main observation from this study was the high potential for improved selectivities with little permeability penalty. A minor improvement in coating deposition results in a major improvement in selectivity. However, it must be said that a large increase in coating level is required to finally approach maximum selectivity which corresponds to the intrinsic selectivity of the polymer.

predicting the effect of coating height allowed comparison to be made with fibres from other workers. As explained, the dependence of selectivity on coating height hinges on the product of the thickness of the active layer and the pore area of a membrane. This factor proved to be very similar for the 40% w/w spun fibres and those representative of both the McIntyre[36] and Smolders[41] groups. Relatively low coating heights were required in

these fibres for selectivity. High selectivities were in fact achieved in practice by the McIntyre and Smolders groups who both used the Sylgard 184 coating system, a different system to that used in this work. It is very probable that a marginal increase in the coating effectiveness would significantly boost the selectivity of at least the 40% spun fibres.

The nitrogen and oxygen permeation results and those relating to gas mixtures are included in Appendix B for completeness. A study of these results in themselves was considered superfluous to the main aims of this project.

Details of the one polysulphone P3500 hollow fibre spinning campaign are included in Appendix A again for completeness. These fibres proved to be redundant for the current purposes.

6.2 Conclusions

1. The extremely low inherent permeability of the polymer caused the polyacrylonitrile membranes to exhibit consistently poor gas separation properties. As a consequence, the investigation of the effect of spinning conditions on membrane performance focused on polysulphone hollow fibres.

2. Fundamental fibre properties such as outer and lumen diameter, porosity (void volume fraction) and linear density are simply related to basic spinning variables.

3. Intrinsic polymer strength as well as hollow fibre mechanical properties improve with increasing dope concentration.

4. Permeability decreases with increasing dope concentration for both uncoated and coated fibres. Coating reduces permeability, the effect being more marked with the high permeability fibres spun at low dope concentration.

5. Membrane active layer thickness and order of magnitude of surface porosity (fraction of surface area that is pores) are determined by the spinning dope concentration. Active layer thickness increases whilst

surface porosity decreases with increasing dope concentration. Permeability increases as the ratio of surface porosity to active layer thickness increases.

6. Uncoated membrane selectivities are poor because surface porosity levels are sufficiently high (> 10^{-6}) to cause pore flow to dominate. Selectivity increases as the product of the active layer thickness and the surface porosity decreases. On coating the effects of surface porosity are diminished allowing the solid polymer to influence selectivity. The lowest coated selectivities occur with the fibres spun from the medium spinning dope concentration because both surface porosity and active layer thickness are high in these membranes.

7. Permeability increases and selectivity decreases with increasing jet stretch ratio for both uncoated and coated fibres. Surface porosity increases and the intrinsic selectivity of the polymer decreases with increasing jet stretch.

8. Permeability increases and selectivity decreases with increasing dope extrusion rate for uncoated membranes. For coated membranes <u>both</u> permeability and selectivity increase with increasing dope extrusion rate. Surface porosity increases with dope extrusion rate accounting for the rise in permeability. However, the rise in the

intrinsic selectivity of the polymer is sufficient to cause an increase in selectivity as well as in permeability with increasing dope extrusion rate on coating.

9. Rheological conditions, controlled by jet stretch and dope extrusion rate, determine the intrinsic separation characteristics of the polymer which correspond to the highest selectivity theoretically attainable by any particular membrane. To maximise the potential selectivity a low jet stretch ratio and high dope extrusion rate should be employed thus achieving the most favourable polymer structure.

10. The influence of surface porosity determines the extent to which the potential properties of a specific membrane are reflected in practice. As the effect of surface porosity decreases, by virtue of increasing silicone coating levels, selectivity rapidly increases approaching the intrinsic maximum. The accompanying decrease in permeability is moderate approaching a level dependent on active layer thickness. A minimum active layer thickness is desirable to maximise this ultimate permeability. A low dope concentration is favourable in this regard.

6.3 Recommendations for Future Work

1. The conditions of phase inversion should be improved with respect to decreasing surface porosity and decreasing active layer thickness. Simply decreasing spinning dope concentration decreases active layer thickness but increases surface porosity. Coating counteracts the detremental effects of surface porosity. The optimisation problem that arises between these various effects could be addressed.

2. The nature of silicone deposition could be investigated with a view to improving coating techniques. The influence of the outer silicone layer compared with penetration depth should be understood. With reference to the particular fibres spun in this work, the Sylgard 184 coating system is likely to provide immediate improvement in coating and hence selectivity.

3. The effect of jet stretch ratio and dope extrusion rate on polymer structure and hence membrane gas separation potential should be further investigated by employing techniques for the direct measurement of polymer orientation.

4. The potentially very high separation properties of polyacrylonitrile should be pursued if techniques to provide low surface porosities, low active layer thicknesses and improved coating techniques were developed. The larger molecules and greater viscoelasticity of the polyacrylonitrile spinning dope may lead to the polymer being more conducive to orientation than polysulphone. The scope to enhance potential selectivity by means of increasing dope extrusion rate may therefore be greater for polyacrylonitrile hollow fibres than for polysulphone.

Appendix A Details of Spinning Campaigns

Table A1. Spinning Campaign 1

Run	D.E.R. (cm^3/min)	L.E.R. (cm/s)	W.I.R. (cm^3/min)	W.U.S. (cm/s)	J.S. (--)
1.1	1.5	12.68	0.585	12.68	1.0
1.2	1.5	12.68	0.585	16.91	1.33
1.3	1.5	12.68	0.585	21.13	1.67
1.4	1.5	12.68	0.585	25.36	2.0
1.5	1.0	8.45	0.585	8.45	1.0
1.6	2.0	16.90	0.585	16.90	1.0
1.7	2.5	21.13	0.585	21.13	1.0

Dope : 30% w/w Polysulphone (P1700) in DMF

Spinneret N^o 1

Dope Temperature 25^oC

N_2 Blanket Pressure 20 psig

Dry Jet Height 3.5 cm

W.I.R. Constant

No Secondary Stretching

Coagulation Bath Temperature 4^oC

All Baths Pure Water

Table A2. Spinning Campaign 2

Run	D.E.R. (cm^3/min)	L.E.R. (cm/s)	W.I.R. (cm^3/min)	W.U.S. (cm/s)	J.S. (--)
2.1	0.7	5.92	0.235	5.92	1.0
2.2	1.0	8.45	0.335	5.92	0.7
2.3	1.0	8.45	0.335	8.45	1.0
2.4	1.0	8.45	0.335	12.68	1.5
2.5	1.0	8.45	0.335	16.90	2.0
2.6	1.5	12.68	0.500	12.68	1.0
2.7	2.0	16.90	0.665	16.90	1.0
2.8	1.0	8.45	0.335	8.45	1.0
2.9	1.0	8.45	0.335	16.90	2.0
2.10	0.7	5.92	0.235	5.92	1.0

Dope : 30% w/w Polysulphone (P1700) in DMF

Spinneret N^o 1

Dope Temperature 25^oC

N_2 Blanket Pressure 20 psig

Dry Jet Height 3.5 cm

D.E.R./W.I.R. = Constant

No Secondary Stretching

Coagulation Bath Temperature 4^oC

All Baths Pure Water

Table A3. Spinning Campaign 3

Run	D.E.R. (cm^3/min)	L.E.R. (cm/s)	W.I.R. (cm^3/min)	W.U.S. (cm/s)	J.S. (--)
3.1	0.7	5.92	0.235	5.92	1.0
3.2	1.0	8.45	0.335	5.92	0.7
3.3	1.0	8.45	0.335	8.45	1.0
3.4	1.0	8.45	0.335	12.68	1.5
3.5	1.0	8.45	0.335	16.90	2.0

Dope : 40% w/w Polysulphone (P1700) in DMF

Spinneret N^o 1

Dope Temperature 25^{o}C

N_2 Blanket Pressure 20 psig

Dry Jet Height 3.5 cm

D.E.R./W.I.R. = Constant

No Secondary Stretching

Coagulation Bath Temperature 4^{o}C

All Baths Pure Water

Table A4. Spinning Campaign 4

Run	D.E.R. (cm^3/min)	L.E.R. (cm/s)	W.I.R. (cm^3/min)	W.U.S. (cm/s)	J.S. (--)
4.1	1.0	8.45	0.335	5.92	0.7
4.2	1.0	8.45	0.335	8.45	1.0
4.3	1.0	8.45	0.335	16.90	2.0
4.4	2.0	16.90	0.665	16.90	1.0

Dope : 20% w/w Polysulphone (P1700) in DMF

Spinneret N^O 1

Dope Temperature 25^oC

N_2 Blanket Pressure 20 psig

Dry Jet Height 3.5 cm

D.E.R./W.I.R. = Constant

No Secondary Stretching

Coagulation Bath Temperature 4^oC

All Baths Pure Water

Table A5. Spinning Campaign 5

Run	D.E.R. (cm^3/min)	L.E.R. (cm/s)	W.I.R. (cm^3/min)	W.U.S. (cm/s)	J.S. (--)
5.1	0.7	5.92	0.235	5.92	1.0
5.2	1.0	8.45	0.335	5.92	0.7
5.3	1.0	8.45	0.335	8.45	1.0
5.4	1.0	8.45	0.335	16.90	2.0
5.5	2.0	16.90	0.665	16.90	1.0

Dope : 30% w/w Polysulphone (P3500) in DMF

Spinneret N^O 1

Dope Temperature 25^oC

N_2 Blanket Pressure 20 psig

Dry Jet Height 3.5 cm

D.E.R./W.I.R. = Constant

No Secondary Stretching

Coagulation Bath Temperature 4^oC

All Baths Pure Water

Table A6. Spinning Campaign 6

Run	D.E.R. (cm^3/min)	L.E.R. (cm/s)	W.I.R. (cm^3/min)	W.U.S. (cm/s)	J.S. (--)
6.1	1.0	8.45	0.335	5.59	0.66
6.2	1.0	8.45	0.335	8.45	1.0
6.3	1.0	8.45	0.335	12.68	1.5
6.4	1.0	8.45	0.335	16.90	2.0
6.5	1.5	12.68	0.500	12.68	1.0

Dope : 25% w/w Polyacrylonitrile (P82) in DMF

Spinneret N^{o} 1

Dope Temperature 25^{o}C

N_2 Blanket Pressure 20 psig

Dry Jet Height 3.5 cm

D.E.R./W.I.R. = Constant

No Secondary Stretching

Coagulation Bath Temperature 4^{o}C

All Baths Pure Water

Table A7. Spinning Campaign 7

Run	D.E.R. (cm^3/min)	L.E.R. (cm/s)	W.I.R. (cm^3/min)	W.U.S. (cm/s)	J.S. (--)
7.1	1.0	8.45	0.335	8.45	1.0
7.2	1.5	12.68	0.500	7.60	0.6
7.3	1.5	12.68	0.500	12.68	1.0
7.4	1.5	12.68	0.500	19.04	1.5
7.5	1.5	12.68	0.500	22.34	1.76
7.6	2.0	16.90	0.665	16.90	1.0
7.7	2.5	21.13	0.835	21.13	1.0
7.8	2.0	16.90	0.665	7.08	0.42
7.9	1.5	12.68	0.500	7.08	0.56

Dope : 25% w/w Polyacrylonitrile (P82) in DMF

Spinneret N^o 1

Dope Temperature 25°C

N_2 Blanket Pressure 20 psig

Dry Jet Height 3.5 cm

D.E.R./W.I.R. = Constant

No Secondary Stretching

Coagulation Bath Temperature 4°C

All Baths Pure Water

Table A8. Spinning Campaign 8

Run	D.E.R. (cm^3/min)	L.E.R. (cm/s)	W.I.R. (cm^3/min)	W.U.S. (cm/s)	J.S. (--)
8.1	1.0	8.45	0.335	8.45	1.0
8.2	1.5	12.68	0.500	12.68	1.0
8.3	2.0	16.90	0.665	16.90	1.0
8.4	2.5	21.13	0.835	21.13	1.0
8.5	3.0	25.35	1.000	25.35	1.0
8.6	1.5	12.68	0.500	7.60	0.6
8.7	1.5	12.68	0.500	14.78	1.17
8.8	1.5	12.68	0.500	16.21	1.28

Dope : 40% w/w Polysulphone (P1700) in DMF

Spinneret N^o 1

Dope Temperature 25°C

N_2 Blanket Pressure 20 psig

Dry Jet Height 3.5 cm

D.E.R./W.I.R. = Constant

No Secondary Stretching

Coagulation Bath Temperature 4°C

All Baths Pure Water

Table A9. Spinning Campaign 9

Run	D.E.R. (cm^3/min)	L.E.R. (cm/s)	W.I.R. (cm^3/min)	W.U.S. (cm/s)	J.S. (--)
9.1	1.0	8.45	0.335	8.45	1.0
9.2	1.5	12.68	0.500	12.68	1.0

Dope : 40% w/w Polysulphone (P1700) in DMF

Spinneret N^o 1

Dope Temperature 25^oC

N_2 Blanket Pressure 20 psig

Dry Jet Height 3.5 cm

D.E.R./W.I.R. = Constant

No Secondary Stretching

Coagulation Bath Temperature 4^oC

All Baths Pure Water

Appendix B Gas Permeation Results

Table B1. Uncoated Fibres - Campaign 2

Pure Gas Permeation Results

Run	P CO_2	P CH_4	P O_2	P N_2	Ω CO_2 / CH_4	Ω O_2 / N_2
2.1	0.809	0.997	0.751	0.782	0.81	0.96
2.2	0.230	0.184	0.152	0.137	1.25	1.11
2.3				1.243		
2.4	4.148	5.196	3.998	4.303	0.80	0.93
2.5	6.369	9.585	6.193	5.833	0.66	1.06
2.6				2.013		
2.7	12.90	20.93	13.80	13.94	0.62	0.99
2.8	1.287	1.754	1.210	1.233	0.73	0.98
2.9				8.271		
2.10	0.830	0.941	0.642	0.684	0.88	0.94

P = Permeability x 10^4 (cm^3(STP)/s cm^2 cmHg)

Ω = Selectivity

Table B2. Uncoated Fibres - Campaign 2

Gas Mixture Permeation Results

Run	P_{CO_2}	P_{CH_4}	$\Omega^{CO_2}_{CH_4}$	$\alpha^{CO_2}_{CH_4}$		P_{O_2}	P_{N_2}	$\Omega^{O_2}_{N_2}$	$\alpha^{O_2}_{N_2}$
2.1	0.880	0.879	1.00	1.00		0.719	0.709	1.01	1.01
2.2	0.234	0.169	1.39	1.31		0.156	0.132	1.18	1.15
2.3									
2.4	3.900	4.280	0.91	0.93		3.600	3.654	0.99	0.99
2.5	7.118	7.970	0.89	0.91		6.837	6.957	0.98	0.99
2.6									
2.7	16.62	16.83	0.99	0.99		16.52	16.39	1.01	1.01
2.8	1.389	1.481	0.94	0.95		1.201	1.206	1.00	1.00
2.9									
2.10	0.840	0.822	1.02	1.02		0.676	0.657	1.03	1.02

P = Permeability X 10^4 (cm^3(STP)/s cm^2 cmHg)

Ω = Selectivity

α = Separation Factor

Table B3. Coated[a] Fibres - Campaign 2

Pure Gas Permeation Results

Run	P CO_2	P CH_4	P O_2	P N_2	CO_2 Ω CH_4	O_2 Ω N_2
2.1	0.388	0.364	0.291	0.260	1.07	1.12
2.2	0.138	0.075	0.076	0.059	1.84	1.29
2.3						
2.4	0.548	0.253	0.228	0.146	2.16	1.56
2.5	0.597	0.269	0.267	0.176	2.22	1.52
2.6						
2.7	11.57	18.29	13.18	13.79	0.63	0.96
2.8	0.468	0.420	0.347	0.302	1.11	1.15
2.9						
2.10	0.397	0.343	0.286	0.261	1.16	1.10

[a] Coating Solution - 3% w/w Silicone in Hexane

P = Permeability x 10^4 (cm^3(STP)/s cm^2 cmHg)

Ω = Selectivity

Table B4. Coated[a] Fibres - Campaign 2

Gas Mixture Permeation Results

Run	P_{CO_2}	P_{CH_4}	$\Omega^{CO_2}_{CH_4}$	$\alpha^{CO_2}_{CH_4}$		P_{O_2}	P_{N_2}	$\Omega^{O_2}_{N_2}$	$\alpha^{O_2}_{N_2}$
2.1	0.463	0.370	1.25	1.20		0.313	0.289	1.08	1.07
2.2	0.151	0.083	1.81	1.64		0.077	0.059	1.30	1.25
2.3									
2.4	0.610	0.305	2.00	1.79		0.249	0.176	1.41	1.34
2.5	0.663	0.316	2.10	1.86		0.291	0.226	1.29	1.23
2.6									
2.7	17.10	16.87	1.01	1.01		16.15	16.15	1.00	1.00
2.8	0.540	0.444	1.22	1.18		0.387	0.358	1.08	1.07
2.9									
2.10	0.438	0.348	1.26	1.21		0.314	0.285	1.10	1.08

[a] Coating Solution - 3% w/w Silicone in Hexane

P = Permeability X 10^4 (cm^3(STP)/s cm^2 cmHg)

Ω = Selectivity

α = Separation Factor

Table B5. Uncoated Fibres - Campaign 3

Pure Gas Permeation Results

Run	**P** CO_2	**P** CH_4	**P** O_2	**P** N_2	CO_2 **Ω** CH_4	O_2 **Ω** N_2
3.1	0.0097	0.0032	0.0042	0.0034	3.03	1.24
3.2	0.0167	0.0069	0.0082	0.0061	2.42	1.34
3.3	0.0140	0.0080	0.0079	0.0067	1.75	1.18
3.4	0.0352	0.0389	0.0303	0.0242	0.90	1.25
3.5						

P = Permeability x 10^4 (cm^3(STP)/s cm^2 cmHg)

Ω = Selectivity

Table B6. Uncoated Fibres - Campaign 3

Gas Mixture Permeation Results

Run	P_{CO_2}	P_{CH_4}	$\Omega^{CO_2}_{CH_4}$	$\alpha^{CO_2}_{CH_4}$		P_{O_2}	P_{N_2}	$\Omega^{O_2}_{N_2}$	$\alpha^{O_2}_{N_2}$
3.1	0.0118	0.0038	3.14	2.63		0.0047	0.0034	1.40	1.33
3.2	0.0193	0.0064	3.00	2.53		0.0080	0.0057	1.42	1.34
3.3	0.0171	0.0065	2.62	2.25		0.0085	0.0064	1.33	1.27
3.4	0.0377	0.0265	1.42	1.34		0.0308	0.0288	1.07	1.06
3.5									

P = Permeability X 10^4 (cm^3(STP)/s cm^2 cmHg)

Ω = Selectivity

α = Separation Factor

Table B7. Coated[a] Fibres - Campaign 3

Pure Gas Permeation Results

Run	P CO_2	P CH_4	P O_2	P N_2	Ω_{CO_2/CH_4}	Ω_{O_2/N_2}
3.1	0.0077	0.0022	0.0031	0.0022	3.50	1.41
3.2	0.0156	0.0031	0.0044	0.0026	5.03	1.69
3.3	0.0172	0.0037	0.0048	0.0035	4.65	1.37
3.4	0.0193	0.0062	0.0126	0.0051	3.11	2.47
3.5						

[a] Coating Solution - 3% w/w Silicone in Hexane

P = Permeability x 10^4 (cm^3(STP)/s cm^2 cmHg)

Ω = Selectivity

Table B8. Coated[a] Fibres - Campaign 3

Gas Mixture Permeation Results

Run	P_{CO_2}	P_{CH_4}	$\Omega^{CO_2}_{CH_4}$	$\alpha^{CO_2}_{CH_4}$		P_{O_2}	P_{N_2}	$\Omega^{O_2}_{N_2}$	$\alpha^{O_2}_{N_2}$
3.1	0.0047	0.0014	3.50	2.88		0.0031	0.0021	1.47	1.38
3.2	0.0125	0.0027	4.63	3.68		0.0048	0.0029	1.63	1.50
3.3	0.0114	0.0031	3.65	2.99		0.0052	0.0031	1.68	1.54
3.4	0.0199	0.0063	3.13	2.62		0.0129	0.0068	1.90	1.71
3.5									

[a] Coating Solution - 3% w/w Silicone in Hexane

P = Permeability X 10^4 (cm^3(STP)/s cm^2 cmHg)

Ω = Selectivity

α = Separation Factor

Table B9: Uncoated Fibres -- Campaign 4

Pure Gas Permeation Results

Run	P CO_2	P CH_4	P O_2	P N_2	Ω_{CO_2/CH_4}	Ω_{O_2/N_2}
4.1	127.6	223.1	148.7	161.0	0.57	0.92
4.2	110.6	164.5	112.4	131.4	0.67	0.86
4.3	18.59	17.13	54.45	61.90	1.09	0.88
4.4	47.50	37.82	53.80	64.30	1.26	0.84

P = Permeability x 10^4 (cm^3(STP)/s cm^2 cmHg)

Ω = Selectivity

Table B10. Uncoated Fibres - Campaign 4

Gas Mixture Permeation Results

Run	P_{CO_2}	P_{CH_4}	$\Omega^{CO_2}_{CH_4}$	$\alpha^{CO_2}_{CH_4}$		P_{O_2}	P_{N_2}	$\Omega^{O_2}_{N_2}$	$\alpha^{O_2}_{N_2}$
4.1	156.2	165.8	0.94	0.99		136.2	139.3	0.98	1.00
4.2	141.1	151.2	0.93	0.99		125.3	127.6	0.98	1.00
4.3	11.91	15.10	0.79	0.87		11.60	12.07	0.96	0.98
4.4	30.62	36.60	0.84	0.92		30.12	30.95	0.97	0.99

P = Permeability X 10^4 (cm^3(STP)/s cm^2 cmHg)

Ω = Selectivity

α = Separation Factor

Table B11. Coated[a] Fibres - Campaign 4

Pure Gas Permeation Results

Run	P CO_2	P CH_4	P O_2	P N_2	Ω CO_2 / CH_4	Ω O_2 / N_2
4.1						
4.2	1.704	0.472	0.418	0.257	3.61	1.63
4.3	1.063	0.263	0.266	0.181	4.04	1.47
4.4	0.726	0.128	0.157	0.077	5.67	2.04

[a] Coating Solution - 3% w/w Silicone in Hexane

P = Permeability x 10^4 (cm^3(STP)/s cm^2 cmHg)

Ω = Selectivity

Table B12. Coated[a] Fibres - Campaign 4

Gas Mixture Permeation Results

Run	P_{CO_2}	P_{CH_4}	$\Omega^{CO_2}_{CH_4}$	$\alpha^{CO_2}_{CH_4}$		P_{O_2}	P_{N_2}	$\Omega^{O_2}_{N_2}$	$\alpha^{O_2}_{N_2}$
4.1									
4.2	1.428	0.444	3.22	2.68		0.428	0.270	1.59	1.47
4.3	0.944	0.261	3.62	2.96		0.321	0.196	1.64	1.51
4.4	0.619	0.126	4.90	3.86		0.177	0.087	2.05	1.82

[a] Coating Solution - 3% w/w Silicone in Hexane

P = Permeability X 10^4 (cm^3(STP)/s cm^2 cmHg)

Ω = Selectivity

α = Separation Factor

Table B13. Uncoated Fibres - Campaign 7

Pure Gas Permeation Results

Run	P CO_2	P CH_4	P O_2	P N_2	CO_2 Ω CH_4	O_2 Ω N_2
7.1						
7.2	0.1760	0.3169	0.2248	0.2425	0.555	0.927
7.3						
7.4						
7.5						
7.6	0.0176	0.0244	0.0185	0.0188	0.721	0.984
7.7						
7.8						
7.9	0.1223	0.2118	0.1452	0.1581	0.577	0.918

P = Permeability x 10^4 (cm^3(STP)/s cm^2 cmHg)

Ω = Selectivity

Table B14. Uncoated Fibres - Campaign 7

Gas Mixture Permeation Results

Run	P_{CO_2}	P_{CH_4}	$\Omega^{CO_2}_{CH_4}$	$\alpha^{CO_2}_{CH_4}$		P_{O_2}	P_{N_2}	$\Omega^{O_2}_{N_2}$	$\alpha^{O_2}_{N_2}$
7.1	0.0090	0.0114	0.786	0.803		0.0112	0.0122	0.918	0.931
7.2	0.2175	0.2926	0.743	0.781		0.2495	0.2672	0.934	0.944
7.3	0.3668	0.4743	0.773	0.807		0.3627	0.3787	0.958	0.965
7.4	0.3532	0.4553	0.776	0.809		0.3599	0.3771	0.954	0.962
7.5	0.3707	0.4912	0.755	0.791		0.3890	0.4150	0.937	0.948
7.6	0.0174	0.0214	0.813	0.829		0.0203	0.0213	0.953	0.956
7.7	0.0391	0.0537	0.727	0.767		0.0444	0.0480	0.925	0.937
7.8	0.1799	0.2399	0.750	0.787		0.2089	0.2226	0.938	0.948
7.9	0.1369	0.1864	0.734	0.773		0.1408	0.1487	0.947	0.956

P = Permeability X 10^4 (cm^3(STP)/s cm^2 cmHg)

Ω = Selectivity

α = Separation Factor

Table B15. Coated[a] Fibres - Campaign 7

Pure Gas Permeation Results

Run	P CO_2	P CH_4	P O_2	P N_2	Ω_{CO_2/CH_4}	Ω_{O_2/N_2}
7.1						
7.2	0.0381	0.0763	0.0507	0.0590	0.499	0.859
7.3						
7.4						
7.5						
7.6	0.0086	0.0126	0.0080	0.0100	0.679	0.794
7.7						
7.8						
7.9	0.0314	0.0499	0.0354	0.0401	0.628	0.883

[a] Coating Solution - 3% w/w Silicone in Hexane

P = Permeability x 10^4 (cm^3(STP)/s cm^2 cmHg)

Ω = Selectivity

Table B16. Coated[a] Fibres - Campaign 7

Gas Mixture Permeation Results

Run	P_{CO_2}	P_{CH_4}	$\Omega^{CO_2}_{CH_4}$	$\alpha^{CO_2}_{CH_4}$		P_{O_2}	P_{N_2}	$\Omega^{O_2}_{N_2}$	$\alpha^{O_2}_{N_2}$
7.1	0.0040	0.0047	0.849	0.862		0.0040	0.0043	0.930	0.951
7.2	0.0545	0.0682	0.799	0.829		0.0477	0.0497	0.960	0.966
7.3	0.1074	0.1349	0.797	0.827		0.0985	0.1029	0.957	0.964
7.4	0.1018	0.1239	0.821	0.849		0.0829	0.0863	0.961	0.967
7.5	0.1223	0.1544	0.792	0.823		0.1156	0.1223	0.945	0.954
7.6	0.0103	0.0121	0.856	0.868		0.0108	0.0115	0.939	0.945
7.7	0.0146	0.0188	0.780	0.813		0.0149	0.0157	0.949	0.957
7.8	0.0384	0.0471	0.815	0.843		0.0332	0.0349	0.951	0.960
7.9	0.0387	0.0502	0.769	0.804		0.0261	0.0275	0.949	0.955

[a] Coating Solution - 3% w/w Silicone in Hexane

P = Permeability X 10^4 (cm^3(STP)/s cm^2 cmHg)

Ω = Selectivity

α = Separation Factor

Table B17. Coated[a] Fibres - Campaign 7

Pure Gas Permeation Results

Run	P CO_2	P CH_4	P O_2	P N_2	CO_2 Ω CH_4	O_2 Ω N_2
7.1						
7.2	0.0025	0.0022	0.0015	0.0017	1.15	0.858
7.3						
7.4	0.0073	0.0066	0.0046	0.0050	1.10	0.927
7.5						
7.6						
7.7	0.0017	0.0026	0.0014	0.0014	0.66	0.987
7.8	0.0022	0.0020	0.0015	0.0018	1.08	0.820
7.9						

[a] Coating Solution - 15% w/w Silicone in Hexane

P = Permeability x 10^4 (cm^3(STP)/s cm^2 cmHg)

Ω = Selectivity

Table B18. Uncoated Fibres - Campaign 8

Pure Gas Permeation Results

Run	P CO_2	P CH_4	P O_2	P N_2	CO_2 Ω CH_4	O_2 Ω N_2
8.1						
8.2	0.0141	0.0073	0.0074	0.0060	1.92	1.23
8.3	0.0605	0.0695	0.0533	0.0515	0.87	1.03
8.4						
8.5						
8.6	0.0107	0.0044	0.0054	0.0036	2.43	1.49
8.7						
8.8						

P = Permeability x 10^4 (cm^3(STP)/s cm^2 cmHg)

Ω = Selectivity

Table B19. Coated[a] Fibres - Campaign 8

Pure Gas Permeation Results

Run	P CO_2	P CH_4	P O_2	P N_2	CO_2 Ω CH_4	O_2 Ω N_2
8.1						
8.2	0.0144	0.0035	0.0055	0.0031	4.13	1.77
8.3						
8.4						
8.5						
8.6	0.0095	0.0030	0.0042	0.0023	3.21	1.87
8.7						
8.8						

[a] Coating Solution - 3% w/w Silicone in Hexane

P = Permeability x 10^4 (cm^3(STP)/s cm^2 cmHg)

Ω = Selectivity

Table B20. Coated[a] Fibres - Campaign 8

Pure Gas Permeation Results

Run	P CO_2	P CH_4	P O_2	P N_2	CO_2 Ω CH_4	O_2 Ω N_2
8.1						
8.2	0.0094	0.0027	0.0038	0.0025	3.48	1.54
8.3	0.0144	0.0036	0.0060	0.0045	4.06	1.32
8.4						
8.5						
8.6	0.0093	0.0018	0.0035	0.0017	5.29	2.06
8.7						
8.8						

[a] Coating Solution - 15% w/w Silicone in Hexane

P = Permeability x 10^4 (cm^3(STP)/s cm^2 cmHg)

Ω = Selectivity

Table B21. Uncoated Fibres - Campaign 9

Pure Gas Permeation Results

Run	P_{CO_2}	P_{CH_4}	P_{O_2}	P_{N_2}	Ω_{CO_2/CH_4}	Ω_{O_2/N_2}
9.1	0.0161	0.0089	0.0084	0.0068	1.82	1.24
9.2	0.0383	0.0172	0.0189	0.0131	2.23	1.44

P = Permeability x 10^4 (cm^3(STP)/s cm^2 cmHg)

Ω = Selectivity

Table B22. Coated[a] Fibres - Campaign 9

Pure Gas Permeation Results

Run	P CO_2	P CH_4	P O_2	P N_2	CO_2 Ω CH_4	O_2 Ω N_2
9.1	0.0140	0.0042	0.0065	0.0041	3.30	1.58
9.2	0.0298	0.0062	0.0128	0.0057	4.83	2.25

[a] Coating Solution - 3% w/w Silicone in Hexane

P = Permeability x 10^4 (cm^3(STP)/s cm^2 cmHg)

Ω = Selectivity

Table B23. Coated[a] Fibres - Campaign 9

Pure Gas Permeation Results

Run	P CO_2	P CH_4	P O_2	P N_2	Ω_{CO_2/CH_4}	Ω_{O_2/N_2}
9.1	0.0121	0.0036	0.0056	0.0034	3.36	1.65
9.2	0.0244	0.0046	0.0093	0.0045	5.32	2.05

[a] Coating Solution - 15% w/w Silicone in Hexane

P = Permeability x 10^4 (cm^3(STP)/s cm^2 cmHg)

Ω = Selectivity

Appendix C Intrinsic Viscosity Results

Table C1. Polyacrylonitrile (P82)

Intrinsic Viscosity Results

Conc^n c (g/dl)	Flow Time t (s)	Relative Viscosity $\eta_R = \frac{t}{t_o}$ (--)	Specific Viscosity $\eta_{Sp} = \eta_R - 1 = \frac{t - t_o}{t_o}$ (--)	Reduced Viscosity $\eta_{Red} = \frac{\eta_{Sp}}{C}$ (dl/g)
0.25	123.56	1.359	0.359	1.437
0.20	118.46	1.303	0.303	1.515
0.15	110.51	1.216	0.216	1.437
0.10	104.13	1.145	0.145	1.454
0.05	97.89	1.077	0.077	1.536
0.02	93.51	1.029	0.029	1.430

Temperature: 25 ^oC

Solvent: Dimethylformamide

Pure Solvent Flow Time, t_o = 90.91 s

Intrinsic Viscosity, $[\eta] = (\eta_{Red})_{C=0} = 1.443 \ \frac{dl}{g}$

Table C2. Polysulphone (P1700)

Intrinsic Viscosity Results

Conc^n C (g/dl)	Flow Time t (s)	Relative Viscosity $\eta_R = \frac{t}{t_o}$ (--)	Specific Viscosity $\eta_{Sp} = \eta_R - 1 = \frac{t - t_o}{t_o}$ (--)	Reduced Viscosity $\eta_{Red} = \frac{\eta_{Sp}}{C}$ (dl/g)
0.949	126.7	1.371	0.371	0.391
0.759	118.4	1.281	0.281	0.371
0.569	111.2	1.203	0.203	0.357
0.380	104.2	1.128	0.128	0.337
0.190	98.0	1.061	0.061	0.319
0.133	95.5	1.034	0.034	0.253

Temperature: 25 ^oC

Solvent: Dimethylformamide

Pure Solvent Flow Time, t_o = 92.40 s

Intrinsic Viscosity, $[\eta] = (\eta_{Red})_{C=0} = 0.267 \ \frac{dl}{g}$

Table C3. Polysulphone (P3500)

Intrinsic Viscosity Results

Conc^n c (g/dl)	Flow Time t (s)	Relative Viscosity $\eta_R = \frac{t}{t_o}$ (--)	Specific Viscosity $\eta_{Sp} = \eta_R - 1 = \frac{t - t_o}{t_o}$ (--)	Reduced Viscosity $\eta_{Red} = \frac{\eta_{Sp}}{C}$ (dl/g)
0.949	128.8	1.394	0.394	0.415
0.759	120.3	1.302	0.302	0.398
0.569	111.6	1.208	0.208	0.365
0.380	104.7	1.133	0.133	0.351
0.190	97.8	1.058	0.058	0.308
0.133	96.1	1.040	0.040	0.302

Temperature: 25 ^oC

Solvent: Dimethylformamide

Pure Solvent Flow Time, t_o = 92.40 s

Intrinsic Viscosity, $[\eta] = (\eta_{Red})_{C=0} = 0.291 \frac{dl}{g}$

Appendix D Computer Model - Flow of a Power Law Fluid Through an Annulus

A listing of the flow program, written in Microsoft Quick Basic, can be found in the pages following.

The enclosed floppy disk, located in the back cover recess, contains the program in 'stand alone' form. To run the software simply type 'EXTRUDE' at the DOS prompt and follow the input instructions. An ASCII code data file will be produced **(Table 5.1)** containing the results.

Due to its iterative nature, the program may take up to half an hour to run depending on the personal computer used.

Computer Model - Flow of a Power Law Fluid Through an Annulus

```
DEFSNG A-Z
DECLARE FUNCTION CFT! (Incr.N%, N.Stps%)
DECLARE FUNCTION EXPR! (Vrbl!)
DECLARE FUNCTION FINDLAMDA! ()
DECLARE FUNCTION NUMINT! (Low.Lim!, Up.Lim!, N.Strps%)
DECLARE FUNCTION VELDIFF! (Lmda!)
COMMON SHARED Flag%, Lamda, Lamda.tp2

REM Inputs are converted to SI immediately
INPUT "Enter name of data file (Drive:Filename.Ext) ", File$
INPUT "Enter Inner Radius of Annulus (mm) ", I1: Rad.In = I1 / 1000
INPUT "Enter Outer Radius of Annulus (mm) ", I2: Rad.Out = I2 / 1000
INPUT "Enter Spinneret Length (mm) ", I3: L.Spin = I3 / 1000
INPUT "Enter Power Law Index (--) ", Ind
INPUT "Enter Power Law Constant (based on SI units) ", C
INPUT "Enter Dope Density (g/cm3) ", I4: Den = I4 * 1000
INPUT "Enter Dope Extrusion Rate (cm3/min) ", I5: D.E.R. = I5 / 6E+07
Index = 1 / Ind
Sigma = I1 / I2

CONST Grav = 9.81
CONST Pi = 3.141593
CONST N.VPnt.I% = 100: REM Number of velocity point intervals.
CONST N.V.Subs% = 10: REM Base number of subdivisions for velocity calcn.
Int.Sz = (1 - Sigma) / N.VPnt.I%
DIM Rad(N.VPnt.I%): DIM Vel(N.VPnt.I%): DIM Rad.vel(N.VPnt.I%): DIM Radius(N.VPnt.I%)
DIM Velocity(N.VPnt.I%): DIM S.Stress(N.VPnt.I%): DIM S.Rate(N.VPnt.I%)

Lamda = FINDLAMDA
Lamda.tp2 = Lamda * Lamda

REM Module Level Program to Calculate Parameter Arrays
qq = 0
FOR k% = 0 TO N.VPnt.I%
Epsilon = Sigma + (k% * Int.Sz)
IF Epsilon = Sigma OR Epsilon > 1 - (Int.Sz / 2) THEN GOTO Atwalls
IF Epsilon <= Lamda THEN Flg% = 0 ELSE Flg% = 1
SELECT CASE Flg%
    CASE 0
       Flag% = 0
       uz = NUMINT(Sigma, Epsilon, (N.V.Subs% * k%))
    CASE 1
       Flag% = 1
       uz = NUMINT(Epsilon, 1, (N.V.Subs% * k%))
END SELECT
GOTO Setarrays
Atwalls:
uz = 0
Setarrays:
Rad(k%) = Epsilon
Vel(k%) = uz
Rad.vel(k%) = Epsilon * uz

qq = qq + (Rad.vel(k%) * CFT(k%, N.VPnt.I%))

NEXT k%
```

```
q = (Int.Sz / 3) * qq
Rad.Out.tp3 = Rad.Out * Rad.Out * Rad.Out
P = ((D.E.R. / (2 * Pi * Rad.Out.tp3 * q)) ^ Ind) * ((2 * C) / Rad.Out)
DPDZ = (Den * Grav) - P
Delta.P = L.Spin * DPDZ

FOR L% = 0 TO N.VPnt.I%
Radius(L%) = Rad(L%) * Rad.Out
Velocity(L%) = (((P * Rad.Out) / (2 * C)) ^ Index) * Rad.Out * Vel(L%)
S.Stress(L%) = ABS(((P * Rad.Out) / 2) * ((Lamda.tp2 / Rad(L%)) - Rad(L%)))
S.Rate(L%) = (S.Stress(L%) / C) ^ Index
NEXT L%

Rad.TO = Lamda * Rad.Out
Flag% = 0
Max.Vel = (((P * Rad.Out) / (2 * C)) ^ Index) * Rad.Out * NUMINT(Sigma, Lamda, 100)

REM Output (Converting to output units from SI where appropriate)

OPEN File$ FOR OUTPUT AS £1
PRINT £1, "Inner Radius of Annulus "; I1; "(mm)"
PRINT £1, "Outer Radius of Annulus "; I2; "(mm)"
PRINT £1, "Spinneret Length "; I3; "(mm)"
PRINT £1, "Power Law Index "; Ind; "(--)"
PRINT £1, "Power Law Constant "; C; "(Based on SI units)"
PRINT £1, "Dope Density "; I4; "(g/cm3)"
PRINT £1, "Dope Extrusion Rate "; I5; "(cm3/min)"
PRINT £1, ""
PRINT £1, "Radius at Zero Stress";
PRINT £1, USING "£££.££££"; 1000 * Rad.TO;
PRINT £1, " (mm)"
PRINT £1, "Maximum Velocity";
PRINT £1, USING "£££.££££"; 100 * Max.Vel;
PRINT £1, " (cm/s)"
PRINT £1, ""
PRINT £1, "Pressure Drop Across Spinneret";
PRINT £1, USING "£££.££££"; -Delta.P / 100000;
PRINT £1, " (bar)"
PRINT £1, ""
PRINT £1, ""
PRINT £1, "    Radius  Velocity  S.Stress    S.Rate"
PRINT £1, "     (mm)    (cm/s)    (N/m2)     (1/s)"
PRINT £1, ""
FOR m% = 0 TO N.VPnt.I% STEP 2
PRINT £1, USING "  £££.££££"; 1000 * Radius(m%); 100 * Velocity(m%);
PRINT £1, USING "  ££££££££"; S.Stress(m%); S.Rate(m%)
NEXT m%
CLOSE £1
```

```
REM Graph Plotting

SCREEN 10
FOR V.Point = 0 TO N.VPnt.I%
PSET ((560 / Rad.Out) * (Radius(V.Point)), 340 - ((330 / Max.Vel) * (Velocity(V.Point))))
NEXT V.Point

IF S.Stress(0) >= S.Stress(N.VPnt.I%) THEN S.S.Max = S.Stress(0) ELSE S.S.Max = S.Stress(N.VPnt.I%)
SCREEN 10
FOR S.S.Point = 0 TO N.VPnt.I%
PSET ((560 / Rad.Out) * (Radius(S.S.Point)), 340 - ((330 / S.S.Max) * (S.Stress(S.S.Point))))
NEXT S.S.Point

IF S.Rate(0) >= S.Rate(N.VPnt.I%) THEN S.R.Max = S.Rate(0) ELSE S.R.Max = S.Rate(N.VPnt.I%)
SCREEN 10
FOR S.R.Point = 0 TO N.VPnt.I%
PSET ((560 / Rad.Out) * (Radius(S.R.Point)), 340 - ((330 / S.R.Max) * (S.Rate(S.R.Point))))
NEXT S.R.Point

FOR Delay2 = 0 TO 200000
NEXT Delay2

FUNCTION CFT (Incr.N%, N.Stps%)
IF (Incr.N% / 2 - Incr.N% \ 2) THEN CFT = 4 ELSE CFT = 2
IF Incr.N% = 0 OR Incr.N% = N.Stps% THEN CFT = 1
END FUNCTION

FUNCTION EXPR (Vrbl)
SHARED Index
SELECT CASE Flag%
    CASE 0
       EXPR = (ABS((Lamda.tp2 / Vrbl) - Vrbl)) ^ Index
    CASE 1
       EXPR = (ABS(Vrbl - (Lamda.tp2 / Vrbl))) ^ Index
END SELECT
END FUNCTION

FUNCTION FINDLAMDA
SHARED Sigma
Grd.Divs = 10
Tol = .001 * (1 - Sigma)
Srch.R1 = Sigma
Srch.R2 = 1
```

```
Start.Srch:
V.diff1 = VELDIFF(Srch.R1)
V.Diff2 = VELDIFF(Srch.R2)
Top = V.diff1: Cnt = 0
Step.Sz = (Srch.R2 - Srch.R1) / Grd.Divs
FOR j = 1 TO Grd.Divs
Pnt = VELDIFF(Srch.R1 + (j * Step.Sz))
IF Pnt >= Top THEN GOTO Outloop
Top = Pnt: Cnt = j
NEXT j
Outloop:
In.Wall.Stpr = Srch.R1
Out.Wall.Stpr = Srch.R2
Srch.R1 = In.Wall.Stpr + ((Cnt - 1) * Step.Sz)
Srch.R2 = In.Wall.Stpr + ((Cnt + 1) * Step.Sz)
IF Cnt = 0 AND In.Wall.Stpr = Sigma THEN Srch.R1 = Sigma
IF Cnt = Grd.Divs AND Out.Wall.Stpr = 1 THEN Srch.R2 = 1
IF Step.Sz < (.5 * Tol) THEN GOTO End.Srch
GOTO Start.Srch

End.Srch:
FINDLAMDA = Srch.R1 + ((Srch.R2 - Srch.R1) / 2)
END FUNCTION

FUNCTION NUMINT (Low.Lim, Up.Lim, N.Strps%)
Sum = 0
Strp.Sz = (Up.Lim - Low.Lim) / N.Strps%
FOR i% = 0 TO N.Strps%
Var = Low.Lim + (Strp.Sz * i%)
Sum = Sum + (EXPR(Var) * CFT(i%, N.Strps%))
NEXT i%
NUMINT = (Strp.Sz / 3) * Sum
END FUNCTION

FUNCTION VELDIFF (Lmda)
SHARED Sigma
Lamda.tp2 = Lmda * Lmda
N.Subs% = 100
Flag% = 0
Area.In = NUMINT(Sigma, Lmda, N.Subs%)
Flag% = 1
Area.Out = NUMINT(Lmda, 1, N.Subs%)
VELDIFF = ABS(Area.In - Area.Out)
END FUNCTION
```

References

REFERENCES

1. Mitchell, J.K., *Philadelphia J. Med. Sci.*, **13**, 36 (1831).
   or
   Mitchell, J.K., *Royal Inst. J.*, **2**, 101, 307 (1831).
2. Fick, A., *Ann. Physik. Chem.*, **94**, 59 (1855).
3. Schönbein, C., G.B. Pat. 11,402 (1846).
4. Graham, T., *Phil. Mag.*, **32**, 401 (1866).
5. von Wroblewski, S., *Weid. Ann. Physik.*, **8**, 29 (1879).
6. Loeb, S. and Sourirajan, S., *Adv. Chem. Ser.*, **38**, 117 (1962).
7. Robinson, W.T. and Mattson, R.J., *J. Water Pollut. Contr. Fed.*, **40**, 439 (1968).
8. Maxwell, J.M., Moore, W.E. and Rego, R.D., U.S. Pat. 3,339,341 (1967).
9. Monsanto Co., U.S. Pat. 4,214,020 (1980).
10. Monsanto Co., G.B. Pat. 1,590,813 (1977).
11. Cabasso, I., Enc. Chem. Tech., 3rd Edn., Ed. Kirk, R.E. and Othmer, D.F., Wiley Interscience, **12**, 492-517 (1980).
12. Monsanto Co., G.B. Pat. 2,047,162A (1980).
13. Aptel, P., Abidine, N., Ivaldi, F. and Lafaille, J.P., *J. Membr. Sci.*, **22**, 199-215 (1985).
14. Espenan, J.M. and Aptel, P., 'Membranes and Membrane Processes', Ed. Drioli, E. and Nakagaki, M., Plenum Press, 151-161 (1986).

15. Cheryan, M., 'Ultrafiltration Handbook', Technomic Publ., (1986).

16. Sourirajan, S. and Matsuura, T., 'Reverse Osmosis and Ultrafiltration', A.C.S. Symp. Ser., (1985).

17. Wojcik, C.K., *Desalination*, **46**, 17-34 (1983).

18. Chae, Y.C., Legendre, G.S. and van Gelder, J.M., Hydrogen Recovery from Ammonia Purge Gas using Hollow Fibre Gas Separators, Monsanto Internal Communications, (1982).

19. Maciula, E.A., *Hydrocarbon Processing*, N° 5, 115-118 (1980).

20. Schendel, R.L., Mariz, C.L. and Mak, J.Y., *Hydrocarbon Processing*, **62**(8), 58 (1983).

21. Bollinger, W.A., MacLean, D.L. and Narayan, R.S., *Chem. Eng. Prog.*, **78**(10), 27-32 (1982).

22. Stern, S.A. and Wang, S.-C., *AIChE J.*, **26**, 891 (1980).

23. Pan, C.-Y. and Habgood, H.W., *Can. J. Chem. Eng.*, **56**, 197-209 (1978).

24. Hwang, S.-T. and Thorman, J.M., *AIChE J.*, **26**, 558-566 (1980).

25. M^{c} Hattie, J.S., Koros, W.J. and Paul, D.R., *Polymer*, **32**(5), 840-850 (1991).

26. Hellums, M.W., Koros, W.J., Husk, G.R. and Paul, D.R., *J. Membr. Sci.*, **46**, 93 (1989).

27. Scott, J., 'Hollow Fibers Manufacture and Applications', Chem. Tech. Review N° 194, Noyes Data Corp., (1981).

28. Monsanto Co., G.B. Pat. 1,305,330 (1970).

29. Monsanto Co., G.B. Pat. 2,100,181 (1980).

30. Du Pont de Nemours, E.I., and Co., Eur. Pat. 179,474 A2 (1986).

31. Henis, J.M.S. and Tripodi, M.K., *J. Membr. Sci.*, **8**, 233-246 (1981).

32. Kramer, P.W. and Yasuda, H., *Polym. Mater. Sci. Eng.*, **56**, 812-816 (1987).

33. Sumitomo Chemical Co., Ltd., G.B. Pat. 2,089,285A (1982).

34. Rautenbach, R. and Albrecht, R., 'Membrane Processes', Wiley, (1989).

35. Cabasso, I. and Lundy, K.A., State Univ. of New York, Research Found., Eur. Pat. 181,772 A2 (1986).

36. Senn, S.C., Ph.D Thesis, University of Leeds, (1988).

37. Monsanto Co., U.S. Pat. 4,654,055A (1987).

38. Koresh, J.E. and Soffer, A., 16th Carbon Conference, Bienn, 367-8 (1983).

39. Henis, J.M.S. and Tripodi, M.K., *Sepn. Sci. and Techn.*, **15**(4), 1059-1068 (1980).

40. East, G.C., M^{c} Intyre, J.E., Rogers, V. and Senn, S.C., '4th BOC Priestly Conference', Royal Soc. of Chem., 130-144 (1986).

41. Borneman, Z., van t'Hof, J.A., Smolders, C.A. and van Veen, H.M., '4th BOC Priestly Conference', Royal Soc. of Chem., 145-157 (1986).

42. de Groot, S.R. and Mazur, P., 'Non-equilibrium Thermodynamics', North-Holland, Amsterdam, (1962).

43. Meares, P., *J. Am. Chem. Soc.*, **76**, 3415 (1954).

44. Newman, A.B., *Trans. AIChE*, **27**, 203, 310 (1931).

45. Daynes, H., *Proc. Roy. Soc. London, Ser. A*, **97A**, 286 (1920).

46. Barrer, R., *Trans. Faraday Soc.*, **35**, 628 (1939).

47. Crank, J., 'Mathematics of Diffusion', 2nd Edn., Oxford University Press, London, (1975).

48. Stern, S.A., 'Industrial Processing with Membranes', Ed. Lacey, R.E., and Loeb, S., Wiley Interscience, 279-339 (1972).

49. Stern, S.A. and Frisch, H.L., *Ann. Rev. Mater. Sci.*, **11**, 523-550 (1981).

50. Rogers, C.E., Fels, M. and Li, N.N., 'Recent Developments in Separation Science', Ed. Li, N.N., CRC Press, **2**, 107-155 (1972).

51. Vieth, W.R., Howell, J.M. and Hsieh, J.H., *J. Membr. Sci.*, **1**(2), 177-220 (1976).

52. Stannett, V.T., Koros, W.J., Paul, D.R., Lonsdale, H.K. and Baker, R.W., *Adv. Polymer Sci.*, **32**, 69-121 (1979).

53. Meares, P., '4th BOC Priestly Conference', Royal Soc. of Chem., 1-25 (1986).

54. Lonsdale, H.K., *J. Membr. Sci.*, **10**, 81-181 (1982).

55. Strathmann, H., 'Membranes and Membrane Processes', Ed. Drioli, E. and Nakagaki, M., Plenum Press, 115-135 (1986).

56. Strathmann, H., 'Materials Science of Synthetic Membranes', Ed. Lloyd, D.R., A.C.S. Symp. Ser., 165-195 (1985).

57. Kesting, R.E., 'Materials Science of Synthetic Membranes', Ed. Lloyd, D.R., A.C.S. Symp. Ser., 131-164 (1985).

58. Kesting, R.E., 'Synthetic Polymeric Membranes', Wiley, (1985).

59. Ziabicki, A., 'Fundamentals of Fibre Formation', Wiley, (1976).

60. Paul, D.R., *J. Appl. Polymer Sci.*, **13**, 817 (1969).

61. Barakat, N. and Hindeleh, A.M., *Textile Res. J.*, **34**, 581 (1964).

62. Perepelkin, K.E. and Pugatch, B.M., *Khimicheskiye Volokna* (1), 48 (1974).

63. Orofino, T.A., 'Reverse Osmosis and Synthetic Membranes', Ed. Sourirajan, S., National Research Council Canada, 313-341 (1977).

64. Monsanto Co., U.S. Pat. 4,493,629 (1985).

65. Brandrup, J. and Immergut, E.H., 'Polymer Handbook', 2nd Edn., Wiley Interscience, (1975).

66. Turbak, A.F., 'Synthetic Membranes: Desalination', A.C.S. Symp. Ser., (1981).

67. Ferguson, J. and Hudson, N.E., Private Communication - to be Published.

68. Hudson, N.E., Ferguson, J. and Mackie, P., *Trans. Soc. Rheol.*, **18**, 541 (1974).

69. Ferguson, J. and Hudson, N.E., *J. Physics (E)*, **8**, 526 (1975).

70. Hudson, N.E. and Ferguson, J., *Trans. Soc. Rheol.*, **20**, 265 (1976).

71. Jackson, K.P., Walters, K. and Williams, R.W., *J. Non-Newtonian Fluid Mechanics*, **14**, 173-188 (1974).

72. Jones, D.M., Walters, K. and Williams, P.R., *Rheol. Acta*, **26**, 20 (1987).

73. Trouton, F.T., *Proc. R. Soc.*, **A77**, 426-440 (1906).

74. Cantor, M., *Ann. Phys. (Newfoundland)*, **47**, 399 (1892).

75. ASTM, *Method 316-70*, (1976).

76. Brock, S.D., 'Membrane Filtration. A User's Guide and Reference Manual', Sci.-Tech, Inc., Madison, WI (1983).

77. Kujawski, W., Adamczak, P. and Narebska, A., *Sepn. Sci. and Techn.*, **24**(7&8), 495-506 (1989).

78. Yasuda, H. and Tsai, J.T., *J. Appl. Polymer. Sci.*, **18**, 805-819 (1974).

79. Fredrickson, A.G. and Bird, R.B., *Ind. Eng. Chem.*, **50**(5), 347 (1958).

80. Russell, C.P. and Christiansen, E.B., *Ind. Eng. Chem. Process Des. Dev.*, **13**, 391 (1974).

81. Hanks, R.W. and Larsen, K.M., *Ind. Eng. Chem. Fundam.*, **18**, 33 (1979).

82. Kirk, A.D., *J. Chem. Education*, **44**(12), 745-750 (1967).

83. Barrer, R.M., 'Diffusion in and through Solids', Cambridge Univ. Press, (1951).

84. Treybal, R.E., 'Mass-Transfer Operations', 3rd Edn., M^{c}Graw-Hill, (1981).

85. Chern, R.T., Koros, W.J., Hopfenberg, H.B. and Stannett, V.T., 'Materials Science of Synthetic Membranes', Ed. Lloyd, D.R., A.C.S. Symp. Ser., 25-46 (1985).

86. Allen, S.M., Fujii, M., Stannett, V., Hopfenberg, H.B. and Williams, J.L., *J. Membr. Sci.*, **2**, 153 (1977).

87. Robb, W.L., *Ann. N.Y. Acad. Sci.*, **146**, 119-137 (1967).

88. Present, R.D. and de Béthune, J.A., *Phys. Rev.*, **75**, 1050-1057 (1949).

89. Dushman, S., 'Scientific Foundations of Vacuum Techniques', 2nd Edn., Wiley, New York, (1962).

90. Sourirajan, S. and Agrawal, J.P., 'Reverse Osmosis and Synthetic Membranes', Ed. Sourirajan, S., National Research Council Canada, 527-540 (1977).

91. Moore, W.J., 'Physical Chemistry', 5th Edn., Longman, (1972).

Enclosure: Computer Model - Flow of a Power Law Fluid Through an Annulus